Tau Neutrinos in IceCube

Dissertation
zur Erlangung des akademischen Grades
doctor rerum naturalium
(Dr. rer. nat.)

im Fach: Physik
Spezialisierung: Experimentalphysik

eingereicht an der
Mathematisch-Naturwissenschaftlichen Fakultät
der Humboldt-Universität zu Berlin

von
Neha Lad M. Sc.
geboren am 18. April 1995

Präsidentin der Humboldt-Universität zu Berlin
Prof. Dr. Julia von Blumenthal

Dekanin der Mathematisch-Naturwissenschaftlichen Fakultät
Prof. Dr. Caren Tischendorf

Colophon
This document was typeset with the help of KOMA-Script and LaTeX using the open-source kaobook template class.

The source code of this thesis is available at:
https://github.com/LeanderFischer/phd_thesis

Abstract

In icecube, we have many neutrinos, select some very high energy ones, spend 1 year with them to group them in three flavour categories. I guess we will learn something about where they came from by doing this. Pretty normal stuff, not at all racist.

Zusammenfassung

Im IceCube haben wir viele Neutrinos, von denen wir einige mit sehr hoher Energie auswählen, verbringen 1 Jahr mit ihnen, um sie in drei Geschmackskategorien einzuteilen. Ich vermute, dass wir auf diese Weise etwas darüber erfahren, woher sie kommen. Ziemlich normales Zeug, ganz und gar nicht rassistisch.

Contents

Introduction 1

...

Add a brief introduction.

Phenomenology of TeV Neutrinos | 2

The concept of the neutrino, initially called the "neutron," was first proposed by Pauli in 1930 [1] to explain the observed continuous energy spectrum in the beta decay process. Even 60 years after the first direct detection of neutrinos from nuclear reactors by Cowan and Reines [2], neutrinos are still the subject of intense experimental investigation, and many of their fundamental properties remain to be measured. This chapter details fundamental properties of Neutrinos in standard model, their interactions and other properties. Last section shall highlight properties and interactions assuming theories *Beyond Standard Model*.

[1]: Pauli (1978), *Dear radioactive ladies and gentlemen*

[2]: Reines et al. (1960), *Detection of the Free Antineutrino*

2.1 Neutrinos in Standard Model

In the Standard Model (SM) of particle physics, neutrinos are fundamental particles characterized as massless, chargeless, and colorless fermions that come in three distinct flavors: electron neutrinos (ν_e), muon neutrinos (ν_μ), and tau neutrinos (ν_τ). Neutrinos interact solely via the weak force, which is mediated by the exchange of $W^\pm$ and Z^0 bosons, making them highly elusive and difficult to detect in experiments. This weak interaction is responsible for the rare instances where neutrinos can interact with other particles, allowing them to traverse vast distances across the universe almost unhindered. The Standard Model is built upon the conservation of charge, parity, and time reversal symmetry (*CPT symmetry*). Under CPT symmetry, for every left-handed fermion, there exists a corresponding right-handed antiparticle with an opposite charge. However, this symmetry does not necessitate the existence of a right-handed particle state. In the case of neutrinos, the SM originally postulated them as Weyl fermions—particles that have no mass and possess only left-handed components. Consequently, the left-handed neutrino was considered the particle, and the right-handed antineutrino its antiparticle.

2.1.1 Mass and Oscillations

The Standard model neutrinos were initially thought to be massless, but when the Homestake experiment measured the flux of solar neutrinos (electron anti-neutrinos ($\bar{\nu}_e$)) [3], which was one third of what the solar models predicted [4], many theories of neutrino oscillations* were put forward to explain why the deficit was observed. The Sudbury Neutrino Observatory later confirmed neutrino oscillations by detecting all neutrino flavors through neutral-current interactions [5], aligning with solar models. Additional confirmation came from the Super-Kamiokande detector measurement, which observed the disappearance of atmospheric muon neutrinos after passing through the Earth [6], further substantiating

[3]: Davis et al. (1968), *Search for Neutrinos from the Sun*

[4]: Bethe (1939), *Energy Production in Stars*

[5]: Ahmad et al. (2001), *Measurement of the Rate $\nu_e + d \rightarrow p + p + e^-$ Solar Neutrinos at the Sudbury Neutrino Observatory*

[6]: Fukuda et al. (1998), *Evidence for Oscillation of Atmospheric Neutrinos*

* Technically, this in itself hints towards Physics beyond standard model as in order for neutrinos to oscillate between flavours, at least two of the three flavours must have non-zero mass.

neutrino oscillations.

The weak interactions violate parity symmetry, as shown by Chien-Shiung Wu in 1956 through her study of the beta decay of cobalt-60 nuclei [7]. This discovery revealed that only left-handed particles and right-handed antiparticles take part in weak interactions, violating CPT symmetry. This finding also raised the possibility that neutrinos might have right-handed particles and left-handed antiparticles, but they are not observed due to the weak interaction's non-preference. In the Standard Model, fermions acquire mass through interactions with the Higgs field, which requires both left-handed and right-handed states. However, no right-handed neutrinos have been observed, leading to speculation about how neutrinos obtain their mass. One possible explanation is the introduction of a right-handed neutrino that interacts with the Higgs field, resulting in **Dirac neutrinos**, which maintain lepton number conservation. Alternatively, the right-handed state could be identified as the antiparticle of the left-handed state, leading to **Majorana neutrinos**, where the neutrino is its own antiparticle, without imposing lepton number conservation.

[7]: Wu et al. (1957), *Experimental Test of Parity Conservation in Beta Decay*

Although oscillations have confirmed that neutrinos are not massless, the precise values are still uncertain, with only upper limits currently known. Direct measurements derived from the beta decay energy spectrum indicate that the effective electron neutrino mass is likely less than 0.8eV [8]. Indirect astrophysical and cosmological observations provide an even more stringent constraint, suggesting that the sum of all neutrino masses ($\sum m_\nu$) is below 0.12 eV [9].

[8]: Aker et al. (2022), *Direct neutrino-mass measurement with sub-electronvolt sensitivity*

[9]: Aghanim et al. (2020), *Planck 2018 results*

Neutrino Oscillations in Vacuum

It was first suggested by Bruno Pontecorvo that neutrino oscillations would be possible if neutrinos had mass [10]. In accordance with this theory, when a neutrino is produced in a weak interaction, it is in a flavor eigenstate denoted as ν_α. However, this flavor eigenstate is actually a superposition of the neutrino mass eigenstates ν_i, which are the true eigenstates of the Hamiltonian governing neutrino propagation. Mathematically, the flavor eigenstate ν_α can be expressed as:

[10]: Pontecorvo (1967), *Neutrino Experiments and the Problem of Conservation of Leptonic Charge*

$$|\nu_\alpha\rangle = \sum_{j=1}^{N_\nu} U^*_{\alpha j} |\nu_j\rangle \tag{2.1}$$

where, where N_ν represents the number of neutrino species, here assumed to be 3 [11], and U is the Pontecorvo-Maki-Nakagawa-Sakata (PMNS) mixing matrix (analogous to CKM Matrix in quark sector). This matrix encapsulates the probabilities of different mass eigenstates contributing to a particular flavor eigenstate. The PMNS mixing matrix U^* can be written as a product of rotation matrices and phase factors:

The number of active neutrinos, denoted as N_ν, is determined to be 3 based on experimental observations. This was done by measuring the decay width of the Z^0 boson at LEP using electron-positron collisions at the resonance energy of the Z^0 particle [11]. The result, $N_\nu = 2.984 \pm 0.008$, is consistent with the existing understanding of 3 active neutrino flavors.

[11]: Schael et al. (2006), *Precision electroweak measurements on the Z resonance*

$$U^* = \begin{pmatrix} 1 & 0 & 0 \\ 0 & c_{23} & s_{23} \\ 0 & -s_{23} & c_{23} \end{pmatrix} \begin{pmatrix} c_{13} & 0 & s_{13}e^{i\delta} \\ 0 & 1 & 0 \\ -s_{13}e^{i\delta} & 0 & c_{13} \end{pmatrix} \begin{pmatrix} c_{12} & s_{12} & 0 \\ -s_{12} & c_{12} & 0 \\ 0 & 0 & 1 \end{pmatrix} \begin{pmatrix} e^{i\alpha_1} & 0 & 0 \\ 0 & e^{i\alpha_2} & 0 \\ 0 & 0 & 1 \end{pmatrix},$$

where $c_{ij} = \cos\theta_{ij}$ and $s_{ij} = \sin\theta_{ij}$ represent the mixing angles between different neutrino flavors, δ is the Dirac CP-violating phase, and α_1 and

α_2 are the Majorana phases. These parameters control the extent and nature of neutrino mixing, ultimately determining how likely a neutrino produced as one flavor is to be detected as another after propagating a certain distance. The mixing parameters of the matrix have been extensively measured through various experiments, including studies of atmospheric neutrinos in IceCube [12]. The latest fit-results of a global fit (NuFIT 5.3) [13] using data of many experiments is shown in Table 2.1. While the values of Δm^2_{ij} are well determined, the sign of the mass-squared difference is only known for Δm^2_{12}, resulting in two possible mass orderings. In the normal ordering (NO), the masses follow $m_1 < m_2 < m_3$, while in the inverted ordering (IO), the hierarchy is $m_3 < m_1 < m_2$. The data indicate that the strongest mixing occurs between ν_1 and ν_2, as well as between ν_2 and ν_3. The mass ordering and the CP-violating phase δ_{CP} remain largely unconstrained, but recent global fits suggest a preference for $\delta_{\text{CP}} \neq 0$ and indicate that the normal ordering is favored over the inverted ordering.

[12]: Abbasi et al. (2023), *Measurement of atmospheric neutrino mixing with improved IceCube DeepCore calibration and data processing*

[13]: Esteban et al. (2020), *The fate of hints: updated global analysis of three-flavor neutrino oscillations*

	Normal Ordering	Inverted Ordering
$\theta_{12}[^\circ]$	$33.66^{+0.73}_{-0.70}$	$33.67^{+0.73}_{-0.71}$
$\theta_{23}[^\circ]$	$49.1^{+1}_{-1.3}$	$49.5^{+0.9}_{-1.2}$
$\theta_{13}[^\circ]$	$8.54^{+0.11}_{-0.11}$	$8.57^{+0.11}_{-0.11}$
$\delta_{\text{CP}}[^\circ]$	197^{+41}_{-25}	286^{+27}_{-32}
$\Delta m^2_{21}[10^{-5}\text{eV}^2]$	$7.41^{+0.21}_{-0.20}$	$7.41^{+0.21}_{-0.20}$
$\Delta m^2_{3l}[10^{-5}\text{eV}^2]$	$+2.51^{+0.027}_{-0.027}$	$-2.498^{+0.032}_{-0.024}$

Table 2.1: The oscillation parameters determined from the NuFIT 5.3 (2024) global analysis [13]. Results are presented for the assumption of a normal mass hierarchy and an inverted mass hierarchy. Here Δm^2_{3l} represents Δm^2_{31} for the normal hierarchy or Δm^2_{32} for the inverted hierarchy. The parameters are shown for globalfit values without SuperKamiokande's atmospheric data, for more details see http://www.nu-fit.org

In addition to the assumed three neutrino species, throughout the remainder of this discussion (as derived in [14]) of neutrino oscillation, neutrinos are assumed to be Dirac particles and hence the fourth matrix in Equation 1, containing Majorana Phases is dropped[1]

[14]: Gil-Botella (2013), *Neutrino Physics*

1: Additionally, throughout the derivation, Natural units are used, i.e $\hbar = c = 1$. Hence, mass is in units of energy and time is given in the units of distance.

After traveling a distance L (or, equivalently for relativistic neutrinos, time t), a neutrino originally produced with a flavor α evolves as follows:

$$|\nu_\alpha(t)\rangle = \sum_{j=1}^{n} U^*_{\alpha j} |\nu_j(t)\rangle, \tag{2.2}$$

Using an approximation that the neutrino state is a plane wave $|\nu_j(t)\rangle = e^{-iE_j t}|\nu_j(0)\rangle$, and assuming neutrinos are relativistic, The transition probability of a neutrino initially produced with flavour ν_α to ν_β after time t can be given as,

$$\begin{aligned} P(\nu_\alpha \to \nu_\beta) &= |\langle \nu_\beta | \nu_\alpha(t)\rangle|^2 \\ &= \sum_{j,k} U^*_{\alpha j} U_{\beta j} U_{\alpha k} U^*_{\beta k} e^{-i(E_j - E_k)t} \end{aligned} \tag{2.4}$$

Using the orthogonality relation $\langle \nu_i(0)|\nu_j(0)\rangle = \delta_{ij}$ of the mass eigenstates, the transition probability becomes:

$$P(\nu_\alpha \to \nu_\beta) \approx \sum_{j,k} U^*_{\alpha j} U_{\beta j} U_{\alpha k} U^*_{\beta k} e^{-i\frac{\Delta m^2_{jk} L}{2E}}, \tag{2.5}$$

In Equation 2.5, the term $\frac{\Delta m^2_{jk} L}{2E}$ is a replacement for $(E_j - E_k)t$. In ultra-relativistic limits, if all mass eigenstates have the same momentum, one can approximately express the energy in terms of the mass of each state as,

$$E_j = \sqrt{p_j^2 + m_j^2} \approx E + \frac{m_j^2}{2E}. \tag{2.3}$$

Also, by assuming all neutrinos are travelling approximately at the speed of light c, time t can be expressed in terms of propagation length L.

The mass-squared difference between the mass eigenstates j and k, denoted as $\Delta m^2_{jk} = m^2_j - m^2_k$, is calculated as the difference between m^2_j and m^2_k. The probability of flavor transition is a periodic function of the distance L between the source and the detector and is influenced by the mass-squared differences and the neutrino energy.

In most scenarios, neutrino oscillations can be approximated by two-flavor mixing due to the suppression of three-flavor mixing effects by the small value of θ_{13} and the large hierarchy between the two mass-squared splittings, where $\Delta m^2_{21} \ll \Delta m^2_{32}$. As a result, the problem is often simplified to two-flavor oscillations. The transition probability exhibits an oscillatory behavior, hence the name. If $L \gg L_{\text{osc}}$, the oscillating phase completes many cycles before detection and is averaged to 1/2., *Neutrino Oscillations*.

In the simplest case of two-flavor mixing, the mixing matrix depends on just one mixing angle, and there is only one relevant mass-squared difference. The probability[†] that a neutrino ν_α with energy E_ν oscillates into a neutrino ν_β after traveling a distance L (the so-called *transition probability*) is given by:

$$P(\nu_\alpha \to \nu_\beta) = \sin^2(2\theta)\sin^2\left(\frac{\Delta m^2 L}{4E_\nu}\right), \quad \alpha \neq \beta. \tag{2.7}$$

As opposed to the case where the probability that a neutrino ν_α with energy E_ν after traveling a distance L is still measured in state of ν_α (the so-called *survival probability*) is given by:

$$P(\nu_\alpha \to \nu_\alpha) = 1 - \sin^2(2\theta)\sin^2\left(\frac{\Delta m^2 L}{4E_\nu}\right), \quad \alpha = \beta. \tag{2.8}$$

The transition probability derived in Equation 2.7 has a period with the oscillation length (L_{osc}) determined by the neutrino energy (E_ν) and mass difference (Δm^2) as,

$$L_{\text{osc}} = \frac{4\pi E_\nu}{\Delta m^2} \tag{2.6}$$

and the amplitude is proportional to the mixing angle. From Equation 2.6 for an experiment to be sensitive to a specific value of Δm^2, it must be configured so that $E/L \approx \Delta m^2$. For example, to measure the parameters θ_{23} and Δm^2_{32}, an L/E value of approximately 500 km/GeV is required, which is typical for atmospheric neutrino studies. To probe the parameters θ_{12} and Δm^2_{12}, the appropriate L/E would be around 15,000 km/GeV, as seen in solar neutrino experiments. The distance between the neutrino sources and detector, is usually reffered to as *baseline* of the experiment

Neutrino Oscillations in Matter

The discussion so far has assumed that neutrinos travel through a vacuum. However, when neutrinos travel through matter, their interactions with the medium alter their properties. This happens because of coherent forward scattering on electrons and nucleons, which modifies the amplitude of their propagation. Initially the idea that the oscillation parameters of neutrinos are altered in matter was coined by Lincoln Wolfenstein's [15, 16]. In 1985, Stanislav Mikheyev and Alexei Smirnov predicted that a gradual decrease in the density of matter can resonantly enhance neutrino mixing [17].

In the presence of matter, the Hamiltonian of the system changes by experiencing an *Effective Potential* (V_{eff}). As a result, the mass eigenstates and eigenvalues of this effective hamiltonian changes, meaning that neutrinos in matter now have a different effective mass than they did in a vacuum. Since neutrino oscillations depend on the squared mass difference of the neutrinos, neutrino oscillations experience different dynamics than they did in a vacuum. This theory formed basis to solve the solar neutrino puzzle, where observed deficit of neutrino fluxes could only be explained by not only neutrino oscillations but also the matter

[15]: Wolfenstein (1978), *Neutrino oscillations in matter*
[16]: Wolfenstein (1979), *Neutrino oscillations and stellar collapse*
[17]: Mikheyev et al. (1985), *Resonance Amplification of Oscillations in Matter and Spectroscopy of Solar Neutrinos*

[†] The probability is the same for neutrinos and antineutrinos.

effects that the produced neutrinos in the sun core goes through while reaching the surface, and later crossing the threshold of higher matter density to vacuum [18, 19].

[18]: Bethe (1986), *Possible Explanation of the Solar-Neutrino Puzzle*
[19]: Rosen et al. (1986), *Mikheyev-Smirnov-Wolfenstein enhancement of oscillations as a possible solution to the solar-neutrino problem*

2.1.2 Interactions

In the Standard Model, neutrinos only interact through the weak interaction, which is mediated by the exchange of the $W^{\pm}$ and Z^0 bosons. These bosons have masses of $M_{W^{\pm}} = 80$ GeV and $M_{Z^0} = 91$ GeV [20]. The massiveness of these bosons contribute to the weakness of the interaction in normal conditions. Processes involving the W-boson are referred to as charged-current (CC) processes, while those involving the Z-boson are called neutral-current (NC) processes Neutrinos interact with charged leptons ($e^{\pm}$, $\mu^{\pm}$, $\tau^{\pm}$) through scattering processes and are produced in the decays of unstable charged leptons such as $\mu^{\pm}$ and $\tau^{\pm}$. They also interact with quarks, both in bound states (e.g., neutrons, protons, pions) through neutrino-nucleon scattering, and as individual quarks (partons) through deep inelastic scattering

[20]: Navas et al. (2024), *Review of Particle Physics*

This section will cover the general properties of neutrino interactions, focusing on their cross-sections across various energy scales. Later subsections will explore high-energy interaction processes, which are important for understanding neutrino behavior in extreme environments and are relevant to the analysis presented in this thesis.

Interaction Cross-Sections

Neutrino interactions can exhibit a wide range of behaviors [21] depending on the energy at which they occur and whether the interaction involves a neutrino or an antineutrino, as shown in Figure 2.1.

[21]: Formaggio et al. (2012), *From eV to EeV: Neutrino Cross Sections Across Energy Scales*

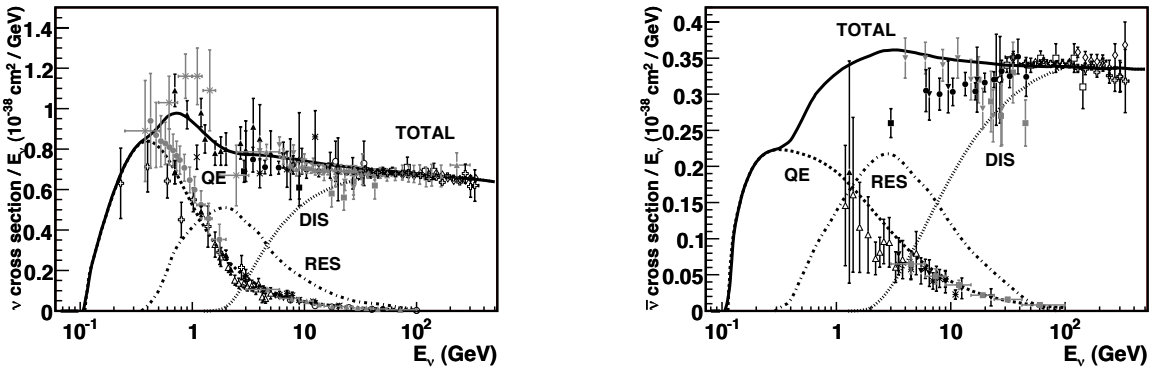

Figure 2.1: Total cross-sections for neutrinos (left) and antineutrinos (right) per nucleon in charged-current interactions (for an isoscalar target) divided by neutrino energy as a function of neutrino energy. Figure taken from [21]

At low energies, typically up to around 1 MeV, neutrino interactions are dominated by scattering off leptons and nuclei, both in charged and neutral forms. Two notable processes in this energy range are **coherent scattering** and **Neutrino Capture on Radioactive Nuclei**. These low-energy interactions can be described through electroweak theory, where the neutrino engages in two-body scattering processes. As the neutrino energy increases, it becomes possible to probe the target nucleus at

Inverse Beta Decay (IBD)

In IBD, $\bar{\nu_e}$ interacts with a proton, producing a e^+ and a neutron. The $\bar{\nu_e}$ must have a minimum kinetic energy of 1.806 MeV to initiate the reaction. This is due to the mass difference between the reactants and products. The positron receives most of the antineutrino's energy due to its smaller mass compared to the neutron.

$$\bar{\nu_e} + p \rightarrow e^+ + n \qquad (2.9)$$

progressively smaller length scales. While coherent scattering treats the nucleus as a unified structure, higher-energy neutrinos can resolve individual nucleons. One significant low-energy process is the Inverse Beta Decay (IBD). This process has been extensively studied in several experiments such as KamLAND [22] and Daya Bay [23], which measures neutrino oscillations using anti-neutrinos produced in fission nuclear reactors, typically probing energies up to around 10 MeV.

[22]: Gando et al. (2011), *Constraints on θ_{13} from A Three-Flavor Oscillation Analysis of Reactor Antineutrinos at KamLAND*

[23]: An et al. (2017), *Measurement of electron antineutrino oscillation based on 1230 days of operation of the Daya Bay experiment*

As the energy increases to the GeV range, neutrinos primarily interact through **quasi-elastic scattering** and **resonance production**. In quasi-elastic scattering, neutrinos interact with nucleons, producing charged leptons without breaking apart the nucleon. At slightly higher energies, resonance production becomes a crucial interaction mode. In this case, neutrinos excite the target nucleon into resonance states, such as Δ or N^*, which subsequently decay into various final states, yielding combinations of nucleons and mesons. The energy range of around 10 GeV is often called *the transition region* because it separates quasi-elastic scattering, where the target is a nucleon, from **the deep inelastic scattering (DIS)**, where the target is a quark (or *parton*) within the nucleon. As shown in Figure 2.1, above this transition region (> 100 GeV), the total cross-section exhibits an almost linear relationship with neutrino energy and DIS becomes the dominant process of all neutrino interactions. This scaling behavior, as predicted by the quark-parton model [24], assumes point-like scattering off quarks. However, these assumptions are not valid at lower neutrino energies, where lower momentum transfers have a greater impact on the interaction dynamics [21]. Since this energy range is critical for high-energy neutrino interactions in IceCube, especially for the analysis presented in this thesis, only DIS (and other relavnt processes at this energy, see Section 3) process shall be discussed in more detail.

[24]: Feynman (1969), *Very High-Energy Collisions of Hadrons*

[21]: Formaggio et al. (2012), *From eV to EeV: Neutrino Cross Sections Across Energy Scales*

Neutrino-Nucleon Deep Inelastic Scattering

In Deep Inelastic Scattering (DIS), neutrinos interact with quarks inside nucleons, breaking them apart and producing a cascade of particles. In this high-energy regime, the neutrino can be seen as scattering off individual partons, but a scattered parton cannot remain free for long. It quickly creates a jet of hadrons through pair production, a process known as hadronization or fragmentation. Both charged-current (CC) and neutral-current (NC) interactions can occur this way, resulting in either an outgoing charged lepton or neutrino. Feynman diagrams of CC and NC interactions for neutrinos are shown in Figure 2.2 and Figure 2.3 respectively, with their corresponding reactions in Equation 2.11 and Equation 2.12. The most general form of the differential neutrino-nucleon cross section for a CC interaction, involving an incoming neutrino with initial four momentum k_1, scattering with a target nucleon with four-momentum p, resulting in an outgoing lepton with four-momentum k_2, and a virtual gauge boson with four-momentum transfer q=$k_1 - k_2$, can be expressed as:

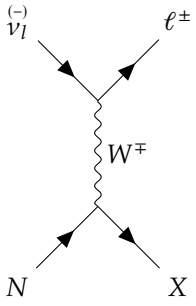

Figure 2.2: Feynman diagram of Neutrino-Nucleon DIS via CC interaction.

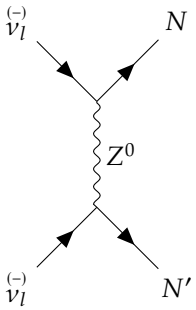

Figure 2.3: Feynman diagram of Neutrino-Nucleon DIS via NC interaction.

$$\frac{d^2\sigma}{dx, dy} = \frac{G_F^2 m_N E_\nu}{\pi} \left(\frac{{M_W^2}^2}{Q^2 + {M_W^2}^2} \right)^2 \left[q(x, Q^2) + (1 - y)^2 \bar{q}(x, Q^2) \right] \quad (2.10)$$

where, G_F represents the Fermi constant, m_N is the nucleon mass, E_ν is the energy of the incoming neutrino, and M_W represents the W-boson mass. The invariant momentum transfer of the scattering process is $Q^2 = -q^2$. **The Bjorken scaling variable**,

$$x = \frac{Q^2}{p.q} \tag{2.13}$$

represents the fraction of the nucleon's momentum carried by the scattered quark, while **the inelasticity variable**,

$$y = \frac{p.q}{p.k_1} = \frac{E_{hadron}}{E_\nu} \tag{2.14}$$

measures the amount of energy transferred to the hadronic system X. The parton distribution functions (PDFs), $q(x, Q^2)$ and $\bar{q}(x, Q^2)$, represent the probability density of a quark or antiquark, respectively, to have a momentum fraction x of the nucleon at the energy scale Q^2 of the interaction.

Charged Current Interaction
(see feynman diagram Figure 2.2)

$$\overset{(-)}{\nu}_l + N \rightarrow \ell^\pm + X \tag{2.11}$$

Neutral Current Interaction
(see feynman diagram Figure 2.3)

$$\overset{(-)}{\nu}_l + N \rightarrow \overset{(-)}{\nu}_l + X \tag{2.12}$$

Here, N is a nucleon, $\overset{(-)}{\nu}_l$ is the $\nu/\bar{\nu}$ of flavour l and X is hadronic particle shower.

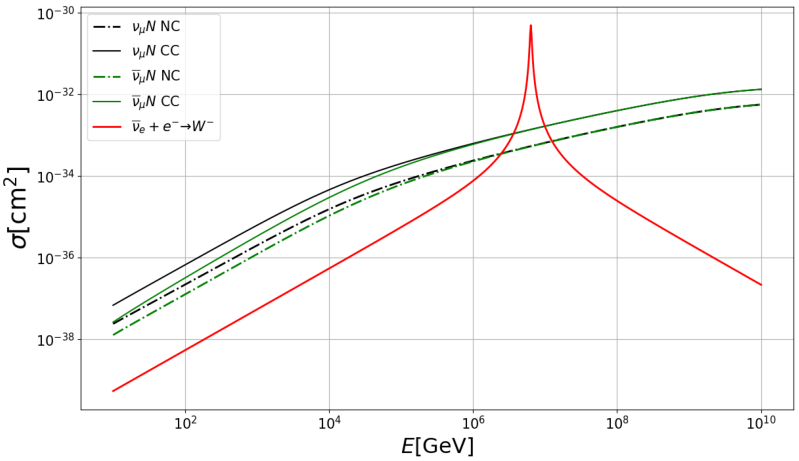

Figure 2.4: The deep inelastic scattering cross-sections for neutrino and antineutrinos are shown for both CC and NC interactions on an isoscalar target. Glashow resonance peak of $\bar{\nu_e}$ interacting with e is also visible at 6.3 PeV. Figure taken from [25]

A key feature of all structure functions is that they become nearly independent of Q^2 in the limit $Q^2 \rightarrow \infty$, meaning cross-section starts to scale linearly with neutrino energy E_ν for up-to $\sim$ 1 PeV as shown in Figure 2.4. This property, known as Bjorken scaling, was crucial in developing the parton model for deep inelastic scattering [26]. The Figure 2.4 illustrates the contributions of CC and NC interactions for both neutrinos and antineutrinos separately. It is evident that the CC cross-section is generally larger than the NC cross-section due to the stronger coupling of the W-boson compared to the Z-boson. At higher energies (> few PeVs), the propagation term from the interaction vertex is no longer dominated by the W-Z boson mass. As a result, the cross-section no longer grows linearly with neutrino energy. Moreover, the $(1-y)^2$ (see second term in bracket of Equation 2.10) suppression that typically allows distinction between neutrino and anti-neutrino interactions is much less pronounced, making the two cross-sections nearly identical [27].

[26]: Bjorken (1969), *Asymptotic Sum Rules at Infinite Momentum*

[27]: Gandhi et al. (1998), *Neutrino interactions at ultrahigh energies*

The calculation of neutrino DIS in the energy range of interest for IceCube has been carried out by Cooper-Sarkar, Mertsch, and Sarkar (CSMS) in 2011

and is the standard that will be used throughout this work to produce neutrino simulation (see Section 5.1) and also to include inelasticity parameter in the forward folding fit (see Section 6.2.1) [28]. However, updated cross-section calculations now exists, that takes into account final state radiations (FSR) [29] and uses updated parton distribution functions [30]. In particular, corrections in visible energy of Glashow events due to FSR were taken into account by introducing a correction in simulation event weight (see Section 5.4.3 for details). In the last decade, several studies have used different event samples at higher energies to measure the total[‡] DIS cross-section in the multi-TeV energy range at IceCube [31, 32].

[28]: Cooper-Sarkar et al. (2011), *The high energy neutrino cross-section in the Standard Model and its uncertainty*

[31]: Aartsen et al. (2017), *Measurement of the multi-TeV neutrino cross section with IceCube using Earth absorption*

[32]: Abbasi et al. (2021), *Measurement of the high-energy all-flavor neutrino-nucleon cross section with IceCube*

Glashow Resonance

Neutrinos typically interact with atomic electrons in a detector medium less frequently than with nucleons due to the smaller mass of the electron [21]. However, an exception occurs during the resonant enhancement of the $\bar{\nu}_e e^-$ scattering cross- section, known as **the Glashow resonance**. This happens when the center-of-mass energy matches the mass of the W-boson. The resonance occurs at an antineutrino energy of $E_{\bar{\nu}} = \frac{M_W^2}{2m_e} \approx 6.3$ PeV, where m_e is the electron mass (see Figure 2.4). Produced W boson, deacays into hadrons/lepton creating a particle shower at around 6 PeV energy. Sheldon Glashow first proposed this phenomenon in 1960 as a method to detect the W-boson [33]. Due to experimental limitations, such high-energy events were not observed for many years. However, the IceCube Neutrino Observatory recently reported detecting a Glashow resonance event, providing the first confirmation of this process [34].

[21]: Formaggio et al. (2012), *From eV to EeV: Neutrino Cross Sections Across Energy Scales*

[33]: Glashow (1960), *Resonant Scattering of Antineutrinos*

[34]: Aartsen et al. (2021), *Detection of a particle shower at the Glashow resonance with IceCube*

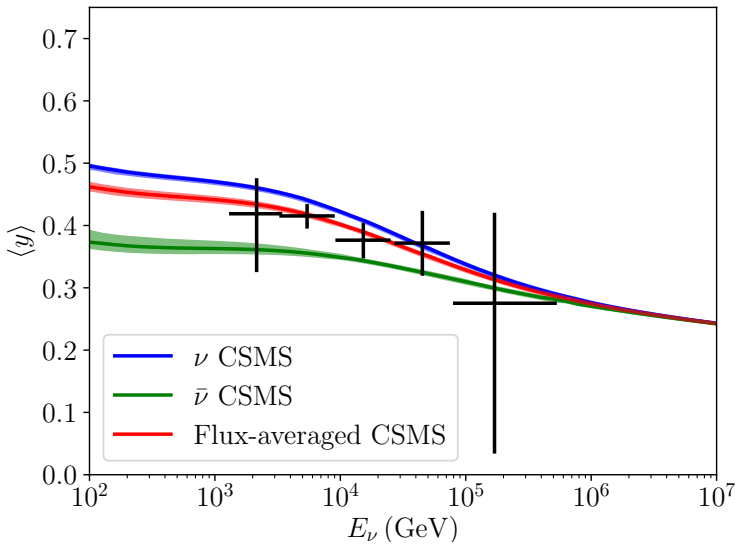

Figure 2.5: The measured mean inelasticity, with error bars indicating 68% confidence intervals. Predictions from the CSMS model are indicated in blue for ν and green for $\bar{\nu}$, with theoretical uncertainties shown by the colored bands, along with atmospheric flux-averaged inelasticity in red. Figure taken from [35].

Inelasticty

Inelasticity, denoted by y as described in Equation 2.14, represents the fraction of the incoming neutrino's energy that is transferred to the

[‡] total cross-sections are inclusive of CC and NC interactions.

hadronic system during deep inelastic scattering (DIS). In neutrino-nucleon DIS, a higher inelasticity corresponds to a larger energy transfer, leading to greater energy deposition in the detector through hadronic showers. Inelasticity can be determined from the kinematics of both the outgoing lepton and the hadronic system. Such a technique was expxloited in an IceCube analysis, to measure inelasticity in TeV range, by using ν_μ-CC events where both interaction vertex (hadronic cascade) and outgoing lepton (*muon track* [2]) are within the detector [35]. The distinction in inelasticity distribution between ν and $\bar{\nu}$ (see Figure 2.5) allows for differentiation between neutrinos and antineutrinos in an event sample. Understanding such an energy dependent inelasticity distribution is crucial for analyzing high-energy neutrino interactions, such as those explored in this thesis, where both hadronic and leptonic energy signatures are used to reconstruct neutrino properties.

2: depending on energy, entire track may or may not be contained within the detector volume, as muon usually deposits some energy along its path and can travel larger distance, possibly leaving the detector, see Section4.3.1 for details

[35]: Aartsen et al. (2019), *Measurements using the inelasticity distribution of multi-TeV neutrino interactions in IceCube*

2.2 Beyond Standard Model Neutrinos

While the minimum extension used in 2.1.1 provides a framework for describing neutrino oscillations, it also predicts the existence of right-handed neutrinos (or left-handed anti-neutrinos) that do not participate in weak interactions. These non-interacting neutrinos are known as ***sterile neutrinos***. Unlike the three active flavors, sterile neutrinos do not contribute to weak interaction processes like Z^0 boson decay. Experimental measurements of the Z^0 decay width constrain the number of light, active neutrino species (those lighter than the Z^0 boson) to 3 [11].

[11]: Schael et al. (2006), *Precision electroweak measurements on the Z resonance*

Although the three-flavor model is consistent with many observations, anomalies have been observed in several experiments. Radiochemical neutrino experiments [36], as well as experiments using neutrinos from particle accelerators [37, 38] and anti-neutrinos from nuclear reactors [39], have reported discrepancies that could be explained by the existence of sterile neutrinos. The simplest theoretical extension to account for these anomalies is the so-called 3+1 model, where one additional sterile neutrino is added to the three active neutrinos. In this model, the PMNS mixing matrix (which describes the mixing between neutrino flavors) is expanded from a 3×3 matrix to a 4×4 matrix [40]. This expanded matrix introduces three new mixing angles (θ_{14}, θ_{24}, θ_{34}) and additional CP-violating phases. These additional parameters allow for the mixing of sterile neutrinos with the active ones, potentially explaining the observed experimental anomalies, though further investigation is required to confirm their existence.

[36]: Elliott et al. (2024), *The gallium anomaly*

[37]: Aguilar et al. (2001), *Evidence for neutrino oscillations from the observation of $\bar{\nu}_e$ appearance in a $\bar{\nu}_\mu$ beam*

[38]: Aguilar-Arevalo et al. (2013), *Improved Search for $\bar{\nu}_\mu \to \bar{\nu}_e$ Oscillations in the MiniBooNE Experiment*

[39]: Mention et al. (2011), *The Reactor Antineutrino Anomaly*

[40]: Abazajian et al. (2012), *Light Sterile Neutrinos: A White Paper*

Cosmological evidence also provides hints for the existence of sterile neutrinos [41]. The presence of sterile neutrinos could have observable consequences on the evolution of the early universe and on large-scale structure formation. Observations of the cosmic microwave background (CMB) and precise measurements by missions such as WMAP indicate that the number of relativistic species during the early universe, typically expressed as the effective number of neutrino species N_{eff}, is slightly higher than the expected value of 3 for the three active neutrinos [42]. This could suggest the presence of additional light particles, such as sterile neutrinos, that contributed to the radiation density in the early universe. Although, another measurement by planck survey is in close

[41]: Abazajian (2017), *Sterile neutrinos in cosmology*

[42]: Komatsu et al. (2011), *SEVEN-YEARWILKINSON MICROWAVE ANISOTROPY PROBE(WMAP) OBSERVATIONS: COSMOLOGICAL INTERPRETATION*

agreement with $N_{\text{eff}} = 3$ [43], making the puzzle of such neutrino species even more intriguing. Moreover, sterile neutrinos could contribute to the dark matter problem [44]. While they are unlikely to account for all dark matter, keV-mass sterile neutrinos are a candidate for *warm dark matter*, a type of dark matter that could impact the formation of structure in the universe on small scales. These cosmological observations, when combined with the experimental anomalies in neutrino oscillation data, make sterile neutrinos an intriguing possibility for both particle physics and cosmology. However, further precision measurements, both in the laboratory and from astrophysical observations, are needed to confirm their existence and determine their exact role in the universe.

In addition to Sterile neutrinos, other exotic phenomena, which are not included in standard model can affect neutrino interaction cross-sections or other fundamental properties assumeed in SM. Such scenarios include interaction of neutrinos with dark matter [45], CPT violation [46] etc. A number of analysis have been made in IceCube to look for sterile neutrinos [47], other exotic neutral leptons [48] and also to look for dark matter signatures [49] have been made. Although, as it will be discussed in the next chapter, for the analysis presneted in this thesis, as none of these scenraios, when probed to measure flavour fraction of astrophysical neutrinos on earth allows for non-zero tau neutrino fraction [50], hence they are not discussed further in detail, and for the remainder of this thesis, 3 flavour of neutrinos shall be assumed.

[43]: Aghanim et al. (2020), *Planck 2018 results. VI. Cosmological parameters*

[44]: Drewes et al. (2017), *A White Paper on keV Sterile Neutrino Dark Matter*

[45]: Salas et al. (2016), *Neutrino propagation in the galactic dark matter halo*

[46]: Hooper et al. (2005), *Lorentz and CPT invariance violation in high-energy neutrinos*

[47]: Trettin (2024), *Search for eV-scale sterile neutrinos with IceCube DeepCore*

[48]: Fischer (2024), *First Search for Heavy Neutral Leptons with IceCube DeepCore*

[49]: Abbasi et al. (2023), *Search for neutrino lines from dark matter annihilation and decay with IceCube*

[50]: Rasmussen et al. (2017), *Astrophysical neutrinos flavored with beyond the Standard Model physics*

Neutrinos in High Energy Universe

3

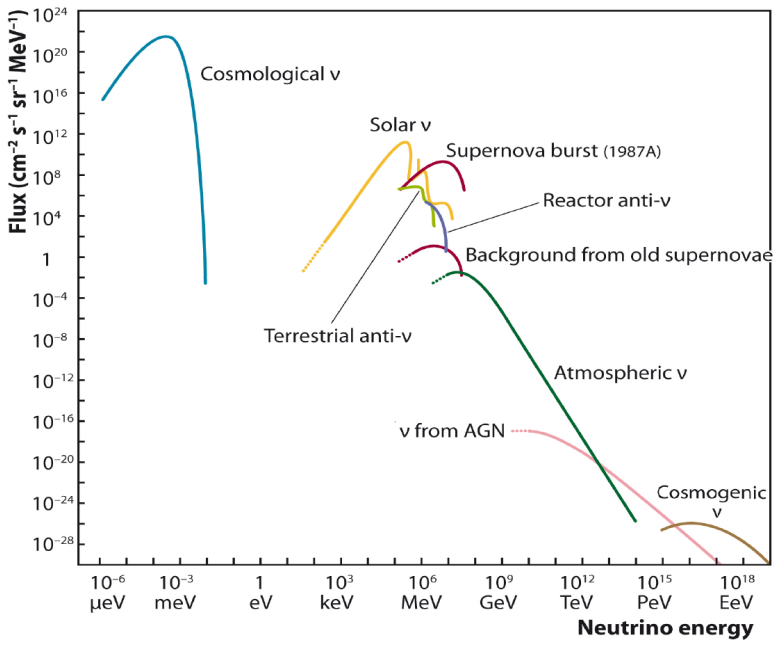

Figure 3.1: Measured and predicted neutrino fluxes of neutrinos from various natural sources. Solar neutrinos are neutrinos, while geo-neutrinos and nuclear reactors (terrestrial) are antineutrinos. Other sources produce roughly equal numbers of neutrinos and antineutrinos. Neutrinos from the Big Bang, diffuse supernova neutrinos, and high-energy cosmogenic neutrinos remain undetected. Figure from [51]

Neutrinos are produced by various sources across a very large energy range (see Figure 3.1), including particle accelerators, nuclear reactors, and several natural processes. The largest flux of neutrinos comes from nuclear fusion in the Sun [52] and naturally occurring β-decay on Earth (the so-called *GeoNeutrinos* or *terrestrial neutrinos*) [53]. Historically, a similar flux was briefly observed during the supernova SN1987a in the Large Magellanic Cloud, though it only lasted a few seconds [54–56]. A more constant, but significantly lower, flux is thought to arise from numerous supernovae throughout the universe [57]. High-energy neutrinos, above 1 TeV, originate from either atmospheric or astrophysical sources and are of particular interest for the work presented in this thesis.

As high-energy neutrinos (above tens of TeV) are expected to be produced alongside cosmic rays at high-energy acceleration sites, this chapter will first introduce cosmic rays. It will then cover the production of neutrinos and muons from cosmic ray interactions with Earth's atmosphere, followed by a discussion on neutrinos generated at cosmic ray acceleration sites.

[52]: Bahcall et al. (1988), *Solar models, neutrino experiments, and helioseismology*

[53]: Krauss et al. (1984), *Anti-neutrinos Astronomy and Geophysics*

[54]: Hirata et al. (1987), *Observation of a neutrino burst from the supernova SN1987A*
[55]: Alexeyev et al. (1988), *Detection of the neutrino signal from SN 1987A in the LMC using the INR Baksan underground scintillation telescope*
[56]: Bionta et al. (1987), *Observation of a neutrino burst in coincidence with supernova 1987A in the Large Magellanic Cloud*

[57]: Vissani et al. (2011), *The diffuse supernova neutrino background: Expectations and uncertainties derived from SN1987A*

3.1 Cosmic Rays

Cosmic rays were first discovered by Victor Hess during his famous balloon flight in 1912, where he measured a significant increase in ionization rates as he ascended in altitude [58]. This finding provided the first direct evidence for the existence of highly energetic particles

[58]: HESS (1972), *1 - Observations of the Penetrating Radiation on Seven Balloon Flights††Physik. Zeitschr. 13, 1804–1091 (1912). (From the Section on Geophysics, Meteorology and Geomagnetism.)*

arriving from outer space. Over a century later, cosmic ray research has evolved, and today various experiments routinely measure their physical properties. Cosmic rays are now understood to consist primarily of ionized atomic nuclei, with less than 1% of their composition being electrons, which are often disregarded due to their negligible contribution. Approximately 90% of cosmic rays are protons, 9% are helium nuclei (α-particles), and the remaining fraction consists of heavier nuclei such as carbon, oxygen, and iron [59].

[59]: Workman et al. (2022), *Review of Particle Physics*

Cosmic radiation that reaches the Earth's atmosphere contains all stable charged particles and atomic nuclei with lifetimes of 10^6 years or more. These particles are divided into *primary* and *secondary* cosmic rays. Primary cosmic rays are particles that are directly accelerated by astrophysical sources. These include protons, helium nuclei, and heavier elements formed in stars. On the other hand, secondary cosmic rays are produced when primary cosmic rays interact with interstellar matter. For example, when primary cosmic rays hit gas particles in space, they can create lighter elements like lithium, beryllium, and boron, which are not typically formed in stars. These secondary particles help scientists understand the interactions cosmic rays experience as they travel through the galaxy [59].

[59]: Workman et al. (2022), *Review of Particle Physics*

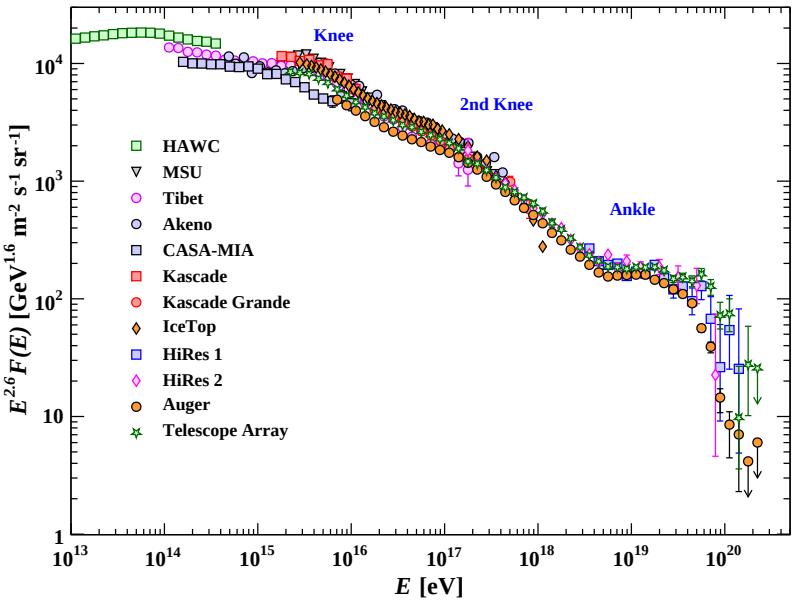

Figure 3.2: The all-particle spectrum as a function of E (energy-per-nucleus) from air shower measurements. The various features of the spectrum discussed in the text are marked with *Knee, 2nd Knee and Ankle*. Data points are referenced in [59]

The energy spectrum of cosmic rays as shown in Figure 3.2 is one of their most fascinating characteristics.. The spectrum follows a power-law distribution, expressed as:

$$\frac{dN}{dE} \propto E^{-\gamma} \tag{3.1}$$

where E is the energy and γ is the spectral index. This form of the spectrum indicates that cosmic rays are accelerated by non-thermal processes, such as shock waves or magnetic reconnection. The spectral index γ is not constant across all energies but changes at specific points in the spectrum (as indicated in Figure 3.2), indicating transitions between different source classes or acceleration mechanisms. Over a vast energy

range (from $\sim 10^9$ eV to $\sim 10^{15}$), the differential flux given in Equation 3.1 follows a power law with index $\gamma \approx 2.7$. The flux in this range, is large enough to be measured be directly detected from spacecraft and balloons before they interact in the atmosphere.

The various features [59] that can be seen in the Figure 3.2 using Equation 3.1 are as follows:

$$\frac{dN}{dE} \sim \begin{cases} E^{-2.7} & \text{(up to knee)} \\ E^{-3.1} & \text{(knee)} \\ E^{-3.3} & \text{(second knee),} \\ E^{-2.5} & \text{(ankle)} \end{cases}$$

At higher energies, where the cosmic ray flux is too low to be measured directly, they can only be observed indirectly through the cascade of secondary particles they produce in the atmosphere. The energy and type of the primary cosmic ray must then be estimated based on the characteristics of this particle shower. The first significant feature in the cosmic ray energy spectrum is known as **the knee**, which occurs at an energy of about 3 PeV. At this point, the spectrum softens, with the spectral index γ increasing from around 2.7 to about 3.1. A milder, **second knee** occurs at around 10^{17} eV (100 PeV), where the spectrum softens further to $\gamma \sim 3.3$. The Cosmic rays above $\sim 10^{18}$ eV are called *Ultra High Energy Cosmic Rays (UHECRs)*. At these ultra higher energies, the spectrum undergoes a hardening at around 10^{18} eV, where the index returns to a value closer to 2.5. This feature of the spectrum is known as **ankle** [60]. At the highest energies, specifically beyond 10^{18} eV, a decline in cosmic ray flux is expected. This decrease can be explained by **the Greisen-Zatsepin-Kuzmin (GZK)** mechanism, which involves the production of pions through photohadronic interactions between high-energy protons (E~50 EeV (50×10^{18} eV)) and photons from the cosmic microwave background (CMB) [61, 62]. For this GZK effect to fully account for the observed spectral cutoff, a proton-only composition is necessary. However, data from the Pierre Auger Observatory (PAO) and the Telescope Array (TA) suggest otherwise, indicating a more mixed composition [63, 64]. Another possible explanation for the observed flux suppression is the finite maximum energy that cosmic ray sources can accelerate particles to [65].

[60]: Hörandel (2007), *Cosmic Rays from the Knee to the Second Knee:* 10^{14} *to* 10^{18} *eV*

[61]: Greisen (1966), *End to the Cosmic-Ray Spectrum?*

[62]: Zatsepin et al. (1966), *Upper limit of the spectrum of cosmic rays*

[63]: Aab et al. (2016), *Evidence for a mixed mass composition at the 'ankle' in the cosmic-ray spectrum*

[64]: Souza (2017), *Testing the agreement between the* $X_{\max}$ *distributions measured by the Pierre Auger and Telescope Array Observatories*

[65]: Das et al. (2021), *Modeling the spectrum and composition of ultrahigh-energy cosmic rays with two populations of extra-galactic sources*

These transitions in the spectrum are believed to be associated with changes in the source population. The initial segment of the cosmic ray energy spectrum, extending up to the knee can largely be explained by the process of particle acceleration occurring within Galactic sources, predominantly supernova remnants [66]. Supernova remnants serve as dynamic environments where powerful shock waves are generated following the explosive death of massive stars. These shock waves facilitate the acceleration of particles, including protons, to high energies through mechanisms such as Fermi acceleration (see below) [67]. The steepening of the spectrum at the knee suggests that accelerators may have reached their maximum capacity for proton acceleration [68]. This limit depends largely on the strength of magnetic fields in the acceleration region, which are crucial for confining charged particles and facilitating energy gain. Additionally, cosmic ray leakage from the Galaxy can reduce high-energy cosmic rays through interactions with interstellar medium particles, contributing to the observed changes in the energy spectrum [69].

[66]: Hoerandel (2004), *Models of the knee in the energy spectrum of cosmic rays*

[67]: Perkins (2003), *Particle astrophysics*

[68]: Hörandel (2003), *On the knee in the energy spectrum of cosmic rays*

[69]: Stanev (2010), *High Energy Cosmic Rays*

The second knee in the cosmic ray spectrum can also be understood using similar principles. This feature may arise from the behavior of heavier elements, which experience different acceleration dynamics compared to protons [68]. These heavy nuclei may encounter limitations in their acceleration processes, preventing them from reaching energies comparable to lighter particles. Moreover, just like protons, these heavier

[68]: Hörandel (2003), *On the knee in the energy spectrum of cosmic rays*

elements may also face barriers that inhibit their escape from the Galactic environment. Consequently, the second knee could signify a threshold beyond which heavier cosmic rays cannot be further accelerated or are unable to exit the Galaxy, leading to a corresponding steepening in the spectrum. Overall, these observations underscore the complex interplay between acceleration mechanisms, magnetic field strengths, and particle interactions that shape the cosmic ray energy spectrum. Regarding the ankle region, several proposed models that seek to explain this phenomenon suggest a transition in the primary component from galactic sources to extragalactic ones [70–72].

[70]: Aloisio et al. (2012), *Transition from galactic to extragalactic cosmic rays*
[71]: Mollerach et al. (2019), *Ultrahigh energy cosmic rays from a nearby extragalactic source in the diffusive regime*
[72]: Unger et al. (2015), *Origin of the ankle in the ultrahigh energy cosmic ray spectrum, and of the extragalactic protons below it*

Anisotropies in the arrival directions of cosmic rays (CRs) offer crucial insights into their origins. Identifying these sources becomes theoretically possible if the properties of cosmic ray charges, as well as galactic and extragalactic magnetic fields, are sufficiently well understood. Ultra-high-energy cosmic rays (UHECRs) are notably affected by the Greisen-Zatsepin-Kuzmin (GZK) effect, which describes the energy losses experienced by protons and heavier nuclei due to their interactions with the cosmic microwave background. The Pierre Auger Observatory has identified a large-scale dipolar anisotropy in cosmic rays with energies above 8 EeV, with a significance of 6.9σ. The amplitude of this dipole is $d = 0.073^{+0.010}_{-0.008}$, and its direction is approximately 115° away from the Galactic Center, supporting the extragalactic origin of UHECRs beyond this energy threshold [73]. These findings align with results obtained by combining the data from both the Pierre Auger Observatory and the Telescope Array (TA) [74].

[73]: Abdul Halim et al. (2023), *An update on the arrival direction studies made with data from the Pierre Auger Observatory*
[74]: Kim et al. (2023), *Anisotropies in the arrival direction distribution of ultra-high energy cosmic rays measured by the Telescope Array surface detector*

3.1.1 Acceleration Mechanism

Even during the most powerful solar flares, the Sun is limited to accelerating particles to around 1 GeV [75]. This limitation leads to the question of how cosmic rays can be accelerated to much higher energies, ranging from tens of GeV up to 100 EeV, and what astrophysical sources and mechanisms are responsible for such acceleration. One leading theory, initially proposed by Enrico Fermi, is that cosmic ray particles gain energy through random scattering across moving shock fronts, a process known as first-order Fermi acceleration [76]. In this process, the relative energy gain ΔE for a particle with energy E during each scattering event is proportional to the shock velocity u, expressed by the equation:

[75]: Kim et al. (1999), *Contribution of High Charge and Energy (HZE) Ions During Solar-Particle Event of September 29, 1989*

[76]: Fermi (1949), *On the Origin of the Cosmic Radiation*

$$\frac{\Delta E}{E} \sim \frac{u}{c}, \tag{3.2}$$

where c is the speed of light [77]. [1] A charged particle, starting in the unshocked region, moves into the shocked medium and experiences elastic scattering from magnetic irregularities. With every crossing of the shock front, the particle gains more energy. After n cycles, the particle's energy is given by $E_n = E_0(1+\alpha)^n$, where E_0 is its initial energy and α represents the fractional energy increase per cycle, approximately $\alpha \approx 4v/3c$ [77]. However, particles cannot remain in the shock zone indefinitely, as they may either just loose the energy or *escape* the region. The latter is determined by their escape probability, $p_{\text{esc}} = 4(u-v)/c$,

[77]: Gaisser et al. (2016), *Cosmic Rays and Particle Physics*

1: For instance, supernova remnants, where the shock front velocity $u/c \gtrsim 10^{-2}$, create a highly efficient environment for particle acceleration.

[77]: Gaisser et al. (2016), *Cosmic Rays and Particle Physics*

which increases as the shock slows down relative to the surrounding medium.

The resulting energy spectrum of the accelerated particles typically follows a power law, with the differential energy distribution given by $dN/dE \propto E^{-\gamma}$, where $\gamma \approx 1 + \frac{p_{\text{esc}}}{\alpha}$ [67]. In non-relativistic shocks moving faster than the speed of sound in the medium, this leads to a spectral index of approximately $\gamma \approx 2.1$, meaning most particles have lower energies, while a smaller number reach higher energies. The steeper cosmic ray spectrum, approximately $\sim E^{-2.7}$, can be explained by energy-dependent diffusion in galactic magnetic fields [78, 79].

[67]: Perkins (2003), *Particle astrophysics*

[78]: Batista et al. (2014), *Diffusion of cosmic rays at EeV energies in inhomogeneous extragalactic magnetic fields*
[79]: Snodin et al. (2016), *Global diffusion of cosmic rays in random magnetic fields*

Although first-order Fermi acceleration is a strong model for non-relativistic shocks, other mechanisms have been proposed to account for even higher-energy particles. These include relativistic shock fronts [80, 81], where shocks travel close to the speed of light, as well as processes like magnetic reconnection [82], where energy is released when magnetic fields reconfigure, and plasma wakefield acceleration [83], where particles are accelerated by intense electric fields in plasmas. Such processes are crucial in extreme astrophysical environments like active galactic nuclei (AGN) and gamma-ray bursts (GRBs), where cosmic rays are believed to be accelerated to ultra-high energies.

[80]: Kirk et al. (1987), *On the Acceleration of Charged Particles at Relativistic Shock Fronts*
[81]: Heavens et al. (1988), *Relativistic shocks and particle acceleration.*
[82]: Yamada et al. (2010), *Magnetic reconnection*
[83]: Chang et al. (2009), *Magnetowave Induced Plasma Wakefield Acceleration for Ultra High Energy Cosmic Rays*

3.1.2 Sources

The notion of Fermi acceleration, as explained in Section 3.1.1 fundamentally relies on the confinement of cosmic rays, which allows them to engage in repeated interactions with a shock front or other magnetized structures. If we assume that this confinement is provided by a magnetic field of strength B, it follows that the size of the confinement region, denoted as r, must be greater than the gyro-radius of the cosmic ray. This relationship is described by the following inequality:

$$r > \frac{E}{ZBc} \tag{3.3}$$

Here, E represents the energy and Z is the charge of the cosmic ray, which we typically consider to be ultra-relativistic. Alternatively, this condition can be reformulated as a constraint on the rigidity R, defined as the ratio of the particle's momentum to its charge:

$$R = \frac{E}{Z} < Bcr. \tag{3.4}$$

This limitation is referred to as **the Hillas criterion** [85]. By employing estimates for the sizes and magnetic field strengths of various astronomical objects, one can identify potential sites for acceleration that align with specific cosmic-ray rigidities. The Hillas diagram as shown in Figure 3.3, effectively illustrates the magnetic field strength and sizes of different classes of objects.

[85]: Hillas (1984), *The Origin of Ultra-High-Energy Cosmic Rays*

Following the aforementioned concept, Hillas proposed a simple model that captures the characteristics observed in the energy spectrum and composition of cosmic rays. In this framework, the diagonal lines in Figure 3.3 signify thresholds below which a source cannot confine a particle with

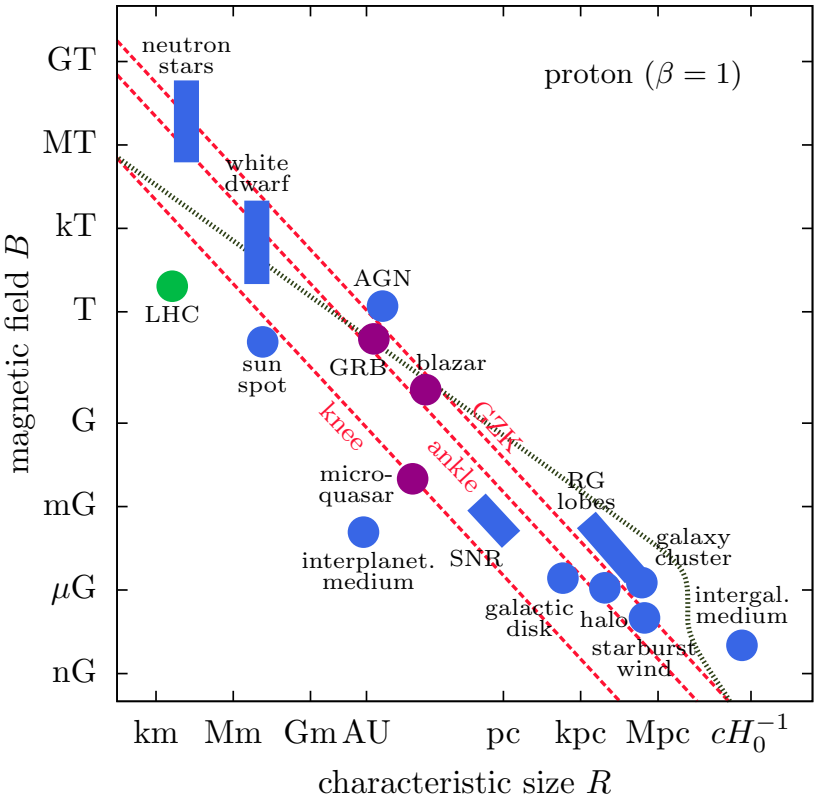

Figure 3.3: Hillas diagram illustrating different candidate source classes of cosmic rays. Figure from [84]

energy E and charge z. Considering that the Milky Way has a thickness of no more than 1 kpc [86] and its magnetic field strength is approximately a few μG [87], the Hillas diagram suggests that UHECRs must originate from extragalactic sources. Conversely, galactic supernova remnants (SNRs) emerge as strong candidates for the source of low-energy cosmic rays. While the exact rate of galactic supernova occurrences remains somewhat uncertain, a conversion of just a few percent of the shock wave's energy into particle acceleration would adequately explain the observed cosmic ray flux below the knee of the cosmic ray spectrum [67].

[86]: Rix et al. (2013), *The Milky Way's stellar disk*
[87]: Haverkorn (2014), *Magnetic Fields in the Milky Way*

[91]: Horvath (2022), *High-Energy Astrophysics. A Primer*
[67]: Perkins (2003), *Particle astrophysics*

The origins of cosmic rays in the intermediate energy range (between knee and second knee) are still not fully understood [88]. Their acceleration is thought to take place within vast magnetic fields generated by substantial bulk flows of relativistic charged particles, which are driven by immense gravitational forces present in the vicinity of neutron stars or black holes. Some plausible candidates for these highest-energy cosmic rays include **Active Galactic Nuclei (AGN)** [89] and **Gamma-Ray Bursts (GRB)** [90].

[88]: Halzen et al. (2010), *IceCube: An Instrument for Neutrino Astronomy*

[89]: Protheroe et al. (1992), *High-energy cosmic rays from active galactic nuclei*
[90]: Wang et al. (2008), *On the Origin and Survival of UHE Cosmic-Ray Nuclei in GRBs and Hypernovae*

Active galactic nuclei are extremely bright and compact regions located at the centers of galaxies, powered by supermassive black holes, as shown in Figure 3.4. In these regions, surrounding matter forms an accretion disk, where gravitational energy is converted into electromagnetic energy, resulting in the emission of a wide spectrum of radiation (specially when viewed from different directions), from radio waves to gamma rays [91]. The intense gravitational pull of the black hole compresses the surrounding material, generating high temperatures and pressures. Some AGNs also produce relativistic jets, which are streams of charged

Figure 3.4: Schematic of the AGN Unification Model, illustrating AGN structures and how observed properties vary by viewing angle.Figure from [91]

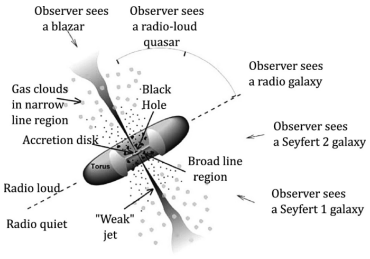

particles moving at speeds close to the speed of light. These jets can terminate in hot spots or lobes, providing an environment capable of accelerating cosmic rays to energies nearing 100 EeV [92].

[92]: Peterson (1997), *An Introduction to Active Galactic Nuclei*

Gamma-ray bursts, on the other hand, are extremely luminous and transient events characterized by their emission of gamma radiation for brief periods, ranging from milliseconds to several minutes. During their short duration, GRBs emit more energy than any other steady gamma-ray source in the universe [91]. Theoretical models describing GRBs, such as the fireball shock model [93], predict an initial short burst of highly energetic gamma rays followed by a more prolonged afterglow that emits across a broad range of wavelengths, from X-rays to radio frequencies. Long GRBs, which last over 2 seconds, are generally believed to be associated with the core collapse of a massive progenitor star [94]. In contrast, shorter GRBs are likely the result of the merger of two neutron stars or a neutron star with a black hole [95, 96]. In both scenarios, the collapse produces highly relativistic jets that exhibit multiple shock fronts, facilitating the acceleration of cosmic rays to extreme energies.

[93]: Piran (1999), *Gamma-ray bursts and the fireball model*

[94]: Hjorth et al. (2011), *The Gamma-Ray Burst - Supernova Connection*

[95]: Abbott et al. (2017), *Gravitational Waves and Gamma-rays from a Binary Neutron Star Merger: GW170817 and GRB 170817A*

[96]: Janka et al. (1999), *Black hole: Neutron star mergers as central engines of gamma-ray bursts*

3.2 High Energy Neutrinos

Cosmic neutrinos are high-energy neutrinos produced through various mechanisms. **Astrophysical neutrinos** are produced in hadronic interactions within extreme environments like active galactic nuclei and gamma-ray bursts, often in conjunction with cosmic rays. **Cosmogenic neutrinos** on the other hand, arise from ultra-high-energy protons interacting with the cosmic microwave background, leading to decays that yield neutrinos. Lastly, **Atmospheric neutrinos** are produced when cosmic rays collide with Earth's atmosphere, initiating air showers that generate mesons like pions and kaons. These mesons decay, leading to the production of neutrinos, along with muons and electromagnetic cascades.

figure should change, i can't find citation and i am too lazy to produce one

Regardless of the location of the source, the basic mechanism of neutirno production of all of the aforementioned neutrinos remains the same, hadronic interactions that producs mesons. The following sections will focus on these neutrino categories, with an emphasis on Astrophysical neutrinos and their production mechanisms, which are most relevant to this thesis.

Figure 3.5: Schematic of progress of a particle cascade when a cosmic ray proton interacts with a nucleus in atmosphere.

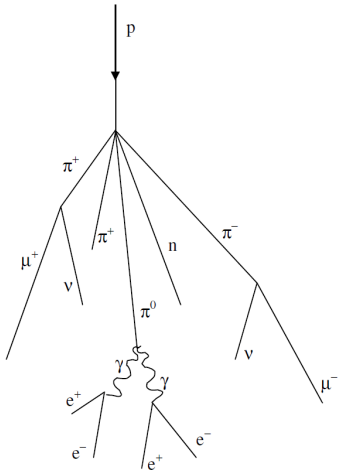

3.2.1 Atmospheric Neutrinos

Extensive air showers (EAS) are a cascades of secondary particles initiated when a high-energy primary cosmic ray—such as a proton, neutron, or heavier nucleus—interacts with the Earth's atmosphere. These showers can result from cosmic rays with energies reaching $E \sim 1$ PeV and beyond, spreading across areas of approximately 10 km^2 at ground level [97]. When the cosmic ray collides with atmospheric nuclei, it produces a large number of secondary particles, primarily charged and neutral pions ($\pi^{\pm}, \pi^0$), along with kaons ($K^{\pm}, K^0$) and other mesons.

The dominant fraction of particles in an EAS consists of pions [20]. Neutral pions (π^0) decay rapidly into photons ($\pi^0 \rightarrow 2\gamma$), feeding

[97]: Gaisser et al. (2012), *Neutrinos and cosmic rays*

[20]: Navas et al. (2024), *Review of Particle Physics*

the electromagnetic component of the shower, which can be observed through detection techniques such as radio emissions, air fluorescence, and Cherenkov light. Charged pions ($\pi^{\pm}$) decay into muons and neutrinos through the processes:

$$\pi^+ \to \mu^+ + \nu_\mu, \quad \pi^- \to \mu^- + \bar{\nu}_\mu,$$

producing muons and muon-neutrinos. These muons often reach the Earth's surface, where they can be detected by large arrays of particle detectors. If the muons have sufficiently high energy, they can penetrate deep into the ground [98], allowing detection by underground observatories like IceCube [99].

[98]: Bugaev et al. (1998), *Atmospheric muon flux at sea level, underground and underwater*

[99]: Aartsen et al. (2016), *Characterization of the Atmospheric Muon Flux in IceCube*

The pions and kaons created in the air shower can either decay or interact, resulting in the production of atmospheric muons and neutrinos, which are collectively referred to as the atmospheric muon and neutrino flux.

The energy spectrum of atmospheric neutrinos can be divided into two main categories: conventional and prompt neutrinos. **The Conventional Atmospheric Neutrinos** are predominantly produced by the decay of charged pions ($\pi^{\pm}$) and kaons ($K^{\pm}$), which are generated in extensive air showers resulting from cosmic-ray interactions with the Earth's atmosphere. The dominant decay channels contributing to the conventional neutrino flux are:

$$\pi^{\pm} \to \mu^{\pm} + \nu_\mu, \quad K^{\pm} \to \mu^{\pm} + \nu_\mu, \quad K_L^0 \to \pi^{\pm} + e^{\mp} + \nu_e\,(\bar{\nu}_e).$$

K_L^0 here refers to long-lived neutral kaon which differes from short lived neutral kaon (K_S^0) by lifetime and also through decay modes [20].

At lower energies (a few GeV), the muons produced in pion and kaon decays usually decay in the atmosphere, leading to an observed flavor ratio of $\nu_e : \nu_\mu \approx 1 : 2$. However, at higher energies (above 100 GeV), most muons reach the ground before decaying, significantly reducing the production of electron-neutrinos and causing the flavor ratio to drop below 1 : 10 at TeV energies. This energy-dependent behavior is a key characteristic of the conventional neutrino flux, which dominates in the GeV to TeV range and follows a power law of $E^{-3.7}$ [20]. At energies well above 100 GeV, the contribution of charged pions to the muon-neutrino flux diminishes, and kaon decays become the predominant source of conventional atmospheric neutrinos. Due to the differing decay channels and branching ratios, muon-neutrinos (ν_μ) are produced in much higher numbers compared to electron-neutrinos (ν_e), with the flavor ratio $\nu_\mu : \nu_e$ varying between 20:1 to 30:1 in the TeV to PeV range.

The production of prompt atmospheric tau-neutrinos is highly suppressed and is expected to occur primarily through the decay channel $D_s^{\pm} \to \tau^{\pm} + \nu_\tau$, followed by the subsequent decay of the tau lepton $\tau^{\pm} \to \mu^{\pm} + \nu_\mu + \nu_\tau$ [100]. The contribution of tau-neutrinos to the overall prompt neutrino flux is approximately 5% and is generally considered negligible.

In contrast, **The Prompt Atmospheric Neutrinos** originate from the rapid decay of charmed mesons (such as $D^{\pm}, D^0, D_s^{\pm}$), which decay almost immediately after their production without significant interaction. These mesons decay into both muon- and electron-neutrinos via the processes:

$$D^{\pm} \to \mu^{\pm} + \nu_\mu, \quad D^0 \to e^{\pm} + \nu_e, \tag{3.5}$$

leading to an expected flavor ratio of $\nu_\mu : \nu_e \approx 1 : 1$ for prompt neutrinos. The prompt neutrino flux follows the energy distribution of the primary cosmic ray and is unaffected by atmospheric density. While charmed D mesons contribute to both prompt neutrino and muon fluxes, short-lived vector mesons like, η, ρ, ω may also contribute to prompt fluxes, but only for muons as they usually have dimuonic decay, without any neutrinos [101].

[101]: Illana et al. (2011), *Atmospheric muon and neutrino fluxes at very high energy*

The atmospheric neutrino energy spectrum is approximately described by two power-law relations:

$$\frac{dN}{dE} \propto \begin{cases} E^{-3.7}, & \text{for conventional neutrinos (above 100 GeV),} \\ E^{-2.8}, & \text{for prompt neutrinos (below 100 TeV).} \end{cases}$$

The steeper spectrum of conventional neutrinos arises from the fact that charged pions and kaons interact several times before decaying, particularly at higher energies. By contrast, prompt neutrinos, produced directly from the decay of charmed mesons without prior interaction, retain an energy distribution similar to that of the primary cosmic ray. The prompt neutrino flux is also independent of zenith angle, whereas the conventional neutrino flux is most pronounced for neutrinos coming from the horizon, due to the increased probability of pion and kaon decay over longer travel distances through the atmosphere.

The energy spectrum of the conventional atmospheric neutrino flux has been measured up to several hundred GeV by underground experiments like Super-Kamiokande [102] and the Fréjus Nucleon-Decay Detector [103], and up to a few hundred TeV by IceCube [104] and ANTARES [105]. However, a prompt atmospheric neutrino flux remains undetected, as the predicted normalization lies below the current detection threshold [100]. Efforts are underway to combine data samples to improve sensitivity and potentially observe this elusive flux [106]. Additionally, IceCube has successfully measured atmospheric muon fluxes up to energies of 1 PeV [99].

[102]: Richard et al. (2016), *Measurements of the atmospheric neutrino flux by Super-Kamiokande: Energy spectra, geomagnetic effects, and solar modulation*

[103]: Daum et al. (1995), *Determination of the atmospheric neutrino spectra with the Fréjus detector*

[104]: Aartsen et al. (2015), *Measurement of the Atmospheric ν_e Spectrum with IceCube*

[105]: Albert et al. (2021), *Measurement of the atmospheric ν_e and ν_μ energy spectra with the ANTARES neutrino telescope*

[100]: Enberg et al. (2008), *Prompt neutrino fluxes from atmospheric charm*

[106]: Boettcher et al. (2023), *Search for the Prompt Atmospheric Neutrino Flux in IceCube*

[99]: Aartsen et al. (2016), *Characterization of the Atmospheric Muon Flux in IceCube*

3.2.2 Cosmogenic Neutrinos

As explained in Section 3.1, a cut-off in the energy spectrum of cosmic rays is hypothesized at energies above a few EeV. This cut-off, known as the GZK cutoff, occurs because cosmic-ray protons with energies around 50 EeV are expected to interact with the cosmic microwave background (CMB) photons via the reaction:

$$p + \gamma_{\text{CMB}} \rightarrow \Delta^+ \rightarrow \begin{cases} p + \pi^0 \\ n + \pi^+ \end{cases}$$

In this reaction, the resulting π^+ produced subsequently decays, generating neutrinos that carry a fraction of the original proton energy and thus appear at extremely high energies. These neutrinos are reffered to as **Cosmogenic Neutrinos** or **GZK neutrinos**.

The detection of the diffuse extra-galactic gamma-ray background by Fermi LAT, which originates from the decay of the π^0 produced in the reaction above, further constrains the expected cosmogenic neutrino flux. This constraint imposes an upper limit on the cosmogenic neutrino flux at roughly $E_\nu^2 \Phi_\nu \lesssim 10^{-8}\,\text{GeV}\,\text{cm}^{-2}\,\text{sr}^{-1}\,\text{s}^{-1}$ for neutrinos near the 1 EeV energy range [107]. However, no neutrinos at such extreme energies have yet been observed by IceCube [108].

[107]: Ahlers et al. (2010), *GZK neutrinos after the Fermi-LAT diffuse photon flux measurement*

[108]: Aartsen et al. (2016), *Constraints on Ultrahigh-Energy Cosmic-Ray Sources from a Search for Neutrinos above 10 PeV with IceCube*

3.2.3 Astrophysical Neutrinos

Astrophysical neutrinos are produced alongside cosmic rays, which are accelerated to ultra-high energies in extreme environments. These cosmic rays interact with nearby matter or radiation, resulting in the production of secondary particles that decay into neutrinos. Due to their weak interactions, neutrinos can travel vast distances through space without being absorbed or deflected, making them valuable messengers for tracing the origins of cosmic rays. The production of astrophysical neutrinos can generally be described by two main mechanisms, depending on the type of interaction the cosmic rays undergo.

The **Hadro-nuclear (pp) Scenario** involves cosmic rays, predominantly protons, colliding with nearby matter, such as dense clouds of interstellar gas composed mainly of hydrogen (neutral or ionized). These proton-proton (pp) interactions are similar to cosmic-ray-induced air showers in the Earth's atmosphere. When a high-energy proton from the cosmic ray flux collides with a thermal proton from the surrounding gas, a cascade of particles is produced, including neutral and charged pions (π^0, $\pi^\pm$). The neutral pions decay into photons (Equation 3.6), while the charged pions decay into muons and neutrinos (Equation 3.7), the produced muons subsequently decay, producing more neutrinos and electrons (Equation 3.8). Thus, the hadronuclear scenario results in the production of multiple neutrinos (of both electron and muon flavors) through the decay of charged pions and muons.

$$\pi^0 \rightarrow 2\gamma \tag{3.6}$$

$$\pi^\pm \rightarrow \mu^\pm + \nu_\mu(\bar{\nu}_\mu) \tag{3.7}$$

$$\mu^\pm \rightarrow e^\pm + \overset{(-)}{\nu}_e + \overset{(-)}{\nu}_\mu \tag{3.8}$$

In the **Photo-hadronic (pγ) Scenario**, cosmic rays interact with photons, i.e., radiation fields present in the source environment. These interactions, known as pγ interactions, lead to the production of pions via,

$$p + \gamma \rightarrow \Delta^+ \rightarrow p(n) + \pi^0(\pi^+), \tag{3.9}$$

The pγ scenario, explained in Equation 3.9 is similar to that described in Section 3.2.2 for GZK neutrinos. The difference here is that the photon is much more energetic than that of a CMB photon, hence the threshold energy for the proton to trigger resonance (Δ^+) is much lower.

Pion production can also happen if the centre of mass energy of $p + \gamma$ is larger than the center of mass energy of the pion. The pγ scenario typically occurs in regions with intense radiation fields, such as the jets of AGNs or gamma-ray bursts (GRBs), where high-energy photons are abundant. The produced pions decay similarly to the hadronuclear scenario, generating neutrinos through the same decay chains.

Each neutrino typically retains about $\sim \frac{1}{20}$ of the energy of the initial cosmic-ray particle, assuming the primary is a proton and secondary particles decay without additional interactions or significant energy loss [109]. Consequently, the neutrino energy spectrum is expected to follow a power-law distribution similar to that of the parent cosmic rays , with variations depending on the production mechanism and the nature of the astrophysical source (see Section 3.1). Furthermore, Equations 3.7 and 3.8 combined results in a flavor composition of neutrinos at the source given by $\nu_e : \nu_\mu : \nu_\tau = 1 : 2 : 0$. This implies that for every electron neutrino produced, approximately two muon neutrinos are generated, while no tau neutrinos are produced directly at the source. However, due to neutrino oscillations, by the time these neutrinos reach Earth, the flavor composition is expected to evolve into a nearly equal mix of the three flavors ($\nu_e : \nu_\mu : \nu_\tau \approx 1 : 1 : 1$). However, other source combinations are also possible depending on the source and its vicinity, thsi will be discussed in SectionZ3.

[109]: Becker (2008), *High-energy neutrinos in the context of multimessenger physics*

Source Candidates

One of the main goals of IceCube is to point back to these high energy neutrino sources. Many studies have been made in past, and are on-going to use various event samples to find these high energy source population [110]. As evident from the discussion above, The simultaneous production of gamma rays and neutrinos implies a tight connection between these messengers within the context of studying cosmic-ray acceleration. A coincidental observation through multi-messenger astronomy and the clear establishment of the connection between the diffuse gamma-ray and neutrino fluxes would be the key ingredients for identifying the sources of cosmic rays. To accomodate such searches, IceCube issues *a realtime alert* of neutrino events that are most promising high energy events [111], sending out possible direction and energy of the event to astronomy community, that can further look for events through respective messenger.

[110]: Neilson et al. (2023), *Highlights from the IceCube Neutrino Observatory*

[111]: Aartsen et al. (2017), *The IceCube Realtime Alert System*

Such an approach gave IceCube its first ever smoking gun signature of a neutrino emitter. the first evidence of an astrophysical neutrino source was the blazar TXS 0506+056, which was spatially coincident with the neutrino alert event IC170922A [112]. While the archival neutrino flare further strengthened the case of TXS 0506+056 as a neutrino source, but it was not coincident with enhanced electromagnetic emission [113]. This further poses a problem for the modeling of particle acceleration in blazars [114]. Another search looking for correlations with blazers was conducted using alert events collected over the years, via a catloague serach, which yielded no significant signal, which is compatible with a small fraction (<1%) of AGNs being neutirno emitter. More recently, strong evidence that the active galaxy NGC 1068 is a neutrino source was found, at the 4.2σ level [115].

[112]: Aartsen et al. (2018), *Multimessenger observations of a flaring blazar coincident with high-energy neutrino IceCube-170922A*

[113]: Aartsen et al. (2018), *Neutrino emission from the direction of the blazar TXS 0506+056 prior to the IceCube-170922A alert*

[114]: Winter et al. (2020), *Multi-messenger interpretation of the neutrinos from TXS 0506+056*

[115]: Abbasi et al. (2022), *Evidence for neutrino emission from the nearby active galaxy NGC 1068*

Another breakthrough occured recently when IceCube reported observation of neutrino fluxes from the Galactic Plane with a 4.5σ significance[116]. This measurement was revolutionazing as due to location of the IceCube, Because the Galactic center is located in the Southern Sky, diffuse emission is expected to be concentrated in the Southern Sky. IceCube is located at the South Pole, so observations in the southern celestial sky are composed of events downgoing in the detector. Searches in this region are particularly difficult due to the large background of atmospheric muons. Thanks to machine learning techniques, used for careful reconnstruction of the cascade like event, it was possible to make use of a sample, which can improve signal-to-background ratio of these events significantly.

[116]: Abbasi et al. (2023), *Observation of high-energy neutrinos from the Galactic plane*

Another proposed source class is **a Tidal Disruption Event (TDE)**. TDEs are transients that occur when a star passes close to a Supermassive Black Hole (SMBH) and gets disrupted by the tidal force due to the strong gravity. This creates a very bright electromagnetic flare that lasts for months. TDEs have been proposed as high-energy neutrino and ultra-high-energy cosmic ray sources [117]. A TDE called AT2019dsg was found by the Zwicky Transient Facility (ZTF) in coincidence with the alert [118], with a chance probability of 0.5%. Recently, one more candidate neutrino event has been associated to be coming from a TDE [119], making this source class a relevant choice as a contributor to diffuse neutrino fluxes [120].

[117]: Hayasaki (2021), *Neutrinos from tidal disruption events*

[118]: Stein et al. (2021), *A tidal disruption event coincident with a high-energy neutrino*

[119]: Reusch et al. (2022), *Candidate Tidal Disruption Event AT2019fdr Coincident with a High-Energy Neutrino*

[120]: Winter et al. (2023), *Interpretation of the Observed Neutrino Emission from Three Tidal Disruption Events*

Gamma-ray bursts (GRBs) have long been considered prime candidates for cosmic-ray and associated neutrino production. Neutrino emissions could theoretically occur at various stages of a GRB: during the pre-burst phase of the progenitor star [121], the prompt gamma-ray emission phase [52], and potentially in the afterglow [122]. However, early investigations by IceCube showed no significant evidence of high-energy neutrinos linked to gamma-bright GRBs [123]. Further analyses strengthened these findings, indicating that GRBs likely contribute less than about 1% of the observed diffuse neutrino flux [124]. This constraint suggests that other sources may play a larger role in the observed astrophysical neutrino fluxes. While individual coincidences with AGNs and starbust galaxy have been established, a conclusive significance to attribute what are the fractional contributions of these source classes to the observed diffusue neutrino fluxes are still remains unknown. Apart from the milkyway observations, all the other mentioned sources hint towards a dominating extragallactic contribution to the observed neutrino fluxes.

[121]: Razzaque et al. (2003), *Neutrino tomography of gamma-ray bursts and massive stellar collapses*

[52]: Bahcall et al. (1988), *Solar models, neutrino experiments, and helioseismology*

[122]: Waxman et al. (2000), *Neutrino afterglow from gamma-ray bursts: Similar to 10**18-eV*

[123]: (2012), *An absence of neutrinos associated with cosmic-ray acceleration in γ-ray bursts*

[124]: Aartsen et al. (2017), *Extending the search for muon neutrinos coincident with gamma-ray bursts in IceCube data*

Diffuse Fluxes

A diffuse astrophysical neutrino flux results from the collective contributions of numerous faint neutrino sources, each too weak to be individually detected. While multiple classes of sources are likely involved, the specific contributions from each remain unknown. At high-energy sites, as discussed in Section 3.2.3, cosmic rays generate neutrinos via pp- or $p\gamma$-interactions in *a beam dump* scenario. This implies a power-law energy spectrum $dN/dE \sim E^{-\gamma}$ for the neutrino flux, with an approximately isotropic arrival distribution due to the unresolved nature of the sources.

The neutrino-to-antineutrino ratio is expected to be around $\nu : \bar{\nu} = 1$ [2] across flavors due to averaging over many sources, though it can vary depending on the charged pion production balance in pp versus $p\gamma$ interactions. In the IceCube detector, this ratio is typically indistinguishable, except in cases like the Glashow resonance, where a $\bar{\nu}_e$ interacts with a detector electron at 6.3 PeV, selectively probing the antineutrino component. See Section 3 for details.

2: This assumption may not hold for every individual source. The neutrino-to-antineutrino ratio depends on the abundance of π^+ relative to π^- (or heavier mesons) produced during cosmic ray interactions with the "beam dump." In pp interactions, charged pions are created in roughly equal amounts, with a slight excess of π^+ due to both cosmic rays and target material being protons. In contrast, $p\gamma$ interactions produce fewer π^- mesons, primarily through multi-pion production. The limited π^- results in the Δ^+ resonance mainly producing ν_μ and ν_e, while antineutrinos are absent, as shown in Equations 3.9, 3.7, and 3.8.

A critical theoretical benchmark for this flux is the Waxman-Bahcall limit, which proposes an upper bound on the neutrino flux if it originates from the same sources responsible for the highest-energy cosmic rays [125]. According to this bound, if ultra-high-energy cosmic rays are generated in environments that are optically thin to these particles, where most escape before interacting, the corresponding neutrino flux should not exceed:

$$\Phi(E) \lesssim 3.4 \times 10^{-8} E^{-2} \,\mathrm{GeV\,s^{-1}\,cm^{-2}\,sr^{-1}} \tag{3.10}$$

This limit assumes that UHECRs are produced with an E^{-2} spectrum and that the cosmic-ray production rate aligns roughly with the star formation rate over time. Although some sources that are optically thick to cosmic rays could potentially exceed this bound, they do not naturally account for the origin of UHECRs. Moreover, this limit may get weaker if the observed softer spectrum of the cosmic ray in regions of interest is used instead of the assume harder spectrum [126].

[125]: Bahcall et al. (2001), *High energy astrophysical neutrinos: The upper bound is robust*

[126]: Mannheim et al. (2000), *Cosmic ray bound for models of extragalactic neutrino production*

In the search for astrophysical neutrinos, even a detector like IceCube, burried deep within the antarctic ice sheets, faces a lot of background noise from atmospheric muons and neutrinos created by cosmic-ray air showers, as mentioned in Section 3.2.1. IceCube detects about 3,000 muons per second at the trigger level, but typical event selections find only around 10 to 100 astrophysical neutrinos each year, with very few having energies above a few hundred TeV (see e.g., [127]). Therefore, the main goal of any event selection is to reduce atmospheric backgrounds enough so that astrophysical neutrinos can be detected. The high rate of muons observed by IceCube is due to the overburden of atmospheric air showers coming straight down the detecto, the so-called **down-going** region in Figure **??**. These poses of course the largest background for astrophysical studies[3]. Ideally, one could look for events that only come from the so-called **up-going** region, as shown in the Figure **??**, where the produced muons and neutrinos in air-showers shall be reduced significantly, as these neutrinos would have to travel through earth to reach the detector, which most of them don't survive. This solution comes at a cost of loosing half of the sky. An alternative solution is to use events that start within the instrumentation volume, but uses outer layer of the detctor to *veto* these muons and neutrinos from the air showers. Such an event sample is used for the analysis presneted in this thesis and will be dicussed in great detail in Chapter 5.

[127]: Aartsen et al. (2015), *A combined maximum-likelihood analysis of the high-energy astrophysical neutrino flux measured with IceCube*

3: but are a great source to study cosmic ray air showers

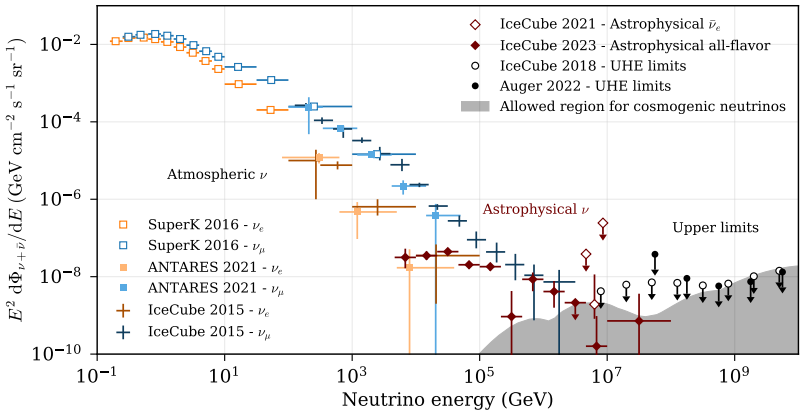

Figure 3.6: The measured energy spectra of atmospheric and cosmic diffuse neutrino fluxes have been obtained. Experimental limits at the highest energies are compared with model predictions for cosmogenic neutrinos. All fluxes are normalized to a single flavor ($\nu + \bar{\nu}$), assuming a ratio of $\nu : \bar{\nu} = 1$, and for cosmic neutrinos, a ratio of $\nu_e : \nu_\mu : \nu_\tau = 1 : 1 : 1$ at Earth. Each measurement is

add the earth schematic to show up and down going regions here

The aforementioned sample, that uses outer layer of the detector as veto was used to find an evidence for astrophysical neutrinos was first observed by IceCube in 2013 [128]. While subsequent analyses reinforced this discovery [129, 130], different studies using various event samples revealed power-law indices spanning from E^{-2} to E^{-3}, suggesting potential substructures within the flux [127, 131–133]. Although initial data hinted at these features, two recent independent IceCube studies confirmed a spectral break in the neutrino spectrum: hardening below 30 TeV and softening at higher energies, with a broken power law preferred over a single power law with more than 4σ significance [134, 135]. This spectral break offers key insights into the underlying astrophysical neutrino production mechanisms.

Figure 3.6 shows the most updated measurements for both atmospheric and astrphysical fluxes of neutrinos, along with limits at higher energies for cosmogenic neutrinos.

[128]: Aartsen et al. (2013), *Evidence for High-Energy Extraterrestrial Neutrinos at the IceCube Detector*

[129]: Kopper et al. (2016), *Observation of Astrophysical Neutrinos in Four Years of IceCube Data*

[130]: Kopper (2017), *Observation of Astrophysical Neutrinos in Six Years of IceCube Data*

[127]: Aartsen et al. (2015), *A combined maximum-likelihood analysis of the high-energy astrophysical neutrino flux measured with IceCube*

[131]: Abbasi et al. (2022), *Improved Characterization of the Astrophysical Muon–neutrino Flux with 9.5 Years of IceCube Data*

[132]: Aartsen et al. (2020), *Characteristics of the Diffuse Astrophysical Electron and Tau Neutrino Flux with Six Years of IceCube High Energy Cascade Data*

[133]: Abbasi et al. (2021), *IceCube high-energy starting event sample: Description and flux characterization with 7.5 years of data*

Flavour Composition

As outlined in Section 3.2.3, neutrinos are produced via the decays of charged pions and muons, leading to the generation of only ν_e and ν_μ in various interaction scenarios.

Flavor composition, or alternatively called the flavor ratio, is described as a set of three numbers, $(f_e : f_\mu : f_\tau)$, often normalized so that $f_e + f_\mu + f_\tau = 1$, representing the fraction of each neutrino flavor in the astrophysical flux.

The flavor composition of neutrinos can significantly vary depending on the environments of high-energy sources. For instance, produced pions and muons may interact before decaying, thereby altering the expected neutrino ratios. This leads to several **source scenarios**, each resulting in different overall flavor compositions.

The scenario discussed in Section 3.2.3 describes the **pion production scenario**, where the source environments are assumed to be sparse enough that the produced muons and pions do not interact with matter before decaying. In this case, the expected flavor composition at the source would be $\nu_e : \nu_\mu : \nu_\tau = 1 : 2 : 0$.

In high-radiation or magnetic field environments, charged pions and muons from pp and $p\gamma$ interactions can undergo significant synchrotron energy losses, around $(m_p/m_{\pi,\mu})^3 \sim 10^3$ times greater than for protons. Given their $\tau_\mu/\tau_{\pi^\pm} \sim 10^2$ times longer lifetimes [20], muons are more likely to interact before decaying, rendering these sources opaque to muons and thus eliminating their contribution to the neutrino flux. In this **muon-damped scenario**, the source flavor composition shifts to $\nu_e : \nu_\mu : \nu_\tau = 0 : 1 : 0$. Since muon interaction probability increases with energy, a realistic model would show an energy-dependent shift in flavor composition from $1 : 2 : 0$ to $0 : 1 : 0$ over 1-2 decades in energy, expected around $\sim$ 100 TeV for GRBs [136].

[20]: Navas et al. (2024), *Review of Particle Physics*

[136]: Kashti et al. (2005), *Astrophysical Neutrinos: Flavor Ratios Depend on Energy*

Additionally, in sources with dominant $p\gamma$ interactions and extremely strong magnetic fields, the **neutron-beam scenario** leads to a flavor composition of $\nu_e : \nu_\mu : \nu_\tau = 1 : 0 : 0$ [137]. Here, highly energetic neutrons are produced, either through processes like those in Equation 3.9 or by photodisintegration of heavy cosmic-ray nuclei. For neutrons to decay via $n \longrightarrow p + e^- + \bar{\nu}_e$, the source environment must be optically thin, as the resulting $\bar{\nu}_e$ are generally lower in energy compared to neutrinos from charged pion or muon decay. Strong magnetic fields are also needed to cool charged pions and muons through synchrotron losses, preventing their decays from contributing to the high-energy neutrino spectrum.

[137]: Anchordoqui et al. (2004), *Galactic point sources of TeV antineutrinos*

For sources with dominant pp interactions at very high energies, heavier mesons such as charmed mesons can form. This **charm-production scenario** has a flavor composition of $\nu_e : \nu_\mu : \nu_\tau = 1 : 1 : 0$ [100], similar to the production of prompt atmospheric neutrinos (see Section 3.2.1). Here, charmed D-meson decay produces equal amounts of ν_e and ν_μ, with tau neutrinos contributing about 5%, which can be neglected. While heavier mesons could form, bottom mesons are produced at roughly 10 times lower rates than charmed mesons [138]. This composition, $\nu_e : \nu_\mu : \nu_\tau = 1 : 1 : 0$, can also arise from energy-dependent secondary acceleration of muons and pions at the source [139].

[100]: Enberg et al. (2008), *Prompt neutrino fluxes from atmospheric charm*

[138]: Choubey et al. (2009), *Flavor Composition of UHE Neutrinos at Source and at Neutrino Telescopes*

[139]: Winter et al. (2014), *Impact of secondary acceleration on the neutrino spectra in gamma-ray bursts*

In general, realistic sources likely exhibit varying flavor compositions that depend on energy and the source environment [140]. These scenarios fit within a broader model that parameterizes flavor composition by the size and magnetic field of the acceleration region in the Hillas phase space [141], incorporating synchrotron cooling and high-energy processes

[140]: Mehta et al. (2011), *Interplay of energy dependent astrophysical neutrino flavor ratios and new physics effects*

[141]: Hummer et al. (2010), *Energy dependent neutrino flavor ratios from cosmic accelerators on the Hillas plot*

to suggest a range of energy-dependent transitions among individual cases.

Due to neutrino oscillations, the flavor composition undergoes changes as neutrinos travel from source to observer. Astrophysical neutrinos are likely produced incoherently in the scenarios described above, possessing varying energies at different locations near the source and traversing cosmic distances before detection on Earth.

Recall the transition probability for neutrino oscillations, where a neutrino from flavor eigenstate α can be measured in flavor eigenstate β as expressed in Equation 2.5:

$$P(\nu_\alpha \rightarrow \nu_\beta) = |U_{\alpha j}||U_{\beta j}| + 2\mathrm{Re}(U_{\alpha j}U_{\beta j}U_{\alpha k}U_{\beta k}e^{i\Delta m^2 L/2E}),$$

where separating diagonal and off-diagonal terms leads to:

$$\langle P(\nu_\alpha \rightarrow \nu_\beta)\rangle = X|U_{\alpha j}|^2|U_{\beta j}|^2.$$

This result is independent of Δm^2, E, and L, meaning that the expected astrophysical neutrino flavor composition at Earth is fully determined by the emitted composition at the source and the mixing parameters θ_{12}, θ_{23}, θ_{13}, and δ_{CP}. Utilizing the current best-fit measurements detailed

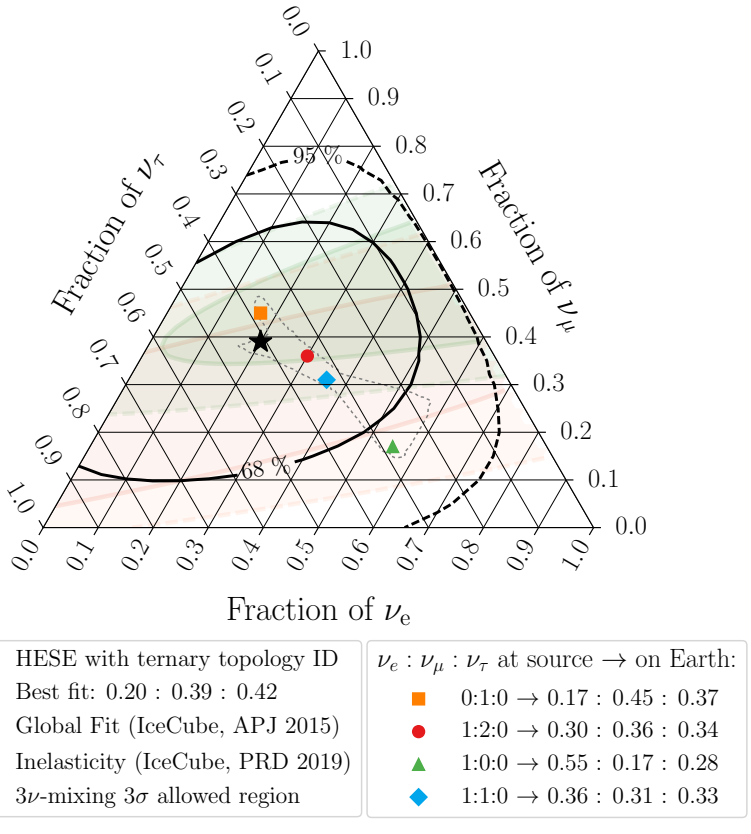

Figure 3.7: The measured flavor composition of IceCube's high-energy starting events (HESE) is shown. The contours represent the 1σ and 2σ confidence intervals. Shaded regions indicate previously published results [35, 127], which lacked direct sensitivity to the tau neutrino component. Expected flavor compositions for various astrophysical neutrino production mechanisms discussed in text marked on the figure. Figure from [142]

in Table **??**, we can derive the measured flavor ratios for the various scenarios:

Pion-production scenario: $1 : 2 : 0 \rightarrow 0.31 : 0.35 : 0.34$
Muon-damped scenario: $0 : 1 : 0 \rightarrow 0.19 : 0.43 : 0.38$
Neutron-beam scenario: $1 : 0 : 0 \rightarrow 0.55 : 0.19 : 0.26$
Charm-production scenario: $1 : 1 : 0 \rightarrow 0.37 : 0.31 : 0.32$

Despite the vast range of conceivable neutrino flavor compositions associated with cosmic rays, the detectable altered compositions on Earth are confined to a narrow phase space, as shown by the dotted grey lines around various colorful points in Figure 3.7. Moreover, this region encompasses the uncertainties in the mixing parameters at the 3σ confidence level. This result has two notable implications: first, the limited phase space of detectable flavor compositions at Earth suggests that high-precision measurements are crucial for excluding specific source models. Second, any production scenario predicts that the detectable astrophysical tau-neutrino fraction at Earth will be significantly greater than zero.

This makes flavor measurement of astrophysical neutrinos an intriguing probe for examining source contributions to the diffuse neutrino spectrum. Several studies within IceCube have attempted to measure this flavor ratio, as shown in Figure 3.7. As emphasized earlier, and visible in the figure, the main factor in measuring flavor composition is identifying tau neutrino events, since regardless of the favored scenario, a non-zero tau fraction is expected. The flavor triangle in Figure 3.7 illustrates a measurement using three distinct IceCube samples [35, 127, 142], where only the most recent measurement, which used the all-flavor starting event sample [142], achieved the first-ever non-zero ν_τ fraction by identifying two tau neutrino candidates in IceCube. A subsequent study used a *convolutional neural network (CNN)* approach to search for ν_τ events and found 7 ν_τ candidates in IceCube data [143], ruling out the absence of an astrophysical ν_τ flux at the 5σ level. The measurement of neutrino flavors in astrophysical sources, aimed at in this thesis, seeks to further refine these observations and provide crucial insights into the flavor composition of the diffuse neutrino spectrum.

[35]: Aartsen et al. (2019), *Measurements using the inelasticity distribution of multi-TeV neutrino interactions in IceCube*
[127]: Aartsen et al. (2015), *A combined maximum-likelihood analysis of the high-energy astrophysical neutrino flux measured with IceCube*
[142]: Abbasi et al. (2022), *Detection of astrophysical tau neutrino candidates in IceCube*
[143]: Abbasi et al. (2024), *Observation of Seven Astrophysical Tau Neutrino Candidates with IceCube*

Neutrinos in IceCube 4

The theoretical discussions from the previous chapters showed how neutrinos are essential for comprehending the origin of cosmic rays, as they serve as clear evidence of particle acceleration and hadronic interactions. However, detecting astrophysical neutrinos is highly challenging due to their small interaction cross-sections and the low fluxes expected from astrophysical objects at Earth. In short, a large detection volume is necessary. In this chapter, the entire process of neutrino detection will be described from the secondary particles produced in neutrino interactions to the propagation of their Cherenkov light in ice to the recording of this light with IceCube's optical sensors.

4.1 IceCube Neutrino Observatory

As described in 2.1.2,the detection of high-energy neutrinos requires a large detector due to their small interaction cross-section. When these neutrinos interact, the secondaries produce Cherenkov photons (see 4.3.2), therefore, the detector must be transparent to these photons. Such a large detector volume can be acquired by using natural resources such as large bodies of water or ice; by deploying photosensors underneath to create a sufficiently sized detector.

This concept was first introduced in 1960 [144]. The groundwork for implementing such a detector began with water-based experiments like DUMAND [145], which was planned to be deployed in the sea near the main island of Hawaii and another detector with a similar design Lake Baikal [146]. First ever large-scale neutrino telescope built was predecessor of IceCube experiment called AMANDA [147] at the geographic South Pole. A few hundred optical modules were dropped under the ice sheet of this dry continent between the depth of 1.5 to 2 km. Needless to say, the IceCube detector, the largest neutrino telescope in the world today, benefitted greatly in terms of design and performance from all the research and development work that was done with AMANDA. There also exists a large volume water-based neutrino telescope in the Northern Hemisphere called ANTARES[148], and its successor KM3NeT[149], located in the Mediterranean Sea.

[144]: Markov (1960), *On high energy neutrino physics*

[145]: Babson et al. (1990), *Cosmic-ray muons in the deep ocean*

[146]: Belolaptikov et al. (1997), *The Baikal underwater neutrino telescope: Design, performance, and first results*

[147]: Andres et al. (2000), *The AMANDA neutrino telescope: principle of operation and first results*

[148]: Ageron et al. (2011), *ANTARES: The first undersea neutrino telescope*

[149]: Margiotta (2014), *The KM3NeT deep-sea neutrino telescope*

The following subsections will discuss various detector and hardware components of the IceCube detector. Additionally, the last section will cover the optical properties of the South Pole ice, as these properties strongly affect the analysis observable and therefore influence the flavor measurements presented in this thesis.

4.1.1 Detector

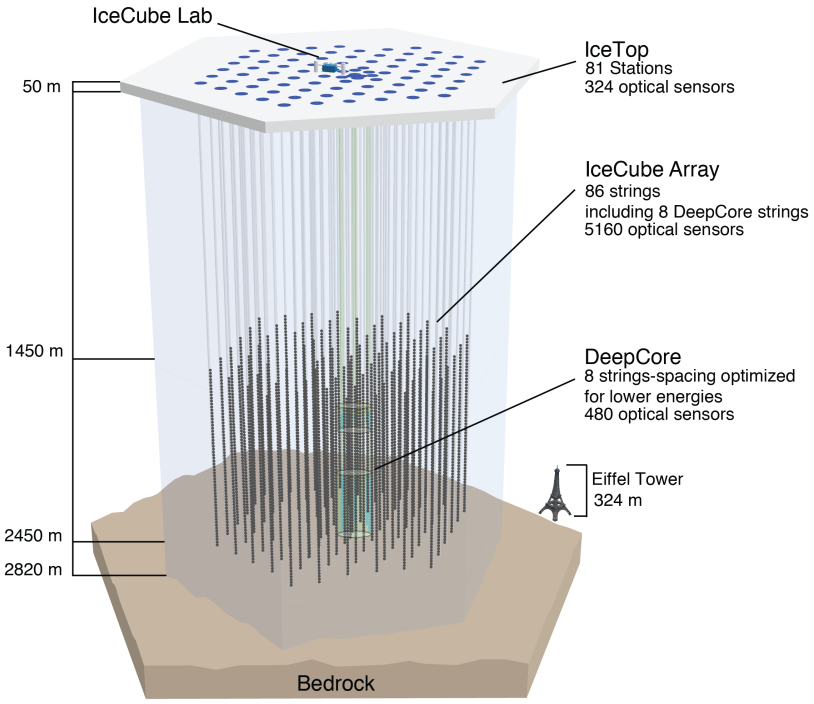

Figure 4.1: A schematic overview of the IceCube detector and its components [150]

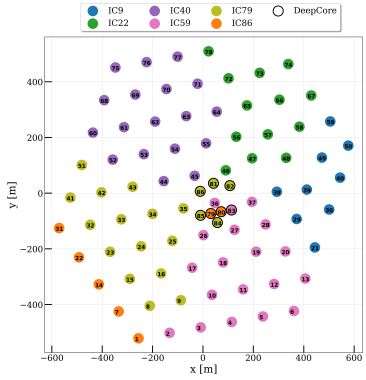

Figure 4.2: Top view of the location of each *in-ice* strings of IceCube. Colour represents set of strings deployed in each seasons as described in Table 4.1. Note: IceTop Stations are not shown here.

The IceCube Neutrino Observatory is located at Amundsen-Scott South Pole Station at the geographic South Pole. It comprises a cubic kilometer of instrumented ice, equipped with 5,160 digital optical modules reffered as *DOMs* from here-on (see 4.1.2), buried deep in the ice and 81 IceTop Stations on the surface of the ice, making itself the largest Neutrino Observatory in the world [150]. A schematic of the detector layout is shown in Figure 4.1. Four main components of the detector are *in-ice array,DeepCore (inner extension of in-ice array),IceTop and IceCube Lab.*

The Main *in-ice* array consists of 78 strings, each consisting of 60 DOMs, spaced vertically at a distance of 17 m between the depth of 1450 m to 2450 m under the ice sheet of Antarctica. Horizontal spacing between each of these strings is 125 m.

DeepCore comprises inner 8 strings (see Figure 4.2) of the main*in-ice* array, placed more closely together with horizontal string distance of 70 m and vertical DOM distance of 7 m [151] between 1750 m to 2450 m depth. There's a region between depth of 1850 m to 2100 m, with no DOMs attached to the string as this region is the so-called *dust layer* (see section 4.2), where optical scattering and absorprion is quite high and thus is not efficient to make reliable physics measurements. The Photomultipliers used in DOMs attached on these 7 strings also have higher Quantum Efficiency, which reduces the energy threshold to 10 GeV. Although, IceCube's main goal is to detect astrophysical neutrinos, current topics of research spans much broader range (e.g fundamental properties of the neutrinos, such as oscillations [152], Physics beyond Standard Model searches such as Dark Matter [153] etc).

IceTop is the surface detector array of the IceCube detector, primarily designed to detect Cosmic-ray airshowers and to be used as a veto layer for downgoing muons produced in these airshowers [154]. It

[150]: Aartsen et al. (2017), *The IceCube Neutrino Observatory: instrumentation and online systems*

***string* in IceCube**

An arrangement of DOMs attached on a twisted copper wire cable makes the so-called *string* in IceCube.

[151]: Abbasi et al. (2012), *The design and performance of IceCube DeepCore*

[152]: Aartsen et al. (2019), *Measurement of atmospheric tau neutrino appearance with IceCube DeepCore*

[153]: Abbasi et al. (2022), *Search for GeV-scale dark matter annihilation in the Sun with IceCube DeepCore*

[154]: Abbasi et al. (2013), *IceTop: The surface component of IceCube*

Season	Configuration	Strings	IceTop Stations
2004-05	IC1	1	4
2005-06	IC9	9	16
2006-07	IC22	22	26
2007-08	IC40	40	40
2008-09	IC59	59	59
2009-10	IC79	79	73
2010-11	IC86	86	81

Table 4.1: IceCube detector components deployed in each season (cumulative). Each configuration is represented as *ICXX* where *IC* stands for IceCube and *XX* stands for number of total *in-ice* strings at the end of that season

consists of 81 *stations* each having 2 tanks filled with clear ice (162 tanks in total). Each of these 162 tanks have 2 DOMs, similar to the ones deployed in *in-ice* array, which makes it easier for both arrays to have a similar trigger and data acquistion system.

***IceCube Lab*(ICL)** serves as the central operations' hub for the experiment, providing a crucial support for data acquisition and filtering. All the string cables connected to the aforementioned detcetor components are routed up to the ICL, from where triggered data is sent back to the northern hemispher via a satellite. Various other operations such as mainting the detector operations etc are also maintained from this building.

For the work presented in this thesis, neither *deepcore* nor *IceTop* data is used.

The construction of the detector started taking place in 2005 and lasted for 7 Antarctic summer seasons till 2011 December. In each season, parts of the current day Hexagonal detector were deployed, as shown in Figure 4.2 and numbers detailed in Table 4.1. A hot water drill was used to unfreeze the ice upto 2.5 km depth and 60 cm diameter into which these strings were then deployed (see Figure 4.3). The geometry of the detcetor, i.e The *xy*-coordinates of the string were calculated from the drill tower position, surveyed during the deployment. Assuming the string was vertical, these coordinates were applied at all depths, with deviations of less than 1 m (later validated using the flasher data, see 4.1.3). Depths of the lowest DOM were determined from pressure readings, corrected for water compressibility and ambient air pressure, with vertical DOM spacings measured via laser ranger. All depths were converted to z-coordinates in the IceCube coordinate system .

IceCube coordinates system

The IceCube coordinate system's origin is at 46500'E, 52200'N, 883.9 m elevation, which is quite close to centre of the *in-ice* array. The y-axis points Grid North (toward Greenwich, UK), the x-axis points Grid East (90 degrees clockwise from North), and the z-axis points "up", forming a right-handed coordinate system.

Maybe draw a small schematic of coordinate system here next to the side note?

4.1.2 The Digital Optical Module (DOM)

The Digital Optical Module (DOM) is a crucial component of the IceCube Neutrino Observatory, functioning as the heart of the detector. Each DOM is responsible for collecting the faint light signals produced by neutrino interactions in the Antarctic ice, amplifying these signals, and transmitting the data to the IceCube Lab [150]. From there, the data is relayed to the Northern Hemisphere via a satellite for further analysis.

Inside each DOM, a 10-inch Photo Multiplier Tube (PMT) is positioned at the bottom, accompanied by essential circuitry for power conversion, data acquisition, calibration, control, and data transfer. Individual components of a DOM are as shown in Figure 4.4, functions of each of which is explained briefly below.

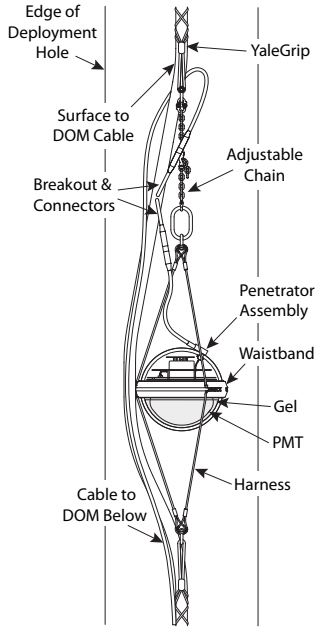

Figure 4.3: A schematic of DOM Cable-Assembly being deployed in a water hole, created by hot water drill [150].

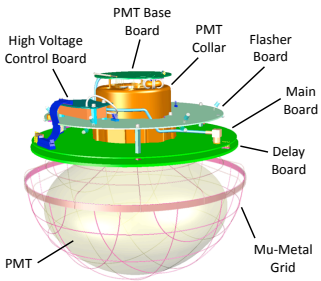

Figure 4.4: A schematic of the DOM, showing its main components [150].

Glass Vessel Properties : The glass vessel of the DOM is engineered to withstand the extreme pressures found in the deep Antarctic ice. This includes the constant long-term pressure of about 250 bar and the temporary pressure spikes of up to 690 bar experienced during the refreezing process after deployment using a hot water drill. The vessel is composed of two 0.5-inch thick hollow glass hemispheres, which are joined together with optical glue. This design not only provides a robust and hermetic seal to protect the internal electronics but also maintains the optical clarity necessary for the PMT to function effectively. The glass material is chosen for its strength, transparency, and resistance to the harsh conditions in the ice.

PMT : The PMT within the DOM is a 10-inch diameter tube that utilizes a box-and-line dynode chain with 10 stages to amplify the faint light signals detected in the ice. The PMTs used in standard in-ice DOMs have a quantum efficiency peaking at 25% whereas, DeepCore DOMs, designed to detect lower energy neutrinos, feature PMTs with a higher peak quantum efficiency of 34% near the 390 nm wavelength. These PMTs are operated at a gain of 10^7.

Gel : A high strength, silicon gel is used between the photocathode area and the glass vessel to provide optical coupling and strong mechanical support to the DOM system. This gel has a high optical clarity, with 97% transmission at 400 nm. It shows no signs of deterioration even after a decade, ensuring reliable performance.

Magnetic Shield : The ambient magnetic field at the South Pole, measuring around 550 milligauss (mG), angled 17 degrees from vertical, can significantly affect the performance of the PMT. This includes reducing collection efficiency by 5-10% and causing gain variations of up to 20%, depending on the PMT's azimuthal orientation. To mitigate these effects, a mu-metal cage is installed around the PMT bulb, extending up to its neck. This cage is constructed from a mesh of 1 mm diameter wires with a spacing of 66 mm. Although this mesh blocks about 4% of the incident light, it substantially reduces the adverse impacts of the magnetic field, ensuring more consistent and reliable performance of the PMT.

PMT Base and High Voltage Boards : The high voltage board includes a Digital to Analog Converter (DAC) and an Analog to Digital Converter (ADC) for precise control and monitoring of the voltages supplied to the PMT. The high voltage generator on this board provides the necessary power, which is then regulated and distributed by the voltage divider circuits on the PMT base board. These circuits are specifically designed for low power consumption, ensuring efficient and stable operation of the PMT.

Main Board : The main board serves as the central processing unit (CPU) of the DOM, managing and coordinating all other electronic components. It digitizes the waveforms detected by the PMT, providing a digital representation of the light signals for further analysis. The main board also temporarily stores data, calibrates the internal clock, and exchanges local coincidence information with neighboring DOMs (see 4.1.3). It communicates directly with the Data Acquisition (DAQ) system, ensuring the seamless transfer of data to the IceCube Lab. Additionally, the main board hosts an adjustable low-intensity optical source, which is used to calibrate

the PMT's gain and timing, ensuring consistent and accurate performance.

Flasher Board : Flasher board contains 12 LEDs each having specified output wavelength of 405 ± 5nm, which generates lights *in situ* to make various caliberation related measurements. In addition, this board can verify timing responses (useful for many, including analysis presented in this thesis, reconstruction processes). Additionaly, to measure *the optical properties* of the South Pole Ice (see section 4.2) and locations of the DOMs in ice.

4.1.3 Trigger and Data Acquisition

Ever Since the initial deployment of the first string, the detector has been consistently gathering data, maintaining an average uptime of nearly 99% [155]. *The photocathode* of the PMT of a DOM, *captures* a photon which then generates *photoelectrons* which are accelerated through the series of 10 dynodes to generate measurable *photocurrent*. This current is integrated over a time to obtain collected charge in units of *photoelectrons or PEs*, through which *photovoltage* is produced at the mainboard, over time, known as *waveform*. These waveforms are then digitized to acquire and relay the data to the Northern Hemisphere.

[155]: Abbasi et al. (2009), *The IceCube data acquisition system: Signal capture, digitization, and timestamping*

Depending on how many photons hit the PMT, these waveforms can have different amplitudes ranging from 1mV upto the linearity limit of the PMT (2 V) in time range of 12-1500 ns. The In Order to access this rather broad dynamic range, the digitiser used, Analog Transient Waveform Digitiser (ATWD) have three channels to amplify the waveform by factor of 0.25, 2 and 16. Moreover, 2 sets of ATWD are used that can operate alternatively in order to reduce the deadtime. ATWD can digitize voltage withinn duration of 427 ns, a window sufficient to reconstruct light produced within 10s of m around a given DOM. Naturally, some photons produced in energetic interactions may travel larger distances, producing faint but detectable waveforms. To amplify and digitize these waveforms, a fast Analog to Digital Converter (fADC) is also used, together ATWD+fADC is reffered as a *DOMLaunch*.

The aforementioned digitization only happens if the voltage threshold of the onboard discriminator is met, which is kept at voltage equivalent to a PE of 0.25, or in other words, a DOM is *hit*. If at least two neighbouring DOMs, on the same string produces individual *hits* within 1 μs called *Hard Local Coincidence(HLC)*, the full *DOMLaunch* is transmitted to the surface. Otherwise, only the timestamp and minimal amplitude/charge information is sent known as *Soft Local Coincidence(SLC)*. The HLC condition helps reduce false triggers from PMT dark noise, which is independent across DOMs. *The Data Acquisition System (DAQ)* processes further uses these HLC hits to look for temporal coincidences. Most commonly used trigger in IceCube is the so-called *The Single Multiplicity Trigger (SMT-8)*, that requires eight or more HLC hits within 5 μs timewindow. If and when SMT8 trigger conditions are met, all launches (HLC and SLC) are combined into what is called an *event*.

Various algorithms are used to make an estimate of event properties such as direction, deposited energy, morphology etc. The South Pole has limited computational resources, so only simple first guess algorithms

can be used there called *online filters*. Processed data is transmitted to the Northern Hemisphere. After this, more sophisticated reconstruction algorithms are applied to reduce and tailor the data as per Physics analysis goal.

cite simulation/reco chapter here

4.2 Optical Properties of the South Pole ice

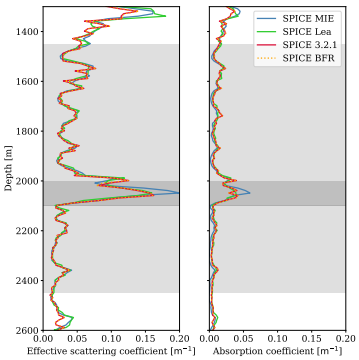

Figure 4.5: Values of effective scattering (left) and absorption (right) coefficents of 400nm photons in South Pole Ice as a function of depth, for four icemodels described in the text. Light grey area shows in-ice array and dark grey region shows the high absorption and scattering region called *the dust layer*.

The ice at the South Pole is a crucial part of the IceCube detector. It acts as both the detection target and the medium through which light propagates. Unlike the DOM hardware, which has been extensively studied in the laboratory, the glacial ice can only be measured in its actual environment, making it more challenging to describe. Understanding and calibrating this medium well is essential for accurate physics measurements as photons produced from particle interactions can get absorbed or scattered from their path, making the inference of the particle interaction points challanging.

In context of Neutrino Detection, The ice at the deep South Pole was initially measured using pulsed in situ light sources (LEDs) at different wavelengths, embedded in the AMANDA array below 1000 m depth[156]. Later, during the construction of IceCube, direct measurements of dust concentration in the glacial ice were obtained using a dust logger deployed into some drill holes [157]. Additionally, the LEDs on the Flasher Board of DOMs are still actively used to calibrate the detector and understand the ice properties [158].

The scattering length (l_s) is the average distance a photon will travel before scattering off of its orignal directory. In practice, only the effective scattering length ($l_{eff} = \frac{l_s}{1-\langle \cos\theta \rangle}$) can be measured, where $\langle \cos\theta \rangle$ is the average deflection angle at each scatter. **The absorption length (l_a)** is the distance after which a photon's survival probability decreases to 1/e, indicating how far the information from an event can travel. In the case of absorption, the photon is lost, while for scattering, its direction changes, affecting both the energy and direction reconstruction of the event. Scattering and absorption parameters in *ice models* are averaged over 10-meter-thick layers of ice and are calculated for a wavelength of 400 nm [158]. Light scattering below a depth of about ~1300 m is mainly due to residual air bubbles. As depth increases, dust becomes the main source of scattering, with concentration varying due to climate and volcanic activity. At around 2000 meters, scattering and absorption significantly increase due to high dust concentration, possibly from a major volcanic eruption in the past, known in IceCube as **the dust layer** [159] (see Figure 4.5). This layer is either ommitted or treated more carefully in most analyses as information carried by photons coming and going throught this layer is difficult to traceback due to higher scattering coeeficient.

The data from the dust logger also revealed that the ice layers are not perfectly horizontal; they are tilted due to the uneven surface of the bedrock [157], the so-called **ice tilt**. Initially, the effect was symmetrically parameterized along an axis (reffered to as *the tilt axis*) that is approximately perpendicular to the glacial flow and also dependent on depth (same as the layers used to characterise absorption and scatetring lengths described before)[158]. As a result, the scattering and absorption coefficients became dependent on the full three-dimensional position in

[156]: Ackermann et al. (2006), *Optical properties of deep glacial ice at the South Pole*

[157]: Aartsen et al. (2013), *South Pole Glacial Climate Reconstruction from Multi-Borehole Laser Particulate Stratigraphy*

[158]: Aartsen et al. (2013), *Measurement of South Pole ice transparency with the IceCube LED calibration system*

[159]: Woschnagg et al. (2000), *Age vs depth of glacial ice at South Pole*

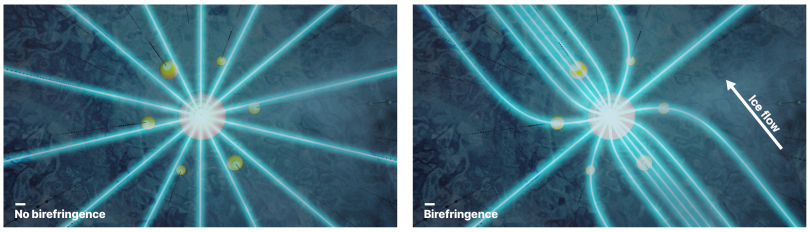

Figure 4.6: The visualisation of deflection due to birefringence. Without it (left panel), light streams out radially from an isotropic source. With this effect however (right panel), rays get deflected towards the flow axis, appearing as though photons are scattered "more" along this axis. The IceCube array around the light source can be seen as well. (Figure taken from [160])

the ice rather than just the depth. A recently developed fully volumetric tilt model now includes a newly discovered tilt component along the flow [161].

[161]: Chirkin et al. (2023), *An improved mapping of ice layer undulations for the IceCube Neutrino Observatory*

Another unique property that the South Pole ice exhibits is optical **anisotropy**, a phenomenon affecting photon propagation depending on their direction relative to the "axis of anisotropy," which coincides within $\sim 1^\circ$ with the direction of the ice flow [158]. This effect was initially implemented as a modification to the scattering function, the only remaining Mie scattering parameter [162], thereby changing the scattering length [163, 164]. However, recent detailed studies suggest that this behavior results from diffusion within the polycrystalline ice microstructure, a previously unknown optical effect, now known as Birefringence [160, 165]. This effect causes the ice crystals to slowly but continuously deflect towards the normal vector of the girdle plane of the crystal orientation fabric (the ice flow axis), as can be seen in Figure 4.6.

[162]: Hahn (2004), *Light Scattering Theory*
[163]: Chirkin et al. (2013), *Evidence of optical anisotropy of the South Pole ice*
[164]: Usner (2018), *Search for Astrophysical Tau-Neutrinos in Six Years of High-Energy Starting Events in the IceCube Detector*
[160]: Abbasi et al. (2024), *In situ estimation of ice crystal properties at the South Pole using LED calibration data from the IceCube Neutrino Observatory*
[165]: Chirkin et al. (2019), *Light diffusion in birefringent polycrystals and the IceCube ice anisotropy*

In the context of the IceCube Detector, South Pole ice can be divided into two types: bulk ice and hole ice. Bulk ice is the undisturbed part of the ice, consisting of sheets that have formed over hundreds of thousands of years, properties of which are described above. **Hole ice**, on the other hand, is the refrozen column of ice that was melted during the deployment of the DOMs [166]. This effect generally affects the forward acceptance of the IceCube DOMs. If not taken care of, it can lead to errors in directional information, therby affecting measurements involving zenith angle reconstructions of the incoming neutrino. Over the years, many efforts have been made to understand various optical properties of the South Pole ice, by fitting the LED data in terms of absorption and scattering lengths of a cherenkov photon in ice, the so-called ***South Pole ICE model (SPICE model)***. These icemodels are used in both simulation and reconstruction of the events, where particles produced in neutrino interactions are propagated (see 4.3.1) based scattering and absorption lengths described by the model. While the base model for the scattering of the photons in-ice is Mie Scattering theory [162] (SPICE MIE), with more dust loggers data, evolved more complex models to include, aniostropy (SPICELea), addition of tilt (SPICELea, SPICE 3.2.1), birefringence to explain anisotropy (SPICEBfr) and the latest, SPICE FTP, which includes a 2D tilt corretion in addition to birefringence. Figure 4.5 shows absorption and scattering coefficients for different ice models at various depths in the detector. The corresponding scattering and absorption lengths are simply the inverse of the coefficients. It can be seen that the ice below the depth of ~ 1400 m is so clear that light can travel for hundreds of meters before being absorbed. However, the light diffuses quickly, making a point-like source appear nearly isotropic at a distance of around 100 m. Effect of different icemodel corrections (specifically that of anisotropy related

[166]: Abbasi et al. (2021), *A calibration study of local ice and optical sensor properties in IceCube*

corrections) becomes quite relevant to reconstruct tau-neutrino events in IceCube (see Section 5.5), which is heart of the analysis presented in this thesis.

4.3 Detection of Neutrinos in IceCube

As described in 2.1.2, regardless of the type of neutrino interaction (NC or CC), a variety of secondary particles are generated. In the case of a CC interaction, an accompanying charged lepton absorbs some energy, which can then undergo further decay or interact within the ice volume, leading to the production of more particles. Moreover, secondary particles, regardless of the interaction type, may also include hadrons, which are not always charged. This can, in turn, reduce the amount of *visible* light in the detector. In this section, propagation of these leptons and hadrons in ice shall be explained in brief, followed by Cherenkov effect, a phenomenon by which IceCube DOMs observes these photons from the neutrino interactions. Lastly, various morphologies of these interactions will be discussed in the context of IceCube and similar detectors.

4.3.1 Particle propgation in-ice

When a charged particle moves through a medium like ice, it loses energy due to interactions with the medium's particles. This energy loss is characterized by the quantity $\frac{dE}{dx}$, where dE represents the energy lost and dx the area of the medium traversed, typically measured in $\mathrm{g/cm^2}$. Four primary processes contribute to the energy loss profile of a particle in such a medium: continuous ionization losses and radiative losses due to bremsstrahlung, pair production, and photonuclear interactions. *Ionization* occurs when the particle collides with shell electrons of the atoms in the medium, causing a continuous energy loss that scales logarithmically with the particle's energy [20]. Additionally, if the particle is unstable, it may decay. In the context of IceCube, secondary leptons travel at nearly the speed of light, simplifying β to approximately 1. Thus, the decay length can be rewritten as $\lambda_{\mathrm{dec}} = \frac{E\tau}{mc}$, where E is the lepton's energy and m its mass. The decay length indicates the distance at which the lepton's survival probability drops to $\frac{1}{e} \approx 36.8\%$, following the exponential decay law $p(L) = \exp(-L/\lambda_{\mathrm{dec}})$.

[20]: Navas et al. (2024), *Review of Particle Physics*

Radiative losses, such as *bremsstrahlung*, occur when the charged particle is deflected through Coulomb scattering off a target atom, while *pair production* involves the creation of an electron-positron pair by an emitted photon. *Photonuclear interactions* occur when a photon emitted by the particle disintegrates an atomic nucleus. These radiative losses are stochastic and scale roughly linearly with the particle's energy, with the radiation length X_0 defining the distance over which the particle's energy decreases to $\frac{1}{e}$ of its initial value [20]. The overall energy loss can be expressed as,

$$-\frac{dE}{dx} = a(E) + b(E)E \tag{4.1}$$

where $a(E)$ represents ionization losses and $b(E)$ encompasses all radiative losses.

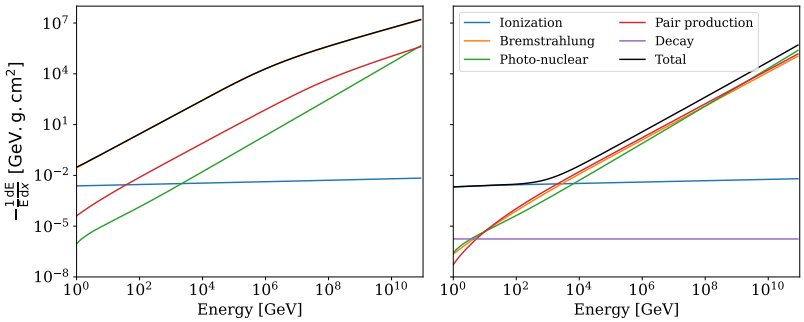

Figure 4.7: The average energy loss rate per energy, for electrons (left) and muons (right) in ice showing the contributions from ionization, bremsstrahlung, photonuclear interactions, and pair production. Note that decay is only shown for Muons as electrons are stable particles that do not decay. Figure reproduced from [167]

Leptons

To determine a neutrino's flavor, it's important to understand the energy losses of the charged lepton created in a CC-interaction. The radiation length varies depending on the lepton's mass, influencing emitted radiation and aiding in lepton identification. For leptons with $\beta\gamma \gg 1$, this ionization loss can be approximated as constant, with a value of $\langle \frac{dE}{dx} \rangle_{\text{ion}} \approx 2\,\text{MeV}/(\text{g}/\text{cm}^2)$ [67]. In ice, this corresponds to a continuous energy loss of approximately 180 MeV per meter. However, at energies exceeding *critical energy* (E_c), radiative losses become dominant, and ionization losses become negligible, as shown in the Figure 4.7 [167].

[67]: Perkins (2003), *Particle astrophysics*

[167]: Chirkin et al. (2004), *Propagating leptons through matter with Muon Monte Carlo (MMC)*

For **electrons**, we mainly consider radiative losses (mainly bremsstrahlung see Figure 4.7) as they are stable and do not decay. Photons from bremsstrahlung then create additional e^+e^- pairs which can create more photons and so on, resulting in a cascade of particles until the energies of electrons and positrons fall below the critical level. This behavior can be described by a gamma distribution, regardless of what the initiating particle is (e^+ e^-or γ) [20]. The rate of energy loss over distance can be calculated using the equation:

$$\frac{dE}{dt} = E_0 b \left(\frac{(bt)^{a-1} e^{-bt}}{\Gamma(a)} \right) \tag{4.2}$$

Where t represents the distance along the cascade in units of radiation length, and E_0 is the initial energy of the injected particle and a and b are dimensionless shower parameters. For an electromagnetic cascade induced by an electron, the parameters are $a = 2.02 + 0.63 \log(E_0/\text{GeV})$ and $b = 0.63$ (determined using `GEANT4` simulations [168]). The distance to the shower maximum, t_{max}, which is given as $t_{\text{max}} = \frac{a-1}{b}$ characterizes the size of electromagnetic cascades, indicating that they grow logarithmically in size with energy and have a characteristic size of several meters. This justifies the common approximation that light is emitted from a single point, a useful assumption for simulation and event reconstruction purposes (see Section 5.3 of Chapter 5 for details).

[168]: Radel et al. (2013), *Calculation of the Cherenkov light yield from electromagnetic cascades in ice with Geant4*

At very high energies (> 10 PeV), *the Landau-Pomeranchuk-Migdal (LPM) effect* becomes significant, causing suppression of bremsstrahlung and pair production cross sections [169–171]. This suppression occurs due to destructive interference between multiple scattering centers, leading to elongated and irregular shower profiles.

[169]: Landau et al. (1953), *Limits of applicability of the theory of bremsstrahlung electrons and pair production at high-energies*
[170]: Landau et al. (1953), *Electron cascade process at very high-energies*
[171]: Migdal (1956), *Bremsstrahlung and Pair Production in Condensed Media at High Energies*

Muons experience similar ionization and radiative losses as described in **??**, but due to their larger mass, the radiation length ($\text{X}_0 \sim 15\text{km}$) is

much longer than that of an electron (($X_0 \sim 36$cm)) of the same energy. This results in a higher critical energy (E_c) of 1 TeV in ice, allowing muons to penetrate more deeply than electrons ($E_c = 79$ MeV) [167], as can be seen in the right panel of Figure 4.7. The average energy loss rate can be approximately parameterized using 4.1, with $a = 0.00268\text{GeV cm}^2/\text{g}$ and $b = 0.47 \times 10^{-5}\,\text{cm}^2/\text{g}$ in ice [20], allowing the calculation of the average range of a 1 TeV muon, which is 2 km in ice [1].

1: If one neglects these radiative losses, due to its longer lifetime ($\tau_\mu = 2.2 \times 10^{-5}$) and small mass ($m_\mu = 105.67$), the same energy muon will travel ~ 6000km distance

The **tau** lepton has an even larger radiation length than a muon, $X_0 \sim 4754$ km, but its decay length is much shorter, $L_\tau(E_\tau = 1\,\text{TeV}) = 4.9\text{c}m$ [20]. Thus, most taus created in IceCube will decay very promptly. τ^- can decay mainly via the following three modes (with the branching rations specified next to each):

$$\begin{aligned} \tau^- &\rightarrow \nu_\tau + \text{Hadrons} \quad (64.79\%) \\ \tau^- &\rightarrow \mu^- + \bar{\nu}_\mu + \nu_\tau \quad (17.39\%) \\ \tau^- &\rightarrow e^- + \bar{\nu}_e + \nu_\tau \quad (17.82\%) \end{aligned} \tag{4.3}$$

where the most commonly produced hadrons are pions and kaons [20]. Similar decay modes are observed for τ^+ too, by keeping in mind Lepton number conservation. Since each mode produces at least one neutrino, part of the tau lepton's energy is not "visible"[2]. In addition, the large radiation length will create much less light during propagation through the ice than a muon of the same energy. As will become clear in the next chapter, a 1 TeV tau cannot be distinguished from an electron due to its short decay length and the large sensor spacing of IceCube. Taus from ν_τ charged-current interactions are polarized [172], and due to the small decay length and large radiation length, the decay products' energy spectrum gets affected. This becomes important in the analysis presented in this thesis, where one of the observables is an estimate of deposited energy in the detector, see Section 5.4.2 for details.

2: Although these neutrinos can regenerate to interact or decay further, the probability of both neutrinos interacting within the 1 km^3 volume is rare

[172]: Argüelles et al. (2022), *Tau depolarization at very high energies for neutrino telescopes*

Hadrons

Hadrons are produced in all flavour NC interactions, or when a tau lepton decays (see 4.3). Hadronic cascades are more complex than electromagnetic cascades because they involve a wider variety of secondary particles and have larger uncertainties in the relevant cross-sections. Unlike electromagnetic cascades that consist solely of electrons, positrons, and photons, hadronic cascades involve numerous neutral particles that do not emit "*visible*" light in the detector, resulting in a lower light yield (see 4.3.2). Additionally, the production threshold for hadrons is higher compared to that for electrons, positrons, and photons [167]. Despite these differences, a significant portion of the cascade's total energy can still be carried by electrons, positrons, and photons, which are produced by electromagnetic sub-cascades initiated by the decay of neutral pions ($\pi^0 \rightarrow \gamma\gamma$).

[167]: Chirkin et al. (2004), *Propagating leptons through matter with Muon Monte Carlo (MMC)*

The longitudinal profile of hadronic showers can be parameterized using 4.2, although the specific values for the shower parameters are $a = 1.81 + 0.39 \log(E_0/\text{GeV})$ and $b = 0.34$ (assuming cascade is induced by a charged pion). It is important to note that the electromagnetic radiation length used in these equations applies to both types of cascades; however, it does not account for the generally larger nuclear interaction length

characteristic of hadronic showers, adding another layer of complexity and resulting in greater fluctuations in the overall development of the particle cascade. This makes modeling hadronic cascades more challenging compared to their electromagnetic counterparts.

4.3.2 Cherenkov effect

When a charged particle moves through a medium at speed exceeding the phase velocity of light in that medium, it emits *Cherenkov radiation* [173], much like the shock wave generated by a supersonic jet. This radiation is emitted in a cone at an angle $\theta_C = \cos^{-1}\left(\frac{1}{\beta n}\right)$ relative to the particle's direction of travel, where n is the refractive index of the medium and $\beta = \frac{v}{c}$ represents the ratio of the particle's velocity to the speed of light in a vacuum (see Figure 4.8). In ice, with a refractive index of $n = 1.31$ at a wavelength of 400 nm, which corresponds to the peak sensitivity of IceCube's optical modules (see, 4.1.2), the emission threshold for Cherenkov radiation is $\beta_{\text{Ch}} \gtrsim 0.76$. This corresponds to a minimum energy of 0.28 MeV for electrons and 58.09 MeV for muons, both of which are below IceCube's detection threshold of around 200 GeV. For high-energy particles in IceCube, where $\beta \simeq 1$, the Cherenkov cone's opening angle is $\theta_{\text{Ch}} \simeq 40.2°$ at the peak sensitivity wavelength. The number of Cherenkov photons emitted within a waveband $d\lambda$ by a particle with charge ze within the propagation length dx is given by the Frank-Tamm formula [174]:

$$\frac{d^2N}{dxd\lambda} = \frac{2\pi\alpha z^2}{\lambda^2}\left(1 - \frac{1}{\beta^2 n(\lambda)^2}\right) \tag{4.4}$$

where, α is fine structure constant [20]. Using this formula, one can calculate that for a high-energy particle with $\beta \simeq 1$ passing through ice, approximately 250 photons/cm are emitted in the wavelength range of 300 nm to 500 nm, which is within IceCube's optimal detection range [168].

Neutrino interactions in IceCube are detected indirectly through Cherenkov radiation from secondary charged particles (leptons, hadrons and electromagnetic showers, see 4.3.1) , reffered to as *visible light* in IceCube. At energies above 1 TeV, the Cherenkov light from a muon itself becomes negligible, and detection primarily depends on light emitted by secondary particle showers along the muon's path.

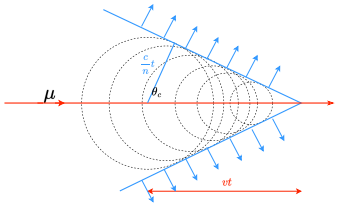

Figure 4.8: The sketch shows the Cherenkov effect for a muon traveling through a dielectric medium with a velocity $v = \beta c$ (in red). The medium has a refractive index n, and the phase velocity of light $v_{\text{phase}} = \frac{c}{n}$ (in blue). The circles in the sketch represent wavefronts with equal phase shifts and illustrate isotropic and coherent emission (blue arrows) at an angle θ_c , for $v > v_{\text{phase}}$.

[173]: Cherenkov (1937), *Visible radiation produced by electrons moving in a medium with velocities exceeding that of light*

[174]: Frank et al. (1937), *Coherent visible radiation of fast electrons passing through matter*

[20]: Navas et al. (2024), *Review of Particle Physics*

[168]: Radel et al. (2013), *Calculation of the Cherenkov light yield from electromagnetic cascades in ice with Geant4*

4.3.3 Event Signatures

The previous sections described the detector and its various components, along with the interactions and passage of neutrinos and the secondary particles they produce. In IceCube, events are visualized with the detector shown as an array of strings, with each colored sphere representing a triggered DOM. The sphere's size scales with the detected cherenkov light amount (charge accumulated), and its color indicates the arrival time. Section 2.1.2, discussed how all-flavor neutral current (NC) interactions result in the transfer of a fraction of the neutrino's energy to the nucleus, initiating a hadronic shower. On the other hand,

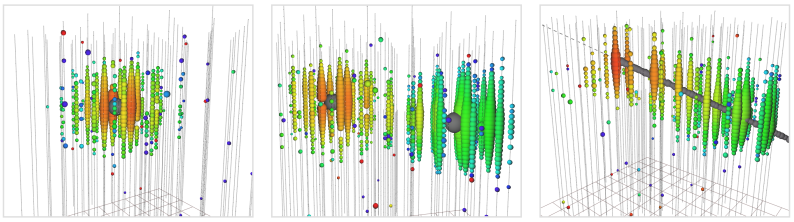

Figure 4.9: Simulated event signatures of single cascade (left), double cascade (middle), and track (right). Sizes of the spheres represent the amount of detected light, and colors show the photon arrival times. Single cascades are caused by electromagnetic and hadronic showers, double cascades by the production and decay of a tau lepton, and tracks by muons traversing the detector.

charged current (CC) interactions are accompanied by a charged lepton, whose propagation patterns were detailed in 4.3.1. The involvement of specific neutrino flavors in CC events leads to a distinct energy deposition patterns (*morphology*), which can be used to identify the neutrino flavor. Additionally, when a neutrino interaction occurs within the volume of the detector, it is classified as a *starting* event, and if the energy deposition is entirely within the detector volume, it is termed a *contained* event. Hadrons and electrons produce showers, which are known in IceCube as **cascades**. Due to the low radiation lengths of electrons and the short shower maximum caused by various secondary particles, cascades are contained within a few meters. This causes Cherenkov light emission to appear as a point-like source relative to the kilometer-scale detector. However, due to a higher scattering coefficient 4.2 the light pattern appears almost spherical for cascades see Figure 4.9, due to which, the angular information is lost (or becomes less reliable) upon reaching the DOMs, leading to a poor angular resolution. In electromagnetic cascades, most of the interaction energy is contained within the cascade, making ν_e - CC events excellent candidates for energy estimation [175].

[175]: Aartsen et al. (2014), *Energy Reconstruction Methods in the IceCube Neutrino Telescope*

Tracks are observed when highly energetic muons traverse the detector, most commonly from atmospheric muons produced by cosmic-ray-induced air showers. Tracks are also caused by CC interactions of $\nu_\mu(\bar{\nu}_\mu)$, which produce a hadronic cascade and a μ^- (μ^+). When the neutrino interaction vertex is outside the detector volume, atmospheric muons and neutrino-induced muons are indistinguishable unless their energy and direction are considered, leading to *a through-going track*. When the vertex is inside the detector volume, both the hadronic cascade and the emerging muon track are visible, resulting in *a starting track*, which can only be caused by neutrino interactions. Although muons exhibit stochastic energy loss and are likely to exit the detector, resulting in poor energy resolution, the light deposition along an extended path (see Figure 4.9) provides good angular resolution (less than 1 degree), making tracks ideal for identifying high-energy astrophysical sources [175].

is there any nu sources paper that can be cited for this claim?

Tau neutrinos in IceCube exhibits variety of signatures, thanks to different tau decay modes (4.3). This leads to various event morphologies [176] based on factors like position of both, the neutrino interaction and tau decay verteces, decay channel and the decay length, as shown in Figure 4.10. The tau decay length (L_τ) is connected to Energy of tau lepton (E_τ) via $L_\tau \simeq \frac{50\text{m}}{1\text{PeV}} E_\tau$. ν_τ CC events typically produce two energy depositions: an initial interaction cascade followed by a tau decay product, which can be a track or cascade, depending on the decay channel. The muonic decay channel results in a dim tau track followed by a brighter muon track.*

[176]: Cowen (2007), *Tau neutrinos in IceCube*

* The stochasticity of muon energy losses and the low branching ratio of the muonic decay channel (17.4%) make it challenging to search for this signature. Therefore, this decay channel is excluded from the analysis presented in this thesis.

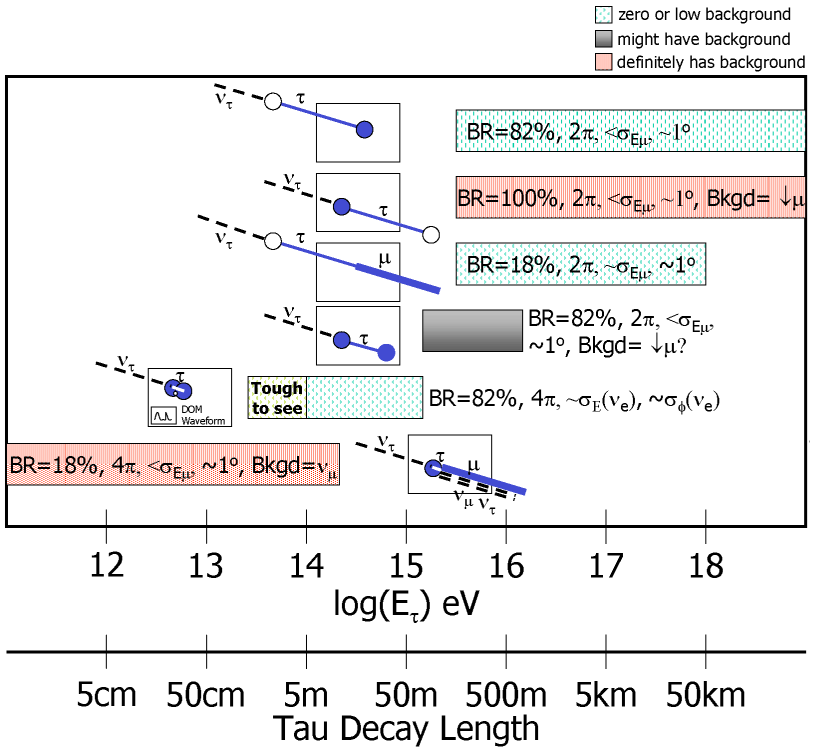

Figure 4.10: Various morphologis of ν_τ cc events in IceCube, as a function of E_τ and L_τ. Circle represent a cascade, dotted line represents primary ν_τ, thin line, Tau lepton track and thick line represent muon track.(Figure taken from [176])

The other decay channels, involving hadrons or electrons, produce a cascade, leading to the so-called **double bang** events [177]. Around 59% of tau-neutrino interactions are double bang events.†

[177]: Learned et al. (1995), *Detecting tau-neutrino oscillations at PeV energies*

These double bang events are further classified based on whether both the interaction vertex and tau decay vertex are within the detector volume (see Figure 4.10). At lower energies (below (~ 100) TeV), the separation between the two cascades is small, making them difficult to resolve. In some cases, if the event occurs close to a string or Digital Optical Module (DOM), two distinct time-connected pulses can be observed, known as the **double pulse** technique. However, identifying tau neutrino events in IceCube is challenging due to background muons and the difficulty in reconstructing such events. Recent developments using CNN classifiers have identified seven astrophysical tau neutrino candidates [143]. Lastly, if both of these caascades are contained in the active volume, and they are far enough to be reconstructed reliably, the morphology is called **double cascade**. This method has low and high tau energy threshold, since below certain energy (~ 100 TeV) the decay length is quite short, making them indistinugishable from a usual cascade event, and energies above 10 PeV, (where theoretically the length should be large enough to separate the two cascades) one of the cascades will always be outside the detector volume. In such case, a larger detector volume, such as in IceCube Gen2, could extend the energy range for identifiable double cascade events (see Chapter 8).

[143]: Abbasi et al. (2024), *Observation of Seven Astrophysical Tau Neutrino Candidates with IceCube*

The analysis performed in this thesis aims to measure neutrino flavour composiition where three of the morphologies explained above, starting

† The muonic decay of the tau has a branching ratio of around 17%, while all other decay channels of the tau produce another cascade with an inclusive branching ratio of approximately 83%. When multiplied by the fraction of the charged-current cross-section over the total cross-section [20], about 59% of all tau-neutrino interactions are double bang events.

tracks, double cascades and cascades (from hereon reffered to as single cascades, to differentiate from double) are used to identify flavour of the neutrino. Double cascades are not only challanging due to their tricky geometry but also because of involvement of both electromagnetic and hadronic particle showers involved. Lastly, as was discussed in **??**the medium (ice) itself has many characteristic properties that affects the reconstruction of these events drastically. Details of sampling these high energy starting events and reconstructing them in to these three morphologies will be explained in the next chapter.

Event Sample,(Re)construction and Particle Identification

5

In the previous chapters, high-energy neutrino interactions within IceCube was discussed, focusing on how the secondary particles generated from these interactions propagate through the ice. From this, one could deduce that different neutrino flavours can create distinct morphological patterns due to the variety of charged particles produced in the interaction processes. As mentioned in Section 4.3.3, these morphological signatures are crucial in identifying the neutrino flavour, although it becomes particularly challenging in the case of tau neutrino-induced double-bang events. Apart from the complexities of reconstruction, another critical aspect is the selection of astrophysical neutrinos from the overwhelming background of atmospheric muons and neutrinos.

In this chapter, the high-energy neutrino sample used for the analysis presented in this thesis will be detailed, along with the reconstruction method used to identify the particles based on the event's morphology. The chapter will begin with a general overview of the simulation chain in IceCube, followed by a brief overview of the SnowStorm simulations used for the analysis. Lastly, the chapter will discuss the influence of the South Pole IceModel on reconstructed Double Cascade events.

5.1 Monte Carlo Simulation

The hunt for astrophysical neutrino interactions in the IceCube detector is conducted without access to actual data, a method known as **blind analysis**. To develop the selection (rejection) criteria for signal (background) events, and their light yield reconstruction, simulated events are used.[1] By comparing the distribution of an observable quantity between simulated and real data events, conclusions can be drawn about the detected neutrino population. Hence, simulating how IceCube responds to neutrinos and other particles is essential for comprehending the collected data.

1: In some cases, typically during the development phase of the analysis sample, selection cuts are validated on small subset (10%) of the experimental data, known as *the burn sample*.

Event simulation in IceCube is based on commonly used Monte Carlo methods. The simulation framework covers all stages, from the generation and propagation of a primary particle to the emission and propagation of Cherenkov light, and finally, the digitized waveforms recorded by all hit DOMs in IceCube.

5.1.1 Icecube simulation chain

The IceCube simulation begins with *a particle generator* that simulates a flux of particles hitting the detector. The primary particle can be a neutrino or a cosmic ray particle reaching Earth's atmosphere. Neutrinos may reach the detector directly, while cosmic rays interact with particles in the atmosphere to produce a shower of particles, from which muons and neutrinos can reach the detector by propagating through ice, forming the so-called atmospheric neutrino and atmospheric muon background.

Particle Generation

The software that generates neutrinos is called `NuGen` (Neutrino Generator) and is based on `ANIS` (All Neutrino Interaction Simulation). To start the simulation, neutrinos of a selected flavour are drawn from a power-law energy spectrum with an equal probability of being a neutrino or antineutrino. Neutrino directions are sampled from an isotropic distribution and aimed to intersect with an imaginary surface centered on the detector. Each neutrino is then propagated in discrete steps through matter encountered on the way to the detector. For each step, a neutrino interacts with a probability[2] of $1 - e^{-\sigma n \Delta x}$, where σ is the total interaction cross-section and n is the density of nucleons at the location in the Earth. The nucleon density is modelled using *the Preliminary Earth Reference Model (PREM)* [178], which provides the mass density of the Earth as a function of radius. Because the tau has a short lifetime and a large radiation length, it usually transfers a significant portion of its energy to the tau neutrino produced in its decay (see Section 4.3.1). This leads to substantial ddecrease of overall ν_τ flux at higher energies, a phenomenon known as *tau-regeneration* [179]. This so-called earth effect is also taken into account by the `NuGen` software.

2: a probabilty that gets stored as propagation weight for each stage and enters in total weight calculations as a *total interaction probability*.

[178]: Dziewonski et al. (1981), *Preliminary reference earth model*

[179]: Halzen et al. (1998), *Tau-neutrino appearance with a 1000 megaparsec baseline*

After enough steps, neutrinos will reach the imaginary cylinder defining the detection volume where they are forced to interact somewhere between the projected entry and exit points of the cylinder according to a uniform distribution.In the case of a muon resulting from a CC ν_μ interaction far outside the surface, the length at which interactions are required to occur is automatically extended backward based on a parameterization of the muon range in ice. When a neutrino interaction is forced, a weight of $p_{\text{int}} = n\sigma L \exp(-n\sigma L_{\text{before}})$ must be assigned, where L_{before} is the distance before the selected interaction point where an interaction may have occurred, and L is the total length where an interaction may have occurred. This weight is often combined with the propagation weight to give a total interaction probability weight $w_{\text{int}} = p_{\text{prop}} p_{\text{int}}$. The interaction type is then randomly selected according to CC, NC, and GR cross-sections, and secondary particles are generated for further propagation by another program. In IceCube, single atmospheric and astrophysical neutrinos cannot be distinguished on an event-by-event basis. Therefore, the NuGen-generated neutrinos are used for both atmospheric and astrophysical fluxes. Neutrinos will have weights assigned to them according to the expected (or tested) atmospheric and astrophysical fluxes, and these weights can be used to calculate an expected event rate.

To generate atmospheric muons and neutrinos, an adapted version of `CORSIKA` [180] is used to simulate the production of muons resulting from cosmic ray showers in the Earth's atmosphere. This process begins with a primary particle, typically a nucleus, initiating a cascading shower of particles upon interaction with the atmosphere. Only neutrinos and muons from these showers are capable of reaching the detector. Due to the impracticality of simulating atmospheric neutrino interactions using `CORSIKA`, only the muons generated in the showers are transmitted to the detector. The software allows for event weighting based on various cosmic ray models. `CORSIKA` is currently the exclusive software capable of producing muon bundles, which are large numbers of muons origi-

[180]: Heck et al. (1998), *CORSIKA: A Monte Carlo code to simulate extensive air showers*

nating from the same cosmic ray shower. However, a major limitation of CORSIKA is its computational expense, as it propagates all particles from a cosmic ray shower, most of which are undetectable in a sub-surface detector like IceCube. To address this drawback, MUONGUN [181] was developed to simulate single muons more efficiently and economically by generating them directly around the detector volume. In the context of HESE (which will be discussed in Section 5.2), the primary background arises from single muons, as muon bundles produce a more continuous light deposition, resulting in a higher likelihood of being vetoed upon entering the detector. Since flux models more complex than a simple power law are often required, NuGen simulations can be re-weighted to match any arbitrary flux. A weight is assigned to each event that reflects the ratio between the desired flux $n_{\text{expected}} = \Phi(E)$ and the generated fluence of neutrinos. The generated fluence can be expressed as,

[181]: Santen (2014), *Neutrino Interactions in IceCube above 1 TeV: Constraints on Atmospheric Charmed-Meson Production and Investigation of the Astrophysical Neutrino Flux with 2 Years of IceCube Data taken 2010–2012*

a block diagram of simulation chain here

$$n_{\text{generated}} = \frac{N(E)}{\Omega A_{\perp}} \tag{5.1}$$

where $A_{\perp}$ is the projected area of the detection surface for each neutrino, and Ω is the solid angle covered by the simulation, typically 4π for neutrinos coming from the entire sky. $N(E)$ represents the energy distribution of simulated neutrinos, which, for a power-law distribution with N_0 events and a power-law index γ, spanning from energy E_{min} to E_{max}, is given by:

$$N(E) = \frac{N_0 E^{-\gamma}}{\int_{E_{\text{min}}}^{E_{\text{max}}} E^{-\gamma} dE} \tag{5.2}$$

Here, N_0 refers to the number of neutrino or antineutrino events, and not the total, when separate fluxes for neutrinos and antineutrinos are known. This implies that N_0 represents half of the total number of events generated for each neutrino flavor. Finally, accounting for the interaction weight, the total weight assigned to each neutrino (in units of Hz) is:

$$\begin{aligned} w &= w_{\text{int}} \frac{n_{\text{expected}}}{n_{\text{generated}}} \\ &= w_{\text{int}} \frac{A_{\perp} \Omega \Phi(E)}{N(E)} \end{aligned} \tag{5.3}$$

By summing these weights over all simulated events that pass the event selection, the expected event rate for any desired flux model can be calculated.

Secondary Charged Particle Propgation

Once a particle interaction occurs within the detector volume, the next step is to generate and propagate secondary particles through the ice. Depending on their nature, these secondary particles may undergo further interactions within the ice, with some of them producing detectable Cherenkov light in the detector volume (see Section **??** for details). Both atmospheric muons from air showers and secondary leptons, such as electrons, muons, and taus from CC neutrino interactions, are propagated

through the ice after they are produced. The software used for lepton propagation is called PROPOSAL (Propagator with Optimal Precision and Optimized Speed for All Leptons) [182] and is based on the previous implementation MMC (Muon Monte Carlo) [167]. The lepton production is simplified by assuming that the emission angle is aligned with the incident angle of the primary particle, and that it travels at the speed of light, which are both reasonable assumptions above the energy threshold of 100 GeV. The various propagation effects of different particle types and energies, as described in 4.3.1, are taken care of by PROPOSAL. In particular, highly energetic muons are simulated to have long tracks that are predominantly characterized by stochastic energy losses. Electromagnetic and hadronic cascades, as described in Section 2, are simulated by CMC (Cascade Monte Carlo) [183]. It generates individual particle showers by randomly sampling energy losses from the energy-dependent shower parametrization and also takes the LPM-effect into account. The shower parametrizations have been determined by fitting the Cherenkov light yield for a full shower simulation using GEANT4 (Geometry And Tracking) [168, 184].

[182]: Koehne et al. (2013), *PROPOSAL: A tool for propagation of charged leptons*

[167]: Chirkin et al. (2004), *Propagating leptons through matter with Muon Monte Carlo (MMC)*

[183]: Voigt (2008), *Sensitivity of the IceCube detector for ultra-high energy electron-neutrino events*

[168]: Radel et al. (2013), *Calculation of the Cherenkov light yield from electromagnetic cascades in ice with Geant4*

[184]: Rädel et al. (2012), *Calculation of the Cherenkov light yield from low energetic secondary particles accompanying high-energy muons in ice and water with Geant 4 simulations*

Photon Propagation

Once all primary and secondary particles have traversed the detector, the next phase of the simulation process involves the emission and propagation of Cherenkov photons from all visible particles or energy losses (as discussed in Section **??**). The number of cherenkov photons is proportional to the combined track length of all charged particles, and the refraction index of ice. Individual photon propagation is traced through an OpenCL-based photon-tracking simulation (as shown in Figure 5.1), known as CLSim [186], derived from *Photon Propagation Code* (PPC) [187]. The SPICE models (as detailed in Section 4.2) are used to describe the scattering and absorption of photons. Each photon is tracked through multiple scatterings until it either reaches the collection area of a DOM or, more often, is absorbed. CLSIM harnesses GPUs for photon propagation due to their efficiency in running numerous simple operations (such as photon scattering) in parallel [187].

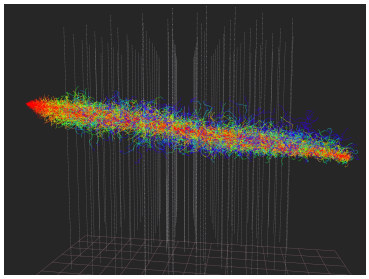

Figure 5.1: Light emission pattern of a simulated muon track event, using the direction propagation program CLSim. The colored lines show individual photon paths through ice, with red indicating earlier and blue indicating later compared to an unscattered photon. Figure taken from [185]

[186]: Kopper (n.d.), *Clsim*

[187]: Chirkin (2013), *Photon tracking with GPUs in IceCube*

Since the direct propagation of photons even by using GPUs can be exteremely time and power consuming, an alternative method is used in IceCube that creates a look-up table that stores the expected timing distribution of photoelectrons at a Digital Optical Module (DOM) for various configurations of the light source and DOM. The concept involves simulating a light source (cascade, track, or flasher) at specific depths and directions multiple times, while tracking the photon yield around the source. Initially, the challenge of creating this table seemed daunting due to the complexity of the problem, as it required a table with 9 dimensions[3]. However, One can take advantage of the approximate horizontal translational and azimuthal symmetry of the ice to reduce the dimensions to 6: depth of the source in ice, zenith angle of the source, displacement vector of the DOM from the source, and time. It is important to note that this approach has its limitations, as it disregards certain effects such as ice layer tilt and anisotropic scattering, which do not adhere to the symmetry assumptions. In recent years, these limitations have been overcome by introducing corrections to scattering lengths (the

3: Three for the source position, three for the DOM position, two for the light source orientation, and one for time.

so-called *effective distance correction*), which was done while developing the double cascade reconstruction [164] that will be explained in Section 5.4, and also by introducing corrections directly in modelling of the ice to account for ice anisotropy and tilt corrections, see Section 4.2 for details. Initially, `Photonics` was used to predict and store the expected photon flux in a multi-dimensional histogram structure, but this method had drawbacks such as binning issues and inaccuracies at great distances. Currently, a more effective approach involves fitting the photoelectron distribution obtained from `CLSim` or `PPC` to a tensor product B-spline surface [188]. This offers the advantage of having a smooth function of all 6 coordinates and can address unphysical fluctuations caused by limited statistics through the use of regularization.

[164]: Usner (2018), *Search for Astrophysical Tau-Neutrinos in Six Years of High-Energy Starting Events in the IceCube Detector*

[188]: Whitehorn et al. (2013), *Penalized splines for smooth representation of high-dimensional Monte Carlo datasets*

Detector Simulation

The detector's response is the final step in the simulation process. The PMT's sensitivity depends on the wavelength and angle of the incoming photon, as well as its quantum efficiency. This means that not every photon will trigger the PMT. The simulation takes into account the varying PMT sensitivity for each photon. Additionally, the simulation considers the angular acceptance of photons, accounting for local scattering variations in the ice. The PMT hardware has been thoroughly calibrated and studied in the lab [189], and these results have been incorporated into the simulation. It's important to model the transit time and jitter of the PMT in the simulation, as these factors affect the timing and width of the pulse. Furthermore, all triggers used in real-time data collection at the South Pole are also included in the simulation. This final step in the simulation process completes the creation of a simulated event.

[189]: Abbasi et al. (2010), *Calibration and characterization of the IceCube photomultiplier tube*

5.1.2 SnowStorm Simulation

As described in previous section, specifically for photon propagation stage precise knowledge of ice is important. While we use calibration measurements to estimate the detector properties, this only provides limited precision. When conducting simulations, which are crucial for estimating the detector's response, one need to be careful not to assume specific detector properties. For most of the IceCube analyses so far, variations of the detector response were included using a particular strategy: A set of Monte Carlo simulations with *baseline* values of all systematic parameters was created to estimate event rate in the analysis. The baseline value of a systematic parameter is its most likely value determined from calibration. Variations of this baseline event rate caused by a different, *off-baseline*, detector response were estimated using different *discrete systematics sets*. The combination of discrete baseline and systematics sets allows the estimation of the analysis variables as well as their variation with the detector systematics. This variation is typically assumed to be small and estimated with a low-order Taylor expansion. The off-baseline systematics sets are then used to estimate the coefficients of this expansion.

A new approach to model detector systematic uncertainties has been developed in IceCube called, **SnowStorm Method** [190]. The significant difference compared to the discrete systematics approach described above

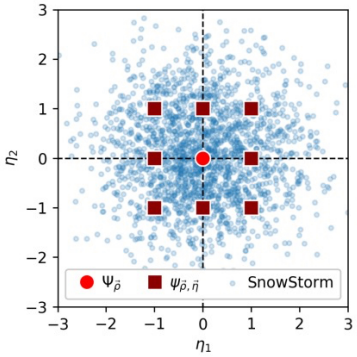

Figure 5.2: Illustration of the SnowStorm method described in the text. It depicts the contrast between numerous discrete shifts in nuisance parameters (indicated by red squares), each necessitating an entire Monte Carlo set, in comparison to a single SnowStorm Monte Carlo (represented by small blue dots). Figure taken from [190]

[190]: Aartsen et al. (2019), *Efficient propagation of systematic uncertainties from calibration to analysis with the SnowStorm method in IceCube*

is that each detector systematic parameter continuously varied while generating the MC events, as visualized in Figure 5.2. Using the SnowStorm method, one obtains a single MC set representing all variations in the detector response. This can help an analysis by reducing the bookkeeping effort necessary for using multiple discrete sets, studying variations in a large number of detector systematic parameters at once without loss in statistics, and allowing analyses of different event selections to use the same MC set and "marginalize" over all detector systematic parameters that are not relevant for a single analysis.

The analysis presented in this thesis uses simulations generated using this aforementioned novel method. It involves uniform and independent sampling distributions for all relevant parameter uncertainties in the flavor analysis. These simulations cover all three flavors of neutrinos and were created using the SPICE-3.2.1 icemodel. They were designed for general use and were also utilized by several other IceCube analyses simultaneously, see [191] and [192] for details. The simulation sets were developed for primary neutrinos in the energy range of E_ν =[100 GeV - 1 PeV] assuming a single power law of $E_\nu^{-1.5}$, and in the range [1-100 PeV] with a E_ν^{-1} spectrum. The harder spectrum is generally chosen, particularly for higher energy datasets, to ensure a sufficiently large number of events at those energies. Using the weighting method described previously, one can reweight the neutrino events to match any desired spectrum.

[191]: Ganster (2024), *Measurement of the high-energy astrophysical neutrino energy spectrum combining muon tracks and cascades measured at the IceCube Neutrino Observatory*

[192]: Naab (2024), *Evidence for a Break in the Diffuse Extragalactic Neutrino Spectrum*

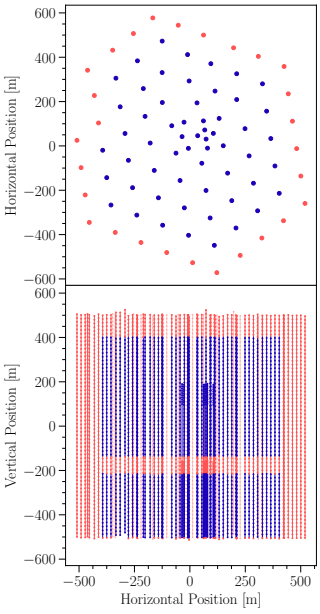

Figure 5.3: The top view (above) and side view (below) display the veto DOMs and the DOMs within the fiducial volume for HESE. DOMs highlighted in red represent the veto region, while those in blue define the fiducial volume. Events where the initial detected light comes from the veto region are excluded from the analysis. Figure taken from [133].

5.2 High Energy Starting Event (HESE) sample

The High Energy Starting Events (HESE) selection is a comprehensive, all-sky, all-flavor sample of astrophysical and atmospheric neutrinos observed in IceCube. This selection process led to IceCube's first significant milestone: the discovery of an astrophysical neutrino flux [128]. Subsequently, a particle identifier was developed using this sample with added years of data, eventually finding two tau neutrino candidates in IceCube [133, 142]. For the analysis presented in this thesis, this sample was again used, along with some updates in Self-Veto calculations, that shall be introduced in Section 5.2. The concept behind HESE is to establish a veto region on the detector's outer edges to select only events where the initial Cherenkov photons are detected inside the fiducial volume. As shown in Figure 5.3, the veto region includes the outer strings, a top layer of 90 m, a central layer of 80 m around the dust layer, and a 10 m bottom layer. The very thicker veto at the top is essential for filtering out atmospheric muons entering from above. However, the veto can be thinner at the bottom of the detector since up-going atmospheric muons do not exist. The inclusion of a veto around the dust layer is crucial, as horizontal events passing through this highly absorptive region can mimic starting events. To pass the veto, events must deposit fewer than 3 photoelectron (PE) in the veto region out of the first 250 PE recorded within the fiducial volume, and a minimum total charge of 6000 PE is required to ensure high-energy events are selected.

The HESE selection is particularly powerful due to its simplicity, as it does not rely on complex reconstructions, making it robust against changes in filtering or reconstruction algorithms. The fact that it is an all-flavour

[128]: Aartsen et al. (2013), *Evidence for High-Energy Extraterrestrial Neutrinos at the IceCube Detector*

[133]: Abbasi et al. (2021), *IceCube high-energy starting event sample: Description and flux characterization with 7.5 years of data*

[142]: Abbasi et al. (2022), *Detection of astrophysical tau neutrino candidates in IceCube*

sample, can help break degeneracies caused by different neutrino flavors producing similar event patterns. Additionally, the all-sky nature of HESE allows for the study of the zenith distribution of events, which can distinguish between atmospheric and astrophysical neutrinos. However, HESE does have limitations: the high-energy threshold introduces uncertainty in estimating background contributions and astrophysical parameters, and the veto region reduces the detector's effective volume. An extension of HESE to lower energies, known as Medium Energy Starting Events (MESE), has been developed [193] (and recently updated [135]) to overcome some of these limitations.

Despite of rejecting a significant fraction of atmospheric background, HESE retains the majority of astrophysical neutrinos within its fiducial volume. The neutrino effective area of the HESE sample, increases with neutrino energy due to the larger amount of visible light deposited (see Figure 5.11). At energies above a few hundred TeV, the effective areas become similar across all flavors, except the Glashow resonance of $\bar{\nu_e}$ at 6.3 PeV. However, at lower energies, the effective area varies by flavor due to differences in energy deposition during charged-current interactions, with electron neutrino interactions producing the highest effective area due to the nearly complete energy deposition in electromagnetic and hadronic cascades. For different zenith angles, the effective area decreases as the zenith angle increases, particularly in the up-going region at high energies. This is a result of Earth absorption, which becomes significant for neutrinos above approximately 1 PeV. The distinction between tau neutrinos and other flavors at the highest energies is due to the phenomenon of tau regeneration, where the tau neutrino regenerates after the decay of a tau lepton. Muon neutrino interactions, on the other hand, produce muons that deposit only part of their energy before escaping the detector, resulting in a higher detection threshold. Neutrino interactions, especially for ν_τ, exhibit effective areas between those of ν_μ and ν_e.

[193]: Aartsen et al. (2015), *Atmospheric and astrophysical neutrinos above 1 TeV interacting in IceCube*

[135]: Basu et al. (2023), *From PeV to TeV: Astrophysical Neutrinos with Contained Vertices in 10 years of IceCube Data*

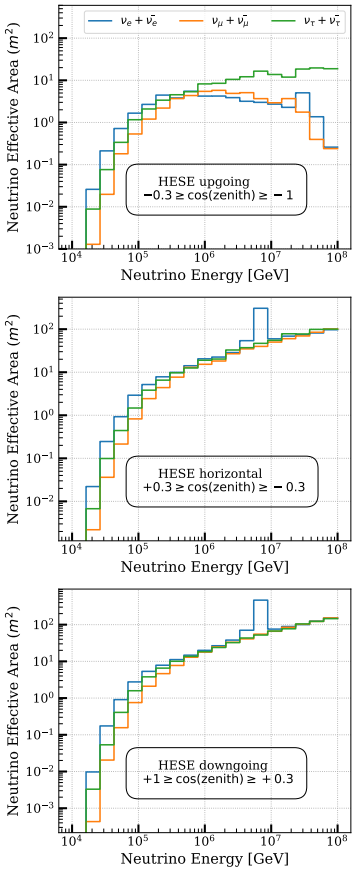

Figure 5.4: The neutrino effective areas for the high-energy starting event selection as a function of neutrino energy. The distributions are shown for all neutrino flavors, broken down by various zenith angle ranges.

Atmospheric Neutrino Self-Veto

As mentioned in Section 3.2.1, high-energy cosmic ray showers produce many neutrinos and muons, which are the only particles able to reach underground detectors such as IceCube. When atmospheric neutrinos reach the detector, they are typically accompanied by other particles from the same CR shower, mostly muons. The chance of a detectable muon accompanied with an atmospheric neutrino is called **the atmospheric self-veto probability**. Several things affect this probability, such as the type, energy, and direction of the neutrino. In the case of high-energy CR showers, some muons may reach the detector and *trigger* the veto that marks the event as background. The likelihood of rejecting an atmospheric neutrino through this self-veto mechanism increases with higher neutrino energy and more vertical shower angles. With such a modelling, one effectively suppresses the flux of atmospheric neutrinos, in down-going region[4]. **The passing fraction** of atmospheric neutrinos—defined as the fraction that is not accompanied by a detectable muon from the same CR shower—varies with both neutrino energy and zenith angle [194]. It tends to increase at larger zenith angles, as muons must travel farther through the atmosphere to reach IceCube, as shown in Figure

4: This process only applies to downward-moving atmospheric neutrinos because muons cannot reach IceCube from below the Earth

[194]: Arguelles Delgado et al. (2018), *Unified atmospheric neutrino passing fractions for large-scale neutrino telescopes*

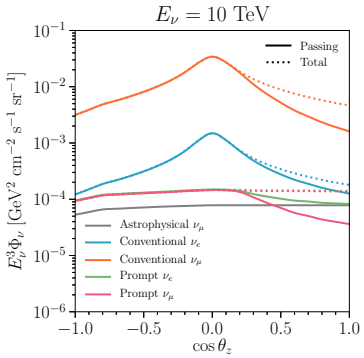

Figure 5.5: The Atmospheric neutrino fluxes at $E_\nu = 10$ TeV. The plot shows the fraction of the flux that is **not** vetoed, known as **passing fluxes** (solid lines), alongside the total flux entering the detector (dashed lines) as a function of the cosine of the zenith angle. Figure is adapted from [194].

[194]: Arguelles Delgado et al. (2018), *Unified atmospheric neutrino passing fractions for large-scale neutrino telescopes*

[195]: Yuan et al. (n.d.), *nuVeto*

[196]: Fedynitch et al. (2015), *Calculation of conventional and prompt lepton fluxes at very high energy*

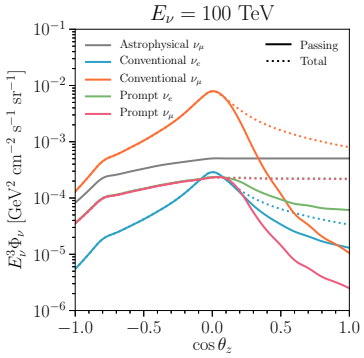

Figure 5.6: The atmospheric neutrino fluxes and the effect of self-vetoing are displayed for a neutrino energy level of $E_\nu = 100$ TeV, see caption of Figure 5.5. Figure atken from [194].

[175]: Aartsen et al. (2014), *Energy Reconstruction Methods in the IceCube Neutrino Telescope*

[188]: Whitehorn et al. (2013), *Penalized splines for smooth representation of high-dimensional Monte Carlo datasets*

[164]: Usner (2018), *Search for Astrophysical Tau-Neutrinos in Six Years of High-Energy Starting Events in the IceCube Detector*

5: to account ice layer tilt and anisotropy due to birefringence (see Section 4.2 for details) separately

[197]: Yuan (2023), *Detecting neutrinos in IceCube with Cherenkov light in the South Pole ice*

5.5. At neutrino energies greater than 100 TeV, the contribution from astrophysical neutrinos begins to outweigh the atmospheric background, improving IceCube's ability to detect astrophysical neutrinos as indicate din Figure 5.6.

The passing fractions used in the analysis presneted in this thesis is based on the calculations derived in [194] a formalism used in 7.5 years of HESE analysis [133] through the `nuVeto` package [195]. The previously used calculations are further updated using MCEq package, MCEQ, a tool designed to solve the cascade equations governing cosmic ray-induced showers, allowing for more precise and computationally efficient predictions of atmospheric lepton fluxes [196].

5.3 Maximum Likelihood Event Reconstruction

With the aforementioned HESE sample, next step is to infer the properties of these events—primarily energy, direction, and the deposited light pattern (morphology). To do so, it is necessary to *reconstruct* each individual event. The reconstructed properties are then used to create probability density functions (PDFs) that facilitate likelihood fits for making the desired physics measurements (as outlined in Section 6.1). Therefore, it is crucial to reconstruct the event properties as accurately as possible. The analysis presented here utilizes a maximum-likelihood estimation (MLE) approach, called `millipede` for event reconstruction.

`millipede` aims to maximize the likelihood of the observed light pattern from an event, given a specific source hypothesis. The input data comprises individual pulses detected by Digital Optical Modules (DOMs), expressed in terms of charge (measured in photoelectrons (PEs)) and time. These pulses are deconvolved from the digitized waveforms using established single-photoelectron (`SPE`) pulse templates. The likelihood function compares the observed data to the expected data for a given hypothesis and adjusts the parameters to maximize this likelihood, details of which can be found in [175].

The expected number of photons detected at DOM j follows a Poisson distribution characterized by a mean $\lambda_j = \Lambda_j E$, where Λ_j represents the expected photon yield from a 1 GeV cascade at DOM j, and E signifies the cascade's energy, stored in tabulated form as photo splines [188], which were originally developed and used in an analysis similar to one presented in this thesis [164] and now have been updated with newer icemodel[5] [197] *. The likelihood of detecting k_j photons at DOM j for a cascade with energy E is given by:

$$L_j = \frac{(E\Lambda_j)^{k_j} e^{-E\Lambda_j}}{k_j!} \tag{5.4}$$

By taking the logarithm and summing over all DOMs, including noise hits ρ_j, along with an expansion to include multiple light sources i and timing information, the log-likelihood can be expressed as:

* These updated tables are used in the analysis presented in this thesis

$$\ln L = \sum_{i,j,t} \left(k_{jt} \ln\left(E_i \Lambda_{ijt} + \rho_{jt}\right) - \left(E_i \Lambda_{ijt} + \rho_{jt}\right) - \ln\left(k_{jt}!\right) \right) \tag{5.5}$$

The hypothesis to be compared encompasses the event parameters $(x_s, y_s, z_s, t_s, \theta_s, \phi_s, E_s)$, which define the source's location, time, direction, and energy respectively.

`millipede` offers a comprehensive set of configurations that allow users to define how photons are organized in terms of time bins, the magnitude of changes in various parameters, and the exclusion of specific modules from the likelihood calculation. One crucial aspect of these settings is the selection of an ice model for data reconstruction. This model plays a vital role in predicting the expected number of photons that will reach a DOM based on variables such as distance and direction from the source. Additionally, the ice model can influence the timing information of these photons [160], which is critical for accurate event reconstruction. [6]. As for exclusions of certain modules, **bright DOMs** and **Saturated DOMs** are excluded from the likelihood fit because they may introduce bias by contributing excessively to Equation 5.5. These particular DOMs generally account for a significant portion of the total observed charge. Hence, bright and saturated DOMs alongwith other DOMs that may have failed during the Run are generally labelled as *Bad DOMs* and are collectively excluded from the reconstruction . `millipede` framework helps reconstruct single and double cascades, along with track source hypotheses. Although they all use the same likelihood from Equation 5.5, they each have different ways to define sources. The hypothesis that fits the observed data best is found by comparing maximum likelihood values, which gives an idea of the interaction type in the detector.

`monopod`: `monopod` does a simple one-particle cascade energy fit, in other words it assumes a single light source. It minimizes parameters such as the cascade's deposited energy, neutrino direction (azimuth and zenith), cascade vertex position (x, y, z), and vertex time, represented as, $\vec{h} = (x, y, z, t, \theta, \phi, E)$ [181]. The reconstructed vertex here refers to the shower maximum, which is the peak of the longitudinal energy loss profile and is typically displaced from the interaction vertex by several meters in the considered energy range.

`taupede`: The double cascade fitting algorithm, `taupede`, maximizes the likelihood of two energy depositions with energy E_1 and E_2 respectively, separated by distance L_{dc}. The second cascade's direction matches the first, and its vertex is determined by the first cascade's vertex, direction, and double cascade length L_{dc}. The parameters for the double cascade hypothesis are $\vec{h} = (x_1, y_1, z_1, t_1, \theta, \phi, E_1, L_{\text{dc}}, E_2)$, with the tau traveling in the same direction as the incoming neutrino due to Lorentz boosting. The light yield and timing at each Digital Optical Module (DOM) are compared with expected values from the two energy depositions. For the second cascade's timing, the conditions are $|\vec{x}_2 - \vec{x}_1| = L_{dc}, \quad t_2 - t_1 = cL_{dc}$[7].

`mumillipede`: Track-like events are parameterized as multiple cascades along its path. The total deposited energy is given by $E_{\text{dep}} = \sum_k E_k$. Although the deposited energy is not a reliable indicator of the primary neutrino energy, the parameters related to direction and time are vital for neutrino point-source searches.

Bright DOM

A Bright DOM generally refers to a situation where a high energy event occurs close to a string, and in first pulse itself, a large amount of charge is observed. Emperically, this *large amount of charge* is assumed to be 10 times the average observed charge of the event.

Saturated DOM

A DOM is considered saturated if its PMT reaches saturation. This can happen if an event occurs close to a string or a very high energy interaction occurs, producing many photons that gets collected by the PMT. These DOMs generally don't have a *complete* digitized waveforms, making them unsuitable to be used in likelihood based reconstruction.

[160]: Abbasi et al. (2024), *In situ estimation of ice crystal properties at the South Pole using LED calibration data from the IceCube Neutrino Observatory*

6: Different approaches to model the ice at the South Pole can significantly affect the reconstructed properties of an event, in particular the double cascade reconstruction using `taupede` (see Section 5.5 at the end of this chapter for such detailed checks)

DeepCore DOM exclusion

DeepCore DOMs have traditionally been excluded from high-energy reconstruction methods like `millipede` because it uses spline tables that assume a uniform single photoelectron (SPE) template for all DOMs. However, the higher quantum efficiency of DeepCore DOMs results in significantly different charge collection, meaning their SPE templates differ from those of other DOMs. Recent efforts have updated simulations to address this issue (as will be discussed in Section **??**).

[181]: Santen (2014), *Neutrino Interactions in IceCube above 1 TeV: Constraints on Atmospheric Charmed-Meson Production and Investigation of the Astrophysical Neutrino Flux with 2 Years of IceCube Data taken 2010–2012*

7: assuming tau travels through the ice at the speed of light c.

The algorithm outlined above relies on the quality of the seed, which serves as the initial hypothesis $\vec{h}_0$. This seed is adjusted until a satisfactory match is achieved between the expected and actual light yield. This process has proven challenging, especially in the case of `taupede`, where the seed combines aspects of both a cascade and a track. Locating an appropriate seed is difficult, and the reconstruction process is influenced by the choice of seed. To reduce this influence, one can either modify the seed or increase the number of iterations[8]; however, both approaches result in greater computational expenses. To tackle the challenges associated with reconstructing double cascade events, an improved method for implementing the `taupede` fit was developed [164]. This method effectively converts the fitting process into a *brute-force* approach, where multiple hypotheses are explored and evaluated.

8: All algorithms are run multiple times, starting with a provided `seed`, where each subsequent iteration uses the output from the previous one, as explained in Section 5.4.

[164]: Usner (2018), *Search for Astrophysical Tau-Neutrinos in Six Years of High-Energy Starting Events in the IceCube Detector*

Simple reconstruction methods like **`LineFit`** and **`SPEFit`** provide fast initial estimates for event properties. These methods use limited event information, such as the first photon arrival time or total photoelectrons, without relying on detailed ice properties. The results are then used as seeds for more refined algorithms like `millipede`. For cascade-like events, simpler MLE methods are used to find a charge-weighted mean position of the source, providing an efficient first estimate.

5.4 Particle Identification of High Energy Neutrinos

Event reconstruction is performed using the aforementioned `millipede` framework, which enables the identification of different interaction types by assigning **a particle identifier (PID)** to each reconstructed event. The PID provides the probability that an event corresponds to a particular type of interaction. **A ternary topology identifier** has been developed (initially developed in [164] and later used to find first two tau candidates in IceCube [142]) based on the three event topologies—single cascade, double cascade, and track. By using these IDs, Monte Carlo templates are constructed to extract the contribution fractions from each neutrino flavor (see Chapter 6).

[142]: Abbasi et al. (2022), *Detection of astrophysical tau neutrino candidates in IceCube*

The analysis presented in this thesis has two main goals: to identify double cascades produced by tau neutrinos and to determine the flavor composition of astrophysical neutrinos. Given the complexity of detecting double cascades and the susceptibility of the reconstruction algorithm to failures and dependence on the initial seed hypothesis, the classification process uses a combination of algorithms offered by the `millipede` framework, which run in parallel on each of the HESE events that provides likelihood for the three event morphologies.

As mentioned before, these methods are `seed` dependent, hence to start with, all selected HESE events are reconstructed using first-guess algorithms to determine their vertex and direction. Result of these quick methods provides an initial fit for the event's position and trajectory, serving as a seed for `monopod`, which performs a fit with four iterations.

Generating a reliable seed for `taupede` is more complex. Multiple seeds are constructed using the monopod fit and generated with varying

lengths (10, 25, 50, and 100 meters), each shifted forward, backward, or centered along the direction of the seed in bruce-force way [164]. An amplitude-only `taupede` fit is performed for each of the 12 seeds [9], and the three best-performing seeds are selected for a full fit, performing 4 iterations of fits again, which incorporates photon arrival times at the Digital Optical Modules (DOMs). This method accounts for the diverse photon arrival patterns produced by scattered photons in single energy depositions [198]. The tracks are reconstructed using the `SPEFit` algorithm, which iteratively (16 times) fits a track based on the first photoelectron detected at each DOM. Although the `mumillipede` algorithm could also reconstruct tracks, it is computationally intensive, so `SPEFit` is preferred. Finally, `mumillipede` unfolding is performed along the directions determined by each topology fit (`monopod`, `taupede`, and `SPEFit16`), allowing for a comparison of likelihood values for each hypothesis. The best fit is selected for final classification based on the highest likelihood value.

Since identifying tau-induced double cascades is main goal of this process, the comparisons of the three likeelihoods is not the only proxy by which the classifier selects a double cascade event. First, the `taupede` fit is vetted through **Quality Criteria**, on the basis of containment, and reconstructed properties. If these criteria are satisfied[10], further classification is performed using additional selection criteria based on observables derived from reconstructed quantities, described below:

The reconstructed direction of a particle is indicated by its zenith and azimuth angles. The azimuthal angle is not useful for distinguishing between atmospheric and diffuse astrophysical neutrino fluxes since both are isotropically distributed. However, it is important for addressing systematic uncertainties in reconstructed track length due to anisotropic light scattering in the ice. However, zenith angle provides a reliable estimate of the neutrino's initial trajectory, espfecially for tracks, which can be reconstructed more accurately than cascades.

The total deposited energy (E_{tot}) refers to the visible energy in the detector, calculated as the sum of all contained energy losses along the best-fit hypothesis. The total deposited energy serves as a lower limit for neutrino energy and is used as a direct observable in the likelihood fit (see Section 6.2.2). Not all energy is deposited in the detector; some may be carried away by secondary neutrinos from tau decays or by muons that leave the detector, while some energy may remain invisible during hadronic showers. Therefore, the sensitivity of total deposited energy to primary neutrino energy varies by event morphology. In single and double cascade topologies, the initial energies of electron and tau neutrinos can be constrained more accurately than those of muon neutrinos, as muon usually leaves the detector and also the energy losses are stochastic, making the proxy weaker.

The Reconstructed length (L_{reco}), represents the distance between two cascades in double cascade events, is a critical observable for tau-neutrino interactions.

The energy asymmetry (E_{A}) measures the distribution of deposited energy between the two cascades in a double cascade event. It is defined as,

$$E_{\text{A}} = \frac{E_1 - E_2}{E_1 + E_2} \tag{5.6}$$

[164]: Usner (2018), *Search for Astrophysical Tau-Neutrinos in Six Years of High-Energy Starting Events in the IceCube Detector*

9: 4 length seeds shifted 3 times, giving total of 12 seeds

[198]: Stachurska (2020), *Astrophysical Tau Neutrinos in IceCube*

Quality Criteria for `taupede` fit

The final-best fit of `taupede` is accepted only if all the following criteria are satisfied:

`taupede` Fit is converged
Energies of both of the fitted cascades $E_1, E_2 \geq 1$ TeV
Both cascades are *softly* contained (vertex ≤ 50 m outside detector)
Opening angle between `taupede` and `mumillipede` fit $\leq 30°$

10: If any of the quality checks are failed, the event is assigned track or cascade morphology depending on which of the fit's likelihood is higher.

Direction definitions in IceCube

The zenith angle (θ) gives the direction of particle origin with respect to the vertical axis that points towards the surface of the ice and upward from the South Pole.
A zenith angle of 0° indicates a particle moving directly downward in the detector, 90° corresponds to horizontal propagation, and 180° signifies a particle moving directly upward.

The azimuth angle (ϕ) gives the direction of particle origin with respect to the horizontal x-axis of the IceCube coordinate system (see Section 4.1.1)

Figure 5.7: A sketch of energy asymmetry, it is a measure of the relative distribution of total deposited energy between the two cascades, as defined in 5.6. Sketch is adapted from [164].

where E_1 and E_2 are reconstructed energies of the first and the second cascades. A *true*[†] single cascade has an energy asymmetry of 1[11], while a double cascade can have any value between -1 and 1, depending on the kinematics of the neutrino interaction. This variable hence, is an excellent estimator to distinguish between a single and a double cascade.

11: since there is no second energy deposition technically, $E_2 = 0$ for a true single cascade

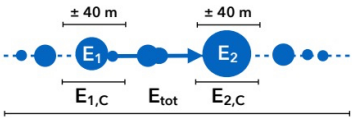

Figure 5.8: A sketch of Energy Confinement, it is a measure of how confined are reconstructed energy depositions E_1 and E_2 are within their reconstructed vertices. The confinement, as shown in the sketch is checked within 40 m of the vertices. Sketch is adapted from [164].

The energy confinement (E_C) measures how much of the total energy is localized near the cascade vertices. It uses the two cascade vertices fitted by `taupede` and deconvolves the energy depositions within 40 m of each of them. It is defined as,

$$E_C = \frac{E_{1,c} + E_{2,c}}{E_{tot}} \tag{5.7}$$

where, $E_{1,c}$ and $E_{2,c}$ are the deconvolved energy depositions within 40 m distance of first and second cascades respectively and E_{tot} is the total deposited energy as defined above. Note that from Equation 5.7, $E_C = 1$ (with $E_{1,c} + E_{2,c} = E_1 + E_2 = E_{tot}$) for a nu_τ induced double cascade, as opposed to tracks which have energy depositions outside the region around the double cascade vertices. It is therefore a suitable estimator to separate single cascades and double cascades from tracks,

classification Criteria Based on Reconstructed Quantities

After meeting Quality requirements, an event is classified as,
a track if $E_C < 0.99$
a single cascade if $E_C \geq 0.99$ **and** ($E_A < -0.98$ **or** $E_A > 0.3$ **or** $L_{reco} < 10$)
a double cascade if $E_C \geq 0.99$ **and** $-0.98 \leq E_A \leq 0.3$ **and** $L_{reco} \geq 10$

The classification chain uses several variables to categorize events into three morphologies. If the `taupede` fit meets all the quality criteria, a series of selection cuts is applied. If the event passes all these cuts, it is classified as a double cascade, as illustrated in Figure 5.9. Initially, only high-energy starting events (HESE) with a total energy $E_{tot} \geq 60$ TeV are selected to almost entirely eliminate atmospheric muons. If the quality criteria fail based on the likelihood value, the event is assigned either a single cascade or track morphology. The next step ensures that the reconstructed length $L_{reco} \geq 10$ m. This condition is necessary because while a double cascade with a length below this threshold could be genuine, the resolution of the reconstruction algorithm does not allow for a definitive classification. Therefore, if the length is below 10 meters, the event is classified as a single cascade. As stated before, cuts on E_A and E_C are applied afterward to further filter out single cascades and tracks from the double cascade samples, respectively. Notably, after the quality cut, it is assumed that the event is a double cascade until any of the selection criteria based on reconstructed properties fail.

A noteworthy point is that none of the events in the HESE sample, with $E_{tot} \geq 60$ TeV, are discarded. They are only separated into three sub-samples based on their tagged morphology. All the cuts and selection criteria introduced so far were determined by evaluating the signal-to-background ratio in the distributions of these variables [164]. The cut values were not strictly enforced to allow for some background contribution in the final sample. The rationale behind this selection is that the analysis performed using these three sub-samples is a forward-folding fit (see Section 6.1). This analysis employs Monte Carlo PDFs that utilize the shapes of signal and background distributions to compare them with data events. Therefore, it is essential to have a sufficient amount of background simulation present in the sample.

[164]: Usner (2018), *Search for Astrophysical Tau-Neutrinos in Six Years of High-Energy Starting Events in the IceCube Detector*

[†] *true* event morphologies are assigned by going through produced charged particles at Secondary Charged Particle Propgation stage of the simulation chain (see Section 5.1.1). Looking at the type of particles, their energy depositions and positions within the detcetor volume, a morphology is assigned to the event.

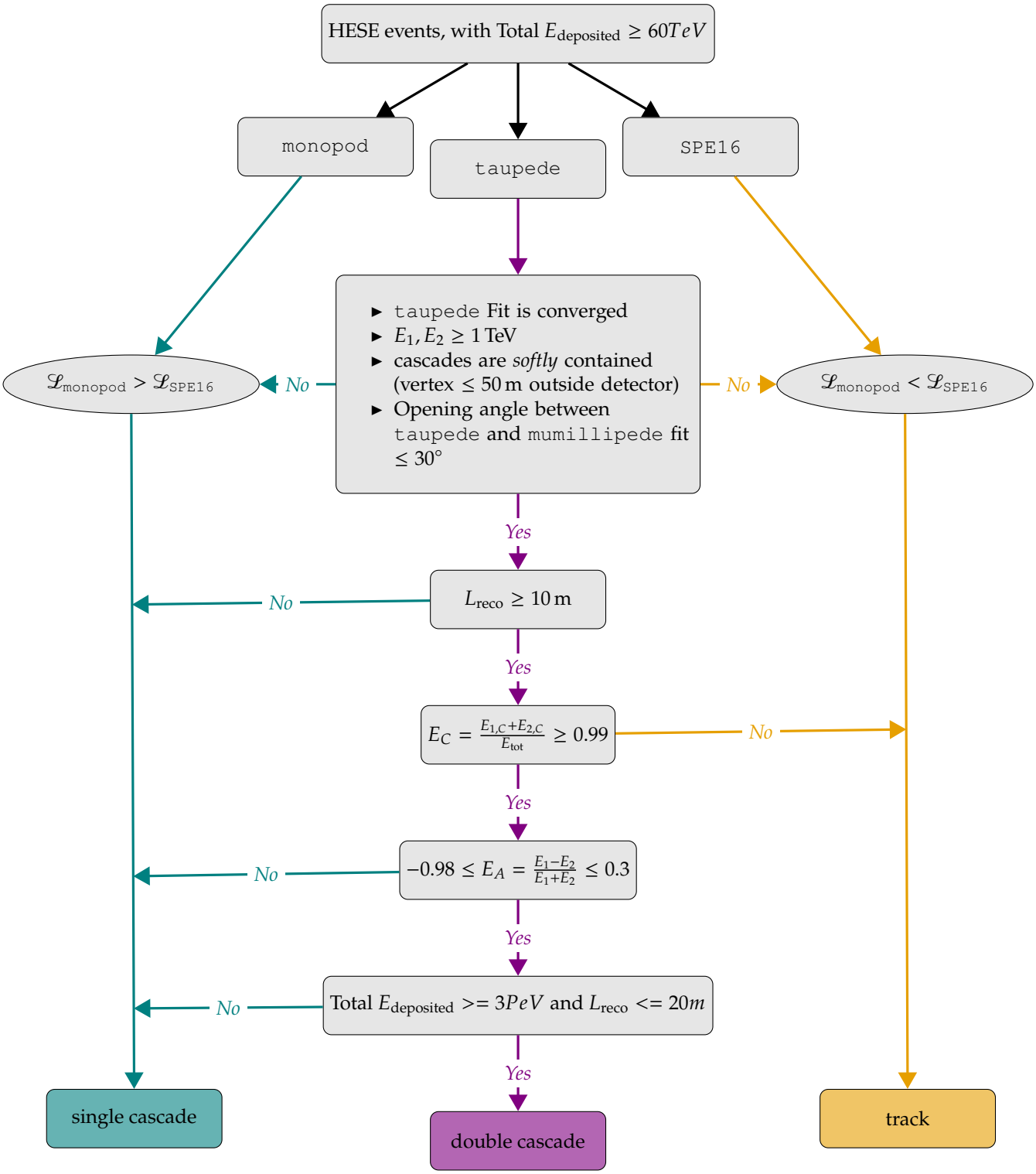

Figure 5.9: The event classification scheme for the Ternary PID. The first level evaluates reconstruction quality; if the criteria are not met, events are classified as single cascades or tracks based on the likelihood values L_{monopod} and L_{SPE16}. The second level considers the reconstructed length, using a threshold below which distinct vertices of double cascades appear as a single cascade. The third and fourth levels focus on energy confinement and energy asymmetry, respectively. The last level is added to improve purity of the double cascade sample at high energies where misclassification is prominent due to glashow events.

So far, all the explained sample selection and Ternary classification has been taken (with updates in simulations and reocnstruction tables) as it was done and used in previous iterations of HESE flavour measurements

[164]: Usner (2018), *Search for Astrophysical Tau-Neutrinos in Six Years of High-Energy Starting Events in the IceCube Detector*
[198]: Stachurska (2020), *Astrophysical Tau Neutrinos in IceCube*

The Sampling correction here refers to changing the weight of the simulated neutrino, and not changing the HESE sample itself. *The weight* of a simulated neutrino, as discussed in Section 5.1 takes into account various probabilities, such as interaction type, propgation through earth etc. Most of these probabilities are derived from underlying theoretical models of particle interactions [28]. The correction applied here refers to updates in calculations of these models that affects shape of the underlying cross-section and kinematics of the inetarctions, that may result in difference in reconstructed variable distributions.

[33]: Glashow (1960), *Resonant Scattering of Antineutrinos*

[164, 198]. For the analysis presneted in this thesis, some changes were made both in **sampling** and classification schemes that are discussed in the following subsections.

5.4.1 Reclassification of PeV Double Cascades

The Double Cascade sample is crucial for flavor measurement, necessitating a more comprehensive assessment. Using the ternary classification described, the **Flavour Purity** of this sample can be determined. Flavour purity is defined as the fraction of a *desired* neutrino flavor within a given morphology sample. This concept is illustrated in Figure Figure 5.10, which displays the reconstructed energy distribution of the Double Cascade sample for each neutrino flavor. Ideally, one would want that each bin in this plot reflects a 100% contribution from the ν_τ flavor. While it does not achieve 100%, it is evident that the Double Cascade sample is predominantly made up of ν_τ events across the energy range. However, a rapid decrease in purity is observed at high energies (around 6 PeV), where the sample becomes dominated by ν_e events (see the left panel of Figure Figure 5.10). This shift is due to the Glashow resonance of $\bar{\nu_e}$, which significantly influences the cross-section of neutrino interactions at these energies [33]. These events are categorized as Double Cascades because of their high energy deposition over a short distance, but they are misclassified as single cascades.

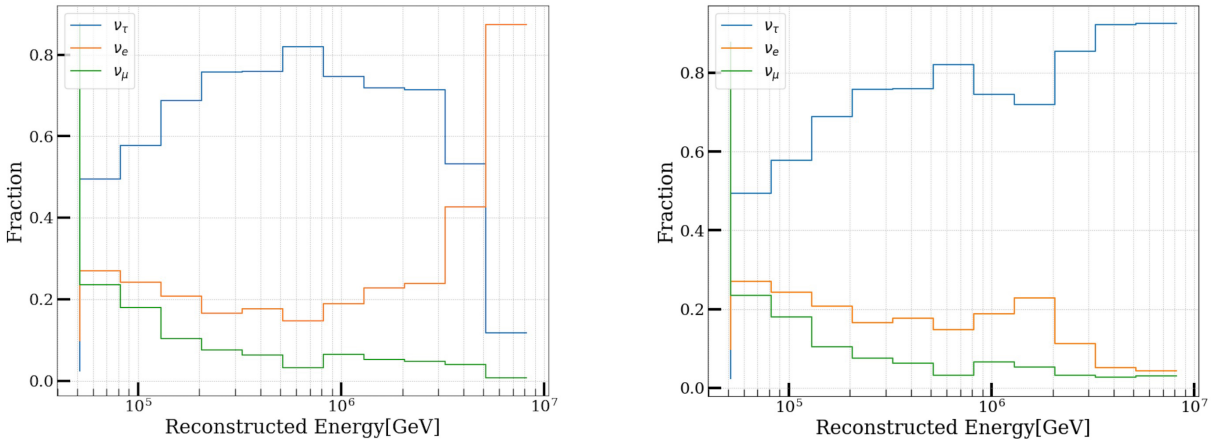

Figure 5.10: Fraction of flavor content per bin in double cascade events. The left panel shows the distribution without the criteria of Total $E_{\text{deposited}} \geq 3$ PeV and $L_{\text{reco}} \leq 20$ m, indicating *purity contamination* at high energies from $\bar{\nu}_e$ Glashow events. The right panel presents the distribution after reclassifying double cascades as single cascades under these conditions.

To address this, **a reclassification** mask was introduced at the end of the classification chain outlined in Figure Figure 5.9. If an event is classified as a Double Cascade with a reconstructed energy of $E_{\text{tot}} \geq 3$ PeV and a reconstructed length $L_{\text{reco}} \leq 20$ m, it is reclassified as a single cascade. These thresholds were chosen based on the purity distribution to maximize the signal-to-background ratio, even at these energies.The distribution before and after applying this mask is shown in the right panel of Figure Figure 5.10. As anticipated, the lower energy distributions remain nearly identical, while purity is restored at higher energies. It is important to note that the fraction of ν_μ remains unchanged in both figures, due to the involvement of only electron neutrinos—technically electron anti-neutrinos—in Glashow interactions, which contribute to

the purity contamination. Since this is merely a reclassification, the total High-Energy Starting Event (HESE) sample remains unchanged.

5.4.2 Tau Polarisation

As discussed in 4.3.3, ν_τ-CC interaction always produces a tau lepton, which has various decay modes. The tau lepton produced in this interaction is polarised, which can siginificantly alter the kinematics of the tau decay [199, 200]. Whether the decay mode is leptonic or hadronic, the fraction of energy going to the decay products ($\frac{E_{hadrons/leptons}}{E_\tau}$), is affected if non-zero tau Polarisation is not taken into account. The `PROPOSAL` software used in simulation presneted in this thesis, to simulate secondary charge particle production, propagation and energy losses does not take into account this factor. That is, the Taus produced in a ν_τ−CC interation is assumed to be produced with no polarisation. Since, the signature which is used for identification of this analysis relies on both, the neutrino interaction cascade and tau decay cascade, not taking in account this correction can lead to an *incomplete* simulation of energy loss profiles. Mainly the energy reconstruction of the second decay cascade, may get affected, which can further alter the Energy asymmetry (E_A) of the event, which is used a s aselection variable in Ternary Classifier (see Figure 5.9).

[199]: Garg et al. (2023), *Neutrino propagation in the Earth and emerging charged leptons with nuPyProp*
[200]: Argüelles et al. (2022), *Tau depolarization at very high energies for neutrino telescopes*

The idea is to test the impact of tau polarisation on analysis variables by reweighting the monte carlo events. The calculations provided in [199], are used to get theoretical fractional energy loss of the electromagnetic equivalent visible energy losses, for both polarised and unpolarised states. The ratio of this is multiplied with the simulated fractional energy (which assumed unpolarised taus), to get a new reweighting factor. The change introduced minor difference in the overall observable distributions, hence this was left as a weight correction only and no further analytical checks were performed.

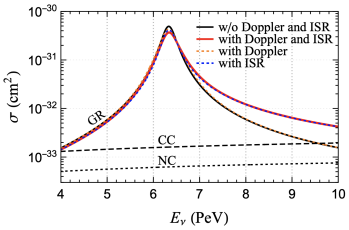

Figure 5.11: The cross section for the Glashow resonance process $\nu_e + e^- \rightarrow W^- \rightarrow X$ is shown with and without initial state radiation and Doppler broadening. The black curve represents the cross section without these effects, the blue dotted curve includes initial state radiation, the orange dotted curve shows Doppler broadening, and the red curve combines both effects. Figure taken from [201].

5.4.3 Glashow Cross-Section correction

The resonance enhancement of $\bar{\nu_e} e^-$ scattering at an energy of approximately 6.3 PeV, known as the *Glashow resonance*, was discussed in Section 3. The cross-section for this process at this energy is significantly larger—about two orders of magnitude greater—than that of Deep Inelastic Scattering (DIS). Since this energy range is relevant to the thesis presented in this work, it is crucial to consider second-order QCD corrections, which can significantly alter the Glashow cross-section [201].

[201]: Huang et al. (2023), *Inferring astrophysical neutrino sources from the Glashow resonance*

The corrections applied to the cross-section, as described in [201], include *Initial State Radiation (ISR)* [202, 203] and the *Doppler broadening effect* [204]. ISR becomes more prominent when the center of mass (COM) energy of the system is much higher than the mass of the initial lepton—since W^- is substantially more massive than e^-, this leads to an enhancement factor of approximately $\frac{M_W}{m_e} \sim 12$ in radiation, on top of contributions from the fine structure constant (α). This results in collinear photon emission. Doppler broadening occurs due to the motion of atomic electrons, where the typical velocity of the electron is assumed to be close to the speed

[202]: Garcia et al. (2020), *Complete predictions for high-energy neutrino propagation in matter*
[203]: Gauld (2019), *Precise predictions for multi-TeV and PeV energy neutrino scattering rates*
[204]: Loewy et al. (2014), *The Effect of Doppler Broadening on the 6.3 PeV W^- Resonance in $\bar{\nu}_e e^-$ Collisions*

of light. This motion causes the COM energy to shift by a factor of $(1 - \beta \cos\theta)$, where θ is the angle between the electron's velocity (β) and the incoming neutrino in the lab frame [204].

The combined results of these effects, based on calculations from [201], were used to adjust the *total weight* of neutrinos. As noted in [201], these effects are smoothed out by the energy resolution of IceCube [175], and the impact of this reweighting on energy distributions and sensitivity was negligible. Nevertheless, the reweighting was retained, similar to the correction for Tau polarization.

[175]: Aartsen et al. (2014), *Energy Reconstruction Methods in the IceCube Neutrino Telescope*

5.5 Influence of South Pole Ice properties on Double Cascades Reconstruction

The identification of ν_τ-induced double cascades in the IceCube detector faces significant systematic uncertainties due to the anisotropy of the ice. As discussed in Section 4.2, the Anisotropy at the south pole ice has been established since 2013 [163]. This phenomenon causes photons to have a directional dependence while scattering, with enhanced scattering occurring perpendicular to the ice flow axis[12] and reduced scattering along it.

[163]: Chirkin et al. (2013), *Evidence of optical anisotropy of the South Pole ice*

12: Technically it coincides within 1°of the ice flow axis, hence this axis was given a special name, *the anisotropy axis*. The axis along which scattering is reduced is called *the major anisotropy axis* and the one perpendicular to it where scattering is enhanced is known as *the minor anisotropy axis*.

Such a direction dependednt scattering pattern can cause a bias in reconstructing specifically a double cascade event using `taupede`, as this algorithm looks for energy depositions around vertices along a given seed direction (see Section 5.4), which can cause bias in length reconstruction. When a single cascade aligns with this major anisotropy axis, reduced scattering can elongate its apparent size, mimicking double cascade characteristics due to altered light timing at the DOMs. Conversely, if a true double cascade aligns with one of the minor anisotropy axes, it may be compressed, increasing the risk of misidentification as a single cascade. Without accounting for anisotropy, true single cascades could be misclassified as double cascades, while genuine double cascades along minor axes might be missed.

Reconstructing these events relies on photo-spline tables introduced in Section 5.3, which provide tabulated light yields for simulated 1 GeV cascades. These cascades are placed in the detector's center at intervals of $\Delta z = 20$ m, between depths of -600 to 600 m and zenith angles from 0° to 180°. The initial model primarily considers the ice layer's depth and zenith angle for light propagation, but an additional azimuthal dimension was necessary to account for anisotropy. A key advancement was the development of **the effective distance spline tables**, which adjusted for anisotropy by using an isotropic-ice-equivalent position instead of position of the DOMs to look-up for the light yield, which resulted in a significant enhancing of length reconstruction accuracy [164].

[164]: Usner (2018), *Search for Astrophysical Tau-Neutrinos in Six Years of High-Energy Starting Events in the IceCube Detector*

Recent developments in icemodel studies have revealed that the directional behavior of light in ice, is due to its molecular structure, a phenomenon known as *birefringence* as already introduced in Section 4.2. This is now incorporated into the new ice model, called as, **SpiceBfr**. However, during the development stage of the analysis presneted in this thesis, the only large-scale Monte Carlo simulations available was the one

While the SpiceBfr model agrees much better with the data, compared to Spice-3.2.1, it is important to note that on the analysis level, where one uses reconstruction algorithms based on all of the pulse information from the DOMs, the ever so significant effects on charge and time level may get smeared off from overall observable distributions. Going from Spice-mie to Spice-Lea was a breakthrough as the former did not consider this anisotropic behavior of photon propagation. But going from Spice-3.2.1 to Spice-Bfr was more in the direction of inherent modeling of the ice (crystal) property, to explain the anisotropy, while Spice-3.2.1 and Spice-Lea used an approximated solution in the form of effectively mimicking an anisotropic scattering of photons.

Table 5.1: The four comparison scenarios that were analyzed. The First icemodel in the name always refers to the one used in simulation (second column) and the second refers to the one used in reconstruction (reconstruction). Last column points to corresponding figures.

Name	Simulation Icemodel	Reconstruction Icemodel	
Spice-3.2.1-Spice-3.2.1	Spice-3.2.1	Spice-3.2.1	Figure 5.12a
Spice-3.2.1-SpiceBfr	Spice-3.2.1	SpiceBfr	Figure 5.12b
SpiceBfr-Spice-3.2.1	SpiceBfr	Spice-3.2.1	Figure 5.12c
SpiceBfr-SpiceBfr	SpiceBfr	SpiceBfr	Figure 5.12d

produced using an earlier icemodel, **Spice-3.2.1** [13]. Naturally, the question arises, if SpiceBfr can further improve reconstruction (or discover any previously unknown biases), hence a comparison was needed.

Such a check between Spice-3.2.1 and SpiceBfr was feasible since the spline tables for SpiceBfr were already available. To facilitate cross-comparison, a small statistics (one-third of the full available statistics) simulation set was produced using SpiceBfr. The succecfully identified true double cascades are considered, and median length bias ($L_{\text{Reco}} - L_{\text{true}}$) is calculated per azimuth bin (see Figure 5.12). An effective reconstruction algorithm should show no bias (i.e. the difference in length should be zero), unless unaccounted asymmetries exist.

13: This icemodel is almost identical to the one used in previous iteration of this analysis [198]

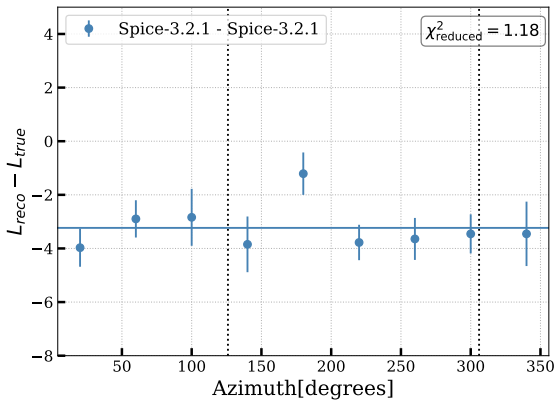

(a) Simulation using Spice-3.2.1 and reconstruction using Spice-3.2.1

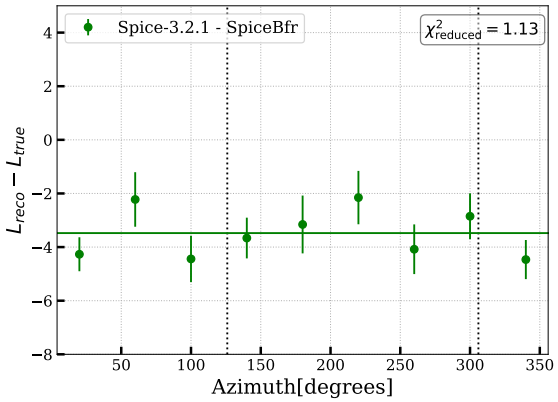

(b) Simulation using Spice-3.2.1 and reconstruction using SpiceBfr

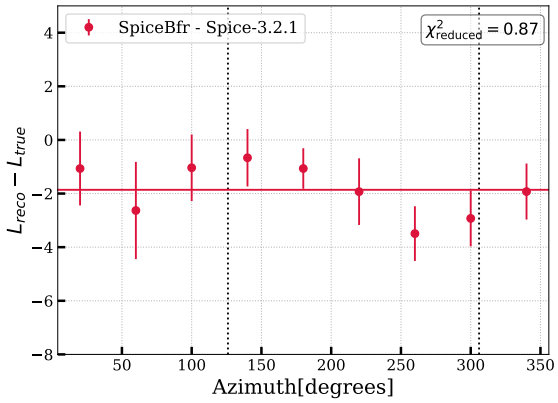

(c) Simulation using SpiceBfr and reconstruction using Spice-3.2.1

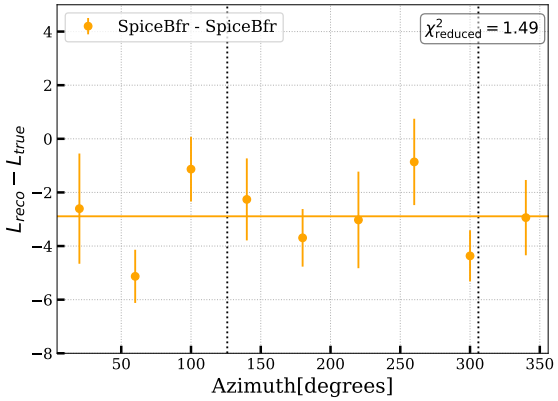

(d) Simulation using SpiceBfr and reconstruction using SpiceBfr

Figure 5.12: Length Bias of true double cascades, classified as double cascades, as function of Azimuth angle. Vertical lines shows the direction of the major anisotropy axis. Caption below each figures shows which combination of icemodel is used in simulation and reconstruction respectively. Each figure also shows reduced value of χ^2 calculated by fitting the showed horizontal line, see text for details.

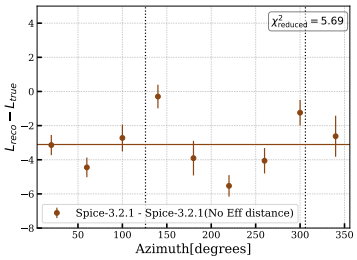

Figure 5.13: Simulation using Spice-3.2.1 and reconstruction using Spice-3.2.1 but no effective distance. See caption of Figure 5.12 for details.

Since all cases involve either the effective distance correction or an inherent anisotropy parametrization (via birefringence), minimal bias was expected along the major anisotropy axis. As shown in the results, only minor structures were observed, and none were deemed statistically significant, particularly along the anisotropy axis. To probe further, a χ^2 goodness-of-fit (gof) test was performed to fit a horizontal line, with the reduced χ^2 calculated for each of the four cases (values indicated on all figures). The results indicated that all four combinations fit well to a horizontal line, signifying no significant biases were present. However, the plots corresponding to the simulation produced using SpiceBfr (both reconstructed with SpiceBfr (Figure 5.12d) and Spice-3.2.1 Figure 5.12c) showed signs of over/underfitting, likely due to the low statistics of the generated SpiceBfr simulation set.

This observed lack of obias aligns with expectations, as Spice-3.2.1 effectively handles anisotropy through the effective distance parameterization. The final step thus, was to verifying if the lack of bias was truly due to the effective distance splines. In Figure 5.13, a distribution is shown where events are simulated using Spice-3.2.1 but reconstructed without the effective distance correction. The resulting reduced χ^2 of 5.69 indicates a poor fit, and a clear bias is visible along the anisotropy axis, as was observed in [164]. This conclusively demonstrates that both Spice-3.2.1 and SpiceBfr, both with appropriate effetive distance corrections are well-suited for analyzing ν_τ-induced double cascades in the presence of ice anisotropy.

Since the SpiceBfr model represents the best current understanding of South Pole ice, the decision was made to proceed with simulations using Spice-3.2.1, reconstructed with the SpiceBfr model. This choice is further supported by the reduced χ^2 values across the four cases, where the combination of Spice-3.2.1 simulation and SpiceBfr reconstruction produced the value closest to 1, indicating the most accurate fit. Consequently, the analysis continued with this combination, ensuring the best possible handling of ice anisotropy in the event reconstruction.

Given that the SpiceBfr model represents the best current understanding of the South Pole ice, the decision was made **to proceed with Spice-3.2.1 simulations reconstructed using the SpiceBfr model**. This approach is further supported by the reduced χ^2 values across the four cases, with the Spice-3.2.1 simulation and SpiceBfr reconstruction yielding the value closest to 1, indicating the most accurate fit. Hence, from here-on, it is to be

Flavour Composition Analysis 6

Using the on the event sample (HESE) introduced in the previous chapter, where each event is reconstructed into one of three distinct morphologies (Single Cascades, Tracks and Double Cascades), a flavour measurement of the high energy diffuse neutrino spectrum can be performed. This chapter focuses on the methods and various components of this flavour measurement.

The chapter begins by detailing these statistical techniques, with a focus on forward folding likelihood fits, which plays a crucial role in distinguishing signal from background and identifying flavour contributions. In addition, different components and parameters introduced (or modified) in this iteration of the analysis are explained subsequently. Following this, the software used to perform the fit is discussed in detail. Finally, the chapter evaluates the sensitivity of the analysis, providing estimates of detection limits and the potential to constrain key physical parameters within the context of neutrino flavour identification.

6.1 Analysis Method

This analysis utilizes a binned maximum likelihood estimation (MLE) approach to perform statistical inferences on observed data. Binning the data offers computational efficiency by reducing the dimensionality of the problem, allowing for quicker calculations of likelihoods over a range of model parameters. Each analysis bin contains data points that represent a specific range of measured quantities, such as energy or angular distributions.

To incorporate the complexities of detector response and model uncertainties, the concept of forward folding is employed. Forward folding integrates theoretical model predictions with the response of the detector, producing expected distributions that can be directly compared to the binned observed data. This method allows for the inclusion of different flux models, systematic uncertainties, and detector efficiencies, all folded into the predicted likelihood. As a result, this approach enables robust and precise inference of underlying physical parameters, particularly in the context of high-energy astrophysics, where signal and background differentiation is challenging.

6.1.1 Binned Maximum-likelihood Fits

When fitting a data sample with a large size (large N), it is common practice to bin the data in order to enhance the computational efficiency of the likelihood function calculation. This binning procedure groups the data into discrete intervals, or *bins*, based on one or more *observables*, such as energy or zenith. This simplification is not harmful as long as the variation of the probability density function (PDF), $f(x|\theta)$, within each bin is insignificant compared to its variation across all the bins. In

other words, the binning should not discard crucial information about the parameter vector θ that governs the underlying physical model. If binning is applied appropriately, the process retains the ability to accurately infer the parameters of interest while significantly speeding up the computational process, particularly in high-dimensional analyses where unbinned likelihood fits may be computationally prohibitive.

The binned likelihood method works by comparing the number of observed events in each bin to the expected number of events, which are typically predicted through Monte Carlo simulations. In the analysis, these Monte Carlo templates are created for various theoretical flux components, such as astrophysical, atmospheric etc. for both signals or background. Each template provides a predicted event distribution based on specific values of the *signal* parameters θ along with *nuisance* parameters, ξ, which describe the physical processes being studied. These templates are then forward folded, meaning they incorporate the effects of the detector response, before being compared to the observed data. By adjusting the model parameters, the predicted event counts in each bin can be varied to find the *best fit* to the data. The number of observed events n, in each bin i (n_i), is assumed to follow a Poisson distribution [205]. The expected number of events in bin i, $\mu_i(\theta, \xi)$, represents the sum of contributions from all signal and background components. The Poisson likelihood for a given bin is defined as:

[205]: Behnke et al. (2013), *Parameter Estimation*

$$P(n_i|\mu_i(\theta,\xi)) = \frac{\mu_i(\theta,\xi)^{n_i} e^{-\mu_i(\theta,\xi)}}{n_i!} \tag{6.1}$$

where $\mu_i(\theta, \xi)$ is the expected number of events in bin i and n_i is the observed number. The total likelihood for the entire dataset is then the product of the likelihoods for all bins:

$$\mathcal{L}(n|\mu_i(\theta,\xi)) = \prod_{i=1}^{N} P(n_i|\mu_i(\theta,\xi)) \tag{6.2}$$

Incorporating systematic uncertainties into the likelihood function is crucial for obtaining realistic results, as these uncertainties often arise from imperfect detector calibration or background estimations. Such systematic uncertainties are modeled as nuisance parameters in the likelihood fit. These parameters are typically constrained by prior knowledge and treated as additional variables in the fitting process. For each of the k nuisance parameters, ξ_j, a Gaussian prior is introduced, penalizing deviations from the central value $\bar{\xi}_j$ by an amount proportional to the known uncertainty σ_{ξ_j}, changing the likeli:

$$\mathcal{L}(n|\mu_i(\theta,\xi)) = \prod_{i=1}^{N} P(n_i|\mu_i(\theta,\xi)) \prod_{j=1}^{k} \exp\left(-\frac{1}{2}\left(\frac{\xi_j - \bar{\xi}_j}{\sigma_{\xi_j}}\right)^2\right) \tag{6.3}$$

By maximizing this likelihood, the best-fit parameters θ can be found. In practice, the fit is performed by minimizing $-\ln\mathcal{L}$, as it simplifies the computation (see 6.4).

$$\ln(\mathscr{L}(n|\mu_i(\theta,\xi))) = \sum_{i=1}^{N}[n_i\ln(\mu_i) - \ln(n_i!) - \mu_i] - \sum_{j=1}^{k}\frac{1}{2}\left(\frac{\xi_j - \bar{\xi}_j}{\sigma_{\xi_j}}\right)^2 \tag{6.4}$$

This modified likelihood is often referred to as the **profile likelihood**, as it profiles over the nuisance parameters by marginalizing or constraining them using prior information.

Once the likelihood function is constructed, the next step is hypothesis testing. A specific model hypothesis can be tested by using a likelihood ratio test. The likelihood ratio compares two hypotheses: the test model (with parameters θ_t) and the best-fit model (with parameters $\hat{\theta}$):

$$-2\Delta\ln\mathscr{L} = -2\ln\left(\frac{\mathscr{L}(n|\mu(\theta_t,\xi_t))}{\mathscr{L}(n|\mu(\hat{\theta},\hat{\xi}))}\right) \tag{6.5}$$

The factor -2 is included for convenience, as it allows the test statistic to follow a χ^2-distribution, according to Wilks' theorem [206]. This enables the calculation of confidence levels (CL) of the parameter of interest without the need for computationally expensive Monte Carlo simulations. However, Wilks' theorem is only valid when the dataset is large and the model parameters are unbounded. If either condition is not met, the test statistic may deviate from a χ^2-distribution, necessitating the use of Monte Carlo pseudo-experiments to determine the confidence intervals via the so-called *Feldman Cousins* method [207], with an extension to incorporate nuisance parameters [208, 209].

[206]: Wilks (1938), *The Large-Sample Distribution of the Likelihood Ratio for Testing Composite Hypotheses*

[207]: Feldman et al. (1998), *Unified approach to the classical statistical analysis of small signals*

[208]: Sen et al. (2009), *On the unified method with nuisance parameters*

[209]: Cowan et al. (2011), *Asymptotic formulae for likelihood-based tests of new physics*

The test statistic derived from the likelihood ratio can be used to construct confidence regions for the parameters of interest. For instance, in one-dimensional parameter scans, the confidence interval is obtained by comparing the test statistic to the cumulative distribution of a χ^2-distribution with one degree of freedom. When scanning over two or more parameters, a multi-dimensional profile likelihood scan is required, which significantly increases the computational complexity. In some cases, the Asimov dataset [209]—a single dataset representing the median outcome of many pseudo experiments—can be used to estimate the median sensitivity of the analysis. This method provides an efficient way to estimate confidence intervals and test the sensitivity of the analysis without the need for exhaustive Monte Carlo trials. Asimov dataset and Wilks' theorem are both used to derive sensitivity presented in 6.3. It is important to point out that the primary parameter of interest in this analysis is the astrophysical neutrino flavour fractions, which are constrained to be non-negative ($\phi_{\nu_\tau} \geq 0$) and limited by the small number of observed double cascade events. As a result, the applicability of Wilks' theorem is evaluated as needed.

6.1.2 SAY Likelihood

The likelihood construction described in section 6.1.1 relies on the Poisson likelihood, which assumes that the expectations for each bin, μ_i, are

known exactly. This assumption holds when the Monte Carlo simulations used in generating the expected distributions have large statistics. However, MC simulations inherently come with their own uncertainties due to finite statistics, particularly in bins with lower event counts.

In binned forward-folding fits, statistical inferences are made by comparing observed data counts in each bin to the expected counts derived from the simulations. As outlined in Equation 6.1, the Poisson likelihood assumes that μ_i, the expected value per bin, is well-determined. However, this is often not the case in analyses like ours, where overall event rates are low, and individual bin expectations may fluctuate significantly due to limited MC statistics. This mismatch can lead to deviations between the observed data and MC predictions if these fluctuations in μ_i are not correctly accounted for.

To address this issue, an extended form of the Poisson likelihood ($\mathcal{L}_{\text{eff}}$), or the so-called **SAY likelihood**, is used in this analysis [210]. This likelihood incorporates the uncertainty from the limited MC statistics and provides more appropriate coverage of the expected μ_i values. Specifically, the distribution of MC event weights in each bin is corrected using a scaled Poisson distribution, which introduces an additional uncertainty term, σ_j^2, for each bin. This term depends on the weights w_i^j of the MC events in the j-th bin and is defined as:

[210]: Argüelles et al. (2019), *A binned likelihood for stochastic models*

$$\sigma_j^2 = \sum_i (w_i^j)^2 \tag{6.6}$$

This uncertainty term, σ_j^2, is larger in bins with low statistics, and smaller in bins with higher statistics, ensuring that fluctuations in low-stat bins are adequately covered. This formalism results in more conservative limits, with generally wider contours for the final result, as the additional statistical uncertainty is incorporated into the fit. One limitation of this approach is that the Asimov dataset [209], described in the previous section, is not applicable with the SAY likelihood. This is because the σ_j term can significantly alter μ_i in each bin, making it impossible to recover the injected model parameters. As a result, deviations from injected values may appear, especially in cases like the `MuonGun`, discussed in the next section. Alternatively, the standard Poisson likelihood can be used, though the resulting limits may be less conservative than the reality accounted for by the SAY likelihood.

[209]: Cowan et al. (2011), *Asymptotic formulae for likelihood-based tests of new physics*

6.2 Components of the fit

The choice of the likelihood function and its subsequent requirement was outlined in the previous section. In this section, the focus shall be on the actual construction of the likelihood and the essential components involved. The construction proceeds as follows:

1. The parameters to be measured, known as *signal parameters* (denoted by θ), along with all *nuisance parameters* (ξ), which may originate from detector systematics or background modeling (such as atmospheric spectra), are identified and bounded where necessary.

2. These parameters are applied in the form of the neutrino *flux*, assigning each Monte Carlo event a specific *weight* based on the individual fluxes.
3. A set of observables that are most sensitive to the signal parameters, such as astrophysical neutrino fluxes, is selected and appropriately binned for analysis.
4. The experiment is performed, and the observed data events n are sorted into the predefined bins of the analysis histograms. A fit is conducted by varying each of the parameters (and, consequently, the fluxes) until the observed data events are optimally described.

This is why a penalty term is introduced in the likelihood. A Gaussian prior ensures that the parameters remain within the 1σ prior region, penalizing the likelihood if the fit favors values outside this range.

6.2.1 Model parameters

All the model parameters used in the fit, along with which fluxes they affect, are listed in Table 6.2. The model parameters consist of either flux components (astrophysical or atmospheric) or detector systematics. Baseline models and their corresponding values, wherever applicable, are specified for each parameter, along with the choice of priors. The astrophysical flux parameters represent the high-energy neutrino contributions from distant sources, while atmospheric flux models account for neutrinos originating from cosmic ray interactions within in atmosphere of Earth. Detector systematics reflect uncertainties in detector performance.

Table 6.1: Parameters used in the likelihood desribed in Equation 6.3. The gaussian priors on the parameters (if applicable) in terms of the mean (μ) and width (σ) are stated on the alongside.

Parameter	Prior (μ, σ)
Astrophysical Flux (Signal) Parameters	
astro. ν_μ normalisation [10^{-18}GeV^{-1}cm^{-2}sr^{-1}s^{-1}](ϕ_{ν_μ})	-
astro. spectral index (γ_{astro})	-
scaling factor to modify total flux norm ($\Phi^{\text{astro}}_{\nu+\bar{\nu}}$) relative to ϕ_{ν_μ} (s_{ν_e} astro. ν_e)	-
astro. ν_τ scaling factor to modify total flux norm ($\Phi^{\text{astro}}_{\nu+\bar{\nu}}$) relative to ϕ_{ν_μ} (s_{ν_τ})	-
Atmospheric Flux Systematics	
Conventional Flux normalisation (Φ_{conv})	(1.0,0.2)
Prompt Flux Normalisation (Φ_{prompt})	-
Interpolation between Cosmic Ray Models (ξ_{CR})	(0,1)
Cosmic Ray Spectral Index Shift ($\Delta\gamma_{\text{CR}}$)	(0,0.05)
Barr-parameter modifying the pion-contribution (H_{Barr})	(0,0.15)
Barr-parameter modifying the kaon-contribution (W_{Barr})	(0,0.40)
Barr-parameter modifying the pion-contribution (Y_{Barr})	(0,0.30)
Barr-parameter modifying the pion-contribution (Z_{Barr})	(0,0.12)
Muon Flux Normalisation (Φ_{muongun})	(1,0.5)
Scale factor for Neutrino Nucleon Inelasticity weight (I_{scale})	(1,0.1)
Detector Systematics	
Optical Efficiency of DOMs (η_{domeff})	(1.0,0.1)
Ice Absorption Scaling (η_{abs})	(1.0,0.05)
Ice Scattering Scaling (η_{scat})	(1.0,0.05)
Parametrization for refrozen icecolumn ($\eta_{\text{h.ice}-\text{p0}}$)	(-0.27,0.5)
Parametrization for refrozen icecolumn ($\eta_{\text{h.ice}-\text{p1}}$)	(-0.042,0.05)
Ice Anisotropy Scaling (η_{aniso})	-

The flux of astrophysical neutrinos is modeled as a single power law of the form

$$\Phi^{\text{astro}}_{\nu+\bar{\nu}} = \Phi^{\text{astro}}_{0} \times (1 + s_{\nu_e} + s_{\nu_\tau}) \times \left(\frac{E_\nu}{100\,\text{TeV}}\right)^{-\gamma_{\text{astro}}} \tag{6.7}$$

where γ_{astro} is the spectral index, E_ν is the neutrino energy, and $\Phi^{\text{astro}}_{\nu+\bar{\nu}}$ is the all-flavor (including particle and anti-particle) normalization. Two scaling factors, s_{ν_e} and s_{ν_τ}, modify the flux of electron and tau neutrinos relative to the muon neutrino flux Φ_0. These scaling factors help determine the flavour ratio $\nu_e : \nu_\mu : \nu_\tau$ as:

$$f_e = \frac{s_{\nu_e}}{(1+s_{\nu_e}+s_{\nu_\tau})}, \quad f_\mu = \frac{1}{(1+s_{\nu_e}+s_{\nu_\tau})}, \quad f_\tau = \frac{s_{\nu_\tau}}{(1+s_{\nu_e}+s_{\nu_\tau})} \tag{6.8}$$

The signal parameters for the flavor analysis are these two scaling factors, Φ_0, and γ_{astro}. All other subsequent parameters explained are the nuisance parameters. In Eq. 6.13, it is assumed that each flavor has an identical spectral shape (γ_{astro}). This assumption is justified because the HESE sample used in this analysis is small and has limited power to constrain individual spectra for each flavor. For the sensitivity study described in **??**, the benchmark spectral parameter values are taken from the previous iteration of this analysis [133], with $\gamma_{\text{astro}} = 2.87$ and $\Phi_0 = 2.12 \times 10^{-18} \text{GeV}^{-1}\,\text{cm}^{-2}\,\text{sr}^{-1}\,\text{s}^{-1}$ assuming an equipartition of flavor ratios (i.e., $\nu_e : \nu_\mu : \nu_\tau = 1 : 1 : 1$).

[133]: Abbasi et al. (2021), *IceCube high-energy starting event sample: Description and flux characterization with 7.5 years of data*

Atmospheric flux components are constrained by priors because they are more accurately measured with other IceCube data samples. The high-energy starting event selection is very efficient in reducing atmospheric muons due to the veto requirement and the down-going atmospheric neutrinos from the same cosmic-ray-induced air shower, thanks to the self-veto effect.

Depending on the parent hadron type, the atmospheric neutrino flux is divided into two components: **Conventional neutrino flux** (produced via decay of charged pions and kaons) and **Prompt Neutrino Flux** (produced via decay of charmed mesons). The various models of atmospheric neutrino fluxes are detailed in 3.2.1. The atmospheric neutrino contribution is modeled using the Matrix Cascade Equation Solver (MCEq) [196]. The baseline primary cosmic-ray model for this calculation is H4a [211], combined with a hadronic interaction model `SIBYLL2.3c` [212], introducing conventional (Φ_{conv}) and prompt (Φ_{prompt}) flux normalizations to account for background contributions from these fluxes. Additionally, they are folded with the generalized self-veto probability, as described in 5.2, to account for the reduced rate of atmospheric neutrinos accompanying vetoed muons from the same cosmic-ray-induced air shower. Other nuisance parameters modifying the shape of these spectra include ξ_{CR}, which interpolates between two primary cosmic-ray models H4a and GST (see section 3.2.1), an approach similar to [131]. The cosmic-ray model uncertainty is critical in this analysis, as it is the largest source of uncertainty in the overall atmospheric background. Furthermore, $\Delta\gamma_{\text{CR}}$ accounts for corrections in the spectral index of the primary cosmic-ray spectrum, following [213]. Uncertainties in the hadronic interaction models, due to various π and K production cross-sections in different energy phases, introduce energy-dependent variations in atmospheric flux expectations [214]. These nuisance parameters, referred to as *Barr*

[196]: Fedynitch et al. (2015), *Calculation of conventional and prompt lepton fluxes at very high energy*

[211]: Gaisser (2012), *Spectrum of cosmic-ray nucleons, kaon production, and the atmospheric muon charge ratio*

[212]: Riehn et al. (2018), *The hadronic interaction model SIBYLL 2.3c and Feynman scaling*

[131]: Abbasi et al. (2022), *Improved Characterization of the Astrophysical Muon–neutrino Flux with 9.5 Years of IceCube Data*

[213]: Niederhausen (2018), *Measurement of the High Energy Astrophysical Neutrino Flux Using Electron and Tau Neutrinos Observed in Four Years of IceCube Data*

[214]: Barr et al. (2006), *Uncertainties in Atmospheric Neutrino Fluxes*

parameters, are computed as described in [215]. A detailed discussion on implementing these parameters within the software framework can be found in [192].

[215]: Fedynitch et al. (2022), *Data-driven hadronic interaction model for atmospheric lepton flux calculations*

[192]: Naab (2024), *Evidence for a Break in the Diffuse Extragalactic Neutrino Spectrum*

As mentioned, the veto and charge/energy cuts effectively reduce atmospheric neutrinos. However, high-energy single muons can still enter the detector, contaminating the sample. A separate nuisance parameter, Φ_{muongun}, is included in the fit to account for these muons. **The atmospheric Muon Flux** component is constrained by a prior partially derived from experimental data. The spectral shape is determined using a dedicated simulation that produces a flux of single muons reaching the detector (MUONGUN, described in 5.1), weighted assuming the same baseline models used for atmospheric spectra (H4a). A pure-proton composition is chosen for these muons as it contributes the highest energy single muons. The normalization is estimated using the tagging method described in [133]. A prior derived from this study is applied in this analysis. The sensitive energy range of this analysis is high, and the sample is specifically designed to minimize background contamination from atmospheric neutrinos and muons (see Section 5.2). The available MUONGUN Monte Carlo was generated for various other IceCube analyses, that targeted lower energies as well, where background contributions are significantly higher. Most Monte Carlo events do not pass the strict cuts of this analysis, with no events at all in the cascade and double cascade bins (see Figure 6.4 and Figure 6.6). Consequently, the statistical uncertainty on this component is high, requiring a Kernel Density Estimate (KDE) template for smoothing.

The remaining nuisance parameters are those arising from the imperfect knowledge of the detector components, such as the Digital Optical Modules (DOMs, see section **??**), and the detection medium, which includes both the bulk ice and hole ice models (see section 4.2), known from here-on as **Detector Systematics**. These detector systematics introduce uncertainties that can affect both the threshold and the shape of observable distributions, thereby altering the expected event rates from different flux components. Unlike previous iterations of this analysis [164, 198], which relied on discrete Monte Carlo sets with different values for systematics that significantly impacted the analysis observables, the current approach uses the SnowStorm simulation technique (see section **??**). The SnowStorm method [190] captures the full range of detector systematic variations in a single Monte Carlo dataset, avoiding the need for generating multiple datasets. It uses a first-order Taylor expansion of the observables, such as event counts in each bin, with respect to the detector systematics. The resulting gradient, called *the nuisance gradient* ($\vec{G}$), allows for efficient computation of observable values as these systematic parameters vary. The expectation value of per bin event count μ, for nuisance parameter variations $\vec{\eta}$ is given as,

[164]: Usner (2018), *Search for Astrophysical Tau-Neutrinos in Six Years of High-Energy Starting Events in the IceCube Detector*

[198]: Stachurska (2020), *Astrophysical Tau Neutrinos in IceCube*

[190]: Aartsen et al. (2019), *Efficient propagation of systematic uncertainties from calibration to analysis with the SnowStorm method in IceCube*

$$\mu(\vec{\eta}) = \mu_{\text{baseline}} + \vec{\eta}.\vec{G} \tag{6.9}$$

where, μ_{baseline} is the expectation value of per bin count at basleine values of all detector systematic parameters (baseline values are the central value at which simulation was generated), when $\vec{\eta} = \vec{0}$. For this approach to be valid, it assumes that systematic effects are small enough to be treated perturbatively, allowing for a linear approximation. By marginalizing

over the full ensemble of systematic variations, the prediction converges to that of the central model, effectively neglecting second-order effects. Because the dataset itself have finite statistics, appropriate uncertainty propagation is applied to the nuisance gradient (see [192] for details of calculations of this gradient, their uncertainties and incorporation within such fits).

[192]: Naab (2024), *Evidence for a Break in the Diffuse Extragalactic Neutrino Spectrum*

For each analysis bin, both the expected number of events and the associated variance are computed. However, two important caveats should be noted with this method. First, the gradients are calculated based on a specific flux assumption[1] and are not recalculated at every minimization step. This significantly reduces the computational time of the minimization process but may introduce inaccuracies if the assumed fluxes deviate significantly from the true values in nature, which could substantially alter the resulting gradients. A potential solution is to compute the gradients over a range of flux assumptions to check for significant deviations in the results. The second caveat arises because the expected event counts per bin, calculated using the gradients as shown in Equation 6.9, are applied as an *additive* correction to the overall flux expectation. Since the gradient is a vector, it can also take negative values. For softer spectra and the limited statistics of the HESE sample, this can result in negative bin counts when the expected values approach zero. This presents a problem for the likelihood fit used in the analysis, as the logarithm of a negative number cannot be computed (which the fitter will attempt to do at some point; see Equation 6.4). To avoid this numerical issue, the expectation value calculated via the gradients is clipped at $\mu = 0 + \epsilon$. This ad hoc correction is justified because, although μ_{baseline} may be zero in these bins, there remains significant statistical uncertainty, which typically dominates over the systematic variations.

1: For the analysis presented in this thesis, the gradients are computed using the best-fit values from the HESE-7.5 year analysis [133], with $\gamma_{\text{astro}} = 2.87$, the per-flavour flux normalization $\Phi^{\text{astro}}_{\nu+\bar{\nu}} = 2.12$, and an equipartition among all three flavour fluxes.

The aforementioned gradient, can be constructed using all or part of detector systematics simulated within the snowstrom ensemble. For the analysis presented in this thesis, it is constructed using 6 parameters, listed in the Table 6.2.

The DOM Efficiency (η_{domeff}) accounts for factors like the quantum efficiency of the PMT and shadowing by attached cables, reducing the efficiency by 1%. The overall uncertainty is estimated at ±10%. This impacts the reconstructed energy, as lower efficiency underestimates the photon light yield. This effect is relevant in the analysis, as it shifts the energy distribution across bins and the energy thresholds in particular.

Absorption (η_{abs}) and Scattering (η_{scat}) Scaling accounts for variations in scattering and absorprion coefficients of ice mapped across depth grid of the south pole ice. The baseline model for this mapping is SPICE-3.2.1, with priors set to a 5% width around the central value, based on the uncertainty derived from calibration data obtained using flasher LEDs.. An increase in scattering coefficients extends the photon scattering path, increasing the chance of absorption before detection. Variations in ice scattering and absorption mainly affect energy reconstruction and may introduce minor directional bias, with the energy shift being the primary concern in this analysis.

hole ice parameters ($\eta_{\text{h.ice}-\text{p0}}$ and $\eta_{\text{h.ice}-\text{p1}}$) accounts for the differences in optical properties between the refrozen ice in the DOM deploy-

ment columns and the surrounding bulk ice. Uncertainties and priors are based on a recent study that analyzed flasher data [216].

Ice anistropy discussed in detail in sections 4.2 and 5.5 affects the double cascade reconstruction greatly. For the icemodel used in simulation, this parameter is modelled as a modulation of the nominal scattering coefficient, analogous to thay used in [142].

[216]: Eller et al. (2023), *A model independent parametrization of the optical properties of the refrozen IceCube drill holes*

[142]: Abbasi et al. (2022), *Detection of astrophysical tau neutrino candidates in IceCube*

Lastly, an additional nuisance parameter, affecting all the neutrino fluxes (Astrophysical and atmospheric) is used that modifies overall normalisation of these fluxes, **Neutrino-Nucleon Inelasticity Scaling (I_{scale})**. This parameter is introduced to account for inelasticity which is a measure of the fraction of the neutrino's energy that is transferred to the hadronic system in an inelastic neutrino nucleon scattering process, mathematically given as,

$$y = \frac{E_{\text{hadron}}}{E_\nu} \tag{6.10}$$

Mean inelasticity $\langle y \rangle$ is the average value of the inelasticity y over many scattering events. It provides a statistical measure of the average fraction of the neutrino's energy that is transferred to the hadronic system. This becomes particularly relevant for the starting tracks as, $\langle y \rangle$ is energy dependednt and hence amount of energy transferred to the muon after ν_μ CC interaction, will therefore be different for different energies of Neutrino (and hence different events). For this analysis, a scaling factor is introduced, which is based on formulation provided in [35], that allows to vary Normalisation N of the inelasticity distribution,

[35]: Aartsen et al. (2019), *Measurements using the inelasticity distribution of multi-TeV neutrino interactions in IceCube*

$$\frac{dp}{dy} = N\left(1 + \epsilon(1-y)^2\right) y^{\lambda-1} \tag{6.11}$$

where N is the normalisation given as,

$$N = \frac{\lambda(\lambda+1)(\lambda+2)}{2\epsilon + (\lambda+1)(\lambda+2)} \tag{6.12}$$

The theoretical prediction of $\langle y \rangle$ from the CSMS tables [28] is calculated for the mean inelasticity distribution for a given event. By fixing $\langle y \rangle$, λ 6.12 is the fitted to apply a reweighting factor to *scale* the inelasticity (I_{scale}). Variations are permitted within 10% of their default value. The parameter is applied to all neutrino fluxes as it can affect any fluxes where a neutrino interacts via Deep Inelastic Scattering.

[28]: Cooper-Sarkar et al. (2011), *The high energy neutrino cross-section in the Standard Model and its uncertainty*

6.2.2 Analysis Observables and their Distributions

In forward folding fits, selecting appropriate observables is crucial for distinguishing between the signal and background hypotheses. The analysis uses all the HESE events above 60 TeV, further divided in 3 sub-samples of *Single Cascades, Tracks and Double Cascades*. These 3 sub-samples are binned in 2-dimensional monte carlo templates of appropriate observables, such that bakground and signal templates are clearly distingishabe. For example, when measuring the spectrum of astrophysical neutrinos, the background consists of neutrinos from other sources, primarily atmospheric fluxes. Key observables that allow for effective differentiation between astrophysical and atmospheric neutrinos include the total deposited energy (E_{tot}) and the zenith angle (θ_{zenith}) of

the interacting neutrino. The motivation for focusing on these variables stems from their distinct behavior in atmospheric and astrophysical neutrino spectra (see Section 3.2.1). In particular, down-going atmospheric neutrinos are efficiently suppressed due to the self-veto effect, while up-going atmospheric neutrinos, which cannot be reduced by this veto, become an irreducible background.

The astrophysical spectrum that is assumed for all the monte carlo templates and sensitivity is using a single-power law based on best-fit values of HESE-7.5 years spectrum measurements [133], given as,

$$\frac{d\Phi^{\text{astro}}_{\nu+\bar{\nu}}}{dE} = 6.98.10^{-18} \left(\frac{E_\nu}{100\,\text{TeV}}\right)^{-2.87} \tag{6.13}$$

In units of $\text{GeV}^{-1}\,\text{cm}^{-2}\,\text{s}^{-1}\,\text{sr}^{-1}$, with flavour composition of $\nu_e : \nu_\mu : \nu_\tau = 1 : 1 : 1$
The prompt component is missing from all templates as best-fit value of Φ_{prompt} of prompt flux normalization was 0.

For the analysis presented in this thesis, the primary goal is to measure the flavor composition of astrophysical neutrinos. A key component of this analysis, as highlighted in Section 5.4, is the identification and classification of ν_τ-induced double cascade events. Note that the PID assigned is not used as a proxy to tag flavour on an individual event bases, but through statistical analyses of the overall data set, by using Monte Carlo templates. Double cascades are a signature of ν_τ interactions, and their identification relies heavily on the observables E_{tot} and the reconstructed double cascade length (L_{dc}), which provide the most discriminatory power for separating the flavors of astrophysical neutrinos, see Figure 6.1. All double cascade events are binned into a two-dimensional Monte Carlo template, with one axis representing the reconstructed tau decay length (L_{dc}) and the other representing the reconstructed total deposited energy (E_{Tot}). The L_{dc} is divided into 10 bins ranging from 10 m to 1000 m, while E_{Tot} is divided into 13 bins spanning 60 TeV to 12.6 PeV, both using logarithmic spacing, as shown in Figure 6.1. It is important to note that adding a third dimension, such as energy asymmetry, offers significant discriminatory power by reducing the low-length single cascade background, enhancing the sensitivity to measure the flavor ratio [217]. However, a detailed study revealed that the limited Monte Carlo statistics and small sample size of the HESE data resulted in many empty bins, which posed challenges for forward-folding fits. As a result, the third dimension was ultimately excluded from the analysis.

[217]: Lad et al. (2023), *Summary of IceCube tau neutrino searches and flavor composition measurements of the diffuse astrophysical neutrino flux*

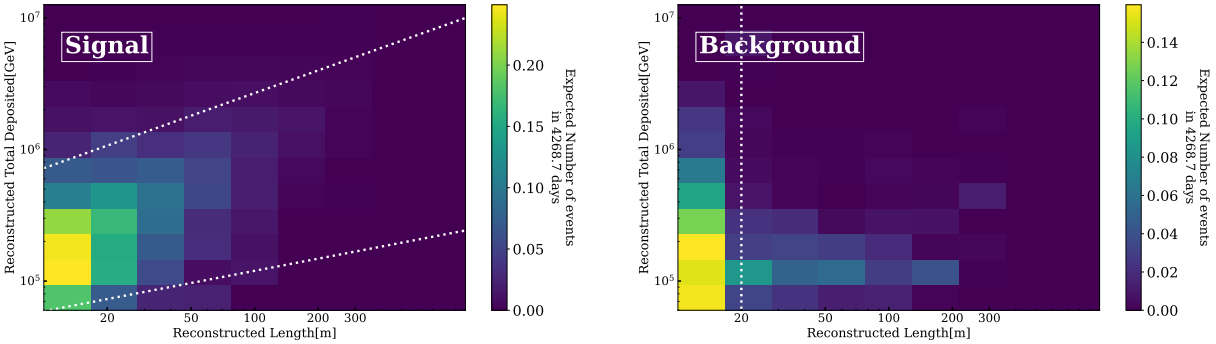

Figure 6.1: 2D Monte Carlo templates, constructed using reconstructed total energy (E_{Tot}) and double cascade length (L_{dc}) for events classified as **double cascades**. The signal (left), representing ν_τ-induced double cascades, shows a clear correlation between L_{dc} and E_{tot}, with 68% of events within the indicated signal region (dotted white line). In contrast, the background (right), consisting of ν_μ and ν_e events, lacks this correlation and clusters at low L_{dc}, 68% of all the background events lying below the indicated white dotted verticle line.

Under the double cascade hypothesis, true single cascades are typically reconstructed with a small L_{dc} but with most of their energy concentrated in the first cascade (with the energy asymmetry $E_A \rightarrow 1$). Hence, misclassified single cascades tend to cluster around low L_{dc} and low E_{Tot}, with the distribution of L_{dc} falling off rapidly, as indicated by the verticle line, on right panel of Figure 6.1. In cases where a track is reconstructed under the double cascade hypothesis, the largest energy depositions are interpreted as the cascade vertices, leading to an arbitrary L_{dc} value.

These tracks, when misclassified as double cascades, typically exhibit low E_{Tot}, consistent with the falling astrophysical spectrum. This is too visible in right panel of Figure 6.1.

True double cascades from ν_τ-CC interactions, on the other hand, exhibit a strong correlation between L_{dc} and E_{Tot}, see. This correlation between L_{dc} and E_{Tot} is primarily used to determine the compatibility of an event with a ν_τ interaction as opposed to another flavor. The Monte Carlo distributions (PDFs) of ν_τ-induced double cascades clearly show this correlation (see left panel of Figure 6.1, indicating 68% region of all classified true double cascade events).

For single cascades and tracks, the observables E_{Tot} (21 bins from 60TeV to 12.6 PeV in log space) and $\cos(\theta_z)$ (10 bins from -1 to 1 in cosine space) are commonly used, as they offer the most significant discrimination between astrophysical and atmospheric neutrinos, as shown in Figure 6.2 for cascades and Figure 6.3 for tracks. In both Figures, the supression of atmospheric neutrinos (right panel) ($\cos(\theta_z)$>0.25, the so-called *down-going region* for in IceCube) is clearly visible due to self-veto effects, whereas astrophysical template (left panel) shows no such pattern, indicating neutrinos from all directions are accepted.

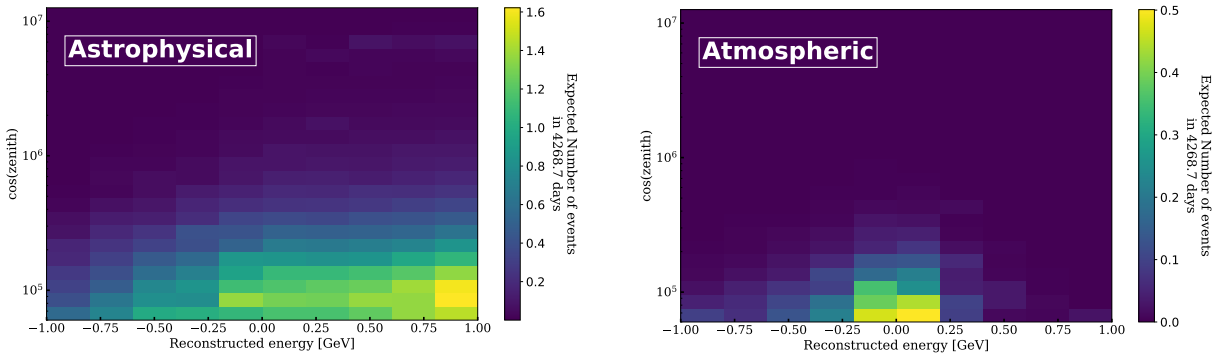

Figure 6.2: 2D Monte Carlo templates, constructed using reconstructed total energy (E_{Tot}) and reconstructed zenith ($\cos(\theta_z)$) for events classified as **single cascades**. The signal (left), representing *Astrophysical neutrinos* of the sample and the background (right), representing *Atmospheric neutrinos*, including conventional, prompt and single muon fluxes.

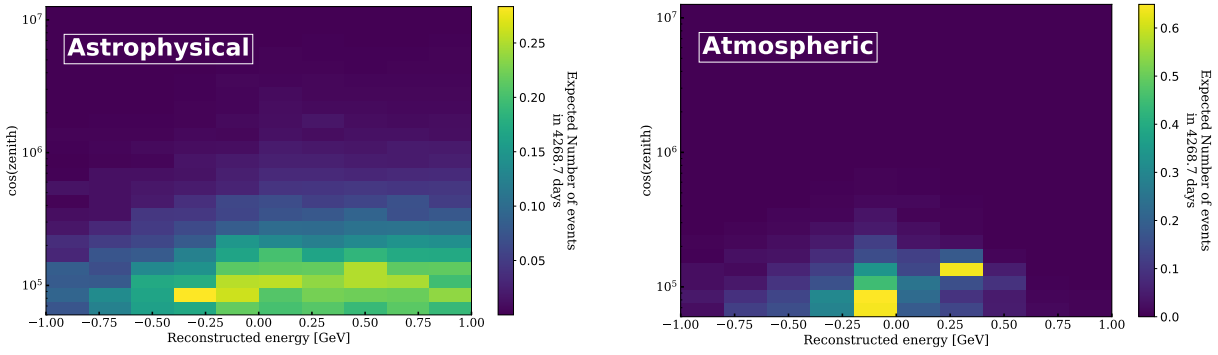

Figure 6.3: 2D Monte Carlo templates, constructed using reconstructed total energy (E_{Tot}) and reconstructed zenith ($\cos(\theta_z)$) for events classified as **tracks**. The signal (left), representing *Astrophysical neutrinos* of the sample and the background (right), representing *Atmospheric neutrinos*, including conventional, prompt and single muon fluxes.

This becomes more evident in one dimensional distribution for both of these subsamples (Figure 6.4 for cascades and Figure 6.5 for tracks), where total expectation is broken down in individual flux contributions (as desribed in 6.2.1). In case of Energy distribution of single cascades

(right panel of Figure 6.4), except for lower energy bins (up to ~ 110 TeV), astrophysical single cascade events dominates. Glashow peak due to $\bar{\nu}_e$ is clearly visible too. Note the missong muon component, due to lack of enough MUONGUN simulation, as described in 6.2.1. For Tracks (Figure 6.5), although there is a similar supression due to self veto effects, but the constribution of single muons, simulated using MUONGUN events, is clearly visible, dominating in the same down-going region. As described before, the template is noisey due to large monte carlo uncertainties. In general, tracks sample shows larger contribution due to atmospheric fluxes compared to single cascades[2]. Similar 1 dimensional distributions of L_{dc} and E_{Tot} are shown for completeness, but as described before, double cascades do not show any striking differences going from astrophysical to atmopsheric fluxes as background is due to ν_e and ν_μ events.

2: recall that single cascades also show contributions from all flavour Neutral Current (NC) interactions

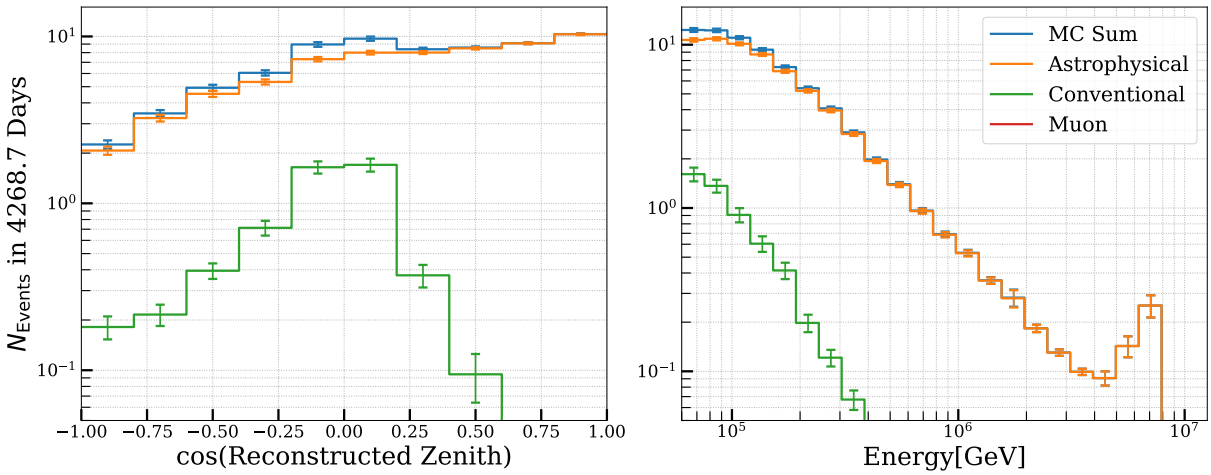

Figure 6.4: One dimensional observable distribution, for HESE Single Cascades showing expected number of events as a function of reconstructed energy (right) and reconstructed zenith (left), broken down into different flux components. Only statistical errors are shown.

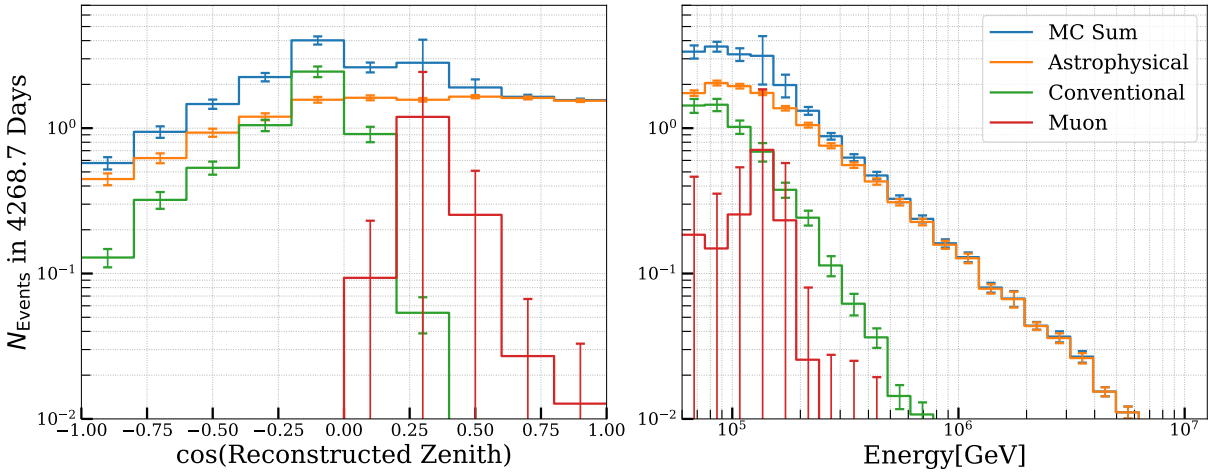

Figure 6.5: One dimensional observable distribution, for HESE Tracks showing expected number of events as a function of reconstructed energy (right) and reconstructed zenith (left), broken down into different flux components. Only statistical errors are shown.

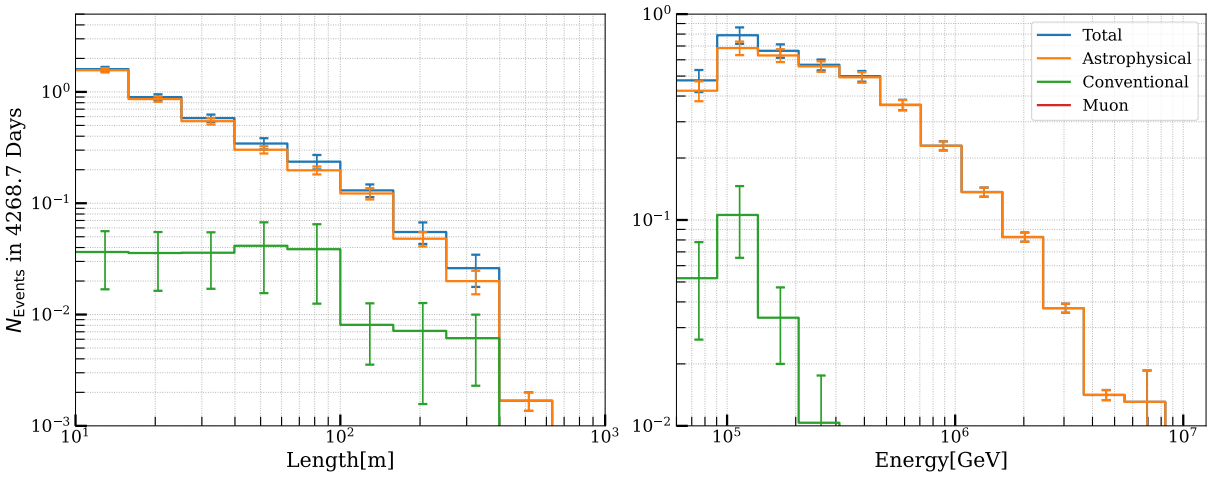

Figure 6.6: One dimensional observable distribution, for HESE DOuble Cascades showing expected number of events as a function of reconstructed energy (right) and reconstructed tau decay length (left), broken down into different flux components. Only statistical errors are shown.

6.3 Analysis Sensitivity

All fits and related calculations are carried out using a software toolkit called **`NNMFit`**. Developed within the IceCube collaboration, `NNMFit` has been applied in many other IceCube analyses. Essentially, the toolkit handles the statistical modeling required for forward-folding fits using high-energy neutrino data with binned likelihoods. It supports Monte Carlo event weighting, testing various flux models using signal and nuisance parameters, applying systematic detector uncertainties, and performing fits to data. The toolkit also enables joint fitting across different event selections. The `aesara` backend allows fast and efficient forward folding of Monte Carlo samples, even for large datasets, and offers automated differentiation that greatly assists in optimizing likelihood functions. More details on this toolkit are found in [192].

[192]: Naab (2024), *Evidence for a Break in the Diffuse Extragalactic Neutrino Spectrum*

any other thesis/paper/links required??

Using all the ingredients in the form of fluxes constructed from signal and nuisance parameters, and following the described method, the flavor composition parameter space is scanned to obtain a two-dimensional confidence region for the flavor composition, as shown in Figure 6.7. To derive these limits, an Asimov dataset is constructed (see Section 6.1), assuming the benchmark astrophysical neutrino spectrum given in 6.13. All other nuisance parameters are fixed at their baseline values listed in Table 6.2. The astrophysical neutrino flavor composition is constrained by evaluating the likelihood ratio in a profile likelihood scan, with confidence regions estimated using Wilks's theorem. The expected number of events over 12 years of HESE data, assuming the spectrum in 6.13, is broken down by flux components and shown in Monte Carlo templates in Table **??**. The fitting procedure bins all HESE events above 60 TeV in reconstructed energy and further categorizes them into three subsamples based on morphology: single cascades, tracks, and double cascades. Each sample is fit using 2D Monte Carlo templates, with the appropriate analysis variables shown in Figure 6.2, Figure 6.3, and Figure 6.1.

The sensitivity results in Figure 6.7 reveal that none of the standard source scenarios discussed in 3 can be rejected with high significance.

Table 6.2: The expected number of events from different flux components for the ~ 12 years of HESE sample, broken down for each individual fluxes, for single cascades, double cascades, and tracks categories. Only Monte Carlo uncertainties are included. The astrophysical spectrum assumed follows Equation **??**

	Single Cascades	Double Cascades	Tracks
Astrophysical	67 ± 1	4 ± 0.2	13 ± 0.5
Conventional	5 ± 0.7	0.2 ± 0.1	5 ± 0.6
Atm. Muons	-	-	2 ± 3
MC Sum	72 ± 2	4 ± 0.3	20 ± 3

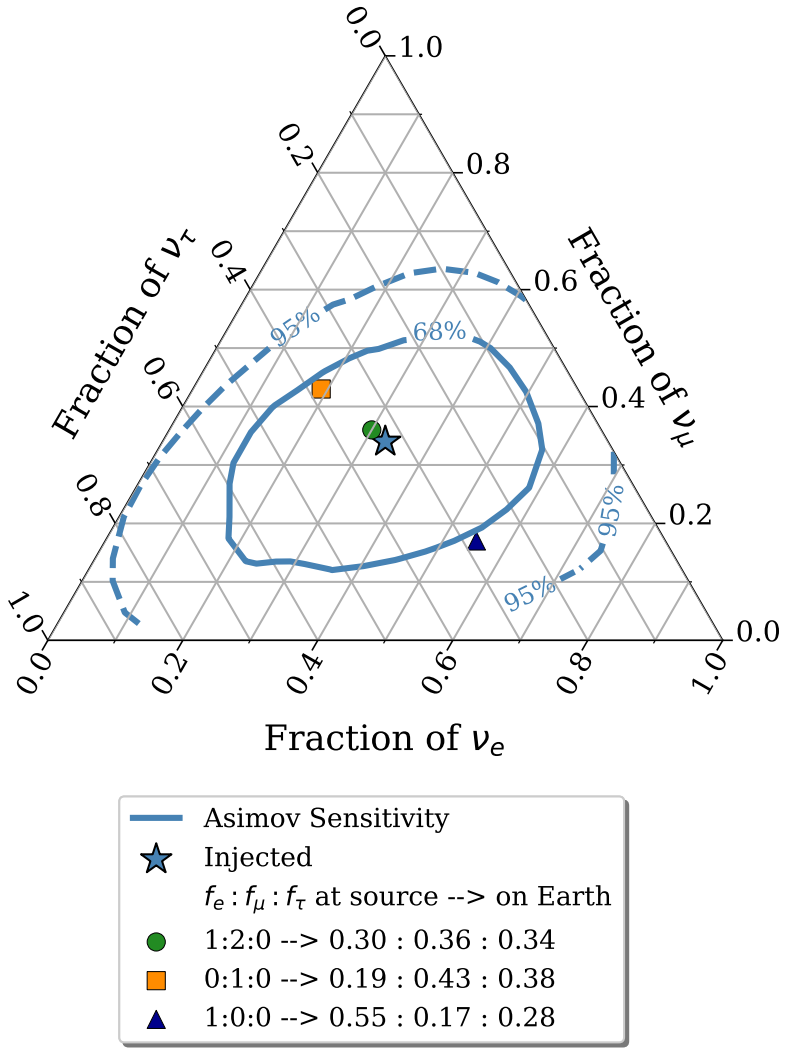

Figure 6.7: Sensitivity of the analysis presented in this thesis to measure the the flavor composition using ~ 12 years of IceCube HESE data assuming single power law given in Equation 6.13, with flavour composition of $\nu_e : \nu_\mu : \nu_\tau = 1 : 1 : 1$. Contours show the 1σ (solid) and 2σ (dashed) confidence intervals assuming Wilks' theorem.

For instance, the neutron beam scenario (represented by the dark blue triangle) is barely excluded at the ~ 1σ level. It is important to recall that the sensitivity of this analysis to the astrophysical tau-neutrino flux depends strongly on the assumed spectral shape of the neutrino flux. This sensitivity arises from the energy-dependent identification efficiency of tau-neutrino interactions. At higher energies, more energy is transferred to the secondary tau, increasing its decay length and enhancing identification efficiency. A softer spectrum, however, leads to more tau-neutrino interactions at lower energies, where they are harder to identify. Additionally, the sudden disappearance of line segments in the 95% confidence contours, particularly in regions where the ν_μ fraction approaches zero, is a result of the flavor fit parameterization (see Equation 6.8). By construction, this fraction cannot be zero, meaning that

this phase space is inaccessible to the fit.

While earlier versions of this analysis explored alternative flux models (or example, a broken power law introduces a break in the conventional single power law, resulting in different spectral indices on either side of the break energy), this was not done here. The decision was based from recent findings from another IceCube analysis that combined two other event samples (Tracks and Cascades), revealing features in the extragalactic astrophysical neutrino spectrum targetting much larger range of Neutrino energies ($\sim$ 10 TeV to $\sim$ 10 PeV) [134]. That study provided evidence of a spectral break at around 24 TeV with more than 4σ significance. The spectrum showed hardness below this break, followed by softening at higher energies, consistent with the softer spectral measurement from HESE-7.5, which targets the higher-energy range. Importantly, this high-statistics analysis, which extends well beyond the energy range of the current analysis, found no significant structures at HESE energies. Furthermore, an independent study using a different event sample [135] reported similar spectral features and closely aligned best-fit values, solidifying the argument even more.

[134]: Naab et al. (2023), *Measurement of the astrophysical diffuse neutrino flux in a combined fit of IceCube's high energy neutrino data*

[135]: Basu et al. (2023), *From PeV to TeV: Astrophysical Neutrinos with Contained Vertices in 10 years of IceCube Data*

Results 7

The 7.5 years of HESE data (2010-2017) was previously used to measure the composition of astrophysical neutrino flavours [142] (in particular to search for ν_τ events) and energy spectrum [133]. This dataset included 102 events, (of which 60 events were above 60 TeV), that passed the HESE selection criteria, as outlined in section 5.2. Two events were identified as Double Cascade candidates using the particle identifier described in section 5.4.

For this iteration, the analysis has undergone significant changes compared to previous versions while maintaining consistent selection criteria and particle identification methods. The most notable difference lies in the ice model, specifically its properties and influence on the reconstruction of tau decay length, detailed in section 4.2. The SPICE-Bfr may have impacts on the overall energy estimates, as the number of photons collected in a given time window have significantly changed in this model of ice depending on the alignment of DOMs with respect to the iceflow axis [160]. Furthermore, the treatment of detector systematics has evolved, utilizing the SnowStorm method (see section 5.1.2) instead of discrete Monte Carlo simulation sets used previously. The update also includes revised reconstruction tables [197] for the maximum likelihood reconstruction method described in section 5.3. Additionally, various corrections have been applied to monte carlo simulations, encompassing reweighting to incorporate corrections due to tau polarization and initial state radiation corrections to the Glashow cross-sections (see section 5.4). Lastly, some of the nuisance parameters and analysis software are also different (see section 6.2). As a first step, the 7.5 years of HESE data were re-unblinded due to these changes.

This chapter presents flavour measurements made using 12 years (11.69 to be exact) of HESE data. It begins by discussing the re-unblinding of 7.5 years of data, followed by results from the 12-year fit, including Data-Monte Carlo agreement and detailed post-unblinding checks. Finally, the flavour measurement results are presented and interpreted in the last sectinons.

[142]: Abbasi et al. (2022), *Detection of astrophysical tau neutrino candidates in IceCube*

[133]: Abbasi et al. (2021), *IceCube high-energy starting event sample: Description and flux characterization with 7.5 years of data*

[160]: Abbasi et al. (2024), *In situ estimation of ice crystal properties at the South Pole using LED calibration data from the IceCube Neutrino Observatory*

[197]: Yuan (2023), *Detecting neutrinos in IceCube with Cherenkov light in the South Pole ice*

7.1 (Re)Unblinding of 7.5 years of HESE Data

The re-unblinding of the HESE-7.5 data provided new insights, revealing that 64 events met the HESE selection criteria, each with a deposited energy exceeding 60 TeV. It included 6 Double Cascade events*, which is a significant increase from the previous analysis that identified only two Double Cascade events. Notably, 4 of the additional events had initially been classified as single cascades. The reclassification was largely driven by the application of the energy asymmetry cut, which proved to be a crucial factor in differentiating between single and double cascades (see

* Unless explicitly specified, all mentioned classifications are by using SPICEBfr, the default icemodel of the analysis presented in this thesis. At some places in this section, specific comparisons are shown using SPICE-3.2.1

section 5.4). A key difference in this re-unblinding was the icemodel used for reconstruction, as mentioned before. Hence, the data was processed using both SPICE-3.2.1 (used in previous iteration) and SPICE-Bfr to make direct comparisons with the previous results. Using SPICE-3.2.1, reunblinded data contained total of 62 HESE events above 60 TeV deposited energy, of which 7 events were classified as Double Cascades. Moreover, of these 6 and 7 observed Double Cascades, using different ice models, only 3 are common, landing 7 new candidate events. Despite the changes in the total number of classified events, the two common Double Cascade events identified in both iterations exhibited nearly identical reconstructed properties, as outlined in Table 7.1 (for SPICE-3.2.1).

should there be a similar table for bfr??

Table 7.1: Comparison of Reconstructed quantities of events classified as Double Cascades upon re-unbling 7.5 years of HESE data using **SPICE-3.2.1 icemodel** with previous results (grey cells). Shown in the table are (from left), MJD (Modified Julian Date), reconstructed length, reconstructed Energy of first (E_1) and second (E_2) cascades, Energy asymmetry (E_A), Energy Confinement (E_C) and classified morphology (as per previous anlaysis) of the event. The two common events, 57134 (*Double Double*) and 56265 (*Big Bird*) have nearly identical reconstructed quantities. The most striking differences here are specifically reconstructed length and the fact that E_1 and E_2 seem to be almost flipped for some events, even though reconstructed directions (zenith and azimuth, not shown in the table) remains almost idnetical. The change in E_1 and E_2 changes the E_A, which is the discrimation cut between single and double cascades.

MJD	Length		E_1		E_2		E_A		E_C		morphology
57677	27 m	37 m	3.1 TeV	128 TeV	148 TeV	4 TeV	-0.96	0.94	1	0.99	Single
57134	16 m	17 m	18 TeV	8.7 TeV	92 TeV	79 TeV	-0.89	-0.80	0.99	0.99	Double
56763	10.2 m	84 m	63 TeV	107 TeV	87 TeV	17 TeV	-0.16	0.72	0.99	0.99	Single
55477	14 m	279 m	70 TeV	184 TeV	84 TeV	67 TeV	-0.09	0.46	0.99	0.98	Single
55800	12 m	20 m	105 TeV	133 TeV	89 TeV	38 TeV	0.08	0.55	1	0.99	Single
56221	12 m	12 m	209 TeV	102 TeV	132 TeV	237 TeV	0.22	-0.4	0.99	0.97	Track
56265	17 m	16 m	0.8 PeV	1.2 PeV	1 PeV	0.6 PeV	-0.08	0.29	0.99	1	Double

No matter what icemodel is used, in reunblinding an excess of double cascade events was observed, suggesting the presence of unnoticed changes not already accounted for. Careful search of each step in the particle identification process revealed a significant change in the reconstruction method from the previous iteration. Notably, this change involved the incorporation of high quantum efficiency Digital Optical Modules (DOMs) from DeepCore. In earlier analyses, these DOMs had been excluded from the reconstruction of high-energy neutrino events, in millipede-based reconstructions outlined in 5.3. The rationale for their exclusion stemmed from the smaller statistical uncertainties of digitized waveforms, in compared to the systematic uncertainties. These systematic uncertainties, which were not well-characterized for individual DOMs, could not be factored into the table-based likelihood fitting method. Nonetheless, due to advancements in simulation, including enhanced reconstruction tables and detector simulations, the analysis presented in this thesis included the DeepCore DOMs, hence the next step was to explore why Monte Carlo predictions had underestimated the number of Double Cascade events.

Figure 7.1 shows the distribution of classified Double Cascade, both with and without the inclusion of DeepCore DOMs. The monte carlo simulations predicts only $\sim$ 2 Double Cascade events, yet the data revealed 6 (7) Double Cascade events using SPICE-Bfr (SPICE-3.2.1) when DeepCore DOMs were included and only 3 (4) when they were excluded. It remains clear that no matter what icemodel is used, the distribution of reconstructed energy and overall expectation remains same irrespective of whether DeepCore DOMs are included or not. This discrepancy pointed

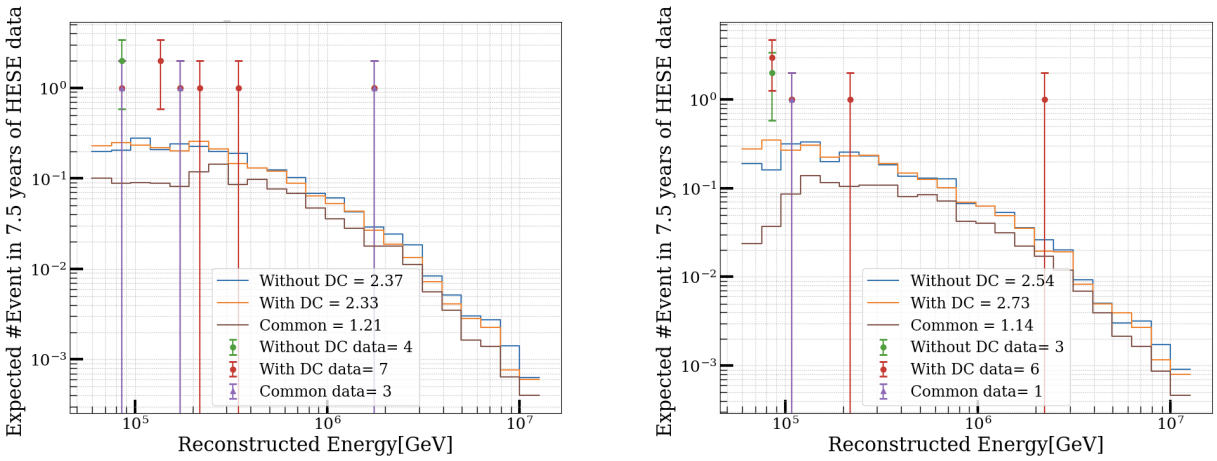

Figure 7.1: Distribution of number of expected classified as double cascacdes in 7.5 years of HESE data usign SPICE-3.2.1 (left) and SPICE-Bfr(right) icemodel with (*With DC*) and without (*Without DC*) DeepCore DOMs, along with data events for the respective configurations.

to potential issues in reconstruction processes involving DeepCore DOMs, indicating that further investigation at the monte carlo level is necessary, see Appendix **??** for details. Such investigations requires efforts that were beyond the timeline of this thesis work and considering the historical exclusion of DeepCore DOMs (as well as other "bad" DOMs like bright or saturated modules) from reconstruction chains in previous iterations of HESE analyses, this analysis ultimately decided not to include DeepCore DOMs in the full sample unblinding. Ultimately, the re-unblinding of the HESE-7.5 data resulted in 62 events with deposited energies above 60 TeV. Of these, 45 were classified as single cascades, 3 as Double Cascades, and 14 as track events. A detailed comparison between these reunblinded results and previous results, including classified morphologies (with different iterations of icemodels and DeepCore inclusion/exclusion) is shown in Table 7.2.

Table 7.2: Event classification of 7.5 years of HESE data (Previous) compared with reunblinded sample outcome (all events have Reconstructed total energy > 60 TeV). The comparison is shown for all 2 different icemodels, each of which further broken down into with and without the deepcore doms. The final outcome of this reunblinding, in order to move forward with the full sample is the last column (without DeepCore using SPICEBfr).

Morphology	Previous	Reunblinded			
		SPICE-3.2.1		SPICE-Bfr	
		DeepCore	No DeepCore	DeepCore	No DeepCore
Cascades	41	41	44	42	45
Double Cascades	2	7	4	6	3
Tracks	17	14	14	16	14
Total	60	62	62	64	62

7.2 Unblinding of 12 years of HESE data

The High-Energy Starting Events (HESE) sample, covering approximately 12 years of IceCube detector live time (4268.7 days) from 2010 to August 2022, was unblinded in January 2024 for the analysis outlined in Section 4.3. This sample includes 167 events that passed the HESE selection criteria, which involved the veto and total charge conditions as detailed

in Section 4.2. Of these, 3 were coincident events that had previously been removed by manual inspection, but were retained this time since the current Monte Carlo simulations now account for such coincidences. Despite this, the energy threshold of 60 TeV effectively filtered them out, resulting in a final sample of 97 events above the 60 TeV deposited energy threshold. Using the ternary topology identification method from this thesis, 64 events were classified as single cascades, 5 as double cascades, and 28 as tracks.

7.2.1 Fit results

Blind Fit results

In IceCube, all the analysis are done in a blind fashion, meaning reconstruction and other fit details are applied to simulation to produce expectations in form of Monte Carlo PDFs and later data is fit to this expectation to make the desired measurement. Details of such a fit are given in 6.1. For such fits, before looking at the full data results, sometimes a middle step is considered where only nuisance parameters are revealed first (and/or only background region is looked at) to see any striking disagreement between the data and monte carlo or unexplainable behaviour of any nuisance parameters (e.g. if they are hitting the fit range boundary etc). Stopping criterions are set-up beforehand in case this step shows any troublesome results. For HESE sample, since overall expectation is quite low, looking at a subsample would certainly be unyielding. Thus, blindfit for this analysis included observing the nuisance parameters behaviour and goodness of the fit. The stopping criterions included, minimum p-value of 5% for the goodness of fit test (see 6.1 for details) and applying priors on systematics in case they hit the boundary. These priors are derived from the so far gathered best knowledge of the ice and detector, and were tested by running pseudo trials (see 6.2.2) to test their effects on signal distributions. As a post-unblinding check, they are to be removed to see if any significant changes are observed in signal parameters.

The bestfir values of nuisance parameters are summarized in Table 7.3 along with their gaussian priors. Initially, the holeice parameters, $\eta_{\text{h.ice-p0}}$ and $\eta_{\text{h.ice-p1}}$ were hitting the boundary, but upon applying the tested priors this effect was resolved. As a post unblinding check, these priors were removed to check any changes in signal parameters, no such significant changes were observed. The likelihood includes a penalty term (see 6.1) which was checked for the 2D scan of flavour ratio triangle to see the effect of pulls due to this prior.

perhaps the triangle plot showing llh penalty due to these priors can be shown here? or should this discussion have its separate appendix?

Most of the nuisance parameters are primarily fitted to their priors with minimal deviations from the modeled uncertainties. The detector systematics are set away from default values, although they still remain within one standard deviation of the applied prior width. This can be explained as follows: The method used to apply systematic uncertainties, known as the "gradient method" (see 6.2.1), in the fit assumes linearity whether moving away from or towards the central value. In an ideal scenario, the range within which the parameter is allowed to vary (and the simulation range) should be narrow enough that the central value can always be recovered. However, these parameters are considered only as

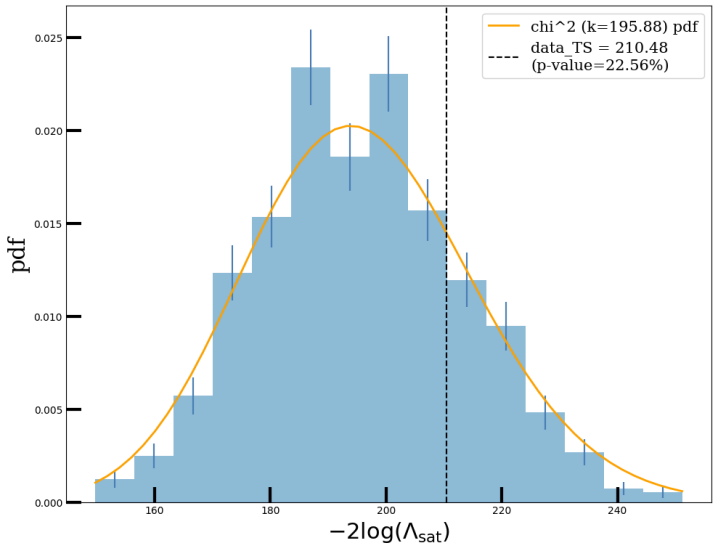

Figure 7.2: Distribution of the test statistics for 1000 pseudotrials injected at best-fit (signal parameters kept blind). Vertical line shows TS of data, which matches quite well with degrees of freedom derived by fitting a χ^2 to the distribution.

nuisance in the fit, and they are not meant to be measured. Furthermore, the detector is not so precisely calibrated as to know the true value of these parameters. Therefore, in practice, the range is kept quite wide. In the analysis presented here, where the overall expectation is low and the data is binned in histograms, such things can happen, causing the nuisance parameters to shift. In order to save computational power, the gradients are calculated once for a given spectrum assumption. If the underlying spectrum of data is far from this assumed spectrum, small changes in these signal parameters can cause larger deviations. Most of these systematics thus ended up having a gaussian prior in the fit, as listed in the Table 7.3.

Lastly, the goodness of the fit (GOF) is tested by using the pseudo data. This data is genereated by injecting the Best Fit Parameter (BFP) values as the true parameters and then fluctuating the expected bin counts to consider MC uncertainty and Poisson fluctuations in the data. A distribution of Test Statistic (TS) values is then observed, which is derived from the ratio of the fitted likelihood to the saturated Poisson likelihood. The saturated likelihood represents the alternative hypothesis, where the data perfectly matches the assumed model. The saturated Poisson likelihood assumes the most ideal scenario, where each analysis bin observes statistically significant data, following a chi-squared distribution with degrees of freedom equal to the difference between the number of analysis bins and the number of free parameters in the fit. However, in reality, not all bins observe data, so some deviations are expected. By comparing the distribution of TS values from these pseudo-data trials to the distribution derived from the real data, a p-value can be calculated. The p-value represents the probability of finding a TS value from the trials that is at least as large as the one from the data fit. Figure 7.2 illustrates this distribution, where the data TS is compared with the distribution of trial TS values. The obtained p-value is 22.56%. Based on this test, it is concluded that the fit result is consistent with the expected outcome from the pseudo-data trials.

Table 7.3: The best-fit parameter values of the nuisance parameters. The uncertainties are calculated at the 68% confidence level through a profile likelihood scan assuming Wilks' theorem, in case of a flat likelihood space, fit boundaries are given as limits. Last column states the gaussian priors on the parameters (if applicable) in terms of the mean (μ) and width (σ). The table is divided in terms of type of the nuisance parameters, above part includes all the parameters that affects the atmosphgeric neutrino components and the lower part consists if parameters stemming through various detector components. For details, see 6.2.1

Parameter		Best-Fit value	Prior (μ, σ)
Φ_{conv}	Conventional Flux normalisation	$0.99^{+0.19}_{-0.2}$	(1.0,0.2)
Φ_{prompt}	Prompt Flux Normalisation	$0.0^{+2.25}_{-0.0}$	-
ξ_{CR}	Interpolation between Cosmic Ray Models	0.042^{+2}_{-1}	(0,1)
$\Delta\gamma_{\text{CR}}$	Cosmic Ray Spectral Index Shift	-0.00^{+1}_{-1}	(0,0.05)
H_{Barr}	Barr-parameter modifying the pion-contribution	$0.0^{+0.5}_{-0.5}$	(0,0.15)
W_{Barr}	Barr-parameter modifying the kaon-contribution	$0.0^{+0.5}_{-0.5}$	(0,0.40)
Y_{Barr}	Barr-parameter modifying the pion-contribution	$0.0^{+0.5}_{-0.5}$	(0,0.30)
Z_{Barr}	Barr-parameter modifying the pion-contribution	$0.0^{+0.5}_{-0.5}$	(0,0.12)
Φ_{muongun}	Muon Flux Normalisation	$1.16^{+0.42}_{-0.43}$	(1,0.5)
I_{scale}	scale factor for Neutrino Nucleon Inelasticity weight	$0.99^{+0.1}_{-0.09}$	(1,0.1)
	Detector Systematics		
η_{domeff}	Optical Efficiency of DOMs	$1.04^{+0.06}_{-0.04}$	(1.0,0.1)
η_{abs}	Ice Absorption Scaling	$0.99^{+0.04}_{-0.04}$	(1.0,0.05)
η_{scat}	Ice Scattering Scaling	$0.98^{+0.04}_{-0.04}$	(1.0,0.05)
$\eta_{\text{h.ice-p0}}$	parametrization for refrozen icecolumn	$-0.27^{+0.28}_{-0.38}$	(-0.27,0.5)
$\eta_{\text{h.ice-p1}}$	parametrization for refrozen icecolumn	$-0.08^{+0.04}_{-0.05}$	(-0.042,0.05)
η_{aniso}	Ice Anisotropy Scaling	$0.99^{+0.54}_{-0.63}$	-

Full fit results

The bestfit values of the signal parameters for the 97 HESE events are summarized in Table 7.4. As explained in 6.2.1, the flavour fractions within `NNMFit` framework are fitted as scaling factors s_{ν_e} and s_{ν_τ}, which modifies the flux of electron and tau neutrinos relative to the muon neutrino flux. Which is why, the signal parameters listed in Table 7.4 needs to be converted to their corresponding flavour fractions (), giving us measured flavoured composition of astrophysical neutrinos as, $\nu_e : \nu_\mu : \nu_\tau = 0.19 : 0.43 : 0.38$. Since the measurement is done for the entire spectrum, this value that of best-fit flavour composition which is expected on earth in case neutrinos at high energy sources are produced with muon damped scenario, hints that diffuse neutrino spectrum at high energies (sensitivity range of this analysis is 100TeV-10PeV) may be dominated by sources with such production mechanisms. Nevertheless, the limits derived (see 7.3) cannot reject either of these scenarios with reasonable significance.

reference fraction conversion formula here

The best-fit value of astrophysical index (γ_{astro}), assuming a single power law is $2.84^{+0.19}_{-0.18}$. This value is in well agreement with the previous results [133]. As for the normalization, as per the formulation of the flavour fit within the `NNMFit` the best-fit value shown in the table is astrophysical ν_μ normalization, which when converted using appropriate transformations

[133]: Abbasi et al. (2021), *IceCube high-energy starting event sample: Description and flux characterization with 7.5 years of data*

Table 7.4: The best-fit parameter values for the signal parameters for a single power-law model at 100 TeV muon neutrino energy for both particle and antiparticle. The uncertainties are calculated at the 68% confidence level through a profile likelihood scan assuming Wilks' theorem.

Parameter		Best-Fit value
ϕ_{ν_μ}	astro. ν_μ normalisation [10^{-18}GeV^{-1}cm^{-2}sr^{-1}s^{-1}]	$2.53^{+1.78}_{-1.49}$
γ_{astro}	astro. spectral index	$2.84^{+0.19}_{-0.18}$
s_{ν_e}	astro. ν_e scaling factor to modify total flux norm ($\Phi^{\text{astro}}_{\nu+\bar{\nu}}$) relative to ϕ_{ν_μ}	$0.45^{+0.68}_{-0.40}$
s_{ν_τ}	astro. ν_τ scaling factor to modify total flux norm ($\Phi^{\text{astro}}_{\nu+\bar{\nu}}$) relative to ϕ_{ν_μ}	$0.896^{+1.34}_{-0.89}$

gives the total flux normalization (for all flavours) $\Phi^{\text{astro}}_{\nu+\bar{\nu}} = 5.94^{+5.64}_{-4.28}$. The larger uncertainity on normalization is expected for such a fit where each flavour components are allowed to be free, that in turn have larger uncertainty on them (see Table 7.4).

check this number again!!

Lastly, the table in Table 7.5 provides the breakdown of expected events classified into specific morphologies and their individual components. Additionally, the comparison includes the expectation based on a $\nu_e : \nu_\mu : \nu_\tau = 1 : 1 : 1$ flavour ratio, which was determined by running the fit with fixed flavour ratios. It is important to note that the expectation aligns more closely with the data when the flavour ratios are independently fitted.

Table 7.5: The expected number of HESE events, classified into three morphologies, assuming a fixed flavour ratio of 1:1:1 and at the best-fit flavour ratio. The total expected event counts are further broken down into each of the flux components, Astrophysical (Astro), Conventional (Conv), Atmospheric Muons (Muon). Prompt component is not shown here as best-fit value of the prompt norm (Φ_{prompt}) is 0.

Reconstructed Morphology	$\nu_e : \nu_\mu : \nu_\tau = 1 : 1 : 1$(fixed)				$\nu_e : \nu_\mu : \nu_\tau = 0.19 : 0.43 : 0.38$ (free)				Data
	Astro	Conv	Muon	Total	Astro	Conv	Muon	Total	
Cascades	58 ± 2	6.8 ± 0.9	-	65 ± 2.7	57 ± 2	6 ± 0.79	-	63.4 ± 2.4	**64**
Tracks	11.8 ± 0.7	6.3 ± 1	2 ± 3	20 ± 3.6	16 ± 0.8	5.7 ± 0.9	1.84 ± 2.7	23.4 ± 3.4	**28**
Double Cascades	3.2 ± 0.3	0.4 ± 0.2	-	3.5 ± 0.5	3.8 ± 0.3	0.3 ± 0.2	-	4.1 ± 0.4	**5**

7.2.2 Data/Monte Carlo Agreement

Even with a reasonably good fit, any significant mismodeling can only be discerned through a comparison with the Monte Carlo expectations. Nonetheless, the subsequent figures demonstrate the distributions of the analysis observables for all three morphologies, for HESE events with deposited energies above 60 TeV. These plots are generated using the best-fit values described in Table 7.4 and Table 7.3. Each figure displays individual components as well as the sum of all components under the label **MC sum**. Additionally, to highlight any noteworthy features, a ratio plot is included for each distribution, illustrating the ratio of data events to each bin of the MC sum. Although there are observed slight fluctuations, the presence of considerable statistical uncertainties makes it challenging to pinpoint any specific spectral features.

Figure 7.3 and Figure 7.4 shows the distribution of reconstructed energy (left) and cosine of reconstructed zenith (right) for events classified as single cascades and tracks resepctively in the 12 years of HESE data. The

zenith plot clearly illustrates the all-sky selection feature of the HESE sample by overall being flat throughout the zenith distribution. It also highlights the decrease of the conventional component in the downgoing region (cos(zenith>0.25)), indicating the self-veto effect. Additionally, the muongun component is exclusively visible in the track histogram due to fact that the ternary classifier predominantly classifies muons as tracks. However, it's important to note that the expectation exhibits substantial statistical uncertainties due to the lack of sufficient `muongun` monte carlo. To mitigate the impact of the noisy distribution caused by extensive Monte Carlo uncertainties, a kernel density estimation (KDE) is employed to smoothen out the fluctuations present. While both morphology distributions reveal some minor structures, they do not demonstrate any statistically significant characteristics.

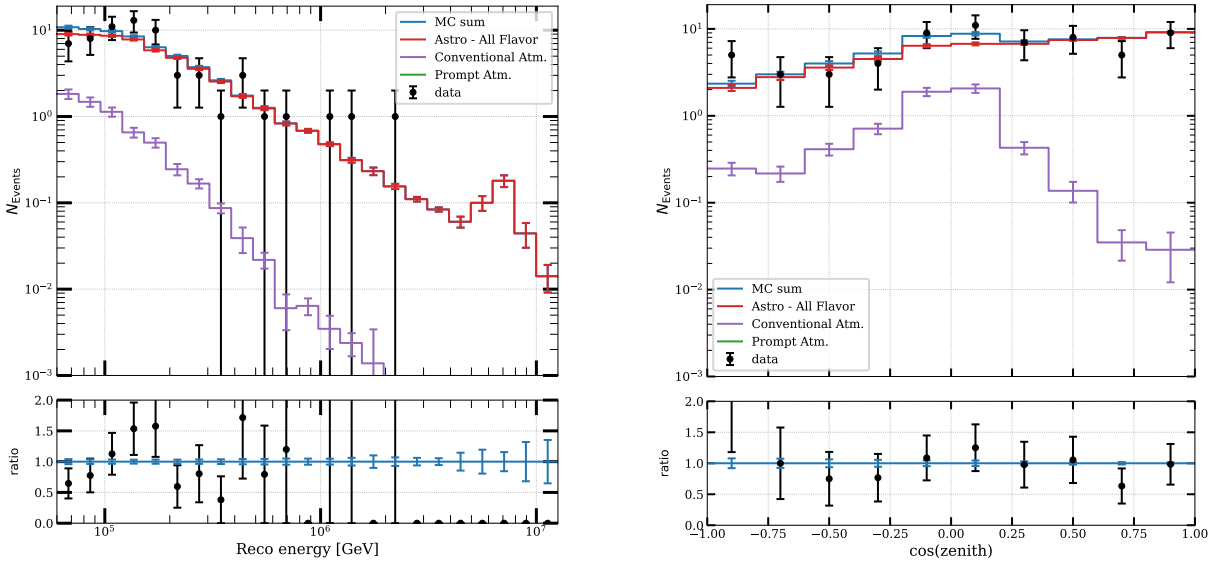

Figure 7.3: Observable distributions of the total deposited energy (left) and the zenith angle (right) for events classified as **single cascades** along with data point positions. Individual components of the fits are produced using bestfit values given in Table 7.4 and Table 7.3 and MC sum is sum of all of these components. Prompt component is missing on account of bestfit value of 0 for the Φ_{prompt}.

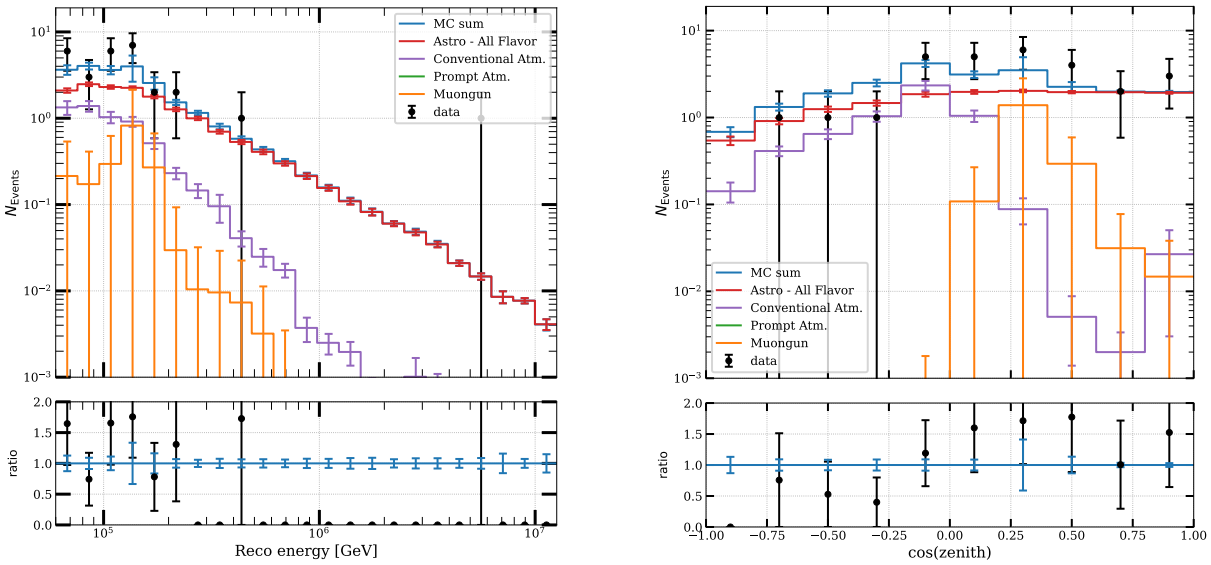

Figure 7.4: Observable distributions of the total deposited energy (left) and the zenith angle (right) for events classified as **tracks** along with data point positions. Individual components of the fits are produced using bestfit values given in Table 7.4 and Table 7.3 and MC sum is sum of all of these components. Prompt component is missing on account of bestfit value of 0 for the Φ_{prompt}.

Figure 7.5 illustrates the distribution of reconstructed energy (left) and reconstructed length (right) for events classified as double cascades in the 12 years of HESE data. In the second energy bin, there is an overfluctuation, but it's challenging to incorporate this as a feature due to the large uncertainties in both the monte carlo and data. An interesting feature of the fit can be seen in the conventional component distribution. The application of gradient correction as an additive factor per component indicates that systematics are trying to adjust this component to account for the excess of double cascades at low energy and high length. This suggests that due to fewer statistics compared to tracks, there is more variability in this parameter across the double cascade bins. Another noteworthy observation is that one event, although close to 100 TeV, has a large length, suggesting that it is a misclassified track. This particular event demonstrates Energy Confinement near the edge (0.97), a cut that is supposed to differentiate between a double cascade and a track, but not quite above the threshold to be a track (0.99). And hence, the event passed all the cuts and ended up being classified as a double cascade. This becomes more evident in 2D distribution of energy and length in Figure 7.6, where this event clearly ends up in a background dominated region of the PDF (see 5.4 for signal and background pdfs of double cascades).

The figure Figure 7.6 illustrates a two-dimensional PID pdf of reconstructed double cascade events, based on the best-fit values described in the tables. The vertical lines demonstrate how quickly the single-cascade background decreases with length. For instance, 68% of misclassified single cascades have reconstructed double-cascade lengths of less than ~ 14 m, 90% have lengths below ~ 20 m, and only 1% have lengths exceeding ~ 25 m. Two of the data events are outside the 68% region, but one of these events is still within the signal region indicated by white lines. The event with a reconstructed length of approximately 95 m but less than 80 TeV energy is clearly in the background region. Another important observation from this figure is the lack of smoothness expected from

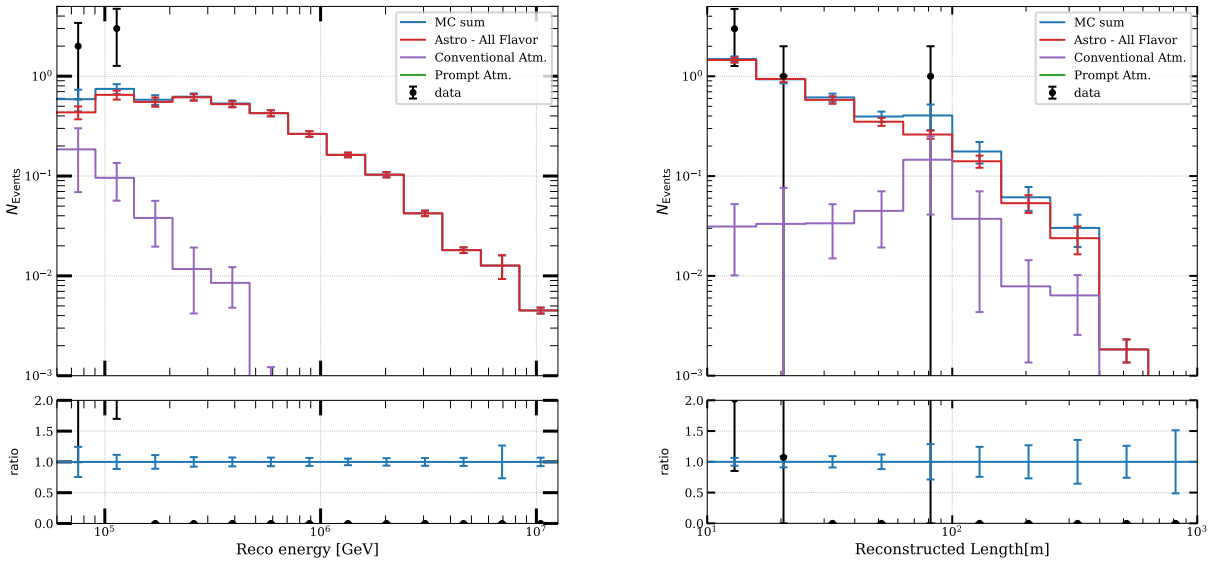

Figure 7.5: Observable distributions of the total deposited energy (left) and the reconstructed length (right) for events classified as **double cascades** along with data point positions. Individual components of the fits are produced using bestfit values given in Table 7.4 and Table 7.3 and MC sum is sum of all of these components. Prompt component is missing on account of bestfit value of 0 for the Φ_{prompt}.

PDFs when performing forward folding fits. The gradients are applied as an additive correction per bin, to allow detector systematic variations in the fit. This in turn can significantly change the per bin expectations, making the distributions more fluctuating.

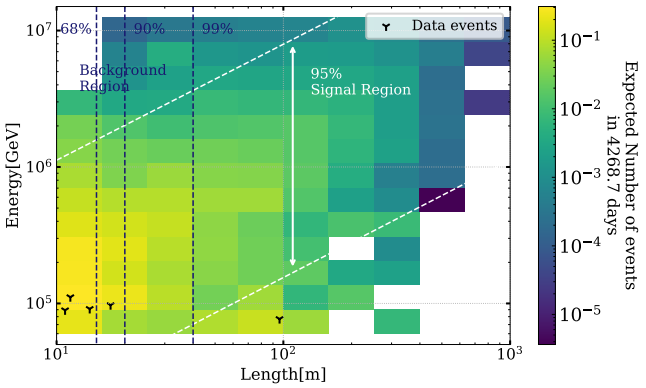

Figure 7.6: Two-dimensional distribution of reconstructed energy vs reconstructed double cascade length of the monte carlo events classified as double cascades. Monte carlo sum is produced using all the bestfit parameters from the Table 7.4 and Table 7.3. Position of the data events are marked with ϒ. Signal (white) and Background (dark blue) dominated regions are marked with their respective percentiles.

Figure 7.7 presents the distribution of the reconstructed energy asymmetry for simulated events in the double-cascade sample, using the best-fit astrophysical and atmospheric spectra. The two vertical lines represent the selection cuts applied to choose the double cascade events, as described in section 4.3. Although two of the 5 events are near the cut edge, they all still fall comfortably within the signal-dominated region of the sample.

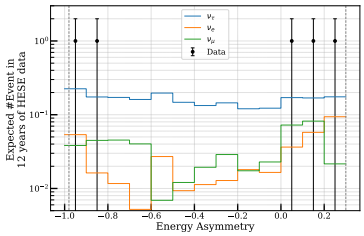

Figure 7.7: Distribution of reconstructed energy asymmetry, defined as $E_A = \frac{E_1 - E_2}{E_1 + E_2}$, (where E_1 and E_2 are energies of first and second cascades, respectively) at best-fit, along with data events. Distribution is shown for all flavours separately, to emphasis domination of ν_τ double cascades in the signal region (verticla grey lines).

7.3 Flavour Composition of Diffuse Astrophysical Neutrinos

The flavour composition of astrophysical neutrinos is measured using 97 high-energy starting event (HESE) events, which are divided among three morphologies. The profile likelihood scans for the flavour scale factors, specifically s_{ν_e} and s_{ν_τ}, are shown in Figure 7.9. The results indicate that the tau scale factor (s_{ν_τ}) is only able to reject the possibility of no ν_τ flux by 1σ ($-2\Delta \log \mathcal{L} = 1$), as reflected in the wide contours in the 2D scan shown in Figure 7.8. The 1D scans are used to derive 1σ (68%) confidence regions, shown in Table 7.4. The test statistic $-2\Delta \log \mathcal{L}$ compares the global best-fit values of the unconstrained fit to the conditional best-fit values of all remaining model parameters at a fixed scan point. The confidence regions depicted in Figure 7.8 are calculated using Wilk's theorem [206] , as a full Feldman-Cousins construction of the entire flavour composition phase space is computationally demanding (see section 6.1 for details). The agreement of Wilk's theorem is verified by comparing the coverage of the test statistic distribution from Monte Carlo pseudo-experiments to the coverage of a χ^2-distribution. A large fraction of the flavour composition phase space is found to be slightly over-covered, indicating that Wilk's theorem yields a conservative confidence region. Although a part of the 90% confidence region seems to suffer from slight under-coverage, the χ^2-approximation is deemed sufficient for presenting the measurement result in Figure 7.8.

[206]: Wilks (1938), *The Large-Sample Distribution of the Likelihood Ratio for Testing Composite Hypotheses*

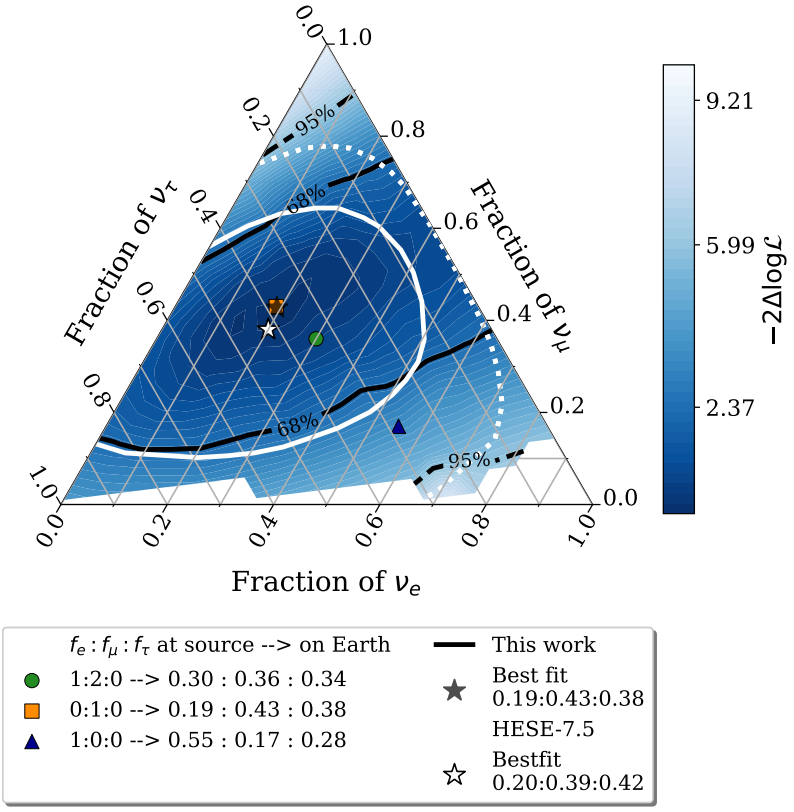

Figure 7.8: A 2 dimensional profile likelihood scan of the astrophysical neutrino flavour composition at Earth using 12 years of HESE data, classified in three event morphologies (see text for details). Each point on the triangle corresponds to a flavour composition of $\nu_e : \nu_\mu : \nu_\tau$ which can be read off the axes along the tick directions specified. The best-fit flavour composition of 0.19 : 0.43 : 0.38 is indicated with a white star. The white solid and dashed lines represent the 68% and 95% confidence regions, respectively, obtained from the χ^2-approximation using Wilk's theorem. Three flavour compositions expected at Earth from different source scenarios are also marked (3.2). The best-fit flavour composition of a previous measurement that used 7.5 years of HESE data is indicated in grey star, with the 68% and 95% confidence regions represented by the grey solid and dotted lines, respectively [142].

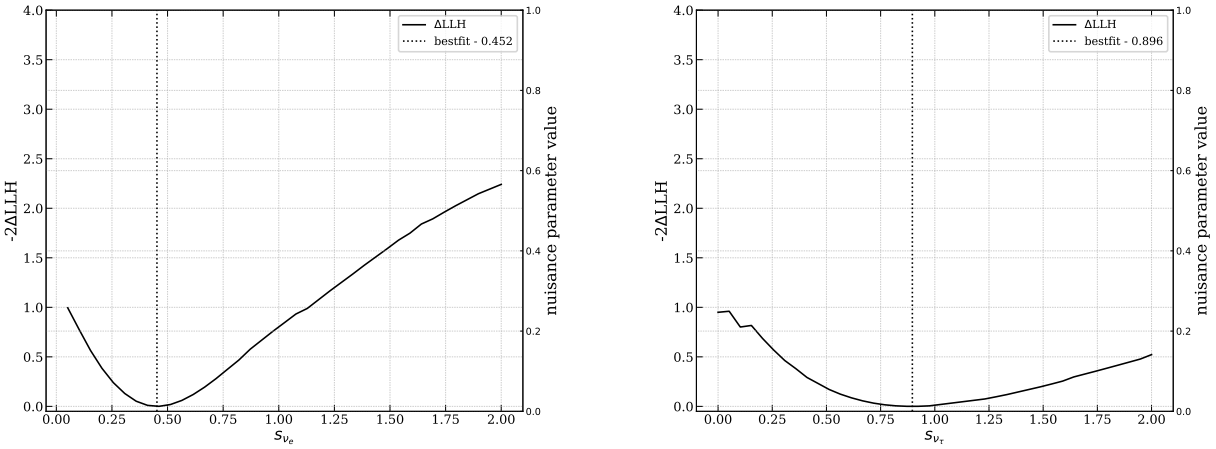

Figure 7.9: 1 dimensional profile likelihood scan of flavour scale factors s_{ν_e} (left) and s_{ν_τ} (right). Solid black line corresponds to the profile likelihood, defined by the likelihood ratio $-2\Delta\log\mathcal{L}$ comparing a fixed value to the best-fit value (denoted by dotted line).

Why are the limits worse than the previous measurements?

The best-fit flavour composition $\nu_e : \nu_\mu : \nu_\tau = 0.19 : 0.43 : 0.38$ aligns well with the previous measurement [142] of $\nu_e : \nu_\mu : \nu_\tau = 0.20 : 0.39 : 0.42$ (grey lines in Figure 7.8). However, with 4 more years of data, which includes more double cascade events, it raises the question of why the limits are not as good. The reason is quite simple, the grey contours are derived using an extended likelihood, based on density estimates by producing a large number ($\sim 10^6$ events per particle) of resimulations of 2 classified double cascades to assess the **tauness** . A dedicated algorithm (RODEO) was developed and used to compute the

[142]: Abbasi et al. (2022), *Detection of astrophysical tau neutrino candidates in IceCube*

density estimate for sparse datasets produced from these resimulations in multiple dimensions (see [198] for details). This updated likelihood can be seen as the unbinned, higher-dimensional version of evaluating the contributions of signal-like and background-like events, which was carried out in a two-dimensional binned way (just as done for the analysis presented in this thesis). Because of this, the limits one should actually compare with the previous measurement should be the one derived using *the non-extended likelihood*, which is the same likelihood and PDF setup used for this iteration of the analysis. Figure 7.10 shows such a comparison. The best-fit flavour composition $\nu_e : \nu_\mu : \nu_\tau = 0.19 : 0.43 : 0.38$ measured using this analysis (black lines) aligns well with the previous measurement of $\nu_e : \nu_\mu : \nu_\tau = 0.29 : 0.43 : 0.28$ (blue lines) using the same likelihood. Although not significantly, the limits derived from this iteration do get better along the ν_μ fraction. Only 68% limits are shown, without the likelihood space to keep the plot easy to read.

[198]: Stachurska (2020), *Astrophysical Tau Neutrinos in IceCube*

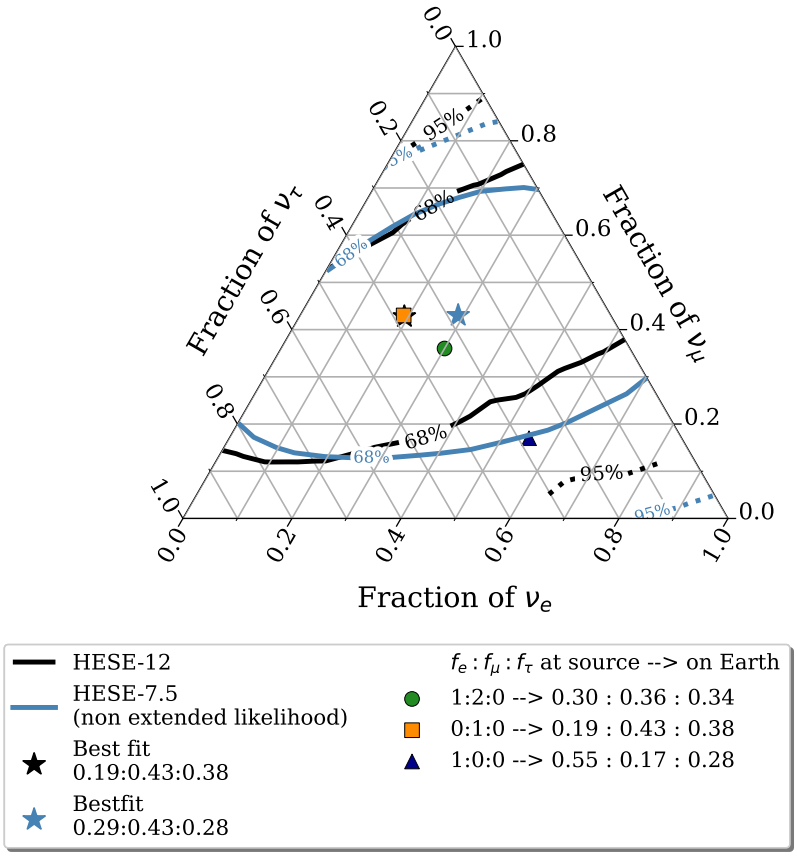

cascade originating from a ν_τ inter-

Figure 7.10: The best-fit flavour composition of 0.19 : 0.43 : 0.38 (black), using 12 years of HESE data (this work) compared with the best-fit flavour composition of a previous measurement that used 7.5 years of HESE data [142]. Comparison is shown by usingth esame likelihood formulation (none extended likelihood without resimulations, see text for details). The solid and dashed lines represent the 68% and 95% confidence regions, respectively, obtained from the χ^2-approximation using Wilk's theorem. Three flavour compositions expected at Earth from different source scenarios are also marked (3.2).

of interaction.

Sensitivity at BestFit

Please remember the following text:

The setup and all the relevant updates to the sample and selection chain for the analysis presented in this thesis were done using the best-fit values from the previous analysis. The two signal parameters that affect the flavour measurement, especially the ν_τ fraction and hence the double cascade events, are the index of the primary neutrino energy spectrum γ_{astro} (assuming a single power law) and the normalization. A harder spectrum (low γ_{astro}) leads to a higher expected flux, resulting

in more expected events, while a softer spectrum (high γ_{astro}) leads to a lower flux for samples with a similar effective area. This point was discussed in section 6.3 while discussing the sensitivity of the analysis. The analysis setup and sensitivity were shown using a spectrum with an index of 2.87, which is almost identical to the best-fit value for this analysis (2.84) assuming equal partition of the neutrino flavour ($\nu_e : \nu_\mu : \nu_\tau = 0.33 : 0.33 : 0.33$). Even though the measured flavour ratio is slightly different, the index remains quite close to what the data agrees with, and the estimated sensitivity projected much tighter constraints on 2D flavour measurements, specifically along the ν_τ axis . To understand the lack of improvement to reduce degeneracy along the ν_e/ν_τ axis, the sensitivity of the flavour measurement was first tested at the best fit.

cite sensitivity figure here

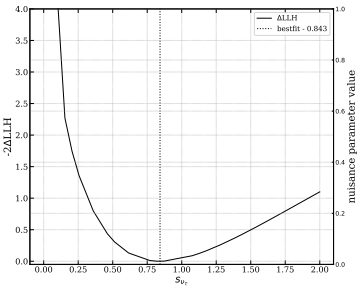

Figure 7.11: 1 dimensional profile likelihood asimov scan of ν_τ scale factor, s_{ν_τ} using **simulation** injected at bestfit point. Solid black line corresponds to the profile likelihood, defined by the likelihood ratio $-2\Delta\log\mathcal{L}$ comparing a fixed value to the best-fit value (denoted by dotted line).

[209]: Cowan et al. (2011), *Asymptotic formulae for likelihood-based tests of new physics*

The sensitivity of the bestfit analysis is demonstrated in Figure 7.12. It is determined by using an asimov dataset [209] created with the best-fit values of all signal and nuisance parameters from Table 7.4 and Table 7.3. For the sake of simplicity in comparison, a Poisson likelihood was utilized, as SAY likelihood tends to yield more conservative limits (refer to the appendix for some comparisons). The objective here is to examine the most ideal scenario. Moreover, constructing pseudotrials where data is drawn from SAY likelihood is not straightforward, therefore, to maintain consistency in comparisons, all fits depicted in Figure 7.12 are computed using Poisson Likelihood. Consequently, the 68% data limits displayed on the same plot (black line) are narrower compared to those shown in Figure 7.8. Additionally, there is a slight shift in the bestfit point. The key point here is that, given these signal parameters, the analysis is sensitive not only to measure a non-zero ν_τ fraction, but also to reject it with better significance (approximately 3σ as shown in Figure 7.11 - the 1D profile likelihood scan of s_{ν_τ} for the asimov dataset used to derive the 2D limits shown in Figure 7.12). The sensitivity results give rise to three questions:

Are data limits reliable?
The contours shown in Figure 7.8 are based on the assumption that Wilk's theorem holds. This theorem states that the $-2\Delta\log\mathcal{L}$ approximately follows a χ^2-distribution with $k = \text{dof}(\hat{\theta}, \hat{\xi}) - \text{dof}(\theta_t, \xi_t)$, where $\text{dof}(\theta, \xi)$ represents the number of free parameters in the fit. In the case of the flavour fit, there are 2 free parameters - s_{ν_e} and s_{ν_τ}. It is important to note that Wilk's theorem is only valid if the sample size is large and the model parameters are not bounded. However, the HESE sample is relatively small with only a few events passing all selection cuts. Additionally, the available Monte Carlo statistics are not large enough to provide sufficient statistics in every bin of the analysis histograms. Furthermore, the parameters are bounded as the flavour fractions cannot be negative. Therefore, it is essential to verify the validity of Wilk's theorem given these conditions.

The validity of Wilk's theorem was tested for a few points on the 68% and 95% contours. This was achieved by generating pseudo datasets, each injected with a specific flavor composition (a point on the contour), while keeping the rest of the fit parameters at their best-fit values, details of which can be found in Appendix B. Each trials are fitted twice, once with a special case of flavour fractions (the one dataset was injected with), and again by leaving all the parameters free. A likelihood ratio is constructed for each trials by taking ratio of likelihood of *the conditional fit*

(fixed flavour fractions) to *the free fit*. The distribution of the constructed likelihood ratio (Test Statsic) is compared with a χ^2 distribution with 2 degree of freedom[1]. The results agrees well with $\chi^2_{k=2}$ with minor deviations that can be explained by the fact that the two parameters of interest are correlated and hence the degree of freedom is expected to be lower than 2.

1: degree of freedom is 2 as both of the signal parameters are fixed simultaneously

Is deriving sensitivity using an asimov dataset a good choice?
The Asimov dataset is a convenient alternative to generating a large number of pseudo trials for testing a specific realization. Computing the test statistic distribution of both conditional and global best-fit values for each point in the triangle is quite expensive. It should not be assumed that the test statistic value that maximizes the likelihood of the Asimov dataset is always equal to the median of the test statistics derived from the full distribution of various pseudo experiments.

To test this, sensitivity was derived using monte carlo pseudotrials, similar to the one described before for wilks' validity, but this time the fixed point for all trials was kept at the data best-fit point, see Appendix C for details. In Figure 7.12, each point denoted with a marker "+" represents the points for which pseudo datasets were generated. Each dataset was generated by injecting the point denoted with "+" and fitted twice: once by keeping s_{ν_e} and s_{ν_τ} fixed at the data best-fit values (from Table 7.4) and once with them free. This was done to test if the true flavour fraction is what the data fit returns and with what confidence the injected point can be rejected. The result is shown in Figure Figure 7.12. The color scheme shows the confidence level each point has to reject the null hypothesis (data best-fit in this case). As can be seen, the pseudo-trial distribution matches quite well with the Asimov sensitivity. In fact, it predicts even tighter constraints compared to the Asimov case, indicating that neither data limits nor Asimov limits are unreliable.

Is the 2 dimesnional monte carlo PDF ideal for the fit to differentiate between signal and background?

Forward-folding fits, as described in section 6.1, heavily relies on the expected values for each bin of the analysis histograms. It is crucial to choose reliable variables so that the likelihood space looks different for signal and background. For this reason, the analysis variables for double cascade bins are different from those for cascades and tracks. This is because the zenith distribution of astrophysical ν_τ flux shows no significant variation between signal and background. The PDF used in this case was selected due to the correlation of the Tau decay length (L_{dc}) with the energy of the second cascade (E_2) for double cascades resulting from ν_τ-cc interactions, contributing to the population of signal events along this diagonal (see Figure 6.1). The 2D Monte Carlo PDF at best fit, shown in Figure 7.6, contains Monte Carlo events populating the bins along the diagonal. However, the data events are in regions where the background population is expected with nearly equal probability. While drawing data using poisson distribution, fluctuations around the best-fit are considered which in principle should give all possible realisations of the data events ending up in bins with high expectations [2]. Since data events are observed in bins with not so high expectations as well, it may happen that most pseudo trial histograms would end up not replicating data event distributions. Therefore, in addition to the

2: This was also the motivation behind the resimulations that were performed for the previous iteration of the analysis to measure the flavour composition

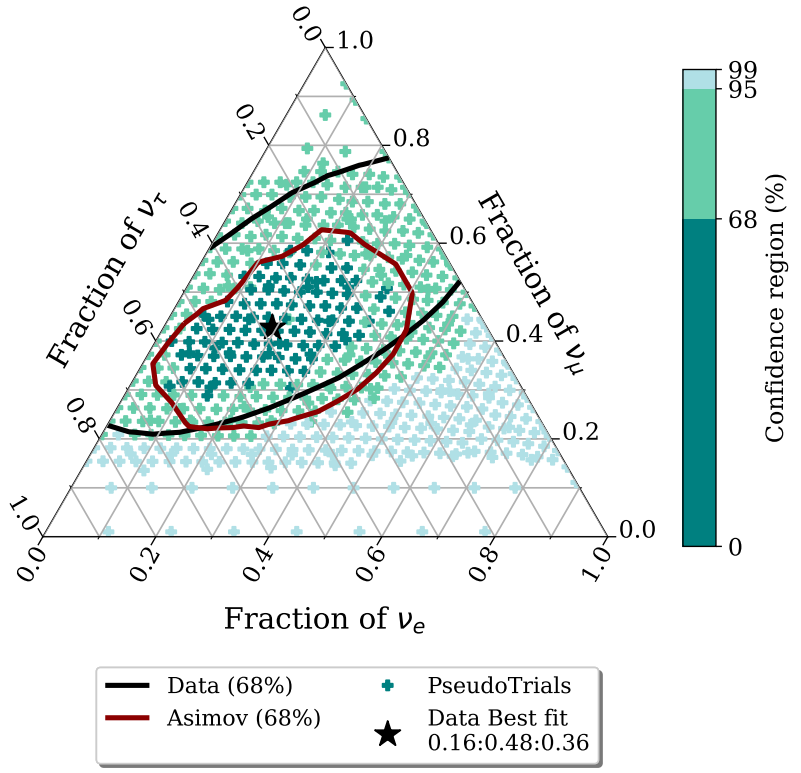

Figure 7.12: Comparison of Measured flavoured ratio (black line) with asimov sensitivity(maroon line) and pseudo trials (marked with '+'). Each + represents a pseudo dataset, drawn from flavour composition of that very point. Colorbar shows confidence intervals of each of these points, to reject the bestfit flavour composition of $\nu_e : \nu_\mu : \nu_\tau = 0.19 : 0.43 : 0.38$. All other parameters of the fit are injected at their bestfit values.

pseudotrials described earlier, the histograms produced for each trial were checked to see how often the events ended up in a region mostly occupied by background-like events.

Ideally, one would generate pseudo trials until all the Poisson-distributed events fall within the same region of the PDF as shown in Figure 7.6. However, this approach was found to be computationally expensive. For instance, each dataset displayed (around 500) in Figure 7.12 was produced from 500 trials, with each trial fitted twice. On average, each fit took approximately one hour to complete. Therefore, before proceeding, the proportion of PDFs that did not meet the cut criteria was estimated to determine whether using computational resources for further trials was justified. Several tested datasets from different regions of the triangle revealed that, for most datasets, only about 20% of the 500 trials resulted in final histograms with events concentrated in the lower energy bins. There was no feasible way to generate a sufficient number of trials to reduce statistical errors and set definitive limits. As a workaround, only the small proportion of trials that met the necessary criteria were used to generate the TS distributions, allowing an update of the sensitivity shown in Figure 7.12. This updated result is presented in Figure 7.13. As evident from the vanished points, not only were most of the trials excluded, but the confidence intervals also became significantly larger—especially along the ν_τ axis—aligning more closely with the data limits. This concludes why both asimov sensitivity and pseudo trials in Figure 7.12 showed such tight constraints. In an ideal case, one can perform resimulations of the 5 double cascade events as it was done for the previous iteration, but this would in turn increase computational resources and was beyond the timeline of work presented in this thesis, hence it was not performed.

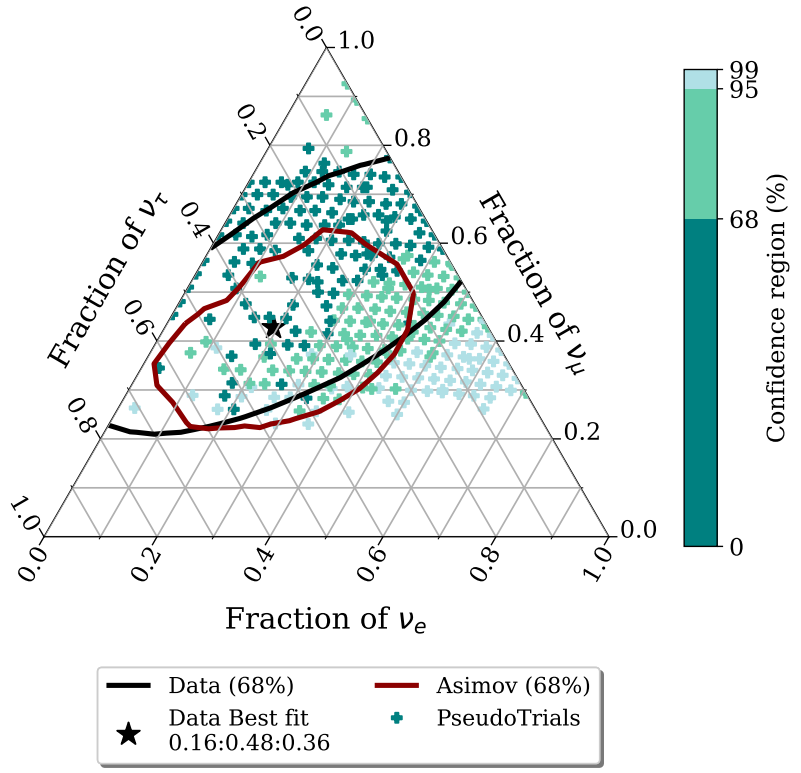

Figure 7.13: Comparison of Measured flavoured ratio (black line) with asimov sensitivity(maroon line) and pseudo trials (marked with '+'). Each + represents a pseudo dataset, drawn from flavour composition of that very point. Colorbar shows confidence intervals of each of these points, to reject the bestfit flavour composition of $\nu_e : \nu_\mu : \nu_\tau = 0.19 : 0.43 : 0.38$. Only trials with final histogram in three lower energy bins are kept in TS distribution. All other parameters of the fit are injected at their bestfit values.

7.4 Discussion

The analysis setup and particle identification methods developed and refined throughout this thesis demonstrate that IceCube is sensitive enough to measure the flavour ratios of the astrophysical neutrino spectrum and set tight constraints. However, more robust techniques, particularly for reconstructing double-cascade events, are needed to produce more reliable Monte Carlo PDFs for these fits. Regarding the measured flavour ratio, as shown in Figure **??**, although the best fit suggests neutrinos are produced by the muon-damped scenario at high-energy sources, no other source scenarios can be excluded with high significance. The neutron beam scenario ($\nu_e : \nu_\mu : \nu_\tau = 1 : 0 : 0$ at the source, evolving to 0.55:0.17:0.28 on Earth) is disfavored by approximately 1σ but remains consistent at 2σ.

A specific measurement of the neutrino energy spectrum was not part of the analysis presented here, as the focus was primarily on flavour measurement, with efforts directed toward improving particle identification. Nonetheless, the HESE sample could also be used to measure, and potentially search for, spectral features. Recent independent studies have discovered a spectral break in the neutrino spectrum at around 30 TeV, softening the spectrum at higher energies, which is within the range of this analysis [134, 218]. This finding offers insight into why previous measurements targeting different energy ranges produced significantly different spectral indices for a single power-law spectrum [131–133]. Since the HESE sample focuses on high-energy events, where no such spectral features have been observed, and has much lower statistical power than those other samples, no spectral feature searches were attempted during this thesis work.

[134]: Naab et al. (2023), *Measurement of the astrophysical diffuse neutrino flux in a combined fit of IceCube's high energy neutrino data*

[218]: Basu et al. (2023), *From PeV to TeV: Astrophysical Neutrinos with Contained Vertices in 10 years of IceCube Data*

[131]: Abbasi et al. (2022), *Improved Characterization of the Astrophysical Muon–neutrino Flux with 9.5 Years of IceCube Data*

[132]: Aartsen et al. (2020), *Characteristics of the Diffuse Astrophysical Electron and Tau Neutrino Flux with Six Years of IceCube High Energy Cascade Data*

[133]: Abbasi et al. (2021), *IceCube high-*

A less model-dependent approach to describing the astrophysical neutrino flux is the differential unfolding of the energy spectrum. This method divides the flux into energy bins, where each bin is fit independently with a constant $\sim E^{-2}$ spectrum, rather than assuming a continuous power-law across the entire energy range. Ideally, this unfolding would be performed separately for each neutrino flavour to avoid assuming a uniform spectral shape for all flavours. Measuring the flavour composition as a function of energy would also be valuable, as neutrino production processes are energy-dependent. However, due to the limited statistical power of the current dataset, meaningful results could not yet be obtained.

Finally, improvements in reconstruction methods and more data are necessary for future experiments to shed more light on flavour measurements. Double-cascade reconstruction currently has an upper energy limit, as higher-energy events are only partially contained within the detector due to their geometry. In addition, improved detection hardware could provide better information on photon charge and direction, enhancing the overall reconstruction process. These points, along with the potential for a proposed new generation of neutrino detectors, will be discussed in detail in the next chapter.

Sensitivity of IceCube-Gen2 to measure flavour composition of Astrophysical Neutrinos

8

This chapter details the sensitivity studies performed for *The IceCube Gen2 detector*. A siginificant portion of this thesis work was dedicated to assess and derive sensitivity to measure the flavour composition of Astrophysical Neutrinos for IceCube Gen2. The detector will be introduced in the following sections, along with the simulations and software framework used to produce the results.

8.1 IceCube Gen2

IceCube-Gen2 is a proposed next generation of neutrino detector, designed to observe the neutrino sky within a wide energy range, from TeV to EeV [219]. Its sensitivity is expected to be at least five times better than IceCube, enabling the observation of individual sources. The instrument layout is designed to detect about ten times more neutrinos annually as compared to IceCube. This increased capability will facilitate in-depth studies of neutrino distribution across the sky, energy spectrum, and flavor composition and beyond standard model physics.

[219]: Aartsen et al. (2021), *IceCube-Gen2: the window to the extreme Universe*

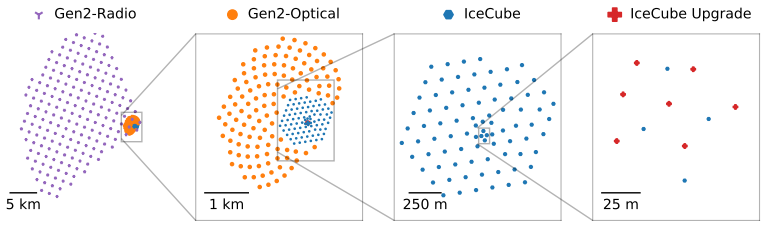

Figure 8.1: Figure depicts the proposed IceCube-Gen2 Neutrino Observatory facility at the South Pole. It includes (from left to right) (i) a radio array with 200 stations, (ii) 120 new in-ice strings, spaced 240 m apart (shown as orange points), as an expansion of (iii) current optical array, (iv) 7 strings of IceCube upgrade, to be deployed soon within currrent in-ice DeepCore volume. Figure taken from [219]

Figure 8.1 illustrates a top view of the IceCube-Gen2 facility, showcasing its various components using optimized technologies for the targeted energy ranges.

The IceCube Upgrade will start deployment this season. Its goal is to lower the detection threshold for neutrinos to 1 GeV (In-line with its predecessor, *DeepCore* in current IceCube)[220]. This improvement will advance oscillation measurements, dark matter searches, and studies of physics beyond the Standard Model. The IceCube Upgrade project will also deploy 693 new types of multi-PMT detector modules, providing an opportunity to test the optical sensor technology for the IceCube-Gen2 observatory.

[220]: Ishihara (2021), *The IceCube Upgrade - Design and Science Goals*

The surface array of IceCube-Gen2 is a unique setup where the surface array measures the electromagnetic shower component and low-energy muons, while the optical array detects TeV and potentially PeV muons from the same air shower [221]. Planned to be used similarly as *IceTop* of IceCube, the stations shall be placed on top of the additional *in-ice* strings of optical array. It can also be used as *surface veto* to reduce the background of atmospheric muons in samples of astrophysical neutrinos from the southern sky.

[221]: IceCube Collaboration et al. (2024), *IceCube-Gen2 Surface Array: Science Case and Plans*

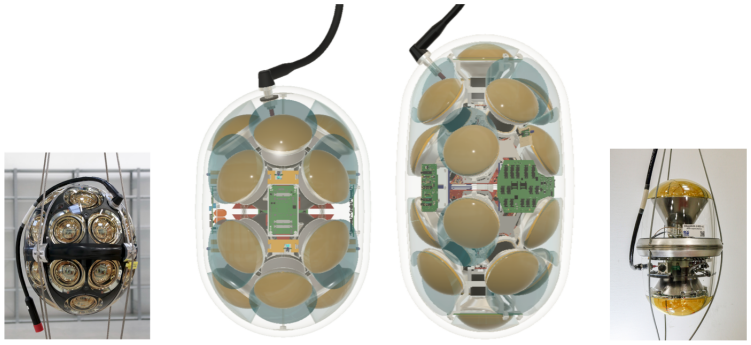

Figure 8.2: The designs of the IceCube-Gen2 optical sensors, DOM-16(second) and DOM-18 (third) with their base designs, to be used in the IceCube Upgrade sensors, are the mDOM on the left and D-Egg on the right [224]

The Radio array aims to discover and characterize high-energy neutrino flux above 10 PeV. It detects nanosecond-scale radio emissions from ultra-high-energy particle showers using the Askaryan effect [222, 223]. This technique is sensitive to energies above PeV and complements the energy range of the optical array by capturing radio emissions from neutral and charged-current interactions, as well as energy losses of secondary leptons.

The optical array The optical array will be expanded with the addition of 120 new strings to the existing IceCube strings. The strings will be arranged in what is referred to as "sunflower geometry," with an average horizontal spacing of 240 meters. The shape of the array and spacing between the strings will be determined through dedicated geometry optimization studies. Each string will contain 80 modules, resulting in a total of 9600 new modules. These modules will be placed between 1325 meters and 2575 meters below the surface, with a vertical spacing of 16 meters. This configuration will create an instrumented geometric volume of 7.9 cubic kilometers. The modules on the string are expected to collect nearly three times the number of photons gathered by an IceCube digital optical module (DOM).

[222]: Askar'yan (1961), *Excess negative charge of an electron-photon shower and its coherent radio emission*
[223]: Meyers et al. (2021), *Radio Detection of EeV Neutrinos in Dielectric Media using the Askaryan Effect* *for Babies*

cite TDR link here? or is whitepaper ok?

For the sensitivity study presented in this thesis, only the optical part of the proposed detector was simulated and used.

8.2 Simulation

To perform this sensitivity study, dedicated simulations were carried out. The study aims not only to assess the sensitivity of IceCube-Gen2 in measuring the flavor composition of astrophysical neutrinos but also to evaluate its capabilities in detecting tau neutrino events, which is a crucial component as described in **??**. The simulations were aligned with the mainline IceCube simulations (detailed in **??**) to enable direct comparisons. However, necessary modifications were made to account for the new-generation optical sensors to be used in IceCube Gen2 and the sparser geometry. The following sections will describe the event samples created using these simulations to conduct the sensitivity analysis.

cite the simulation section here and not the chapter

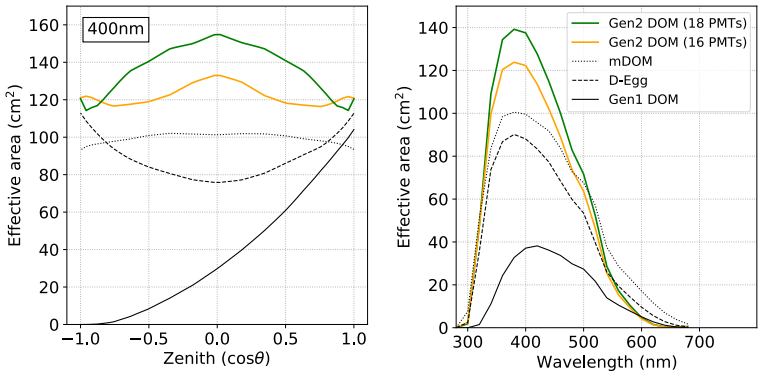

Figure 8.3: The effective area is compared for IceCube-Gen2 DOM candidates, 16, and 18 PMT models, in relation to IceCube-Gen1 DOM (pDOM), D-Egg, and mDOM, as functions of zenith angle (left) and wavelength averaged over solid angle (right). Figure taken from [224]

8.2.1 Isotropic Sensor

The optical sensors to be used in the IceCube-Gen2 project depends a lot on how well the reference optical sensors to be deployed in the IceCube upgrade perform.[224]. The designs have been carefully optimized to balance cost-effectiveness, logistical efficiency, and enhanced performance. Figure 8.2 shows both the 16 and 18 PMT modules, which are being considered to use in IceCube Gen2, along with **mDOM** (*multi PMT Digital Optical Module*) [225, 226] and **D-Egg** (*Dual optical sensors in an Ellipsoid Glass for Gen2*) [227] that are to be deployed in ice for IceCube Upgrade.

[224]: "Abbasi et al. (2023), *The IceCube Gen2 Technical Design Report*

[225]: Classen et al. (2017), *The mDOM - A multi-PMT digital optical module for the IceCube-Gen2 neutrino telescope*

[226]: Classen et al. (2019), *A multi-PMT Optical Module for the IceCube Upgrade*

[227]: Abbasi et al. (2023), *D-Egg: a dual PMT optical module for IceCube*

The maturity of the design, along with extensive in-situ testing using a large number of sensors for the IceCube Upgrade, leads us to consider the mDOM-type sensor as the baseline for evaluating the IceCube Gen2 detector's capabilities in identifying Tau neutrino-induced Double Cascade events. Unlike IceCube's single large 10" PMT, the mDOM consists of 24 smaller 3" PMTs. The key advantages of the mDOM over pDOM [228] are its 2.2 times higher effective photocathode area, omnidirectional sensitivity, and the directional information obtained from the individual "pixels" (the 24 PMTs). Due to the large number of PMTs and their strategic placement within the module sphere, this module offers nearly isotropic angular acceptance, unlike IceCube DOMs with only one downward-facing PMT.

pDOM

pDOM stands for PINGU Digital Optical Module. It was first coined for an R&D upgrade of IceCube DeepCore called **PINGU** (The Precision IceCube Next Generation Upgrade) [228].

[228]: "Aartsen et al. (2014), *Letter of Intent: The Precision IceCube Next Generation Upgrade (PINGU)*

did this project eventually become Upgrade?

The effective area of the optical modules is the equivalent physical cross-section that would detect all the incident photons from a plane perpendicular to a given direction. As illustrated in Figure 8.3 (Left plot) , the mDOM has a nearly linear effective area for collecting photons from all directions, unlike the Gen1 DOMs (pDOMs) which have a downward-facing PMT. As a result, the effective area for pDOMs increases as the arrival direction shifts from 180 degrees ("down-going" in the IceCube coordinate system) to 0 degrees ("up-going" in the IceCube coordinate system).

reproduce this figure, without the right plot

However, current sophisticated methods do not yet provide a full-scale simulation of a multi-PMT module, so a simulated sensor called *iso-pDOM* (isotropic-pDOM) was developed [229]. This sensor can be thought of as a 'spherical PMT' encased in a glass vessel similar to an IceCube DOM but with 2.2 times higher quantum efficiency, capable of capturing photons arriving from all the directions (see Figure 8.4). The sphere was simulated by assuming an upward-facing PMT along with a downward

[229]: Omeliukh (2021), *Optimization of the optical array geometry for IceCube-Gen2*

cite Evangelia's Summer school report?

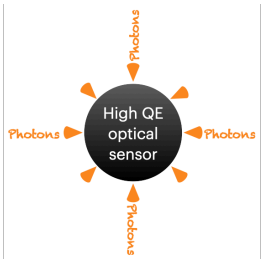

Figure 8.4: Conceptual representation of Simulated sensor with isotropic angular acceptance (iso-pDOM)

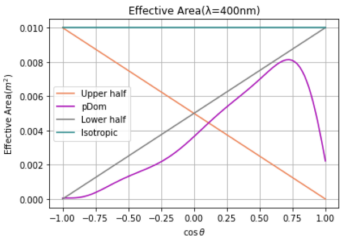

Figure 8.5: Results of simulating a sensor that *mimics* the behaviour of a typical mDOM. The blue line shows changed effective area of the so-called *isopDOM*, achieved by combining acceptance curves of pDOMs having a PMT in "upper" (orange) and "lower" (grey) halves of the DOM respectively

many references from chapter 4 need to be cited correctly in this section

one and combining the results while maintaining the same area under the curves at all wavelengths . The resultant iso-pDOM has an effective area very similar to that of an mDOM.

8.2.2 Event Selection

Monte Carlo events were produced using the so-called isoPDOM for all three flavors of primary neutrinos with energies ranging from 100 TeV to 50 PeV. The simulation chain is identical to that described in **??**. It is important to note that since the IceCube in-ice array is inherently part of the proposed Gen2 detector, all simulated events still include 'hits' from the IC86 configuration. Additionally, during the DetectorSim stage of the simulation chain, where PMT responses, noise, etc., are added, responses are incorporated separately for IceCube DOMs and isoPDOMs. If an event passes all the basic triggers, two separate triggers are stored depending on the event location: IC86 and ICGen2. By default, ICGen2 has a combined response of both detector configurations, while IC86 only contains current IceCube volume events. This feature is crucial as it facilitates direct comparison of events produced with IceCube simulations for IceCube-only analyses.

As discussed in analysis chapter, a fundamental aspect of flavor measurement studies is the ability to identify the flavor of the neutrino involved in an interaction. This identification is possible due to the distinct by-products produced by different neutrino interactions, which result in unique light deposition patterns, or "morphologies" reco chapter. These patterns, illustrated in cite morphology figures, allow us to reconstruct the events by analyzing the morphology of the light deposited in the detector. By doing so, the flavor of the original interacting neutrino can be determined.

To utilize the same particle identifier used in the analysis presented in analysis chapter for this sensitivity study, a dedicated event selection process for high-energy starting events (HESE) was implemented, similar to the approach described in reco chapter. However, since the outer-layer detector veto is specific to the detector geometry and the characteristics of the DOM pulses—which is still under development for the IceCube-Gen2 simulation chain, starting events were selected by examining the interaction vertex of the primary neutrino. This interaction vertex was further refined by considering the deposited charge (measured in single photoelectrons) and calculating the charge-weighted mean positions. This charge information is crucial for applying a HESE-like charge cut. Unlike the 6000 photoelectrons threshold used previously, the threshold for this analysis was set at 2000 photoelectrons. The lower threshold is due to the higher quantum efficiency and isotropic sensitivity of the new sensors, which enhance the detection capability for high-energy events. All the approximations made were in parallel checked for IC86 configuration to reproduce MonteCarlo PDFs within statstical erros to the ones presented in analysis chapter.

Moreover, to appropriately weight the simulated events and account for the probability of an atmospheric neutrino being rejected by an accompanying muon triggering the veto, a dedicated calculation similar to the one used in the HESE-7.5 analysis [133] was used. Additionally,

[133]: Abbasi et al. (2021), *IceCube high-energy starting event sample: Description and flux characterization with 7.5 years of data*

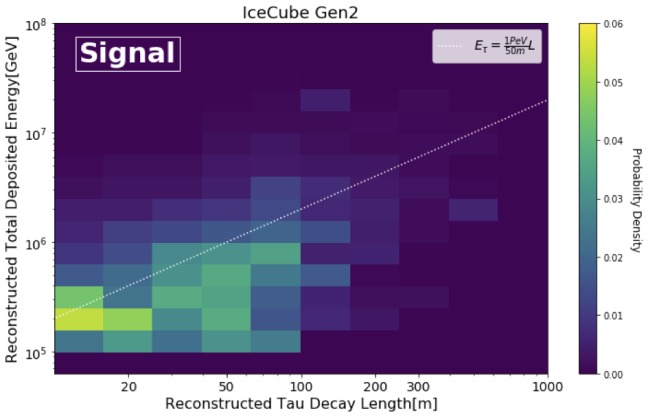

(a) Double Cascades from ν_τ interactions (signal). The signal double cascades show a correlation between (L_{dc}) and (E_{tot}).

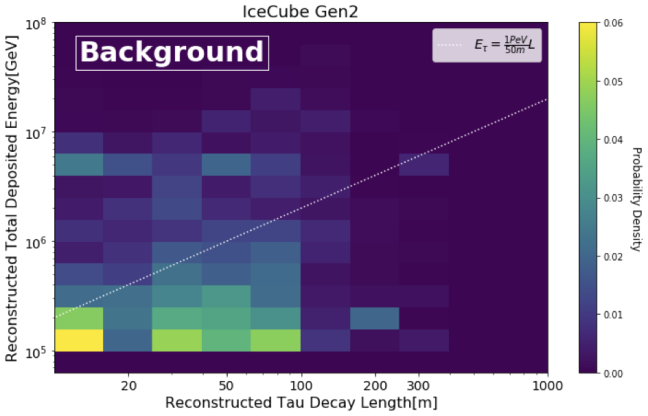

(b) Double Cascades from ν_e and ν_μ interactions (background). The background contributions do not show any correlations, but rather clusters at low L_{dc} and E_{tot}.

Figure 8.6: Total reconstructed energy (E_{tot}) versus reconstructed double cascade length (L_{dc}) for events classified as double cascades.

the reconstructed energy cut, initially set at 60 TeV, was adjusted to 100 TeV. This adjustment was based on the signal-to-background probability density functions (see Figure 8.6a and Figure 8.6b) to ensure a similar signal-to-background ratio (2:1) as achieved in the HESE-7.5 analysis [142] and the HESE-12 analysis (). After applying all the necessary filters, the final sample includes starting events with a reconstructed deposit energy of 100 TeV or more and a charge exceeding 2000 PE. These events originate from interactions of all six types of neutrinos (particle and antiparticle versions of 3 flavors) beginning within the simulated IceCube-Gen2 fiducial volume. They are divided into three categories: Tracks, Single Cascades, and Double Cascades.

[142]: Abbasi et al. (2022), *Detection of astrophysical tau neutrino candidates in IceCube*

cite analysis chapter

8.3 Analysis tool : `toise`

Understanding and enhancing the sensitivity of the detector can result in more precise and dependable performance, thus improving the scientific impact of the experiment. The main goal of the sensitivity studies carried out in this work is to optimize the design of the detector in order to be capable of reconstructing tau neutrino events using existing methods but with a larger detection volume and new generation optical sensors. Additionally, one can also assess the performance of the detector against

theoretical model [230] by combining both radio and optical arrays of the proposed detector to investigate flavor measurements in the energy ranges from TeV to EeV [231].

[230]: Bustamante et al. (2015), *Theoretically Palatable Flavor Combinations of Astrophysical Neutrinos*

[231]: Coleman et al. (2024), *The flavor composition of ultra-high-energy cosmic neutrinos: measurement forecasts for in-ice radio-based EeV neutrino telescopes*

[232]: Santen et al. (2022), *toise: a framework to describe the performance of high-energy neutrino detectors*

It's impractical to run comprehensive simulations for evolving detector designs due to the large amount of computing power required. The `toise` [232] framework was created to estimate sensitivity using a simplified model of the detector response based on targeted Monte Carlo (MC) simulations. This allows for efficient comparisons of different detector designs without repeating the entire simulation process. `toise` was used for a sensitivity study presented in the next section. This section will provide a brief overview of its workflow. In order to distinguish the influence of design choices on detector performance from the intrinsic restrictions imposed by neutrino interaction physics, the event rate calculation in this framework is conducted through two distinct stages: Neutrino Physics and Detection.

In the Physics stage, the neutrino fluxes at the Earth's surface are converted to the detector's area or volume. This involves using a transfer tensor to model the conversion between the initial neutrino flavor states and the observable final states (muons, hadrons, etc.). In addition, various aspects of neutrino interactions, including neutrino-nucleon cross-sections and different interaction types (neutral current or charged current) are also taken into account. The transfer tensor is subsequently combined with the final-state effective area to establish a neutrino effective area. The effective area $A_{\text{eff}}(E, \theta)$ of the detector is calculated by multiplying the geometric area $A_{\text{geo}}(\theta)$ with an energy and zenith-dependent efficiency $\eta(E, \theta)$:

$$A_{\text{eff}}(E, \theta) = A_{\text{geo}}(\theta) \times \eta(E, \theta) \tag{8.1}$$

For the optical array of the proposed IceCube-Gen2, the geometric area is approximately calculated by placing a convex hull around the instrument's geometric boundary. ***The selection efficiency*** $\eta(E, \theta)$ characterizes the detector's triggering efficiency and the probability of an event passing a set of analysis criteria. It is defined as *the ratio of events passing these cuts to the number of events generated*. Depending on the type of sensitivity study being performed—such as expected limits, discovery potential, or flavor measurement—additional parameterizations like energy and angular resolutions and classification efficiency are used. For flavor measurement, ***the classification efficiency*** generates an event classification smearing matrix (Figure **??**) and is defined as *the fraction of topology per energy bin for a given neutrino flavor*. When estimating sensitivities, it is essential to account for backgrounds that may mimic the signal. The framework handles backgrounds by either adding their contributions to the event rate or ignoring regions where they are expected to contribute. For all detectors and science cases, atmospheric neutrino flux is added as a background using the same effective area as for astrophysical neutrinos. Optionally, atmospheric neutrino flux in the downward-going region can be reduced to account for vetoing by accompanying muons from the same air shower.

perhaps a block diagram/-dummy figure to show the whole flow on the side?

more discription will be there in analysis chapter for HESE12, if not, make this more detailed?

8.4 Result of Flavour Sensitivity Measurements

Using the HESE-like sample, described in 8.2.2, a detector response tensor is generated using `toise`. Selection efficiency, detailed in 8.3, is a key factor in generating the detector's neutrino effective area. This efficiency is determined using Figure **??**, which shows the true deposited energy at which the analysis starts to select events. The plot illustrates the ratio of events passing all selection cuts in 8.2.2 to all simulated neutrinos reaching the fiducial volume, per energy bin. The curve is fitted, and the resultant plot shows that neutrinos are selected starting from approximately 200 TeV. This value is used as the selection threshold for events beginning or contained in the fiducial volume.

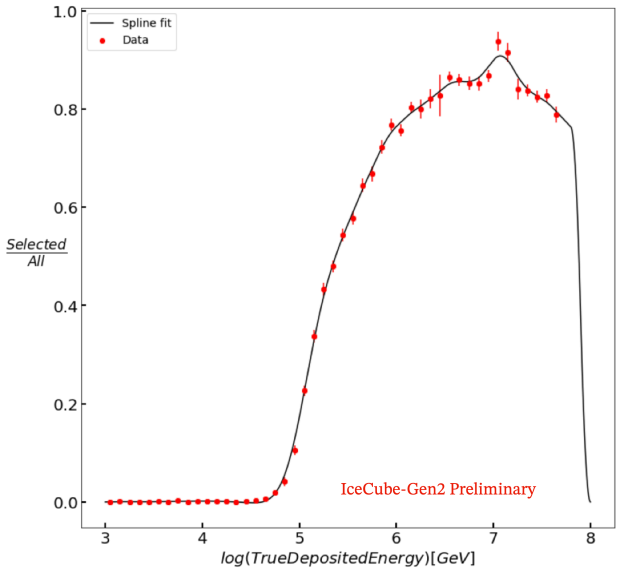

Figure 8.7: Selection Efficiency : Ratio of neutrinos that got classified into a topology to all the neutrinos that interacted in active volume. Data here refers to monte-carlo events per energy bin.

A specific parameterized tensor is used to determine the efficiency of particle identification during flavor measurements. Figure 8.8 shows how well the reconstruction process can identify different types of particles based on their shapes. In an ideal scenario, events involving charged current interactions with electron neutrinos (ν_e) are classified as single cascades, those involving muon neutrinos (ν_μ) as tracks, and those involving tau neutrinos (ν_τ) as double cascades (all neutral current events appear as single cascades, as explained in). The diagonal elements of the plot show how accurate the classifier is, while the off-diagonal elements indicate the fractions of misidentified flavors. The plot shows that as the true deposited energy increases, the number of double cascade events (from ν_τ interactions) initially plateaus and then decreases. This occurs because at higher energies, the individual energy depositions are further apart (due to correlation of L_{dc} and E_{tot}), making it easier for the reconstruction process to distinguish them apart. However, at even higher energies, one of the cascades may be partially or completely outside the detector, causing these events to be misclassified as single cascades due to strict containment criteria (). For single cascades involving ν_e, the efficiency decreases at high energies because some DOMs may become saturated, and their data is excluded from the analysis. In contrast, the efficiency for starting tracks remains relatively consistent across the entire energy range.

chapter 4 section 2

see reco section

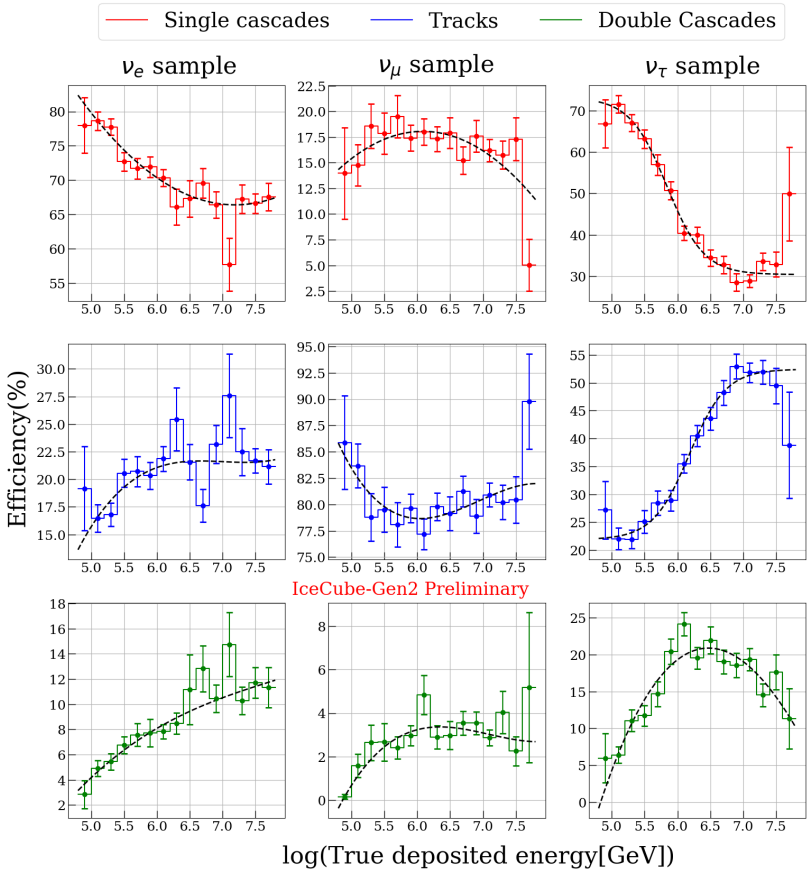

Figure 8.8: Classification Efficiency: Three subplot columns are true neutrino flavors, where each energy bin (true Monte Carlo energy) contains the fraction of topologies, summing to 100%. Diagonal plots show the flavor identification efficiency of the classifier, whereas off-diagonal plots show misidentification fractions.

Lastly, a significant advantage of `toise` is its ability to combine different event selections and detector types. The starting event sample from this detailed study can be combined with the efficiencies of through-going tracks (see Chapter 4). In toise, these efficiencies are included by extrapolating IceCube analysis limits [131] to calculate angular resolutions, PSF, etc. The flavor measurement presented here demonstrates the sensitivity of IceCube Gen2 by combining starting events with through-going muons, a method already realized and updated in IceCube [217].

Figure 8.9 shows the projected flavor measurement sensitivity of IceCube-Gen2 with 10 years of data [233]. The Asimov dataset assumes equal partition of all flavors, with a diffuse neutrino spectrum following a single power-law with an index of 2.5 and a per-flavor normalization of 2.3 [127]. It is worth to note that systematic errors are excluded from this study. Figure 8.10 illustrates the sensitivity change if no dedicated ν_τ identifier is used in the starting event sample, resulting in the sample containing only single cascades and tracks, making it impossible to resolve the ν_e and ν_τ fraction degeneracy.

[131]: Abbasi et al. (2022), *Improved Characterization of the Astrophysical Muon–neutrino Flux with 9.5 Years of IceCube Data*

[217]: Lad et al. (2023), *Summary of IceCube tau neutrino searches and flavor composition measurements of the diffuse astrophysical neutrino flux*

[233]: Lad et al. (2023), *Sensitivity of IceCube-Gen2 to measure flavor composition of Astrophysical neutrinos*

[127]: Aartsen et al. (2015), *A combined maximum-likelihood analysis of the high-energy astrophysical neutrino flux measured with IceCube*

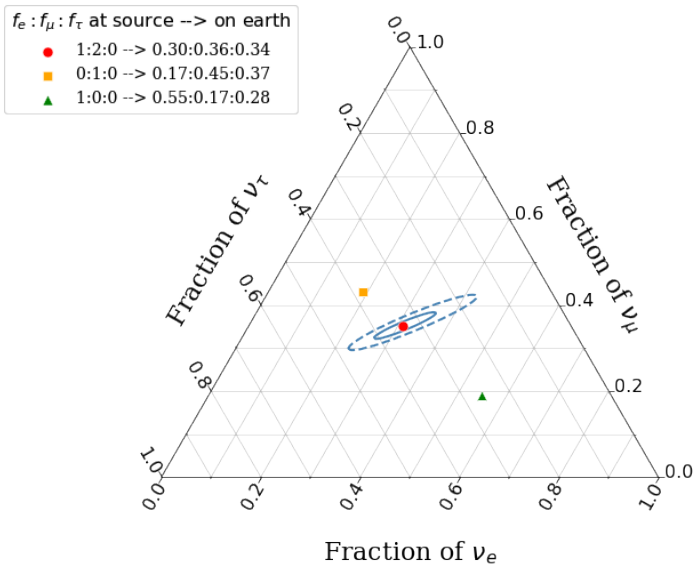

Figure 8.9: Projected sensitivity of IceCube-Gen2 to measure flavor composition of Astrophysical neutrino with 10 years of its lifetime. The dashed (solid) outlines depict the corresponding 99% (68%) constraints.

The sensitivity shown in Figure 8.9 and Figure 8.10 applies to the entire diffuse neutrino spectrum. With this study, flavour measurement for a given 'slice' of energy was also done to see if it has any dependence on it. Diffuse neutrinos originate from various high-energy sources in all directions. Depending on the environments of the acceleration sites (magnetic fields, accretion disks, dust, etc.), the production ratios of neutrinos at the sites may differ . The most commonly assumed model, described in Chapter 1, Section 4, is the pion decay scenario.

add proper citations here

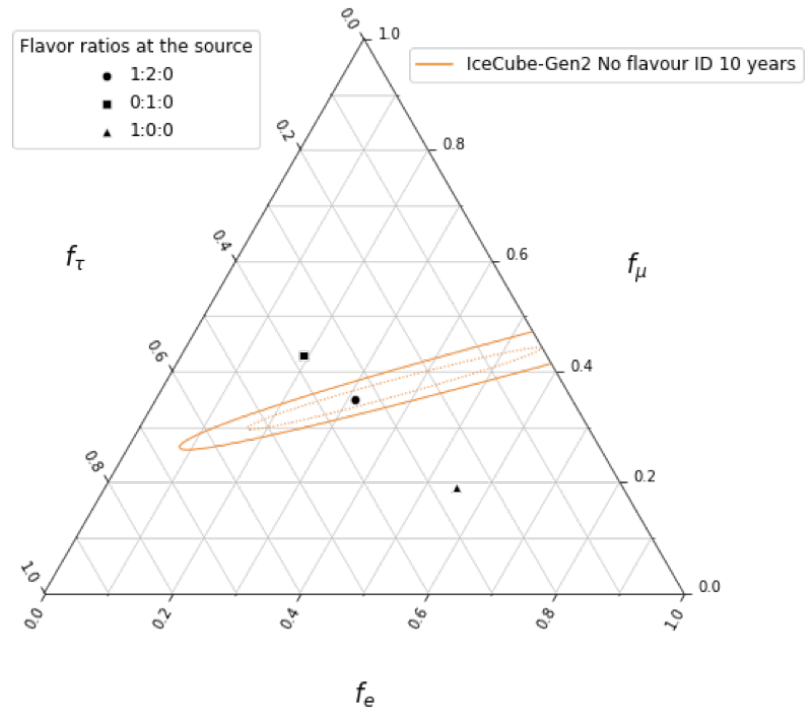

Figure 8.10: Projected sensitivity of IceCube-Gen2 to measure flavor composition of Astrophysical neutrino with 10 years of its lifetime, without a dedicated ν_τ identifier. The dashed (solid) outlines depict the corresponding 99%

combine Figure 8.9 and Figure 8.10 in 1 figure

Above a critical energy, however, the flux of electron neutrinos is suppressed due to strong magnetic fields, leading to muon damping [230] . This changes the neutrino production ratio ($\nu_e : \nu_\mu : \nu_\tau$) from 1:2:0 to 0:1:0. If such sources dominate the overall flux above a certain energy, a

[230]: Bustamante et al. (2015), *Theoretically Palatable Flavor Combinations of Astrophysical Neutrinos*

reference the muon-damped scenario, detailed in Chapter 1, Section 4

transition in measured neutrino flavor fluxes can be observed. Figure 8.11 shows IceCube-Gen2's sensitivity to detecting such a flavor transition. The assumed "critical energy" for this mechanism for the study is 2 PeV. This transition is detectable with IceCube-Gen2 due to its extended energy range, enabled by its approximately eightfold increase in volume [224].

[224]: "Abbasi et al. (2023), *The IceCube Gen2 Technical Design Report*

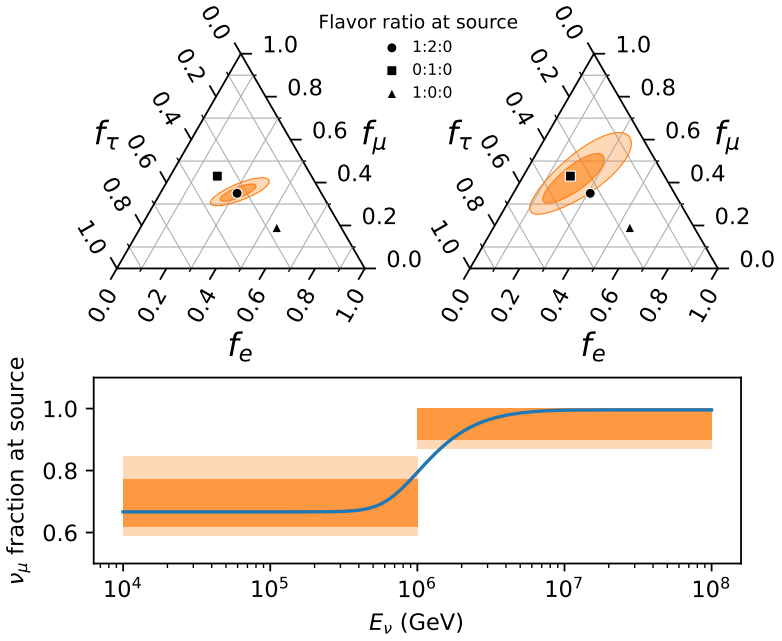

Figure 8.11: The bottom section displays the proportion of ν_μ at the source based on energy, with the assumption that the muon critical energy is 2 PeV. The error bars represent the 68% confidence level limitations on the ν_μ fraction below and above 1 PeV, derived from the observed flavor composition of ν_μ at Earth using IceCube-Gen2 and assuming standard oscillations. In the upper sections, the dark (light) shaded regions depict the corresponding 68% (99%) constraints, without making any assumptions about the mixing matrix.

9 Summary and Outlook

Appendix

A

Mean SPE Charge Distribution of DOMs

One of the stages of the unblinding stage of the analysis presneted in Chapter 7 involved a strong Data-Monte Carlo disagreement between obsreved and expected number of Doubel Cascade events when DeepCore DOMs were included in the analysis. While DeepCore DOMs have been excluded from the previous iterations of this analysis [164, 198] due to the bias they bring to `millipede` based reconstructions used in this analysis (see Section 5.3), recent modifications in the simulations made it possible to use them again. Nevertheless, the access of observed double cascade events in 7.5 years of HESE data, initiated a series of detailed checks to understand the root of the problem, *Why is inclusion of the DeepCore DOMs causing a Data/Monte Carlo mismatch?*. The following section describes some issues observed in regards to single photoelctron (spe) charge templates used in simulation and data, that are used in `millipede` to calculate the observed light yield of the event. This work was done in collaboration with Jakob Van Santen*.

[164]: Usner (2018), *Search for Astrophysical Tau-Neutrinos in Six Years of High-Energy Starting Events in the IceCube Detector*

[198]: Stachurska (2020), *Astrophysical Tau Neutrinos in IceCube*

In the Monte Carlo processing chain described in Section 5.1, at the Detetcor Simulation stage, the acceptance of a photon arriving at a Digital Optical Module (DOM) and the charge assigned to it are determined by several key factors. The acceptance is influenced by the global DOM efficiency, which scales the overall probability of photon detection, as well as the relative DOM efficiency, which accounts for variations in performance among individual DOMs. Additionally, angular acceptance curves are employed, which consider the interaction location and the angle of the photon relative to the DOM surface. This multi-faceted approach ensures a more accurate representation of the photon acceptance process. [1] To enhance the charge assignment, the new Single PhotoElectron (SPE) Templates (right panel of Figure A.1) have replaced the previous method (left panel of Figure A.1) of sampling from the general TA0003 charge distribution [234]. Each DOM now features a uniquely measured in-ice charge distribution, which is stored in the Geometry, Calibration, and Detector (GCD) file. This distribution is characterized by the sum of two exponential functions and a Gaussian, accurately reflecting the single-photoelectron response. Furthermore, the SPE Templates incorporate a global residual correction, a DOM efficiency scaling factor, and a charge scaling factor to account for shifts observed between processing passes. This comprehensive methodology enables the DOM Launcher to assign a charge that more accurately represents each DOM's behavior in the detector simulation.

1:

Note that High QE DeepCore DOMs exhibit a distinctly different shape compared to non-DeepCore DOMs, leading to a mean charge that is 3.6% lower than that of NQE DOMs. To account for this difference, the compensation factor is adjusted to be 3.6% higher (effectively resulting in a 3.6% higher Relative DOM Efficiency, or RDE), ensuring that the total charge collected remains consistent following the implementation of the SPE Templates.

[234]: Aartsen et al. (2020), *In-situ calibration of the single-photoelectron charge response of the IceCube photomultiplier tubes*

While this update has been implemented in the simulation used for the analysis presented in this thesis, which employs the updated Single

* DESY - Deutsches Elektronen-Synchrotron Platanenallee 6, D-15738, Zeuthen

email : jakob.van.santen@desy.de

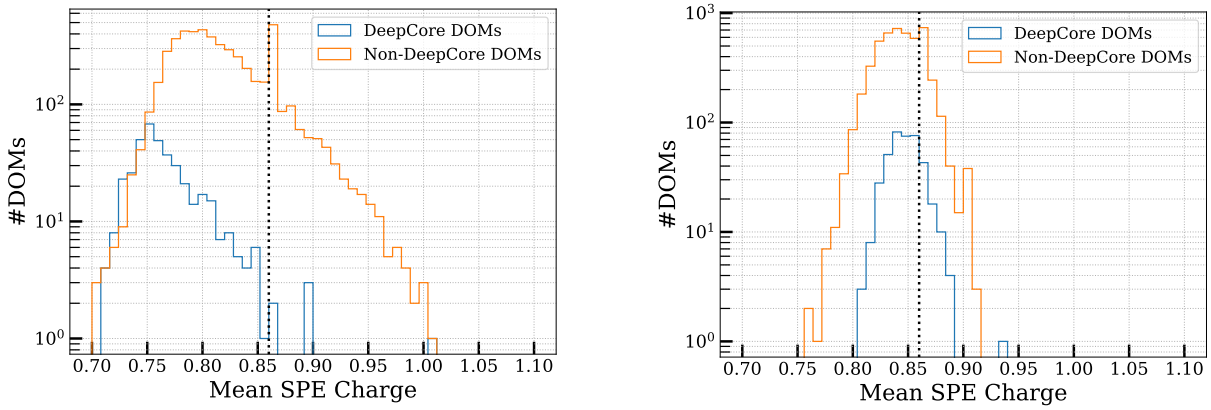

Figure A.1: Distribution of the Single Photoelectron (spe) charge distribution for DOMs, shown separately for High Quantum Efficiency DeepCOre DOMs (blue) and for rest of the DOMs (orange). The vertical line shows the average SPE charge per DOM, after applying the compensation factor. Left Panel shows the old distribution, and right panel shows the updated distribution.

PhotoElectron (SPE) template (see Figure A.2), the corresponding data files were not updated with this new parameterization until 2023. The Data GCD files still contained the parameterization based on the old template, as illustrated in the left panel of Figure A.1. The figures show the distribution of mean SPE charge for both DeepCore and Non-DeepCore DOMs. Notably, the old template reveals a significantly larger deviation (greater than 10%) for DeepCore DOMs compared to Non-DeepCore DOMs, which display only about a 5% deviation. This occurs against a backdrop where the mean SPE charge is approximately 0.85, where we define 1 PE as the mean of the Gaussian component of the SPE charge distribution. It's important to note that while this value represents 1 PE, the distribution is not purely Gaussian and includes a population below the valley, leading to an average value of less than 1.

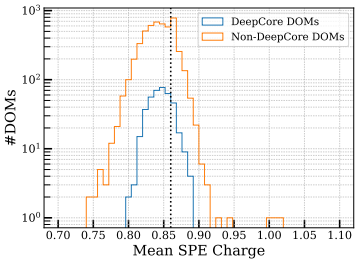

Figure A.2: Distribution of the Single Photoelectron (spe) charge distribution for DOMs used in Simulation. See caption of Figure A.1 for details.

The lack of observation of this effect in previous iterations of the analysis can likely be attributed to the fact that these variations are primarily observed in DeepCore DOMs, which were initially excluded from the analysis. The 5% difference observed among Non-DeepCore DOMs can be effectively compensated for by the DOM Efficiency nuisance parameter, denoted as η_{domeff}, which is incorporated in the fit and allowed to vary within 10% of its nominal range. While it remains inconclusive whether the excess of observed double cascades was due to the inaccurate parameterization of the SPE template, it is evident that updating all existing GCD files for the data would be necessary to substantiate this claim, a task that lies beyond the scope of this thesis work. The study ultimately concludes that, for the sake of achieving better Data-Monte Carlo agreement, a straightforward solution would be to remove the DeepCore DOMs from the reconstruction process. This approach simplifies the comparison between the SPE template distributions available for the Data (left panel of Figure A.1) and the one utilized in the simulation (see Figure A.2).

B

Validity Of Wilks' Theorem

Throughout this thesis, the results (Chapter 7) and sensitivity analyses (Chapter 6) have been presented under the assumption that Wilks' theorem is valid. Wilks' theorem is a statistical approximation that simplifies the interpretation of likelihood ratios by predicting that the log-likelihood ratio will follow a χ^2-distribution with k degrees of freedom [206]. It is given as,

[206]: Wilks (1938), *The Large-Sample Distribution of the Likelihood Ratio for Testing Composite Hypotheses*

$$TS = -2ln\frac{\mathscr{L}_{\text{fixed}}}{\mathscr{L}_{\text{free}}} = -2\ln\left(\frac{\mathscr{L}\left(n \mid \mu\left(f_{\nu_e} = \hat{\hat{f}}^{\text{s.p.}}_{\nu_e},\, f_{\nu_\tau} = \hat{\hat{f}}^{\text{s.p.}}_{\nu_\tau},\, \theta,\, \xi\right)\right)}{\mathscr{L}\left(n \mid \mu\left(f_{\nu_e},\, f_{\nu_\tau},\, \theta,\, \xi\right)\right)}\right) \tag{B.1}$$

where, $\hat{\hat{f}}^{\text{s.p.}}_{\nu_e}$ and $\hat{\hat{f}}^{\text{s.p.}}_{\nu_\tau}$: Conditional best-fit values for electron and tau neutrino flavor compositions, where flavor fractions are fixed at specific values during the scan. $\hat{f}_{\nu_e}$ and $\hat{f}_{\nu_\tau}$: Values of flavor compositions for free fits, where parameters can vary freely. θ: Remaining model parameters, such as astrophysical normalization and the spectral index. ξ: Nuisance parameters accounting for uncertainties not directly of interest.

Here, k is defined as the difference in degrees of freedom between the tested model (with likelihood $\mathscr{L}_{\text{fixed}}$) and the model that best fits the data (with likelihood $\mathscr{L}_{\text{free}}$). This approximation, however, relies on several conditions for accuracy: (1) the tested hypothesis must be a nested case of the free-fit hypothesis, meaning the tested model is a subset of the parameters of the best-fit model, (2) neither the parameters of interest nor nuisance parameters can be bounded (they must be able to vary freely to any values), and (3) the sample size n must be large to ensure the distribution converges to χ^2.

The first condition of nested hypotheses is satisfied. For example, when testing for different astrophysical flavor compositions or constraining the tau neutrino contribution, the tested models serve as special cases of the unconstrained model, having fewer degrees of freedom. However, the remaining two conditions are more problematic. The flavor fractions, for instance, are constrained to positive values, meaning that the parameters of interest are restricted to never go below zero. While not all of the nuisance parameters are not exactly restricted by a bound, the atmospheric spectra norms are also restricted to be positive, always. This violates the second assumption. Lastly, the HESE sample size is relatively small (with only a handful of double cascades from tau neutrinos and a total of < 200 events). While this doesn't necessarily mean that wilks' theorem does not hold anymore, an assessment is required to verify its validity.

This is done by comparing the coverage of the test statistic distribution from the monte carlo pseudo experiments to the coverage of $\chi^2_{k=2}$. The

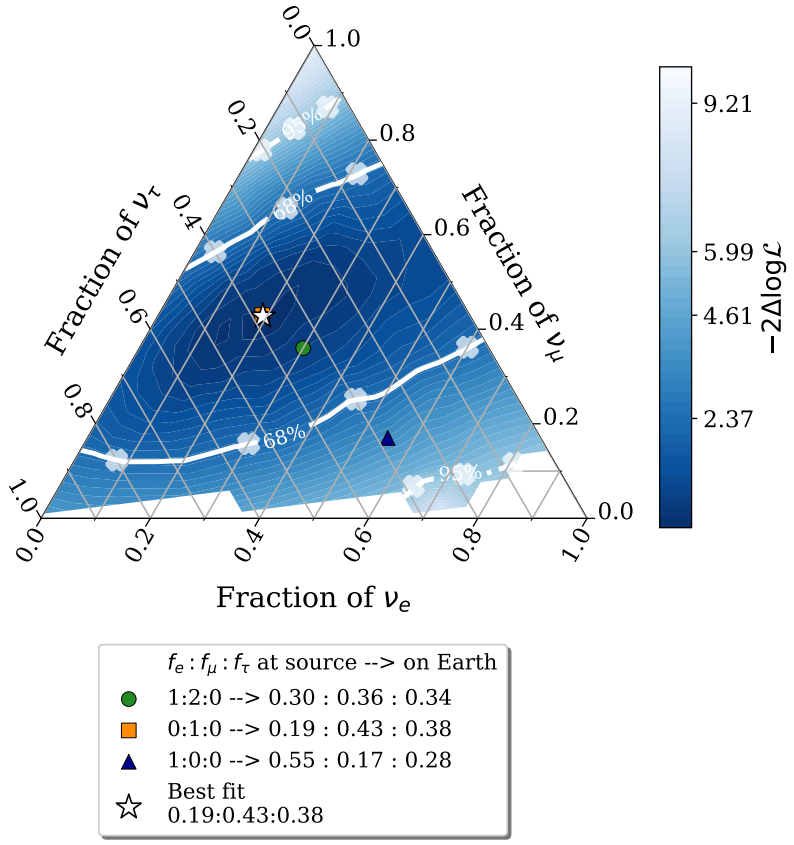

Figure B.1: Illustration of the selected scan points to check coverage in phase space of astrophysical neutrino flavour fractions. The profile likelihood scan is same as in Figure 7.8, representing 68% (solid) and 95% (dashed) confidence region.

coverage was tested at various points along the 68% and 95% confidence contours to check if the log-likelihood ratio truly followed the expected χ^2-distribution. Five representative points were selected along each confidence contour (see Figure B.1), and 500[1] pseudo datasets were generated at each of these points by injecting a specific flavor composition (indicated by 'x' on the plot) while holding the other model parameters at their best-fit values given in Table 7.3 and Table 7.4. Each pseudo dataset was fitted twice: once with the flavor composition fixed to the injected point, and once allowing all parameters to vary freely. A likelihood ratio test was applied to each trial by taking the ratio of the likelihoods from the free and fixed fits.

1: The nubers of trials was selected to keep statistical errors low for the points on 68%, as for 95%, the numbers of trials need to be as high as 1000, which becomes computationally expensive. Idea was to check for any significant deviations on 68% region and later produce more trials if needed for points on 95% contours.

The distribution of the test statistic (TS), represented by $-2\Delta\log\mathcal{L}$, was then compared to a χ^2-distribution with $k = 2$ degrees of freedom (shown as a black line) to assess if it conformed to the expected distribution. Figure B.2 shows the TS distributions for points along the 68% confidence contour, and Figure B.3 shows the distributions for points along the 95% contour. Although minor deviations were observed in some of the TS distributions, these deviations were not significant enough to indicate a substantial departure from Wilks' theorem. An exact fit to the χ^2-distribution is not fully expected, as there is some correlation between the two fitting parameters, likely reducing the effective degrees of freedom to just below 2. In addition, some of the points (especially the ones on 95% contour) are in a phase space of the triangle whice often fit experiences minimisation faliure due to large deviation from the best-fit values. Overall, Wilks' theorem appears to hold consistently across the entire parameter space, indicating that it should also be valid for the

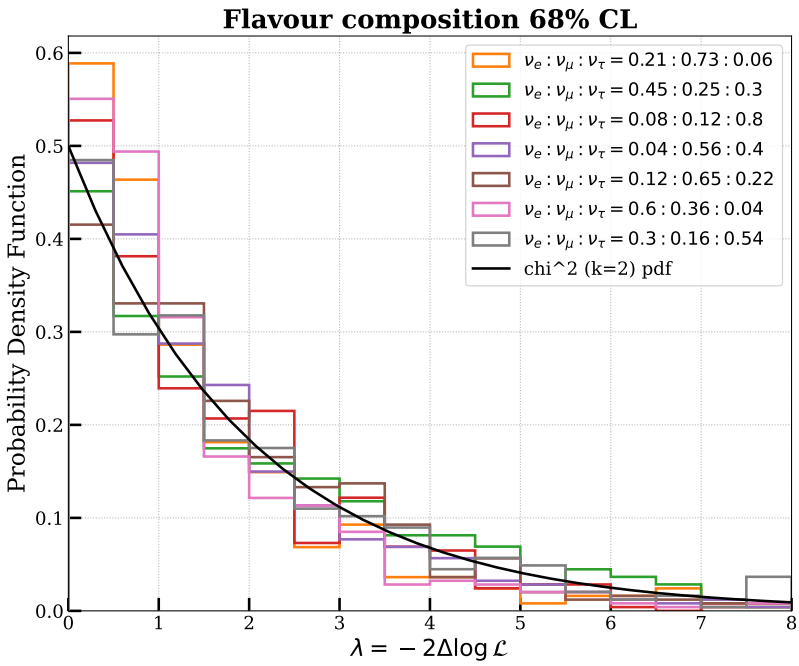

Figure B.2: The TS distributions for each scan point at the 68% confidence levels (shown in Figure **??**). The likelihood ratio is defined in Equation B.1. Each distribution results from injecting the corresponding flavor compositions (indicated also in the plot legend) into the Monte Carlo simulation, as described in the text. Statistical uncertainties are omitted for clarity. A χ^2-distribution with two degrees of freedom is included for comparison in each plot.

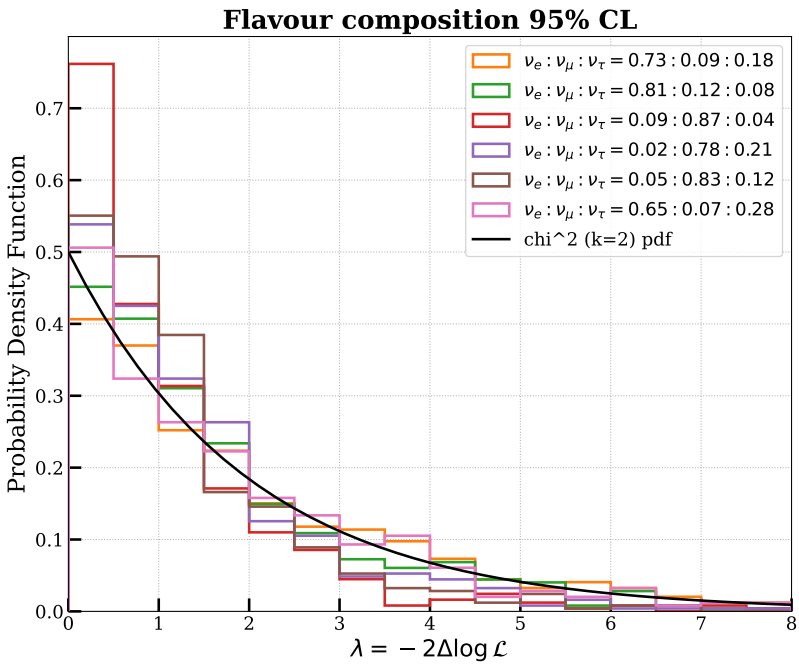

Figure B.3: The TS distributions for each scan point at the 95% confidence levels. See caption of Figure B.2 for details.

true physical parameter values. Therefore, Wilks' theorem can be reliably used for both one- and two-dimensional parameter scans, enabling the calculation of confidence intervals presented in Section 7.3 for deriving the main results and in Section 6.3 for determining the sensitivity.

C

Sensitivity Estimation using Monte Carlo PseudoTrials

The sensitivty derived at best-fit using an asimov dataset [209] was discussed in 7.3. In Figure 7.12, the marroon line shows asimov sensitivity of the analysis at the best-fit, which predicts that ideally, analysis should be able to put tighter constraints on the measured flavour fraction (specifically the $\nu_t au$ fraction). As there is a strong mismatch between results and the sensitivty, a test was made to generate sensitivity estimation using monte carlo pseudo trials.

[209]: Cowan et al. (2011), *Asymptotic formulae for likelihood-based tests of new physics*

Construction of monte carlo pseudo datasets and TS distribution is done in the similar way as it was done in Appendix B with two main differences. First, instead of a few points on the contours, a grid across entire triangle is considered (see blue + in Figure C.1), each of which (about 500) represents the points for which a pseudo dataset were generated. Second, unlike the case of coverage test, in this case, conditional best-fit, i.e $\hat{\hat{f}}^{\text{s.p.}}_{\nu_e}$ and $\hat{\hat{f}}^{\text{s.p.}}_{\nu_\tau}$ in B.1 is **always** kept at signal bestfit values of flavour fractions ($f_{\nu_e} = 0.19$ and $f_{\nu_{tau}} = 0.38$), for every set of trials. The goal of this approach is to capture the potential variability in the TS under different hypothetical "true" parameter configurations and to understand how likely the best-fit hypothesis would be rejected if any of these points were the actual parameter values. By spanning the parameter space, we also avoid any bias toward the best-fit configuration, providing a fair estimate of sensitivity.

A critical first step is the selection of injected points within the parameter space of the flavour triangle. Figure C.1 shows the grid of injected points chosen to span the entire range of flavour compositions, extending beyond the best-fit values, $\nu_e : \nu_\mu : \nu_\tau = 0.19 : 0.43 : 0.38$. This approach ensures a comprehensive sensitivity estimate across various possible configurations. For each of these injected points, a corresponding pseudo dataset was generated to simulate observations that would arise if the true parameter values were equal to the injected values.

To interpret the TS values derived from each pseudo dataset, a critical value needs to be established first. For this purpose, a TS distribution is generated using, pseudo data generated at best-fit values and fitted twice in the same manner described before. This distribution is displayed in Figure C.2, which shows the TS survival function under the best-fit hypothesis with the median value marked. This median TS value serves as a critical threshold, allowing us to evaluate the TS values obtained from pseudo datasets generated at other injected points. If a pseudo dataset generated at an alternative parameter configuration produces a TS greater than the critical TS, the dataset provides evidence against the best-fit hypothesis at the corresponding confidence level, in other words, the fraction of pseudo datasets injected at a given points below

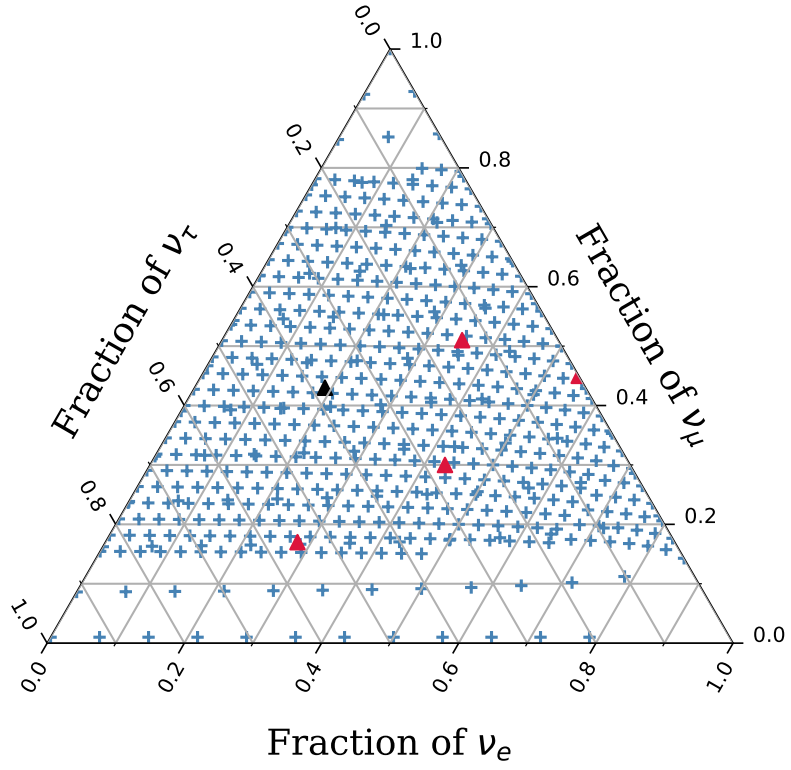

Figure C.1: Illustartion of various points on the flavour composition phase space, used in sensitivity derivation. Each + represents a pseudo dataset, drawn from flavour composition of that very point. The best-fit flavour composition of ν_e : ν_μ : ν_τ = 0.19 : 0.43 : 0.38 is indicated with a black triangle, while the few TS distributions discussed in Figure C.3 and text are shown with red triangle. All other parameters of the fit are injected at their bestfit values.

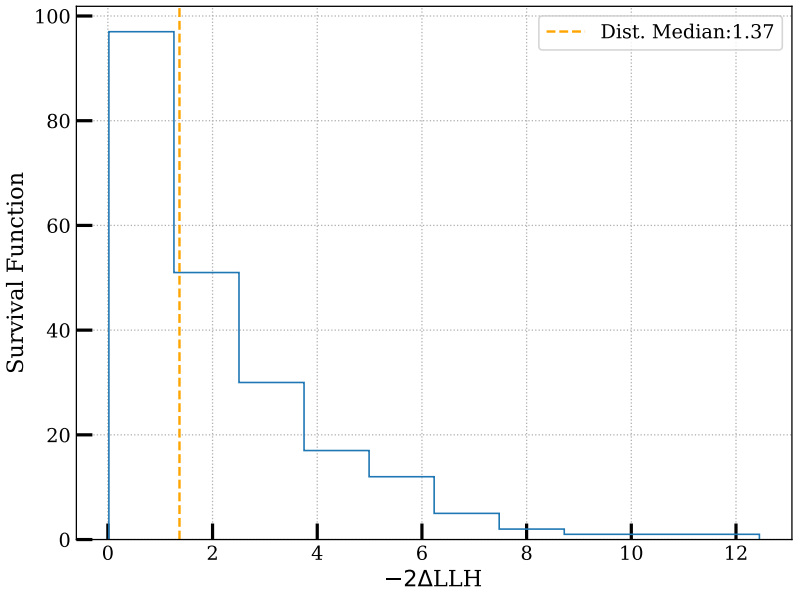

Figure C.2: The distribution of TS of pseudo dataset produced by injecting best-fit flavour composition (black triangle in Figure C.1). TS is calculated using likelihood ratio defined in B.1

, by taking ratio of conditional best-fit (flavour fractions fixed at best-fit values) to free fit. The vertical line shows median of the distribution that serves as a critical TS for the rest of the trial' TS distributions.

the critical value gives significance with which best-fit hypothesis can be rejected.

Figure C.3 displays the survival distributions of TS values for four specific injected points (indicated with red triangle in Figure C.1), each corresponding to different confidence levels (67%, 90%, 96%, and 99%). In each figure, the fraction of the TS distribution that exceeds the median TS benchmark for the best-fit hypothesis is highlighted as a shaded orange

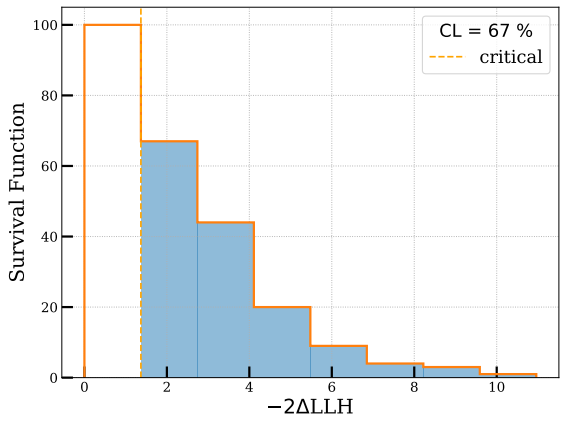

(a) injected point $\nu_e : \nu_\mu : \nu_\tau = 0.35 : 0.51 : 0.14$

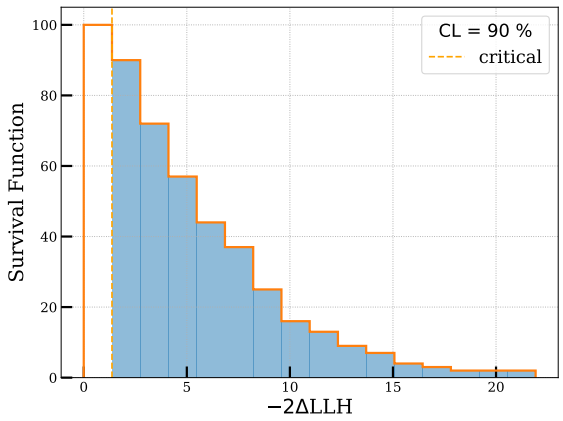

(b) injected point $\nu_e : \nu_\mu : \nu_\tau = 0.55 : 0.445 : 0.0$

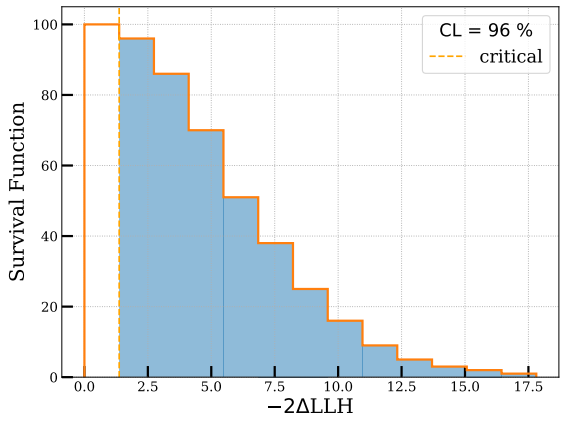

(c) injected point $\nu_e : \nu_\mu : \nu_\tau = 0.43 : 0.3 : 0.27$

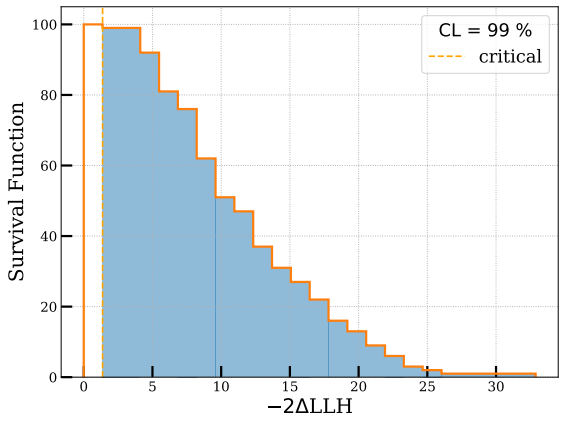

(d) injected point $\nu_e : \nu_\mu : \nu_\tau = 0.28 : 0.17 : 0.55$

Figure C.3: The distribution of TS for pseudo datasets generated by injecting various best-fit flavor compositions (indicated below each plot and by red triangles in Figure C.1) is shown. The shaded regions represent the fraction of trials exceeding the critical value defined in Figure C.2. This fraction, indicated on each plot, conveys the confidence level (CL) with which the best-fit hypothesis is rejected.

region. These shaded areas represent the fraction of pseudo datasets, generated for each injected configuration, that yield a TS value above this critical threshold. This fraction quantifies the probability that the analysis would reject the best-fit hypothesis if the true values of flavour fractions correspond to the injected values used for each pseudo dataset. Therefore, these survival distributions illustrate how distinguishable each injected configuration is from the best-fit hypothesis, providing a clear measure of the sensitivity of the analysis.

After calculating the TS distributions for each injected point and comparing them to the critical threshold, we aggregate the results across all injected points to construct confidence intervals. Figure 7.12 displays these sensitivity-derived confidence intervals, representing the regions in parameter space where the analysis is sensitive enough to distinguish between the best-fit hypothesis and alternative configurations at specified confidence levels (e.g., 90% or 95%).

The implications of the results are discussed in detail in Section 7.3, but the point to take away is asimov sensitivity derived at the best-fit is rather stricter and analysis is in-fact sensitive to measure the flavour ratio (especially the ν_τ fraction) of astrophysical neutrinos.

List of Figures

List of Tables

Bibliography

Here are the references in citation order.

[1] W. Pauli. "Dear radioactive ladies and gentlemen". In: *Phys. Today* 31N9 (1978), p. 27 (cited on page 3).

[2] F. Reines et al. "Detection of the Free Antineutrino". In: *Phys. Rev.* 117 (1 Jan. 1960), pp. 159–173. DOI: 10.1103/PhysRev.117.159 (cited on page 3).

[3] R. Davis, D. S. Harmer, and K. C. Hoffman. "Search for Neutrinos from the Sun". In: *Phys. Rev. Lett.* 20 (21 1968), pp. 1205–1209. DOI: 10.1103/PhysRevLett.20.1205 (cited on page 3).

[4] H. A. Bethe. "Energy Production in Stars". In: *Phys. Rev.* 55 (5 1939), pp. 434–456. DOI: 10.1103/PhysRev.55.434 (cited on page 3).

[5] Q. R. Ahmad et al. "Measurement of the Rate $\nu_e + d \rightarrow p + p + e^-$ Solar Neutrinos at the Sudbury Neutrino Observatory". In: *Physical Review Letters* 87.7 (2001). DOI: 10.1103/physrevlett.87.071301 (cited on page 3).

[6] Y. Fukuda et al. "Evidence for Oscillation of Atmospheric Neutrinos". In: *Phys. Rev. Lett.* 81 (8 1998), pp. 1562–1567. DOI: 10.1103/PhysRevLett.81.1562 (cited on page 3).

[7] C. S. Wu et al. "Experimental Test of Parity Conservation in Beta Decay". In: *Phys. Rev.* 105 (4 Feb. 1957), pp. 1413–1415. DOI: 10.1103/PhysRev.105.1413 (cited on page 4).

[8] M. Aker et al. "Direct neutrino-mass measurement with sub-electronvolt sensitivity". In: *Nature Phys.* 18.2 (2022), pp. 160–166. DOI: 10.1038/s41567-021-01463-1 (cited on page 4).

[9] N. Aghanim et al. "Planck 2018 results". In: *Astronomy Astrophysics* 641 (2020), A6. DOI: 10.1051/0004-6361/201833910 (cited on page 4).

[10] B. Pontecorvo. "Neutrino Experiments and the Problem of Conservation of Leptonic Charge". In: *Zh. Eksp. Teor. Fiz.* 53 (1967), pp. 1717–1725 (cited on page 4).

[11] S. Schael et al. "Precision electroweak measurements on the Z resonance". In: *Phys. Rept.* 427 (2006), pp. 257–454. DOI: 10.1016/j.physrep.2005.12.006 (cited on pages 4, 11).

[12] R. Abbasi et al. "Measurement of atmospheric neutrino mixing with improved IceCube DeepCore calibration and data processing". In: *Phys. Rev. D* 108.1 (2023), p. 012014. DOI: 10.1103/PhysRevD.108.012014 (cited on page 5).

[13] I. Esteban et al. "The fate of hints: updated global analysis of three-flavor neutrino oscillations". In: *JHEP* 09 (2020), p. 178. DOI: 10.1007/JHEP09(2020)178 (cited on page 5).

[14] I. Gil-Botella. "Neutrino Physics". In: *6th CERN-Latin-American School of High-Energy Physics*. 2013, pp. 157–205. DOI: 10.5170/CERN-2013-003.157 (cited on page 5).

[15] L. Wolfenstein. "Neutrino oscillations in matter". In: *Phys. Rev. D* 17 (9 May 1978), pp. 2369–2374. DOI: 10.1103/PhysRevD.17.2369 (cited on page 6).

[16] L. Wolfenstein. "Neutrino oscillations and stellar collapse". In: *Phys. Rev. D* 20 (10 Nov. 1979), pp. 2634–2635. DOI: 10.1103/PhysRevD.20.2634 (cited on page 6).

[17] S. P. Mikheyev and A. Y. Smirnov. "Resonance Amplification of Oscillations in Matter and Spectroscopy of Solar Neutrinos". In: *Sov. J. Nucl. Phys.* 42 (1985), pp. 913–917 (cited on page 6).

[18] H. A. Bethe. "Possible Explanation of the Solar-Neutrino Puzzle". In: *Phys. Rev. Lett.* 56 (12 Mar. 1986), pp. 1305–1308. DOI: 10.1103/PhysRevLett.56.1305 (cited on page 7).

[19] S. P. Rosen and J. M. Gelb. "Mikheyev-Smirnov-Wolfenstein enhancement of oscillations as a possible solution to the solar-neutrino problem". In: *Phys. Rev. D* 34 (4 Aug. 1986), pp. 969–979. DOI: 10.1103/PhysRevD.34.969 (cited on page 7).

[20] S. Navas et al. "Review of Particle Physics". In: *Phys. Rev. D* 110 (3 Aug. 2024), p. 030001. DOI: 10.1103/PhysRevD.110.030001 (cited on pages 7, 19, 20, 25, 26, 36–39, 41).

[21] J. A. Formaggio and G. P. Zeller. "From eV to EeV: Neutrino Cross Sections Across Energy Scales". In: *Rev. Mod. Phys.* 84 (2012), pp. 1307–1341. DOI: 10.1103/RevModPhys.84.1307 (cited on pages 7, 8, 10).

[22] A. Gando et al. "Constraints on θ_{13} from A Three-Flavor Oscillation Analysis of Reactor Antineutrinos at KamLAND". In: *Phys. Rev. D* 83 (2011), p. 052002. DOI: 10.1103/PhysRevD.83.052002 (cited on page 8).

[23] F. P. An et al. "Measurement of electron antineutrino oscillation based on 1230 days of operation of the Daya Bay experiment". In: *Phys. Rev. D* 95.7 (2017), p. 072006. DOI: 10.1103/PhysRevD.95.072006 (cited on page 8).

[24] R. P. Feynman. "Very High-Energy Collisions of Hadrons". In: *Phys. Rev. Lett.* 23 (24 Dec. 1969), pp. 1415–1417. DOI: 10.1103/PhysRevLett.23.1415 (cited on page 8).

[25] J. Stasielak et al. "High-Energy Neutrino Astronomy—Baikal-GVD Neutrino Telescope in Lake Baikal". In: *Symmetry* 13.3 (2021). DOI: 10.3390/sym13030377 (cited on page 9).

[26] J. D. Bjorken. "Asymptotic Sum Rules at Infinite Momentum". In: *Phys. Rev.* 179 (5 Mar. 1969), pp. 1547–1553. DOI: 10.1103/PhysRev.179.1547 (cited on page 9).

[27] R. Gandhi et al. "Neutrino interactions at ultrahigh energies". In: *Physical Review D* 58.9 (Sept. 1998). DOI: 10.1103/physrevd.58.093009 (cited on page 9).

[28] A. Cooper-Sarkar, P. Mertsch, and S. Sarkar. "The high energy neutrino cross-section in the Standard Model and its uncertainty". In: *JHEP* 08 (2011), p. 042. DOI: 10.1007/JHEP08(2011)042 (cited on pages 10, 56, 69).

[29] P. L. R. Weigel, J. M. Conrad, and A. Garcia-Soto. "Cross Sections and Inelasticity Distributions of High-Energy Neutrino Deep Inelastic Scattering". In: (Aug. 2024) (cited on page 10).

[30] K. Xie et al. "High-energy neutrino deep inelastic scattering cross sections". In: *Phys. Rev. D* 109 (11 June 2024), p. 113001. DOI: 10.1103/PhysRevD.109.113001 (cited on page 10).

[31] M. G. Aartsen et al. "Measurement of the multi-TeV neutrino cross section with IceCube using Earth absorption". In: *Nature* 551 (2017), pp. 596–600. DOI: 10.1038/nature24459 (cited on page 10).

[32] R. Abbasi et al. "Measurement of the high-energy all-flavor neutrino-nucleon cross section with IceCube". In: *Phys. Rev. D* 104 (2 July 2021), p. 022001. DOI: 10.1103/PhysRevD.104.022001 (cited on page 10).

[33] S. L. Glashow. "Resonant Scattering of Antineutrinos". In: *Phys. Rev.* 118 (1 Apr. 1960), pp. 316–317. DOI: 10.1103/PhysRev.118.316 (cited on pages 10, 56).

[34] M. G. Aartsen et al. "Detection of a particle shower at the Glashow resonance with IceCube". In: *Nature* 591.7849 (Mar. 2021), pp. 220–224. DOI: 10.1038/s41586-021-03256-1 (cited on page 10).

[35] M. G. Aartsen et al. "Measurements using the inelasticity distribution of multi-TeV neutrino interactions in IceCube". In: *Phys. Rev. D* 99.3 (2019), p. 032004. DOI: 10.1103/PhysRevD.99.032004 (cited on pages 10, 11, 27, 28, 69).

[36] S. R. Elliott, V. Gavrin, and W. Haxton. "The gallium anomaly". In: *Prog. Part. Nucl. Phys.* 134 (2024), p. 104082. DOI: 10.1016/j.ppnp.2023.104082 (cited on page 11).

[37] A. Aguilar et al. "Evidence for neutrino oscillations from the observation of $\bar{\nu}_e$ appearance in a $\bar{\nu}_\mu$ beam". In: *Phys. Rev. D* 64 (2001), p. 112007. DOI: 10.1103/PhysRevD.64.112007 (cited on page 11).

[38] A. A. Aguilar-Arevalo et al. "Improved Search for $\bar{\nu}_\mu \to \bar{\nu}_e$ Oscillations in the MiniBooNE Experiment". In: *Phys. Rev. Lett.* 110 (2013), p. 161801. DOI: 10.1103/PhysRevLett.110.161801 (cited on page 11).

[39] G. Mention et al. "The Reactor Antineutrino Anomaly". In: *Phys. Rev. D* 83 (2011), p. 073006. DOI: 10.1103/PhysRevD.83.073006 (cited on page 11).

[40] K. N. Abazajian et al. “Light Sterile Neutrinos: A White Paper”. In: (Apr. 2012) (cited on page 11).

[41] K. N. Abazajian. “Sterile neutrinos in cosmology”. In: *Phys. Rept.* 711-712 (2017), pp. 1–28. DOI: 10.1016/j.physrep.2017.10.003 (cited on page 11).

[42] E. Komatsu et al. “SEVEN-YEARWILKINSON MICROWAVE ANISOTROPY PROBE(WMAP) OBSERVATIONS: COSMOLOGICAL INTERPRETATION”. In: *The Astrophysical Journal Supplement Series* 192.2 (2011). DOI: 10.1088/0067-0049/192/2/18 (cited on page 11).

[43] N. Aghanim et al. “Planck 2018 results. VI. Cosmological parameters”. In: *Astron. Astrophys.* 641 (2020). [Erratum: Astron.Astrophys. 652, C4 (2021)], A6. DOI: 10.1051/0004-6361/201833910 (cited on page 12).

[44] M. Drewes et al. “A White Paper on keV Sterile Neutrino Dark Matter”. In: *JCAP* 01 (2017), p. 025. DOI: 10.1088/1475-7516/2017/01/025 (cited on page 12).

[45] P. F. de Salas, R. A. Lineros, and M. Tórtola. “Neutrino propagation in the galactic dark matter halo”. In: *Phys. Rev. D* 94.12 (2016), p. 123001. DOI: 10.1103/PhysRevD.94.123001 (cited on page 12).

[46] D. Hooper, D. Morgan, and E. Winstanley. “Lorentz and CPT invariance violation in high-energy neutrinos”. In: *Phys. Rev. D* 72 (2005), p. 065009. DOI: 10.1103/PhysRevD.72.065009 (cited on page 12).

[47] A. Trettin. “Search for eV-scale sterile neutrinos with IceCube DeepCore”. PhD thesis. Humboldt-Universität zu Berlin, Mathematisch-Naturwissenschaftliche Fakultät, 2024. DOI: http://dx.doi.org/10.18452/27595 (cited on page 12).

[48] L. Fischer. “First Search for Heavy Neutral Leptons with IceCube DeepCore”. PhD thesis. Humboldt-Universität zu Berlin, Mathematisch-Naturwissenschaftliche Fakultät, 2024. DOI: http://dx.doi.org/10.18452/29182 (cited on page 12).

[49] R. Abbasi et al. “Search for neutrino lines from dark matter annihilation and decay with IceCube”. In: *Phys. Rev. D* 108.10 (2023), p. 102004. DOI: 10.1103/PhysRevD.108.102004 (cited on page 12).

[50] R. W. Rasmussen et al. “Astrophysical neutrinos flavored with beyond the Standard Model physics”. In: 96.8, 083018 (Oct. 2017), p. 083018. DOI: 10.1103/PhysRevD.96.083018 (cited on page 12).

[51] U. Katz and C. Spiering. “High-energy neutrino astrophysics: Status and perspectives”. In: *Progress in Particle and Nuclear Physics* 67.3 (2012), pp. 651–704. DOI: https://doi.org/10.1016/j.ppnp.2011.12.001 (cited on page 13).

[52] J. N. Bahcall and R. K. Ulrich. “Solar models, neutrino experiments, and helioseismology”. In: *Rev. Mod. Phys.* 60 (2 Apr. 1988), pp. 297–372. DOI: 10.1103/RevModPhys.60.297 (cited on pages 13, 24).

[53] L. M. Krauss, S. L. Glashow, and D. N. Schramm. “Anti-neutrinos Astronomy and Geophysics”. In: *Nature* 310 (1984), pp. 191–198. DOI: 10.1038/310191a0 (cited on page 13).

[54] K. Hirata et al. “Observation of a neutrino burst from the supernova SN1987A”. In: *Phys. Rev. Lett.* 58 (14 Apr. 1987), pp. 1490–1493. DOI: 10.1103/PhysRevLett.58.1490 (cited on page 13).

[55] E. Alexeyev et al. “Detection of the neutrino signal from SN 1987A in the LMC using the INR Baksan underground scintillation telescope”. In: *Physics Letters B* 205.2 (1988), pp. 209–214. DOI: https://doi.org/10.1016/0370-2693(88)91651-6 (cited on page 13).

[56] R. M. Bionta et al. “Observation of a neutrino burst in coincidence with supernova 1987A in the Large Magellanic Cloud”. In: *Phys. Rev. Lett.* 58 (14 Apr. 1987), pp. 1494–1496. DOI: 10.1103/PhysRevLett.58.1494 (cited on page 13).

[57] F. Vissani and G. Pagliaroli. “The diffuse supernova neutrino background: Expectations and uncertainties derived from SN1987A”. In: *Astron. Astrophys.* 528 (2011), p. L1. DOI: 10.1051/0004-6361/201016109 (cited on page 13).

[58] V. F. HESS. "1 - Observations of the Penetrating Radiation on Seven Balloon Flights††Physik. Zeitschr. 13, 1804–1091 (1912). (From the Section on Geophysics, Meteorology and Geomagnetism.)" In: *Cosmic Rays*. Ed. by A. HILLAS. The Commonwealth and International Library: Selected Readings in Physics. Pergamon, 1972, pp. 139–147. DOI: https://doi.org/10.1016/B978-0-08-016724-4.50013-6 (cited on page 13).

[59] R. L. Workman et al. "Review of Particle Physics". In: *PTEP* 2022 (2022), p. 083C01. DOI: 10.1093/ptep/ptac097 (cited on pages 14, 15).

[60] J. R. Hörandel. "Cosmic Rays from the Knee to the Second Knee: 10^{14} to 10^{18} eV". In: *Modern Physics Letters A* 22.21 (2007), pp. 1533–1551. DOI: 10.1142/s0217732307024139 (cited on page 15).

[61] K. Greisen. "End to the Cosmic-Ray Spectrum?" In: *Phys. Rev. Lett.* 16 (17 Apr. 1966), pp. 748–750. DOI: 10.1103/PhysRevLett.16.748 (cited on page 15).

[62] G. T. Zatsepin and V. A. Kuzmin. "Upper limit of the spectrum of cosmic rays". In: *JETP Lett.* 4 (1966), pp. 78–80 (cited on page 15).

[63] A. Aab et al. "Evidence for a mixed mass composition at the 'ankle' in the cosmic-ray spectrum". In: *Phys. Lett. B* 762 (2016), pp. 288–295. DOI: 10.1016/j.physletb.2016.09.039 (cited on page 15).

[64] V. de Souza. "Testing the agreement between the $X_{\max}$ distributions measured by the Pierre Auger and Telescope Array Observatories". In: *PoS* ICRC2017 (2017), p. 522. DOI: 10.22323/1.301.0522 (cited on page 15).

[65] S. Das, S. Razzaque, and N. Gupta. "Modeling the spectrum and composition of ultrahigh-energy cosmic rays with two populations of extragalactic sources". In: *The European Physical Journal C* 81.1 (2021). DOI: 10.1140/epjc/s10052-021-08885-4 (cited on page 15).

[66] J. R. Hoerandel. "Models of the knee in the energy spectrum of cosmic rays". In: *Astropart. Phys.* 21 (2004), pp. 241–265. DOI: 10.1016/j.astropartphys.2004.01.004 (cited on page 15).

[67] D. H. Perkins. *Particle astrophysics*. 2003 (cited on pages 15, 17, 18, 37).

[68] J. R. Hörandel. "On the knee in the energy spectrum of cosmic rays". In: *Astroparticle Physics* 19.2 (2003), pp. 193–220. DOI: 10.1016/s0927-6505(02)00198-6 (cited on page 15).

[69] T. Stanev. *High Energy Cosmic Rays*. Springer Berlin, Heidelberg, 2010 (cited on page 15).

[70] R. Aloisio, V. Berezinsky, and A. Gazizov. "Transition from galactic to extragalactic cosmic rays". In: *Astroparticle Physics* 39-40 (2012), pp. 129–143. DOI: 10.1016/j.astropartphys.2012.09.007 (cited on page 16).

[71] S. Mollerach and E. Roulet. "Ultrahigh energy cosmic rays from a nearby extragalactic source in the diffusive regime". In: *Phys. Rev. D* 99 (10 May 2019), p. 103010. DOI: 10.1103/PhysRevD.99.103010 (cited on page 16).

[72] M. Unger, G. R. Farrar, and L. A. Anchordoqui. "Origin of the ankle in the ultrahigh energy cosmic ray spectrum, and of the extragalactic protons below it". In: *Physical Review D* 92.12 (2015). DOI: 10.1103/physrevd.92.123001 (cited on page 16).

[73] A. Abdul Halim et al. "An update on the arrival direction studies made with data from the Pierre Auger Observatory". In: *PoS* ICRC2023 (2023), p. 252. DOI: 10.22323/1.444.0252 (cited on page 16).

[74] J. Kim et al. "Anisotropies in the arrival direction distribution of ultra-high energy cosmic rays measured by the Telescope Array surface detector". In: *PoS* ICRC2023 (2023), p. 244. DOI: 10.22323/1.444.0244 (cited on page 16).

[75] M.-h. Kim et al. "Contribution of High Charge and Energy (HZE) Ions During Solar-Particle Event of September 29, 1989". In: (July 1999) (cited on page 16).

[76] E. Fermi. "On the Origin of the Cosmic Radiation". In: *Phys. Rev.* 75 (8 Apr. 1949), pp. 1169–1174. DOI: 10.1103/PhysRev.75.1169 (cited on page 16).

[77] T. K. Gaisser, R. Engel, and E. Resconi. *Cosmic Rays and Particle Physics*. 2nd ed. Cambridge University Press, 2016 (cited on page 16).

[78] R. A. Batista and G. Sigl. "Diffusion of cosmic rays at EeV energies in inhomogeneous extragalactic magnetic fields". In: *Journal of Cosmology and Astroparticle Physics* 2014.11 (2014), p. 031. DOI: 10.1088/1475-7516/2014/11/031 (cited on page 17).

[79] A. P. Snodin et al. "Global diffusion of cosmic rays in random magnetic fields". In: *Mon. Not. Roy. Astron. Soc.* 457.4 (2016), pp. 3975–3987. DOI: 10.1093/mnras/stw217 (cited on page 17).

[80] J. G. Kirk and P. Schneider. "On the Acceleration of Charged Particles at Relativistic Shock Fronts". In: *ApJ* 315 (Apr. 1987), p. 425. DOI: 10.1086/165147 (cited on page 17).

[81] A. F. Heavens and L. O. Drury. "Relativistic shocks and particle acceleration." In: 235 (Dec. 1988), pp. 997–1009. DOI: 10.1093/mnras/235.3.997 (cited on page 17).

[82] M. Yamada, R. Kulsrud, and H. Ji. "Magnetic reconnection". In: *Rev. Mod. Phys.* 82 (1 Mar. 2010), pp. 603–664. DOI: 10.1103/RevModPhys.82.603 (cited on page 17).

[83] F.-Y. Chang et al. "Magnetowave Induced Plasma Wakefield Acceleration for Ultra High Energy Cosmic Rays". In: *Phys. Rev. Lett.* 102 (2009), p. 111101. DOI: 10.1103/PhysRevLett.102.111101 (cited on page 17).

[84] M. G. Aartsen et al. "Astrophysical neutrinos and cosmic rays observed by IceCube". In: *Adv. Space Res.* 62 (2018), pp. 2902–2930. DOI: 10.1016/j.asr.2017.05.030 (cited on page 18).

[85] A. M. Hillas. "The Origin of Ultra-High-Energy Cosmic Rays". In: *Annual Review of Astronomy and Astrophysics* 22.1 (1984), pp. 425–444. DOI: 10.1146/annurev.aa.22.090184.002233 (cited on page 17).

[86] H.-W. Rix and J. Bovy. "The Milky Way's stellar disk". In: *Astron. Astrophys. Rev.* 21 (2013), p. 61. DOI: 10.1007/s00159-013-0061-8 (cited on page 18).

[87] M. Haverkorn. "Magnetic Fields in the Milky Way". In: (June 2014). DOI: 10.1007/978-3-662-44625-6_17 (cited on page 18).

[88] F. Halzen and S. R. Klein. "IceCube: An Instrument for Neutrino Astronomy". In: *Rev. Sci. Instrum.* 81 (2010), p. 081101. DOI: 10.1063/1.3480478 (cited on page 18).

[89] R. J. Protheroe and A. P. Szabo. "High-energy cosmic rays from active galactic nuclei". In: *Phys. Rev. Lett.* 69 (1992), pp. 2885–2888. DOI: 10.1103/PhysRevLett.69.2885 (cited on page 18).

[90] X.-Y. Wang, S. Razzaque, and P. Meszaros. "On the Origin and Survival of UHE Cosmic-Ray Nuclei in GRBs and Hypernovae". In: *Astrophys. J.* 677 (2008), pp. 432–440. DOI: 10.1086/529018 (cited on page 18).

[91] J. E. Horvath. *High-Energy Astrophysics. A Primer*. Undergraduate Lecture Notes in Physics. Springer, 2022 (cited on pages 18, 19).

[92] B. M. Peterson. *An Introduction to Active Galactic Nuclei*. Cambridge University Press, 1997 (cited on page 19).

[93] T. Piran. "Gamma-ray bursts and the fireball model". In: *Physics Reports* 314.6 (1999), pp. 575–667. DOI: https://doi.org/10.1016/S0370-1573(98)00127-6 (cited on page 19).

[94] J. Hjorth and J. S. Bloom. *The Gamma-Ray Burst - Supernova Connection*. 2011. URL: https://arxiv.org/abs/1104.2274 (cited on page 19).

[95] B. P. Abbott et al. "Gravitational Waves and Gamma-rays from a Binary Neutron Star Merger: GW170817 and GRB 170817A". In: *Astrophys. J. Lett.* 848.2 (2017), p. L13. DOI: 10.3847/2041-8213/aa920c (cited on page 19).

[96] H. T. Janka et al. "Black hole: Neutron star mergers as central engines of gamma-ray bursts". In: *Astrophys. J. Lett.* 527 (1999), p. L39. DOI: 10.1086/312397 (cited on page 19).

[97] T. K. Gaisser and T. Stanev. "Neutrinos and cosmic rays". In: *Astroparticle Physics* 39-40 (Dec. 2012), pp. 120–128. DOI: 10.1016/j.astropartphys.2012.08.004 (cited on page 19).

[98] E. V. Bugaev et al. "Atmospheric muon flux at sea level, underground and underwater". In: *Phys. Rev. D* 58 (1998), p. 054001. DOI: 10.1103/PhysRevD.58.054001 (cited on page 20).

[99] M. G. Aartsen et al. "Characterization of the Atmospheric Muon Flux in IceCube". In: *Astropart. Phys.* 78 (2016), pp. 1–27. DOI: 10.1016/j.astropartphys.2016.01.006 (cited on pages 20, 21).

[100] R. Enberg, M. H. Reno, and I. Sarcevic. "Prompt neutrino fluxes from atmospheric charm". In: *Phys. Rev. D* 78 (2008), p. 043005. DOI: 10.1103/PhysRevD.78.043005 (cited on pages 20, 21, 26).

[101] J. I. Illana et al. "Atmospheric muon and neutrino fluxes at very high energy". In: *Astroparticle Physics* 34.9 (2011), pp. 663–673. DOI: https://doi.org/10.1016/j.astropartphys.2011.01.001 (cited on page 20).

[102] E. Richard et al. "Measurements of the atmospheric neutrino flux by Super-Kamiokande: Energy spectra, geomagnetic effects, and solar modulation". In: *Phys. Rev. D* 94 (5 Sept. 2016), p. 052001. DOI: 10.1103/PhysRevD.94.052001 (cited on page 21).

[103] K. Daum et al. "Determination of the atmospheric neutrino spectra with the Fréjus detector". In: *Zeitschrift für Physik C Particles and Fields* 66.3 (1995). Cited by: 218, pp. 417–428. DOI: 10.1007/BF01556368 (cited on page 21).

[104] M. G. Aartsen et al. "Measurement of the Atmospheric ν_e Spectrum with IceCube". In: *Phys. Rev. D* 91 (12 June 2015), p. 122004. DOI: 10.1103/PhysRevD.91.122004 (cited on page 21).

[105] A. Albert et al. "Measurement of the atmospheric ν_e and ν_μ energy spectra with the ANTARES neutrino telescope". In: *Physics Letters B* 816 (2021), p. 136228. DOI: https://doi.org/10.1016/j.physletb.2021.136228 (cited on page 21).

[106] J. Boettcher et al. "Search for the Prompt Atmospheric Neutrino Flux in IceCube". In: *PoS* ICRC2023 (2023), p. 1068. DOI: 10.22323/1.444.1068 (cited on page 21).

[107] M. Ahlers et al. "GZK neutrinos after the Fermi-LAT diffuse photon flux measurement". In: *Astroparticle Physics* 34.2 (2010), pp. 106–115. DOI: https://doi.org/10.1016/j.astropartphys.2010.06.003 (cited on page 21).

[108] M. G. Aartsen et al. "Constraints on Ultrahigh-Energy Cosmic-Ray Sources from a Search for Neutrinos above 10 PeV with IceCube". In: *Phys. Rev. Lett.* 117.24 (2016). [Erratum: Phys.Rev.Lett. 119, 259902 (2017)], p. 241101. DOI: 10.1103/PhysRevLett.117.241101 (cited on page 21).

[109] J. K. Becker. "High-energy neutrinos in the context of multimessenger physics". In: *Phys. Rept.* 458 (2008), pp. 173–246. DOI: 10.1016/j.physrep.2007.10.006 (cited on page 22).

[110] N. K. Neilson et al. "Highlights from the IceCube Neutrino Observatory". In: *PoS* ICRC2023 (2023), p. 017. DOI: 10.22323/1.444.0017 (cited on page 23).

[111] M. G. Aartsen et al. "The IceCube Realtime Alert System". In: *Astropart. Phys.* 92 (2017), pp. 30–41. DOI: 10.1016/j.astropartphys.2017.05.002 (cited on page 23).

[112] M. G. Aartsen et al. "Multimessenger observations of a flaring blazar coincident with high-energy neutrino IceCube-170922A". In: *Science* 361.6398 (2018). DOI: 10.1126/science.aat1378 (cited on page 23).

[113] M. G. Aartsen et al. "Neutrino emission from the direction of the blazar TXS 0506+056 prior to the IceCube-170922A alert". In: *Science* 361.6398 (2018), pp. 147–151. DOI: 10.1126/science.aat2890 (cited on page 23).

[114] W. Winter et al. "Multi-messenger interpretation of the neutrinos from TXS 0506+056". In: *PoS* ICRC2019 (2020), p. 1032. DOI: 10.22323/1.358.1032 (cited on page 23).

[115] R. Abbasi et al. "Evidence for neutrino emission from the nearby active galaxy NGC 1068". In: *Science* 378.6619 (2022), pp. 538–543. DOI: 10.1126/science.abg3395 (cited on page 23).

[116] R. Abbasi et al. "Observation of high-energy neutrinos from the Galactic plane". In: *Science* 380.6652 (2023), adc9818. DOI: 10.1126/science.adc9818 (cited on page 23).

[117] K. Hayasaki. "Neutrinos from tidal disruption events". In: *Nature Astronomy* 5.5 (Feb. 2021), pp. 436–437. DOI: 10.1038/s41550-021-01309-z (cited on page 23).

[118] R. Stein et al. "A tidal disruption event coincident with a high-energy neutrino". In: *Nature Astronomy* 5.5 (2021), pp. 510–518. DOI: 10.1038/s41550-020-01295-8 (cited on page 23).

[119] S. Reusch et al. "Candidate Tidal Disruption Event AT2019fdr Coincident with a High-Energy Neutrino". In: *Phys. Rev. Lett.* 128 (22 June 2022), p. 221101. DOI: 10.1103/PhysRevLett.128.221101 (cited on page 23).

[120] W. Winter and C. Lunardini. "Interpretation of the Observed Neutrino Emission from Three Tidal Disruption Events". In: *Astrophys. J.* 948.1 (2023), p. 42. DOI: 10.3847/1538-4357/acbe9e (cited on page 23).

[121] S. Razzaque, P. Meszaros, and E. Waxman. "Neutrino tomography of gamma-ray bursts and massive stellar collapses". In: *Phys. Rev. D* 68 (2003), p. 083001. DOI: 10.1103/PhysRevD.68.083001 (cited on page 24).

[122] E. Waxman and J. N. Bahcall. "Neutrino afterglow from gamma-ray bursts: Similar to 10**18-eV". In: *Astrophys. J.* 541 (2000), pp. 707–711. DOI: 10.1086/309462 (cited on page 24).

[123] "An absence of neutrinos associated with cosmic-ray acceleration in γ-ray bursts". In: *Nature* 484.7394 (Apr. 2012), pp. 351–354. DOI: 10.1038/nature11068 (cited on page 24).

[124] M. G. Aartsen et al. "Extending the search for muon neutrinos coincident with gamma-ray bursts in IceCube data". In: *Astrophys. J.* 843.2 (2017), p. 112. DOI: 10.3847/1538-4357/aa7569 (cited on page 24).

[125] J. Bahcall and E. Waxman. "High energy astrophysical neutrinos: The upper bound is robust". In: *Phys. Rev. D* 64 (2 June 2001), p. 023002. DOI: 10.1103/PhysRevD.64.023002 (cited on page 24).

[126] K. Mannheim, R. J. Protheroe, and J. P. Rachen. "Cosmic ray bound for models of extragalactic neutrino production". In: *Phys. Rev. D* 63 (2 Dec. 2000), p. 023003. DOI: 10.1103/PhysRevD.63.023003 (cited on page 24).

[127] M. G. Aartsen et al. "A combined maximum-likelihood analysis of the high-energy astrophysical neutrino flux measured with IceCube". In: *Astrophys. J.* 809.1 (2015), p. 98. DOI: 10.1088/0004-637X/809/1/98 (cited on pages 25, 27, 28, 102).

[128] M. G. Aartsen et al. "Evidence for High-Energy Extraterrestrial Neutrinos at the IceCube Detector". In: *Science* 342.6161 (2013), p. 1242856. DOI: 10.1126/science.1242856 (cited on pages 25, 48).

[129] C. Kopper, W. Giang, and N. K. Neilson. "Observation of Astrophysical Neutrinos in Four Years of IceCube Data". In: *PoS* ICRC2015 (2016), p. 1081. DOI: 10.22323/1.236.1081 (cited on page 25).

[130] C. Kopper. "Observation of Astrophysical Neutrinos in Six Years of IceCube Data". In: *PoS* ICRC2017 (2017), p. 981. DOI: 10.22323/1.301.0981 (cited on page 25).

[131] R. Abbasi et al. "Improved Characterization of the Astrophysical Muon–neutrino Flux with 9.5 Years of IceCube Data". In: 928.1 (2022), p. 50. DOI: 10.3847/1538-4357/ac4d29 (cited on pages 25, 66, 93, 102).

[132] M. G. Aartsen et al. "Characteristics of the Diffuse Astrophysical Electron and Tau Neutrino Flux with Six Years of IceCube High Energy Cascade Data". In: *Phys. Rev. Lett.* 125 (12 Sept. 2020), p. 121104. DOI: 10.1103/PhysRevLett.125.121104 (cited on pages 25, 93).

[133] R. Abbasi et al. "IceCube high-energy starting event sample: Description and flux characterization with 7.5 years of data". In: *Physical Review D* 104.2 (2021). DOI: 10.1103/physrevd.104.022002 (cited on pages 25, 48, 50, 66–68, 70, 77, 82, 93, 98).

[134] R. Naab et al. "Measurement of the astrophysical diffuse neutrino flux in a combined fit of IceCube's high energy neutrino data". In: *PoS* ICRC2023 (2023), p. 1064. DOI: 10.22323/1.444.1064 (cited on pages 25, 75, 93).

[135] V. Basu et al. "From PeV to TeV: Astrophysical Neutrinos with Contained Vertices in 10 years of IceCube Data". In: *PoS* ICRC2023 (2023), p. 1007. DOI: 10.22323/1.444.1007 (cited on pages 25, 49, 75).

[136] T. Kashti and E. Waxman. "Astrophysical Neutrinos: Flavor Ratios Depend on Energy". In: *Phys. Rev. Lett.* 95 (18 Oct. 2005), p. 181101. DOI: 10.1103/PhysRevLett.95.181101 (cited on page 26).

[137] L. A. Anchordoqui et al. “Galactic point sources of TeV antineutrinos”. In: *Physics Letters B* 593.1 (2004), pp. 42–47. DOI: https://doi.org/10.1016/j.physletb.2004.04.054 (cited on page 26).

[138] S. Choubey and W. Rodejohann. “Flavor Composition of UHE Neutrinos at Source and at Neutrino Telescopes”. In: *Phys. Rev. D* 80 (2009), p. 113006. DOI: 10.1103/PhysRevD.80.113006 (cited on page 26).

[139] W. Winter, J. Becker Tjus, and S. R. Klein. “Impact of secondary acceleration on the neutrino spectra in gamma-ray bursts”. In: 569, A58 (Sept. 2014), A58. DOI: 10.1051/0004-6361/201423745 (cited on page 26).

[140] P. Mehta and W. Winter. “Interplay of energy dependent astrophysical neutrino flavor ratios and new physics effects”. In: *JCAP* 03 (2011), p. 041. DOI: 10.1088/1475-7516/2011/03/041 (cited on page 26).

[141] S. Hummer et al. “Energy dependent neutrino flavor ratios from cosmic accelerators on the Hillas plot”. In: *Astropart. Phys.* 34 (2010), pp. 205–224. DOI: 10.1016/j.astropartphys.2010.07.003 (cited on page 26).

[142] R. Abbasi et al. “Detection of astrophysical tau neutrino candidates in IceCube”. In: *The European Physical Journal C* 82.11 (2022). DOI: 10.1140/epjc/s10052-022-10795-y (cited on pages 27, 28, 48, 52, 69, 77, 88, 89, 99).

[143] R. Abbasi et al. “Observation of Seven Astrophysical Tau Neutrino Candidates with IceCube”. In: *Phys. Rev. Lett.* 132.15 (2024), p. 151001. DOI: 10.1103/PhysRevLett.132.151001 (cited on pages 28, 41).

[144] M. A. Markov. “On high energy neutrino physics”. In: *10th International Conference on High Energy Physics*. 1960, pp. 578–581 (cited on page 29).

[145] J. Babson et al. “Cosmic-ray muons in the deep ocean”. In: *Phys. Rev. D* 42 (11 Dec. 1990), pp. 3613–3620. DOI: 10.1103/PhysRevD.42.3613 (cited on page 29).

[146] I. Belolaptikov et al. “The Baikal underwater neutrino telescope: Design, performance, and first results”. In: *Astroparticle Physics* 7.3 (1997), pp. 263–282. DOI: https://doi.org/10.1016/S0927-6505(97)00022-4 (cited on page 29).

[147] E. Andres et al. “The AMANDA neutrino telescope: principle of operation and first results”. In: *Astroparticle Physics* 13.1 (2000), pp. 1–20. DOI: https://doi.org/10.1016/S0927-6505(99)00092-4 (cited on page 29).

[148] M. Ageron et al. “ANTARES: The first undersea neutrino telescope”. In: *Nuclear Instruments and Methods in Physics Research Section A: Accelerators, Spectrometers, Detectors and Associated Equipment* 656.1 (2011), pp. 11–38. DOI: https://doi.org/10.1016/j.nima.2011.06.103 (cited on page 29).

[149] A. Margiotta. “The KM3NeT deep-sea neutrino telescope”. In: *Nuclear Instruments and Methods in Physics Research Section A: Accelerators, Spectrometers, Detectors and Associated Equipment* 766 (2014). RICH2013 Proceedings of the Eighth International Workshop on Ring Imaging Cherenkov Detectors Shonan, Kanagawa, Japan, December 2-6, 2013, pp. 83–87 (cited on page 29).

[150] M. G. Aartsen et al. “The IceCube Neutrino Observatory: instrumentation and online systems”. In: *Journal of Instrumentation* 12.03 (Mar. 2017), P03012–P03012. DOI: 10.1088/1748-0221/12/03/p03012 (cited on pages 30–32).

[151] R. Abbasi et al. “The design and performance of IceCube DeepCore”. In: *Astroparticle Physics* 35.10 (2012), pp. 615–624. DOI: 10.1016/j.astropartphys.2012.01.004 (cited on page 30).

[152] M. G. Aartsen et al. “Measurement of atmospheric tau neutrino appearance with IceCube DeepCore”. In: *Physical Review D* 99.3 (2019). DOI: 10.1103/physrevd.99.032007 (cited on page 30).

[153] R. Abbasi et al. “Search for GeV-scale dark matter annihilation in the Sun with IceCube DeepCore”. In: *Physical Review D* 105.6 (2022). DOI: 10.1103/physrevd.105.062004 (cited on page 30).

[154] R. Abbasi et al. “IceTop: The surface component of IceCube”. In: *Nuclear Instruments and Methods in Physics Research Section A: Accelerators, Spectrometers, Detectors and Associated Equipment* 700 (2013), pp. 188–220. DOI: https://doi.org/10.1016/j.nima.2012.10.067 (cited on page 30).

[155] R. Abbasi et al. "The IceCube data acquisition system: Signal capture, digitization, and timestamping". In: *Nuclear Instruments and Methods in Physics Research Section A: Accelerators, Spectrometers, Detectors and Associated Equipment* 601.3 (2009), pp. 294–316. DOI: 10.1016/j.nima.2009.01.001 (cited on page 33).

[156] M. Ackermann et al. "Optical properties of deep glacial ice at the South Pole". In: *J. Geophys. Res.* 111.D13 (2006), p. D13203. DOI: 10.1029/2005JD006687 (cited on page 34).

[157] M. Aartsen et al. "South Pole Glacial Climate Reconstruction from Multi-Borehole Laser Particulate Stratigraphy". In: *Journal of Glaciology* 59 (Sept. 2013), pp. 1117–1129. DOI: 10.3189/2013JoG13J068 (cited on page 34).

[158] M. G. Aartsen et al. "Measurement of South Pole ice transparency with the IceCube LED calibration system". In: *Nuclear Instruments and Methods in Physics Research Section A: Accelerators, Spectrometers, Detectors and Associated Equipment* 711 (May 2013), pp. 73–89. DOI: 10.1016/j.nima.2013.01.054 (cited on pages 34, 35).

[159] K. Woschnagg and D. Chirkin. "Age vs depth of glacial ice at South Pole". In: *Geophysical Research Letters* 27 (July 2000), pp. 2129–2132. DOI: 10.1029/2000GL011351 (cited on page 34).

[160] R. Abbasi et al. "In situ estimation of ice crystal properties at the South Pole using LED calibration data from the IceCube Neutrino Observatory". In: *The Cryosphere* 18.1 (2024), pp. 75–102. DOI: 10.5194/tc-18-75-2024 (cited on pages 35, 51, 77).

[161] D. Chirkin et al. "An improved mapping of ice layer undulations for the IceCube Neutrino Observatory". In: *PoS* ICRC2023 (2023), p. 975. DOI: 10.22323/1.444.0975 (cited on page 35).

[162] D. Hahn. "Light Scattering Theory". In: (Jan. 2004) (cited on page 35).

[163] D. Chirkin and IceCube Collaboration. "Evidence of optical anisotropy of the South Pole ice". In: *International Cosmic Ray Conference*. Vol. 33. International Cosmic Ray Conference. Jan. 2013, p. 3338 (cited on pages 35, 58).

[164] M. Usner. "Search for Astrophysical Tau-Neutrinos in Six Years of High-Energy Starting Events in the IceCube Detector". PhD thesis. Humboldt-Universität zu Berlin, Mathematisch-Naturwissenschaftliche Fakultät, 2018. DOI: http://dx.doi.org/10.18452/19458 (cited on pages 35, 47, 50, 52–54, 56, 58, 60, 67, 109).

[165] D. Chirkin and M. Rongen. "Light diffusion in birefringent polycrystals and the IceCube ice anisotropy". In: *PoS* ICRC2019 (2019), p. 854 (cited on page 35).

[166] R. Abbasi et al. "A calibration study of local ice and optical sensor properties in IceCube". In: *PoS* ICRC2021 (2021), p. 1023. DOI: 10.22323/1.395.1023 (cited on page 35).

[167] D. Chirkin and W. Rhode. "Propagating leptons through matter with Muon Monte Carlo (MMC)". In: (Aug. 2004) (cited on pages 37, 38, 46).

[168] L. Radel and C. Wiebusch. "Calculation of the Cherenkov light yield from electromagnetic cascades in ice with Geant4". In: *Astropart. Phys.* 44 (2013), pp. 102–113. DOI: 10.1016/j.astropartphys.2013.01.015 (cited on pages 37, 39, 46).

[169] L. D. Landau and I. Pomeranchuk. "Limits of applicability of the theory of bremsstrahlung electrons and pair production at high-energies". In: *Dokl. Akad. Nauk Ser. Fiz.* 92 (1953), pp. 535–536 (cited on page 37).

[170] L. D. Landau and I. Pomeranchuk. "Electron cascade process at very high-energies". In: *Dokl. Akad. Nauk Ser. Fiz.* 92 (1953), pp. 735–738 (cited on page 37).

[171] A. B. Migdal. "Bremsstrahlung and Pair Production in Condensed Media at High Energies". In: *Phys. Rev.* 103 (6 Sept. 1956), pp. 1811–1820. DOI: 10.1103/PhysRev.103.1811 (cited on page 37).

[172] C. A. Argüelles et al. "Tau depolarization at very high energies for neutrino telescopes". In: *Phys. Rev. D* 106.4 (2022), p. 043008. DOI: 10.1103/PhysRevD.106.043008 (cited on page 38).

[173] P. A. Cherenkov. "Visible radiation produced by electrons moving in a medium with velocities exceeding that of light". In: *Phys. Rev.* 52.4 (1937), pp. 378–379. DOI: 10.1103/PhysRev.52.378 (cited on page 39).

[174] I. M. Frank and I. E. Tamm. "Coherent visible radiation of fast electrons passing through matter". In: *Compt. Rend. Acad. Sci. URSS* 14.3 (1937). Ed. by V. L. Ginzburg, B. M. Bolotovsky, and I. M. Dremin, pp. 109–114. DOI: 10.3367/UFNr.0093.196710o.0388 (cited on page 39).

[175] M. G. Aartsen et al. "Energy Reconstruction Methods in the IceCube Neutrino Telescope". In: *JINST* 9 (2014), P03009. DOI: 10.1088/1748-0221/9/03/P03009 (cited on pages 40, 50, 58).

[176] D. F. Cowen. "Tau neutrinos in IceCube". In: *J. Phys. Conf. Ser.* 60 (2007). Ed. by F. Halzen, A. Karle, and T. Montaruli, pp. 227–230. DOI: 10.1088/1742-6596/60/1/048 (cited on pages 40, 41).

[177] J. G. Learned and S. Pakvasa. "Detecting tau-neutrino oscillations at PeV energies". In: *Astropart. Phys.* 3 (1995), pp. 267–274. DOI: 10.1016/0927-6505(94)00043-3 (cited on page 41).

[178] A. M. Dziewonski and D. L. Anderson. "Preliminary reference earth model". In: *Phys. Earth Planet. Interiors* 25 (1981), pp. 297–356. DOI: 10.1016/0031-9201(81)90046-7 (cited on page 44).

[179] F. Halzen and D. Saltzberg. "Tau-neutrino appearance with a 1000 megaparsec baseline". In: *Physical Review Letters* 81 (1998), pp. 4305–4308 (cited on page 44).

[180] D. Heck et al. "CORSIKA: A Monte Carlo code to simulate extensive air showers". In: (Feb. 1998) (cited on page 44).

[181] J. van Santen. "Neutrino Interactions in IceCube above 1 TeV: Constraints on Atmospheric Charmed-Meson Production and Investigation of the Astrophysical Neutrino Flux with 2 Years of IceCube Data taken 2010–2012". PhD thesis. Wisconsin U., Madison, Nov. 2014 (cited on pages 45, 51).

[182] J. H. Koehne et al. "PROPOSAL: A tool for propagation of charged leptons". In: *Comput. Phys. Commun.* 184 (2013), pp. 2070–2090. DOI: 10.1016/j.cpc.2013.04.001 (cited on page 46).

[183] B. Voigt. "Sensitivity of the IceCube detector for ultra-high energy electron-neutrino events". PhD thesis. Humboldt-UniversitÃ¤t zu Berlin, Mathematisch-Naturwissenschaftliche FakultÃ¤t I, 2008. DOI: http://dx.doi.org/10.18452/15850 (cited on page 46).

[184] L. Rädel and C. Wiebusch. "Calculation of the Cherenkov light yield from low energetic secondary particles accompanying high-energy muons in ice and water with Geant 4 simulations". In: *Astroparticle Physics* 38 (June 2012) (cited on page 46).

[185] C. Kopper. *Photons from IceCube Muon*. URL: https://www.psu.edu/news/research/story/national-science-foundation-funds-supercomputer-cluster-penn-state (cited on page 46).

[186] C. Kopper. *Clsim*. URL: https://github.com/claudiok/clsim (cited on page 46).

[187] D. Chirkin. "Photon tracking with GPUs in IceCube". In: *Nuclear Instruments and Methods in Physics Research Section A: Accelerators, Spectrometers, Detectors and Associated Equipment* 725 (2013), pp. 141–143. DOI: https://doi.org/10.1016/j.nima.2012.11.170 (cited on page 46).

[188] N. Whitehorn, J. van Santen, and S. Lafebre. "Penalized splines for smooth representation of high-dimensional Monte Carlo datasets". In: *Computer Physics Communications* 184.9 (2013), pp. 2214–2220. DOI: https://doi.org/10.1016/j.cpc.2013.04.008 (cited on pages 47, 50).

[189] R. Abbasi et al. "Calibration and characterization of the IceCube photomultiplier tube". In: *Nuclear Instruments and Methods in Physics Research Section A: Accelerators, Spectrometers, Detectors and Associated Equipment* 618.1 (2010), pp. 139–152. DOI: https://doi.org/10.1016/j.nima.2010.03.102 (cited on page 47).

[190] M. G. Aartsen et al. "Efficient propagation of systematic uncertainties from calibration to analysis with the SnowStorm method in IceCube". In: *JCAP* 10 (2019), p. 048. DOI: 10.1088/1475-7516/2019/10/048 (cited on pages 47, 67).

[191] E. Ganster. "Measurement of the high-energy astrophysical neutrino energy spectrum combining muon tracks and cascades measured at the IceCube Neutrino Observatory". PhD thesis. RWTH Aachen University, RWTH Aachen U., 2024 (cited on page 48).

[192] R. Naab. "Evidence for a Break in the Diffuse Extragalactic Neutrino Spectrum". PhD thesis. Humboldt-Universität zu Berlin, Mathematisch-Naturwissenschaftliche Fakultät, 2024 (cited on pages 48, 67, 68, 73).

[193] M. G. Aartsen et al. "Atmospheric and astrophysical neutrinos above 1 TeV interacting in IceCube". In: *Phys. Rev. D* 91 (2 Jan. 2015), p. 022001. DOI: 10.1103/PhysRevD.91.022001 (cited on page 49).

[194] C. Arguelles Delgado et al. "Unified atmospheric neutrino passing fractions for large-scale neutrino telescopes". In: *Journal of Cosmology and Astroparticle Physics* 2018 (July 2018), pp. 047–047. DOI: 10.1088/1475-7516/2018/07/047 (cited on pages 49, 50).

[195] T. Yuan et al. *nuVeto*. URL: https://github.com/tianluyuan/nuVeto (cited on page 50).

[196] A. Fedynitch et al. "Calculation of conventional and prompt lepton fluxes at very high energy". In: *EPJ Web Conf.* 99 (2015). Ed. by D. Berge et al., p. 08001. DOI: 10.1051/epjconf/20159908001 (cited on pages 50, 66).

[197] T. Yuan. "Detecting neutrinos in IceCube with Cherenkov light in the South Pole ice". In: *Nucl. Instrum. Meth. A* 1054 (2023), p. 168440. DOI: 10.1016/j.nima.2023.168440 (cited on pages 50, 77).

[198] J. Stachurska. "Astrophysical Tau Neutrinos in IceCube". PhD thesis. Humboldt-Universität zu Berlin, Mathematisch-Naturwissenschaftliche Fakultät, 2020. DOI: http://dx.doi.org/10.18452/21611 (cited on pages 53, 56, 59, 67, 89, 109).

[199] D. Garg et al. "Neutrino propagation in the Earth and emerging charged leptons with nuPyProp". In: *JCAP* 01 (2023), p. 041. DOI: 10.1088/1475-7516/2023/01/041 (cited on page 57).

[200] C. A. Argüelles et al. "Tau depolarization at very high energies for neutrino telescopes". In: *Phys. Rev. D* 106.4 (2022), p. 043008. DOI: 10.1103/PhysRevD.106.043008 (cited on page 57).

[201] G.-y. Huang, M. Lindner, and N. Volmer. "Inferring astrophysical neutrino sources from the Glashow resonance". In: *JHEP* 11 (2023), p. 164. DOI: 10.1007/JHEP11(2023)164 (cited on pages 57, 58).

[202] A. Garcia et al. "Complete predictions for high-energy neutrino propagation in matter". In: *JCAP* 09 (2020), p. 025. DOI: 10.1088/1475-7516/2020/09/025 (cited on page 57).

[203] R. Gauld. "Precise predictions for multi-TeV and PeV energy neutrino scattering rates". In: *Phys. Rev. D* 100.9 (2019), p. 091301. DOI: 10.1103/PhysRevD.100.091301 (cited on page 57).

[204] A. Loewy, S. Nussinov, and S. L. Glashow. "The Effect of Doppler Broadening on the 6.3 PeV W^- Resonance in $\bar{\nu}_e e^-$ Collisions". In: (July 2014) (cited on pages 57, 58).

[205] O. Behnke and L. Moneta. *Parameter Estimation*. John Wiley and Sons, Ltd, 2013. Chap. 2, pp. 27–73 (cited on page 62).

[206] S. S. Wilks. "The Large-Sample Distribution of the Likelihood Ratio for Testing Composite Hypotheses". In: *Annals Math. Statist.* 9.1 (1938), pp. 60–62. DOI: 10.1214/aoms/1177732360 (cited on pages 63, 87, 111).

[207] G. J. Feldman and R. D. Cousins. "Unified approach to the classical statistical analysis of small signals". In: *Phys. Rev. D* 57 (7 Apr. 1998), pp. 3873–3889. DOI: 10.1103/PhysRevD.57.3873 (cited on page 63).

[208] B. Sen, M. Walker, and M. Woodroofe. "On the unified method with nuisance parameters". In: *Statistica Sinica* 19 (Jan. 2009), pp. 301–314 (cited on page 63).

[209] G. Cowan et al. "Asymptotic formulae for likelihood-based tests of new physics". In: *Eur. Phys. J. C* 71 (2011). [Erratum: Eur.Phys.J.C 73, 2501 (2013)], p. 1554. DOI: 10.1140/epjc/s10052-011-1554-0 (cited on pages 63, 64, 90, 115).

[210] C. A. Argüelles, A. Schneider, and T. Yuan. "A binned likelihood for stochastic models". In: *JHEP* 06 (2019), p. 030. DOI: 10.1007/JHEP06(2019)030 (cited on page 64).

[211] T. K. Gaisser. "Spectrum of cosmic-ray nucleons, kaon production, and the atmospheric muon charge ratio". In: *Astroparticle Physics* 35.12 (2012), pp. 801–806. DOI: https://doi.org/10.1016/j.astropartphys.2012.02.010 (cited on page 66).

[212] F. Riehn et al. "The hadronic interaction model SIBYLL 2.3c and Feynman scaling". In: *PoS* ICRC2017 (2018), p. 301. DOI: 10.22323/1.301.0301 (cited on page 66).

[213] H. M. Niederhausen. “Measurement of the High Energy Astrophysical Neutrino Flux Using Electron and Tau Neutrinos Observed in Four Years of IceCube Data”. PhD thesis. Stony Brook U., 2018 (cited on page 66).

[214] G. D. Barr et al. “Uncertainties in Atmospheric Neutrino Fluxes”. In: *Phys. Rev. D* 74 (2006), p. 094009. DOI: 10.1103/PhysRevD.74.094009 (cited on page 66).

[215] A. Fedynitch and M. Huber. “Data-driven hadronic interaction model for atmospheric lepton flux calculations”. In: *Phys. Rev. D* 106.8 (2022), p. 083018. DOI: 10.1103/PhysRevD.106.083018 (cited on page 67).

[216] P. Eller et al. “A model independent parametrization of the optical properties of the refrozen IceCube drill holes”. In: *PoS* ICRC2023 (2023), p. 1034. DOI: 10.22323/1.444.1034 (cited on page 69).

[217] N. Lad et al. “Summary of IceCube tau neutrino searches and flavor composition measurements of the diffuse astrophysical neutrino flux”. In: *PoS* ICRC2023 (2023), p. 1122. DOI: 10.22323/1.444.1122 (cited on pages 70, 102).

[218] V. Basu et al. “From PeV to TeV: Astrophysical Neutrinos with Contained Vertices in 10 years of IceCube Data”. In: *PoS* ICRC2023 (2023), p. 1007. DOI: 10.22323/1.444.1007 (cited on page 93).

[219] M. G. Aartsen et al. “IceCube-Gen2: the window to the extreme Universe”. In: *Journal of Physics G: Nuclear and Particle Physics* 48.6 (2021), p. 060501. DOI: 10.1088/1361-6471/abbd48 (cited on page 95).

[220] A. Ishihara. “The IceCube Upgrade - Design and Science Goals”. In: *PoS* ICRC2019 (2021), p. 1031. DOI: 10.22323/1.358.1031 (cited on page 95).

[221] IceCube Collaboration and F. Schröder. *IceCube-Gen2 Surface Array: Science Case and Plans*. Vortrag gehalten auf DPG Frühjahrstagung: Fachverband Teilchenphysik (2024), Karlsruhe, Deutschland, 4.–8. März 2024. 51.13.04; LK 01. 2024 (cited on page 95).

[222] G. A. Askar’yan. “Excess negative charge of an electron-photon shower and its coherent radio emission”. In: *Zh. Eksp. Teor. Fiz.* 41 (1961), pp. 616–618 (cited on page 96).

[223] Z. S. Meyers et al. *Radio Detection of EeV Neutrinos in Dielectric Media using the Askaryan Effect* *for Babies*. DESY, 2021, pp. 1–14 (cited on page 96).

[224] R. "Abbasi and others". *The IceCube Gen2 Technical Design Report*. https://icecube-gen2.wisc.edu/wp-content/uploads/2023/07/IceCube_Gen2_TDR_0.05_July27.2023_Part_I_and_II.pdf. [Accessed 18-06-2024]. 2023 (cited on pages 96, 97, 104).

[225] L. Classen et al. “The mDOM - A multi-PMT digital optical module for the IceCube-Gen2 neutrino telescope”. In: *PoS* ICRC2017 (2017), p. 1047. DOI: 10.22323/1.301.1047 (cited on page 97).

[226] L. Classen et al. “A multi-PMT Optical Module for the IceCube Upgrade”. In: *PoS* ICRC2019 (2019), p. 855. DOI: 10.22323/1.358.0855 (cited on page 97).

[227] R. Abbasi et al. “D-Egg: a dual PMT optical module for IceCube”. In: *JINST* 18.04 (2023), P04014. DOI: 10.1088/1748-0221/18/04/P04014 (cited on page 97).

[228] M. "Aartsen et al. “Letter of Intent: The Precision IceCube Next Generation Upgrade (PINGU)”. In: *E-Print: arXiv* 1401.2046 [physics.ins-det] (Jan. 2014) (cited on page 97).

[229] A. Omeliukh. “Optimization of the optical array geometry for IceCube-Gen2”. Master’s thesis. Kyiv, Ukraine: Taras Schevchenko national University of Kyiv, 2021 (cited on page 97).

[230] M. Bustamante, J. F. Beacom, and W. Winter. “Theoretically Palatable Flavor Combinations of Astrophysical Neutrinos”. In: *Phys. Rev. Lett.* 115 (16 Oct. 2015), p. 161302. DOI: 10.1103/PhysRevLett.115.161302 (cited on pages 100, 103).

[231] A. Coleman et al. “The flavor composition of ultra-high-energy cosmic neutrinos: measurement forecasts for in-ice radio-based EeV neutrino telescopes”. In: (Feb. 2024) (cited on page 100).

[232] J. van Santen et al. “toise: a framework to describe the performance of high-energy neutrino detectors”. In: *Journal of Instrumentation* 17.08 (2022), T08009. DOI: 10.1088/1748-0221/17/08/t08009 (cited on page 100).

[233] N. Lad et al. “Sensitivity of IceCube-Gen2 to measure flavor composition of Astrophysical neutrinos”. In: *PoS* ICRC2023 (2023), p. 1123. DOI: 10.22323/1.444.1123 (cited on page 102).

[234] M. G. Aartsen et al. “In-situ calibration of the single-photoelectron charge response of the IceCube photomultiplier tubes”. In: *JINST* 15.06 (2020), P06032. DOI: 10.1088/1748-0221/15/06/P06032 (cited on page 109).